Optics on materials with strong spin-orbit coupling: topological insulators $Bi_{2-x}Sb_xTe_{3-y}Se_y$ and the $j = 1/2$ compounds Na_2IrO_3 and α-$RuCl_3$

Inaugural-Dissertation

zur

Erlangung des Doktogrades

der Mathematisch-Naturwissenschaftlichen Fakultät

der Universität zu Köln

vorgelegt von

Nick Borgwardt

aus Berlin-Neukölln

Köln 2019

Berichterstatter: Prof. Dr. Markus Grüninger
(Gutachter)

Prof. Dr. Paul H. M. van Loosdrecht

Tag der mündlichen Prüfung: 19.06.2018

Contents

1 Introduction 1

1.1 Strong spin-orbit coupling 1

1.2 Outline 2

I Optical response of matter 3

2 Light as electromagnetic wave 5

2.1 Dielectric function 5

2.2 Linear response 7

2.3 Interfaces 9

2.4 Multilayer systems 11

2.5 Thin film 15

3 Models and relations 17

3.1 Lorentz oscillator 17

3.2 Drude oscillator 18

3.3 Tauc-Lorentz oscillator 19

3.4 Fano line shape 19

3.5 Franck-Condon principle 20

3.6 Kramers-Kronig relation 20

3.7 Maxwell Garnett approximation 21

II Methods 23

4 Measuring instruments 25

4.1 FTIR spectrometer 25

4.2 THz spectrometer 27

4.3 Ellipsometer 27

5 Data analysis 29

5.1 Inverting transmittance and reflectance 29

5.2 Modeling the transmittance and reflectance 29
5.3 Analysis of Fabry-Pérot fringes 30
5.4 Determining the n from R 31

III Topological insulators 33

6 Introduction to topological insulators 35
6.1 Band inversion 35
6.2 Chern number 35
6.3 Topologically protected surface states 36
6.4 Compensated semiconductors 39

7 Thin films of topologically insulating $(\mathrm{Bi}_x\mathrm{Sb}_{1-x})_2\mathrm{Te}_3$ 47
7.1 Crystal structure and fundamental properties 47
7.2 Data and analysis for $\mathrm{Bi_2Te_3}$ 51
7.3 Thin film of compensated $(\mathrm{Bi}_{0.57}\mathrm{Sb}_{0.43})_2\mathrm{Te}_3$ 59

8 Compensated topological insulators 65
8.1 $\mathrm{BiSbTeSe_2}$ 66
8.2 $\mathrm{Bi}_{2-x}\mathrm{Sb}_x\mathrm{Te}_{3-y}\mathrm{Se}_y$ 94
8.3 Summary 105

IV Spin-orbit-entangled Mott insulators 107

9 Introduction to spin-orbit-entangled Mott insulators 109
9.1 Mott insulators 109
9.2 Hubbard model 110
9.3 From spherical harmonics to the $j = 1/2$ groundstate 110

10 Results on spin-orbit-entangled Mott insulators 125
10.1 $4d^5$ Mott insulator α-$\mathrm{RuCl_3}$ 125
10.2 $\mathrm{Na_2IrO_3}$ 140

V Appendix 151

Abstract

We performed temperature-dependent infrared transmittance and reflectance measurements on topological insulators and spin-orbit-entangled Mott insulators. Both material classes exhibit strong spin-orbit coupling which gives rise to topologically protected phases. Potential applications are hindered, due to various deviations of the synthesized crystals from the ideal topological insulator or spin-orbit-entangled Mott insulators, respectively. In this thesis several promising candidates for the realization of either models are investigated.

For topological insulators the bulk conductivity poses a problem. We report on thickness-dependent data on thin films of $\mathrm{Bi_2Te_3}$ which show that the bulk optical conductivity $\sigma_1(\omega)$ superimposes the surface conductance. Therefore, we continue the search for signatures of the surface state on compensated $\mathrm{(Bi_{0.57}Sb_{0.43})_2Te_3}$, for which we report on a very low $\sigma_1(\omega)$, but we find no direct evidence for the topologically protected surface state. The compensation of topological insulators can be performed more sophisticated by partly substituting Te with Se. Thereby, the family of topological insulators $\mathrm{Bi}_{2-x}\mathrm{Sb}_x\mathrm{Te}_{3-y}\mathrm{Se}_y$ with insulating behavior is created. Nevertheless, compensated topological insulators have a reduced activation energy compared to the intrinsic gap, which is usually attributed to impurity band. Lately, the formation of charge puddles in compensated topological insulators, due to the random distribution of defects, thus reducing the activation energy, was predicted. We report on the experimental verification of charge puddles and reveal the highly non-monotonic temperature dependence of them. Additionally, we describe, in collaboration with the group of Prof. Rosch of the Institute for Theoretical Physics at the University of Cologne, the observations semiquantitatively by Monte Carlo simulations. Thereby, we gain insight into, *e.g.*, the defect density and the level of compensation depending on the composition which allows to choose the composition best suited the each purpose.

One of the thrilling phenomena in Kitaev physics is the occurrence of a quantum spin liquid in the ground state. However, finite Heisenberg exchange due to a trigonal crystal field or finite mixing of the t_{2g} and e_g states, causes deviations from pure $j = 1/2$ states, which results in a zigzag-ordered ground state instead of the sought-after quantum spin liquid. Due to these deviations even the formation of quasi-molecular orbitals instead of local $j = 1/2$ states was suggested for $\mathrm{RuCl_3}$ and $\mathrm{Na_2IrO_3}$. We investigate $\sigma_1(\omega)$ and identify different excitations, thereby gaining insight into the underlying physics. In $\alpha-\mathrm{RuCl_3}$ we reveal the single, double, and triple spin-orbit exciton. Hence, local $j = 1/2$ states are formed in this compound. For $\mathrm{Na_2IrO_3}$ precise predictions on the optical spectrum depending on the underlying physics allow us to conclude from $\sigma_1(\omega)$ that the local $j = 1/2$ scenario is appropriate. Furthermore, we report on signatures of a controversially discussed peak obtained by RIXS, in the optical spectrum including magnon sidebands.

Zusammenfassung

Wir führen temperaturabhängige infrarot Transmissions- und Reflektionsmessungen an topologischen Isolatoren, sowie an Spin-Bahn-entartete Mott-Isolatoren durch. Beide Materialklassen weisen starke Spin-Bahn-Wechselwirkung auf, welche topologisch geschützte Phasen verursachen. Potentielle Anwendungen werden durch verschiedene Abweichungen der hergestellten Kristalle von einem idealen topologischen Isolator, bzw. idealen Spin-Bahn-entartete Mott-Isolatoren verhindert. In dieser Arbeit werden mehrere vielversprechende Kandidaten für die Realisation beider Modelle untersucht. Bei topologischen Isolatoren stellt die Volumenleitfähigkeit ein Problem dar. Wir berichten von dickenabhängigen Daten, die an dünnen Filmen von $\mathrm{Bi_2Te_3}$ gemessen wurden und zeigen, dass die Volumenleitfähigkeit den Oberflächenleitwert überlagert. Deshalb suchen wir nach Hinweisen auf den topologischen Oberflächenzustand bei kompensierten topologischen Isolatoren BiSbTe weiter. Für $(\mathrm{Bi_{0.57}Sb_{0.43}})_2\mathrm{Te_3}$ finden wir sehr kleine $\sigma_1(\omega)$, allerdings keine direkten Belege für topologisch geschützt Oberflächenzustände. Die Kompensation von topologischen Isolatoren kann raffinierter betrieben werden, indem man Te teilweise mit Se ersetzt. Dabei erzeugt man die Familie der topologischen Isolatoren $\mathrm{Bi}_{2-x}\mathrm{Sb}_x\mathrm{Te}_{3-y}\mathrm{Se}_y$, die isolierend im Volumen ist. Allerdings weisen kompensierte topologische Isolatoren eine kleiner Aktivierungsenergie im Vergleich zu ihrer Bandlücke auf. Dies wird häufig mit Defektbändern in Zusammenhang gebracht. Vor Kurzem wurde vorhergesagt, dass Pfützen von Ladungsträgern in kompensierten topologischen Isolatoren entstehen, welche die reduzierte Aktivierungsenergie verursachen. Wir konnten die Ladungsträger Pfützen experimentell nachweisen und beobachteten ihr stark nicht monotones Verhalten. Zusätzlich konnten wir, in Kollaboration mit der Gruppe von Prof. Rosch aus dem Institut für theoretische Physik der Universität zu Köln, die Beobachtungen semiquantitativ durch die Monte-Carlo Simulation beschreiben. Dabei erhielten wir Einblick in, z.B. die Defektdichte und den Grad der Kompensation, abhängig von der Zusammensetzung. Dies erlaubt es die richtige Zusammensetzung für die entsprechende Anforderung zu wählen. Eins der spannendsten Phänomene der Kitaev-Physik ist das Auftreten von Quanten-Spin-Flüssigkeiten im Grundzustand. Allerdings führt endlicher Heisenberg Austausch, durch trigonales Kristallfeld oder endliches Mischen zwischen t_{2g} und e_g Zuständen zu Abweichungen von reinen $j = 1/2$ Zuständen, was im Zickzack geordneten Grundzustand anstatt der gewünschten Quanten-Spin-Flüssigkeit resultiert. Wegen dieser Abweichungen wurde die Bildung von Quasi-molekularen Orbitalen, anstatt von lokalen $j = 1/2$ Zuständen in $\mathrm{Na_2IrO_3}$ und $\mathrm{RuCl_3}$ vorgeschlagen. Wir untersuchen $\sigma_1(\omega)$ und finden verschiedene Anregungen, wodurch wir Einsicht in die zugrundeliegenden physikalischen Eigenschaften bekommen. In $\mathrm{RuCl_3}$ haben wir einfache, doppelte und dreifache Spin-Bahn Anregungen entdeckt. Das bedeutet, dass sich lokale $j = 1/2$ Zustände ausgebildet haben. Für $\mathrm{Na_2IrO_3}$ gibt es präzise Vorhersagen bezüglich des optischen Spektrums, in Abhängigkeit von der zugrundeliegenden Physik durch $\sigma_1(\omega)$ können wir darauf schließen, dass das lokale $j = 1/2$ Szenario zutreffend ist. Desweitern finden wir eine Anregung mit Seitenbanden im optischen Spektrum die mit einer kontrovers diskutierten Anregung im

RIXS Spektrum zusammenfällt.

Chapter 1

Introduction

1.1 Strong spin-orbit coupling

Physics is all about distinguishing parts of the reality; cutting the world we have excess to into small processes and finding rules that can predict the outcome of these processes. By now we are way beyond the observations of acceleration, due to a force on a macroscopic object. We gain insight into the world that is hidden to our senses with the help of complex experiments. In order to explain the observations of these experiments, we describe (most) macroscopic objects as accumulation of atoms. Some of these macroscopic objects can transfer charges if a potential difference is applied, others not. The energies of the allowed states for charge carriers in a crystal can be described as bands in k-space. This theory enables us to predict whether a crystal is a metal or an insulator.

The theory of band structure is a great success. But like every theory it has certain restrictions, which require an advanced theory. An important modification was supplied by John Hubbard introducing the Hubbard repulsion which gives the strength of the Coulomb repulsion for hopping to an occupied site [1]. The relevant parameter is the Hubbard repulsion divided by the hopping amplitude U/t. The crystals that are insulating, due to a large Hubbard repulsion are called Mott insulators, see figure 1.1. This theory sufficiently describes the electronic properties of a large variety of crystals. Often the limits of a theory are noticed due to experiments, which are not in agreement with the accepted theory. In the case of topological insulators it was the theory, which was developed in 2005 [3, 4], before the experiment found its prove in 2007 [5]. Topological insulators are a new material class like metals or trivial insulators. Therefore, a lot of attention has been drawn to this new field of physics [6–8] as far as the Nobel prize in 2016. To realize a topological insulator the spin-orbit interaction needs to become the dominant energy in a crystal, see figure 1.1. For most crystals the spin-orbit interaction can be treated as a perturbation. This is not the case for crystals made out of heavy atoms, due to their large atomic number. The topological insulators are not the only new material class, which was discovered by focusing on crystals with strong spin-orbit coupling (SOC). Moreover, considering a large Hubbard repulsion

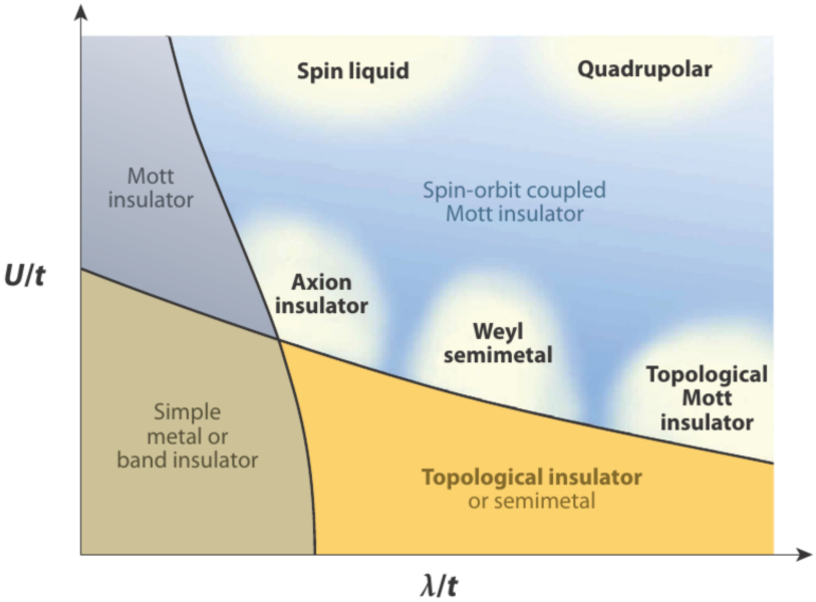

Figure 1.1: The interaction strength U/t and SOC λ/t span the phase diagram where material are distinguished by its electronic properties. The diagram is split into four regions. For the spin-orbit coupled Mott insulator examples are given (bold text). The figure has been taken from reference [2] `https://doi.org/10.1146/annurev-conmatphys-020911-125138` {DOI}. Copyright (2014) by the Annual Reviews.

plus a strong SOC leads us to spin-orbit coupled Mott insulators, which in combination with bond-directional interactions leads to quantum spin-liquid ground states [9, 10].
Both material classes hold great properties, which make them interesting for many applications, especially quantum computing. Even though these fields evolve rapidly, an ideally suited crystal compound for realizing an ideal topological insulator or an ideal spin-orbit-coupled Mott insulator has not been found. A small contribution on this road by investigating the most promising candidates is documented in the following.

1.2 Outline

In the beginning of this thesis we will briefly describe the interactions of electromagnetic waves with solids, before we focus on cases that are close to our experiments. In the following the relevant models and relations are summarized. We introduce the different experimental setups that were used and sketch the general analysis of the optical data.
The results are split into two main parts. The first part deals with thin films of topological insulators and single crystals of topological insulators, especially with effects resulting from compensation. The second part discusses the results on the spin-orbit-entangled Mott insulators $\alpha-\mathrm{RuCl}_3$ and $\mathrm{Na}_2\mathrm{IrO}_3$. Here, the focus lies on understanding the ground state by the observed excitations, which is assisted by sketching the relevant calculations.

Part I

Optical response of matter

Chapter 2

Light as electromagnetic wave

A complete description of the optical response of matter can only be given by quantum electrodynamics. However, in this part of the thesis the focus lies on the effects that are needed to describe the experimental results, which can often be described in a classical or pseudo-classical picture.

2.1 Dielectric function

Light is an electromagnetic transverse wave. The amplitude of the electromagnetic wave is given by the vector of the electric field or the magnetic field. Their direction is called the polarization direction. They are perpendicular to each other and to the propagation direction. The wave equation can be derived by the Maxwell equations. In the absence electric charges or currents the two needed Maxwell equations are

$$rot\mathbf{E} = -\frac{\partial \mathbf{B}}{\partial t}, \tag{2.1.1}$$

and

$$rot\mathbf{B} = \mu_0 \epsilon_0 \frac{\partial \mathbf{E}}{\partial t}, \tag{2.1.2}$$

where ϵ_0 is the vacuum permittivity and μ_0 the vacuum permeability. By combining the equations, we get a new equation, which is

$$rot(rot\mathbf{E}) = -\mu_0 \epsilon_0 \frac{\partial^2 \mathbf{E}}{\partial t^2}. \tag{2.1.3}$$

With the information, that we have no free charges, $div\mathbf{E} = 0$, we obtain the wave equation

$$(\frac{\partial}{\partial x^2} + \frac{\partial}{\partial y^2} + \frac{\partial}{\partial z^2})\mathbf{E}(\mathbf{r}, t) = \Delta\mathbf{E}(\mathbf{r}, t) = \mu_0 \epsilon_0 \frac{\partial^2 \mathbf{E}(\mathbf{r}, t)}{\partial t^2}. \tag{2.1.4}$$

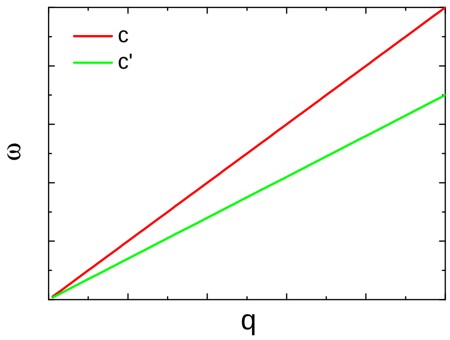

Figure 2.1: Dispersion of light in vacuum (red curve) and in a medium with a constant refractive index larger than 1 (green curve).

The solution of this equation yields the equation for the electromagnetic wave

$$\mathbf{E}(\mathbf{r},t) = \mathbf{E}(\mathbf{q},w)\exp(i(\mathbf{qr}-\omega t)). \tag{2.1.5}$$

The spatial coordinate is given by $\mathbf{r}$, the wave vector is given by $\mathbf{q}$, and the angular frequency is given by ω. In equation 2.1.4 the prefactor $\mu_0\epsilon_0$ can be replaced by the speed of light c in vacuum, yielding

$$c = \frac{1}{\sqrt{\mu_0\epsilon_0}}. \tag{2.1.6}$$

The solution of the equation 2.1.5 plugged into the wave equation 2.1.4 gives the linear dispersion (for a constant refractive index) of a photon

$$\omega = c \cdot q. \tag{2.1.7}$$

The speed of light in a medium is

$$c' = \frac{1}{\sqrt{\mu_0\mu_r\epsilon_0\epsilon_r}}, \tag{2.1.8}$$

where μ_r denotes the relative permeability and ϵ_r the relative permittivity of the medium. Besides the wave character, light has the character of a particle according to wave-particle dualism, developed mainly by Max Planck, Einstein, Louis de Broglie, Arthur Compton, Niels Bohr [11]. The particle is called photon. It has an energy

$$E = h\nu \tag{2.1.9}$$

and a momentum

$$p = \frac{h}{\lambda}, \tag{2.1.10}$$

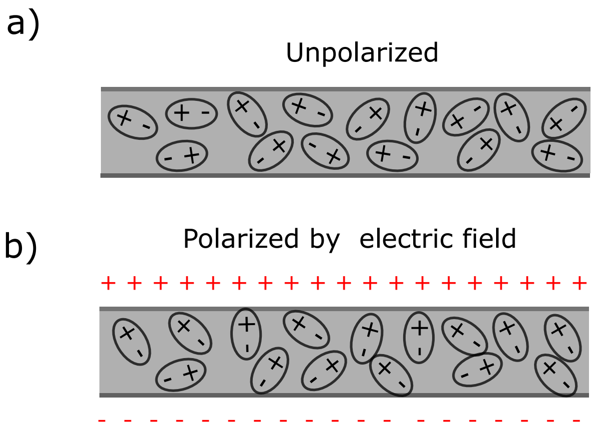

Figure 2.2: a) Unpolarized solid with randomly distributed dipoles b) Aligned dipoles, giving rise to a polarization of the solid.

where h is the Plank constant, ν the frequency and λ the wavelength. Whether the particle or the wave properties are observed depends on the experimental setup. Most of the phenomena in linear optics can be described with the wave character of light.

2.2 Linear response

The linear response has its name from the case if an electric field penetrating a medium and the medium responds with a linear polarization

$$\mathbf{P} = (\epsilon - 1)\epsilon_0\mathbf{E} = \chi\epsilon_0\mathbf{E}. \tag{2.2.1}$$

The dielectric function is ϵ and χ is the susceptibility. The linear approach is valid until the strength of the electromagnetic field leads to non-linear effects, like having all dipoles aligned or removing electrons from the atom. The response of the medium can be described by the average polarization of a dipole moment μ_e in the sample. This way the polarization can be expressed as

$$\boldsymbol{P} = N\boldsymbol{\mu}_e, \tag{2.2.2}$$

where denotes N the dipole density. The polarization is the response of the solid to an electrical field $\mathbf{E}$. Therefore, it is linked to the dielectric function by

$$\boldsymbol{P} = \epsilon_0(\epsilon - 1)\mathbf{E}. \tag{2.2.3}$$

In the static case ($\omega = 0$), the dielectric function is a real constant. For $\omega \neq 0$ the dielectric function and therefore, the dielectric susceptibility, are complex and depending on the frequency. This means that they affect the amplitude and the phase of electromagnetic wave. In other words, the polarization and the dissipation are given by the frequency depending complex dielectric function $\epsilon(\mathbf{q},\omega)$. The dielectric function $\epsilon(\mathbf{q},\omega)$ carriers the same information as the frequency-dependent complex optical conductivity $\sigma(\mathbf{q},\omega)$. The relation between both quantities is

$$\epsilon(\mathbf{q},\omega) = 1 + i\frac{\sigma(\mathbf{q},\omega)}{\omega\epsilon_0}. \tag{2.2.4}$$

This equation relates the imaginary (real) part of the dielectric function to the real (imaginary) part of the conductivity

$$\epsilon_1 = 1 - \frac{\sigma_2}{\omega\epsilon_0}, \tag{2.2.5}$$

and

$$\epsilon_2 = \frac{\sigma_1}{\omega\epsilon_0}. \tag{2.2.6}$$

The wave equation 2.1.4 defines the properties of an electromagnetic wave in vacuum. In the case of an electromagnetic wave in matter the Maxwell equation 2.1.2 needs to be modified to

$$rot\mathbf{B} = \epsilon(\mathbf{q},\omega)\cdot\mu_0\epsilon_0\frac{\partial\mathbf{E}}{\partial t}. \tag{2.2.7}$$

Therefore, the states for the photon in matter, so-called polariton, are given by

$$q^2 = \frac{\epsilon(\mathbf{q},\omega)}{c^2}\omega^2. \tag{2.2.8}$$

The polarization is the result of the mixture of a photon and an excitation of the solid, *e.g.*, a phonon. In order to have a mixture of a photon and a phonon, or any other excitation, it is essential to have coupling between the photon and the excitation. This is the case if the excitation has a dipole moment or a dipole moment can be induced by the electromagnetic wave. The phonon dispersion is almost constant from $q = 0$ to the point where the photon dispersion crosses it, since the photon is a massless particle. The dispersion of the polarization, which is transverse, is for small frequencies close to the dispersion of the photon. But when it reaches the frequency of the phonon, it approaches the dispersion of the phonon asymptotically. The dispersion above the frequency of the phonon shows a gap. It depends on the coupling strength between the phonon and the photon; a large coupling causes a large gap. The longitudinal wave causes a macroscopic charge density, in contrast to the case of the transverse wave. Hence, the longitudinal wave costs more energy than the transverse wave. Light with an energy which lies in the gap cannot penetrate the medium. It will be reflected. The reflection of light at the medium is defined by the dielectric function. In this context, it is useful to define the complex refractive index

$$N^2 = (n + i\kappa)^2 = \epsilon, \tag{2.2.9}$$

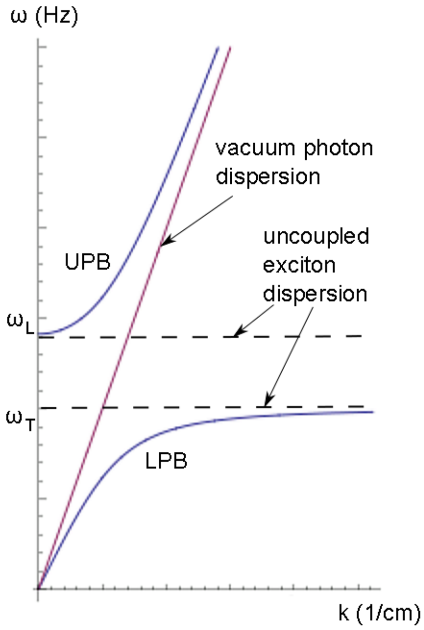

Figure 2.3: Dispersion of a lower polariton branch (LPB) and upper polariton branch (UPB). Dotted lines resemble the uncoupled excitation dispersion. Figure has been taken from reference [12].

where n represents the refractive index and κ the extinction coefficient. The complex refractive index contains the same information as the complex dielectric function or the complex optical conductivity. The refractive index can be used to modify equation 2.1.8 to

$$c = \frac{1}{n\sqrt{\mu_0\epsilon_0}}. \tag{2.2.10}$$

The extinction coefficient defines the absorption in a medium. The intensity of an electromagnetic wave decays with

$$I(r) = I(r=0) \cdot \exp(-2\kappa\frac{\omega}{c}r). \tag{2.2.11}$$

Therefore, the exponent defining the spatial dependence is defined as absorption coefficient

$$\alpha = 2\kappa\frac{\omega}{c}. \tag{2.2.12}$$

The discussed quantities provide the basis for the description of an electromagnetic wave at an interface.

2.3 Interfaces

Photons are particles which interact with charges. Different atoms can have very different charge configurations. The challenge is to describe the interaction of large amounts of photons with large amounts of atoms, which further interact with each other. The problem seems to be extremely complex. Nevertheless, many questions concerning the interaction have an easy answer. The common method is to apply Maxwell's equations to the interface and satisfy the boundary conditions. In certain cases the solution is even simpler.

Let us assume that the interface is the interface of a homogenous and isotropic medium. Suppose that the electric field is not large enough to cause non-linear effects. Furthermore, no scattering or absorption is present at the interface. The plane of incidence is defined by the normal of the interface and the wave vector of the incoming light. In the general case, the incoming light is partly polarized parallel and partly polarized orthogonal to the plane of incidence.

In the simplest case the incident of light is normal to the surface of the sample with light completely polarized perpendicular to the normal of the interface. In this case the ratio of the amplitude of incoming electromagnetic wave E_0 and transmitted electromagnetic wave E_t is given by the transmission coefficient t. The transmission coefficient is given by

$$\frac{E_t}{E_0} = t = \frac{2N_1}{N_1 + N_2}, \tag{2.3.1}$$

where n_1 stands for the complex refractive index of the medium, from where the light penetrates the second medium with the refractive index n_2. The reflection coefficient r is defined as

$$\frac{E_r}{E_0} = r = \frac{N_2 - N_1}{N_1 + N_2}, \tag{2.3.2}$$

where E_r denotes the amplitude of the reflected electromagnetic wave. The amplitude of an electromagnetic wave equals the square root of its intensity, respectively

$$\left(\frac{E_r}{E_0}\right)^2 = \frac{I_r}{I_0} = r^2 = R. \tag{2.3.3}$$

I_r and I_0 is the reflected and the incoming intensity. R is the reflectance. A similar relation is valid for the transmittance T_s of a single interface,

$$\left(\frac{E_t}{E_0}\right)^2 = \frac{I_t}{I_0} = t^2 = T_s. \tag{2.3.4}$$

The transmittance and the reflectance at a lossless interface need to equal unity,

$$T_s + R = 1. \tag{2.3.5}$$

The equation 2.3.1 and 2.3.2 are valid for normal incidence. The angle-dependent formulas need to take the polarization plane into account. This scenario is plotted in figure 2.4. In this case, the transmittance and the reflectance coefficient are given by

$$\left(\frac{E_t}{E_0}\right)_s = t_s = \frac{2N_1 \cos\alpha}{N_1 \cos\alpha + \frac{\mu_1}{\mu_2} N_2 \cos\beta}, \tag{2.3.6}$$

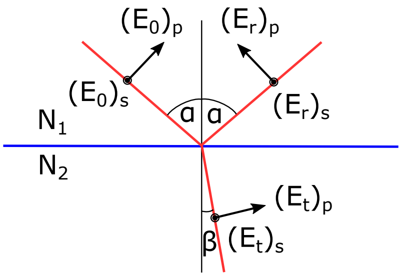

Figure 2.4: The red trajectories stand for the path the electromagnetic wave takes when N$_1$ <N$_2$. The blue line is the border between the indices. The electromagnetic wave is split into the parallel and the perpendicular component.

and

$$\left(\frac{E_r}{E_0}\right)_s = r_s = \frac{N_1 \cos\alpha - \frac{\mu_1}{\mu_2} N_2 \cos\beta}{N_1 \cos\alpha + \frac{\mu_1}{\mu_2} N_2 \cos\beta}, \tag{2.3.7}$$

where μ_1 and μ_2 represent the permeability in first and second medium. The angle α is the smaller angle between the normal of the interface and the incoming light. The angle β is the smaller angle between the normal of the interface and the transmitted light. For parallel polarization two similar formula exist,

$$\left(\frac{E_t}{E_0}\right)_p = t_p = \frac{2N_1 \cos\alpha}{N_1 \cos\beta + \frac{\mu_1}{\mu_2} N_2 \cos\alpha}, \tag{2.3.8}$$

and

$$\left(\frac{E_r}{E_0}\right)_p = r_p = \frac{N_1 \cos\alpha - \frac{\mu_1}{\mu_2} N_2 \cos\beta}{N_1 \cos\beta + \frac{\mu_1}{\mu_2} N_2 \cos\alpha}. \tag{2.3.9}$$

The difference in reflectance for parallel and orthogonal polarized light is made use of in an ellipsometer, see section 4.3. For non-magnetic materials and normal incidence the reflectance R simplifies to

$$\left(\frac{E_r}{E_0}\right)^2 = R = \left(\frac{N_1 - N_2}{N_1 + N_2}\right)^2. \tag{2.3.10}$$

Considering only one interface for a measurement is only possible for reflection at a semi infinite sample. All reflectance measurements with a finite transmittance and all transmittance measurements need to take a second interface into account.

2.4 Multilayer systems

The reflectance and the transmittance of simple multilayer systems can be derived by the laws from section 2.3 and 2.2. In the following the transmittance and reflectance for normal incidence will be investigated for a plane-parallel bar (with N_2). For convenience we will consider the initial medium (with N_1) and the finale medium (with N_3) to have same optical properties, see figure 2.5. Multiple reflections within the bar will take place at the interfaces. Therefore, infinite rays need to be taken into account. A ray is partly reflected and partly transmitted at an interface. By traveling from one interface to the other, a beam collects a phase $\phi = d\frac{n}{c}\omega$ and is absorbed by a factor of $\exp(i\frac{\kappa}{c}\omega d)$. Hence, a ray with x numbers of reflection within the bar can be expressed by a factor of

$$a = \exp(i\frac{N}{c}\omega \cdot dx), \tag{2.4.1}$$

where N denotes the complex refractive index. Each transmitted ray must be transmitted at each interface exactly once. However, each ray has an additional factor t_{12} from the first interface and a factor t_{23} from the second interface. Finally, each transmitted beam has a factor $(r_{23}r_{21})^x$, taking the reflections into account. In total this yields for the transmission coefficient

$$t_{123} = t_{12}^2 \cdot \exp(i\frac{N}{c}\omega d) + t_{12}^2 \cdot (\exp(i\frac{N}{c}\omega d))^3 \cdot r_{23}^2 + t_{12}^2 \cdot (\exp(i\frac{N}{c}\omega d))^5 \cdot r_{23}^4 + ... \tag{2.4.2}$$

This expression can be simplified with the help of the geometric series, to

$$t_{123} = \sum_{x=0}^{\infty} t_{12}^2 \cdot \exp(i\frac{N}{c}\omega d) \left(\exp(i\frac{N}{c}2\omega d) \cdot r_{23}^2\right)^x = t_{12}^2 \cdot \exp(i\frac{N}{c}\omega d) \cdot \frac{1}{1 - \exp(i\frac{N}{c}2\omega d) \cdot r_{23}^2}. \tag{2.4.3}$$

Similar arguments are used to calculate the reflection coefficient of the bar. The result of r_{123} is

$$r_{123} = \frac{r_{12} + r_{21}\exp(i\frac{N}{c}2\omega d)}{1 + r_{12}r_{21}\exp(i\frac{N}{c}2\omega d)}. \tag{2.4.4}$$

The transmission and the reflection coefficient have an frequency-dependent contribution, which causes fringes in the transmittance and the reflectance as a function of frequency. The fringes are called Fabry-Pérot fringes. The period of the fringes depends on the thickness and the refractive index of the bar. Coherent reflections between the interfaces cause different conditions for the superposition of the rays depending on the frequency, see figure 2.5. A maximum in the transmittance is reached when twice the optical path between the two interfaces is an even multiple of the wavelength $\lambda_{vac} = c/\nu$ in vacuum, which can be written as

$$2nd = m\lambda_{vac}, \tag{2.4.5}$$

where d denotes the distance between the interfaces, m an integer and λ_{vac} the wavelength in vacuum. With this formula the refractive index at the maximum can be determined when the order of the maximum is known. Furthermore, the formula can be used to determine the refractive index by assuming that the change of the refractive index is negligible between two maximum. Therefore, we rewrite equation 2.4.5 as function of the frequency of the mth maximum

$$\nu_m = \frac{c}{2nd}m, \tag{2.4.6}$$

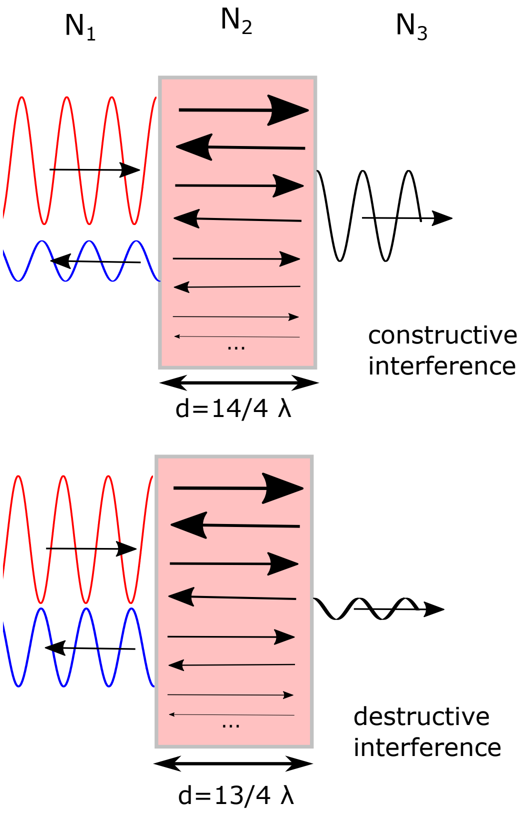

Figure 2.5: The destructive and constructive interference for $\lambda = 4/14 \cdot d$ and $\lambda = 4/13 \cdot d$ is sketched. The red wave represents the initial electromagnetic wave. The blue wave represents the electromagnetic wave which is reflected, while the black wave is the transmitted wave. The black arrows in the bar denote the multiple reflections within the sample. We assume $N_1 = N_3 < N_2$.

and neglect changes in the refractive index for the $(m+1)$th maximum. The result is

$$\nu_{m+1} - \nu_m = \frac{c}{2nd}(m+1-m) = \delta\nu, \tag{2.4.7}$$

with $\delta\nu$ the distance between two maximum in frequency.
For more than two interfaces the above described method for calculating the transmittance and the reflectance is still valid, yet it becomes very costly. A more elegant way to calculate the optical properties, with additional features, uses a transfer-matrix method [13] [14].
The transfer matrix method needs two different types of matrices. The matrix A is the medium boundary matrix. It is a 4×4 matrix that relates the electric and magnetic field at the interface. The second matrix takes the decay and the propagation in between two interfaces into account. It is called the propagation matrix (D). For details see Appendix of Qiu and Bader [13]. An electric field moving through a multilayer system will be reflected many times, transmitted twice and absorbed, but in the end an electric field is reflected into the initial medium and one is transmitted to the final medium (considering a measurement with continuous waves). The calculations are done according to Qiu and Bader [13]. The electric field in the initial medium P_i can be described in general by

$$P_i = \begin{pmatrix} E_s^i \\ E_p^i \\ E_s^r \\ E_p^r \end{pmatrix} = \begin{pmatrix} E_s^i \\ E_p^i \\ r_{ss}E_s^i + r_{sp}E_p^i \\ r_{ps}E_s^i + r_{pp}E_p^i \end{pmatrix}, \tag{2.4.8}$$

and in the final medium by

$$P_f = \begin{pmatrix} E_s^i \\ E_p^i \\ 0 \\ 0 \end{pmatrix} = \begin{pmatrix} t_{ss}E_s^i + t_{sp}E_p^i \\ t_{ps}E_s^i + t_{pp}E_p^i \\ 0 \\ 0 \end{pmatrix}, \tag{2.4.9}$$

where p and s refer to parallel and normal polarization. Accordingly, t_{sp} is the transmission coefficient for s-polarized light transmitted as p-polarized light. This contribution is zero when the dielectric function is a scalar. This description treats the multilayer system as black-box. However, P_i and P_f for a system of N layers can be linked by transfer and propagation matrices in the following way:

$$A_iP_i = A_1D_1A_1^{-1}A_2P_2 = A_1D_1A_1^{-1}A_2D_2A_2^{-1}A_3P_3... = \prod_{m=1}^{N}(A_mD_mA_m^{-1})A_fP_f. \tag{2.4.10}$$

To calculate the total transfer matrix T, which has the form $P_i = TP_f$ the equation needs to be multiplied by A_i^{-1}. The result is

$$T = A_i^{-1} \prod_{m=1}^{N} (A_m D_m A_m^{-1}) A_f. \tag{2.4.11}$$

From this matrix the different transmission and reflection coefficients can be obtained by splitting T into four 2×2 matrices. The matrices G, H, I, and J are defined as

$$T := \begin{pmatrix} G & H \\ I & J \end{pmatrix}. \tag{2.4.12}$$

The transmission coefficients are given by

$$G^{-1} = \begin{pmatrix} t_{ss} & t_{sp} \\ t_{ps} & t_{pp} \end{pmatrix}. \tag{2.4.13}$$

The reflection coefficients are given by

$$IG^{-1} = \begin{pmatrix} r_{ss} & r_{sp} \\ r_{ps} & r_{pp} \end{pmatrix}. \tag{2.4.14}$$

Furthermore, the Kerr rotation ϕ' and the ellipticity ϕ'' are given by

$$\phi_s = \phi_s' + i\phi_s'' = \frac{r_{ps}}{r_{ss}}, \tag{2.4.15}$$

and

$$\phi_p = \phi_p' + i\phi_p'' = \frac{r_{sp}}{r_{pp}}. \tag{2.4.16}$$

2.5 Thin film

Topological insulators harbor a surface state, which has a defined conductance, but no well defined spatial extension. In this case, it is convenient to describe the transmission coefficient of the topological insulator by the $2D$ conductivity σ^{2D}. The transmission coefficients for a thin film are [15]

$$t_{xx} = \frac{4 + 2Z_0\sigma_{xx}^{2D}}{(2 + Z_0\sigma_{xx}^{2D})^2 + (Z_0\sigma 2D_{xy})^2}, \tag{2.5.1}$$

and

$$t_{xy} = \frac{2Z_0\sigma_{xy}^{2D}}{(2 + Z_0\sigma_{xx}^{2D})^2 + (Z_0\sigma 2D_{xy})^2}, \tag{2.5.2}$$

where σ_{xx} and σ_{xy} are the components of the optical conductivity tensor. We convert the transmission coefficients for linear polarized light to the transmission coefficient of circular polarized light $t_\pm$, which results in [16]

$$t_\pm = \frac{2}{1 + n_s + Z_0 \sigma^{2D}_\pm}, \tag{2.5.3}$$

with $Z_0 = (c\epsilon_0)^{-1} = 376.7\Omega$ the impedance of vacuum and n_s the refractive index of the substrate. The rotation angle for circular polarized light is given by

$$\phi_\pm = \arctan \frac{Im(t_\pm)}{Re(t_\pm)} = \mp \arctan \frac{Z_0 |\sigma^{2D}_{xy}|}{1 + n_s}. \tag{2.5.4}$$

The Faraday angle for linear polarized light can be calculated to [17]

$$\theta_F = \frac{1}{2}(\phi_- - \phi_+) = \arctan \frac{Z_0 |\sigma^{2D}_{xy}|}{1 + n_s}. \tag{2.5.5}$$

The Kerr rotation can be derived very similar. The reflection coefficients for a thin film are given by

$$r_{xx} = \frac{1 - (1 + Z_0 \sigma^{2D}_{xx})^2 - (Z_0 \sigma^{2D}_{xy})^2}{(2 + Z_0 \sigma^{2D}_{xx})^2 + (Z_0 \sigma^{2D}_{xy})^2}, \tag{2.5.6}$$

and

$$r_{xy} = \frac{2 Z_0 \sigma^{2D}_{xy}}{(2 + Z_0 \sigma^{2D}_{xx})^2 + (Z_0 \sigma^{2D}_{xy})^2}. \tag{2.5.7}$$

The reflection coefficients yield the two angles for circular polarized light ϕ_- and ϕ_+. The difference of them defines the Kerr angle θ_K to

$$\theta_K = \arctan \left(\frac{1}{Z_0} \frac{2 \sigma^{2D}_{xy}}{(\sigma^{2D}_{xx})^2 + (\sigma^{2D}_{xy})^2 + 2\sigma^{2D}_{xx}/Z_0} \right). \tag{2.5.8}$$

The result for $\sigma_{xx} = 0$ is

$$\theta_K = \arctan \frac{2}{Z_0 \sigma^{2D}_{xy}}. \tag{2.5.9}$$

Chapter 3

Models and relations

3.1 Lorentz oscillator

The transmittance and the reflectance harbor the full information about the dielectric function. By fitting oscillators to the spectra we gain insight to position, strength, and width of the excitations. One of the simplest, but still powerful, models is the Lorentz model. By using the relation between the polarization and the orientation of the dipoles, see equation 2.2.2, the Lorentz model links the dielectric function to the optical spectrum. This is done by considering the solid in the electric field as many forced harmonic oscillators. The motion of the electrons is described by the differential equation

$$m^*\ddot{x} + m^*\gamma\dot{x} + m^*\omega_0^2 = e\mathbf{E}_0\exp(-i\omega t), \tag{3.1.1}$$

where m^* corresponds to the effective mass, ω_0 is the resonance frequency of the oscillator, and γ is a damping term. The distortion gives the polarization, which is linked to dielectric function by equation 2.2.2. However, the dielectric function of the harmonic oscillators is

$$\epsilon(\omega) = 1 + \frac{Ne^2}{\epsilon_0 m^*}\frac{1}{\omega_0^2 - \omega^2 - i\gamma\omega}, \tag{3.1.2}$$

where N is the charge carrier density. The combination of oscillators is additive,

$$\epsilon(\omega) = 1 + \sum_j \frac{\omega_p^2}{\omega_{0,j}^2 - \omega^2 - i\gamma_j\omega}, \tag{3.1.3}$$

where ω_p denotes the plasma frequency. It is defined as the square root of the prefactor in equation 3.1.2

$$\omega_p^2 = \frac{Ne^2}{\epsilon_0 m^*}. \tag{3.1.4}$$

From the integral over the excitation in $\epsilon_2(\omega)$, respectively the plasma frequency, the number of charge carriers can be derived. The equation 3.1.3 can be split into a real part ϵ_1 and an

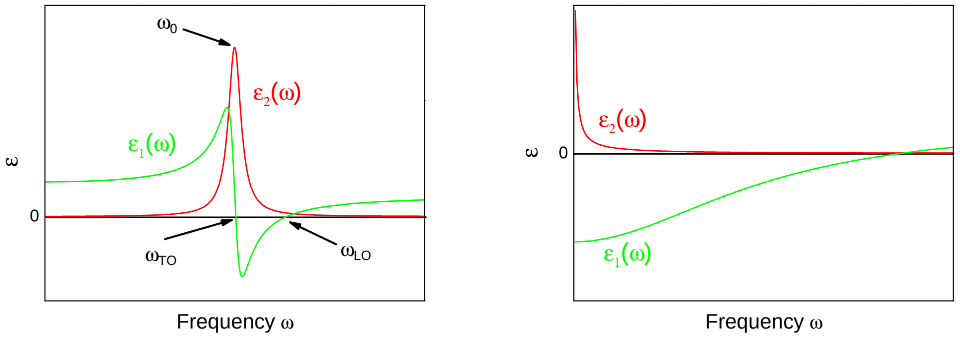

(a) (b)

Figure 3.1: a) The shape of the dielectric function of a phonon with the transverse optical mode ω_{TO} and the longitudinal optical mode ω_{LO}. b) The shape of the dielectric function of a Drude peak.

imaginary part ϵ_2 like

$$\epsilon_1 = 1 + \sum_j \frac{\omega_{p,j}^2(\omega_{0,j}^2 - \omega^2)}{(\omega_{0,j}^2 - \omega^2)^2 + \gamma_j^2\omega^2}, \tag{3.1.5}$$

and

$$\epsilon_2 = i\sum_j (\frac{\omega_{p,j}^2 - \gamma_j\omega)}{(\omega_{0,j} - \omega^2)^2 + \gamma_j^2\omega^2}. \tag{3.1.6}$$

Not all excitations can be described by the upper model for the dielectric function, but two important excitations that can be described are phonons and free charge carriers. In ϵ_2 a phonon is sharp, due to its low scattering rate. The strength of the phonon, the so-called optical weight, is proportional to the integral over the excitation in $\sigma_1 \propto \omega \cdot \epsilon_2(\omega)$, which is directly proportional to ω_p^2. The resonance frequency ω_0 gives the position of the maximum in ϵ_2. The real part of the dielectric function ϵ_1 has a pole at ω_0 for no damping, $\gamma = 0$. For finite damping a maximum is reached below the resonance frequency, see figure 3.1a. At the resonance frequency the real part of the dielectric function is zero, before it exhibits a minimum. After the minimum the real dielectric function crosses zero at the frequency of the longitudinal optical resonance frequency ω_{LO}. The ratio of the squares of the longitudinal ω_{LO} and the transverse ω_{TO} is given by the Lyddane-Sachs-Teller relation

$$\frac{\omega_{LO}^2}{\omega_{TO}^2} = \frac{\epsilon_{st}}{\epsilon_\infty}, \tag{3.1.7}$$

with $\epsilon_{st} = \epsilon_1(\omega = 0)$ and $\epsilon_\infty = \epsilon_1(\omega = \infty)$.

3.2 Drude oscillator

The Drude oscillator is obtained in the limit of the resonance frequency $\omega_0 = 0$ for a Lorentz oscillator. This scenario is valid for a free electron gas. Typically, the scattering rates are much higher. The result is a sharp peak in the imaginary part of the dielectric function, that diverges at zero frequency, called Drude peak. Its spectral weight is directly related to the DC conductivity σ_{dc} by the plasma frequency and the scattering rate γ,

$$\sigma_{DC} = \frac{Ne^2\tau}{m^*} = \epsilon_0 \frac{\omega_p^2}{\gamma}. \tag{3.2.1}$$

For the real part of the dielectric function the broad Drude peak gives a negative contribution, which approaches ϵ_∞ with increasing frequency, see figure 3.1b.
In contrast, the dielectric function of trapped charge carriers will have a maximum at finite frequency in ϵ_2. When the charge carriers are trapped the imaginary part of the dielectric function reaches zero at $\omega_0 = 0$. Hence, the carriers will not contribute to the DC conductivity. This scenario applies to an electron gas trapped by potential fluctuations, see chapter 8.2.4.
An important excitation that cannot be modeled properly with a Drude oscillator or a Lorentz oscillator is the excitation across the gap. The Tauc-Lorentz oscillator is designed to model the excitation to a continuum which suits it to model excitations across the gap.

3.3 Tauc-Lorentz oscillator

The Tauc-Lorentz oscillator has a sudden onset, representing the band edge [18]. It needs only one additional parameter compared to the Lorentz oscillator, which is the energy gap ω_{Gap}. The formula for the imaginary part of the dielectric function is given by [18]

$$\epsilon_2(\omega) = 1 + \frac{1}{\omega} \frac{S^2 \omega_0 \omega_t (\omega - \omega_{Gap})^2}{(\omega^2 - \omega_0^2)^2 + \omega^2 \omega_t^2} \Theta(\omega - \omega_{Gap}), \tag{3.3.1}$$

where S denotes the strength of the oscillator, ω_t the scattering constant, and ω_0 the resonance frequency. Below the gap the imaginary part off the dielectric function, as well as the absorption, is zero. The real part of the dielectric function is a lengthy analytical formula [18]. Therefore, the real part is often obtained by Kramers-Kronig analysis of the imaginary part, see section 8.1.1.9.

3.4 Fano line shape

The interaction between a broad continuum and a discrete oscillator is described by the Fano resonance [19]. This resonance is present in many different fields of physics. The phenomenological formula is [20]

$$\epsilon(\omega) = \frac{\omega_p^2}{\omega_0^2 - \omega^2 - i\gamma\omega} \left(1 + i\frac{\omega_q}{\omega}\right)^2 + \left(\frac{\omega_p \omega_q}{\omega_0 \omega}\right)^2, \tag{3.4.1}$$

where ω_q denotes the parameter describing the asymmetry.

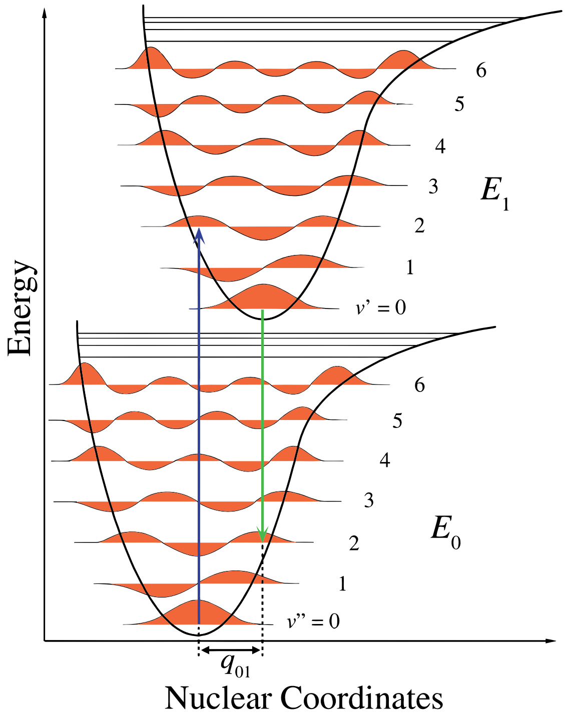

Figure 3.2: Excitation between E_0 and E_1 with different lattice constants, and a difference in the core distance q_{01}, have the highest probability for excitations from the ground state to vibrationally excited states with $\nu \neq 0$, marked with green and blue arrows. Figure has been taken from reference [25].

3.5 Franck-Condon principle

The Franck-Condon principle describes the probability for electronic excitations in a crystal in considerations of the vibrational modes [21–23]. The electronic excitation causes a change in the electronic wave function which in general goes along with a change of the lattice constant, see figure 3.2. Although, the lattice constant changes very slowly compared to the changes of the electronic wave function by vibrational excitations. Excitations with maximal overlap of the electronic wave functions between the ground state and electronically excited states plus a vibrational excitation are favorable, since the probability for the excitations is proportional to the square of the overlap between the original and the final state. The probability for a transition between both states under the creation of a phonon increases. As a result phonon sidebands can be observed in the optical spectrum, see figure 10.15. For details on the mathematical description of the Franck-Condon factors see [24].

3.6 Kramers-Kronig relation

The Kramers-Kronig relation links the imaginary and the real part of a function to each other [26]. More precisely, the imaginary part can be determined from the real part if it is known from 0 to ∞ and vice versa. The relation is not valid for every function, but the complex dielectric function satisfies the requirements. Therefore, the real part is related to the imaginary part by [26]

$$\epsilon_1(\omega) = 1 + \frac{2}{\pi} \cdot CH \int_0^{\infty} \frac{\omega \cdot \epsilon_2(\omega)}{\omega^2 - \omega^2} d\omega, \tag{3.6.1}$$

where CH is the Cauchy principal value. The Kramers-Kronig relation also enables us to calculate the transmittance or conductivity from the reflectance, if it is known from 0 to ∞. This is very useful, but measuring the reflectance from 0 to ∞ is impossible. Hence, the low and high frequency ranges need to be extrapolated. This is a source for errors. Another source for errors is the measured reflectance itself. An error in the absolute value will propagate in $\sigma_1(\omega)$. In general, Kramers-Kronig relations needs to be treated with care and is useful if the transmittance is not available.

3.7 Maxwell Garnett approximation

So far, the considerations assumed a homogenous medium. This is not always the case. Small inclusions with different optical properties in the medium change the response of the medium to electromagnetic waves. The Maxwell Garnett approximation assumes that the inclusions are much smaller than the wavelength of the incoming light and inclusions in the form of uniformly distributed and similarly oriented ellipsoids. Under this assumption the effective dielectric function is

$$\epsilon_{\text{eff}} = \epsilon_m \frac{2\epsilon_m + \epsilon_i + 2f(\epsilon_i - \epsilon_m)}{2\epsilon_m + \epsilon_i + f(\epsilon_m - \epsilon_i)}. \tag{3.7.1}$$

The dielectric function of the medium is given by ϵ_m and the dielectric function of the inclusion is given by ϵ_i. The factor f represents the filling factor and ranges from zero to one. The inclusions can be modeled as $\epsilon_i = \epsilon_m + \epsilon_\Delta$. This simplifies equation 3.7.1 to

$$\epsilon_{\text{eff}} = \epsilon_m + f\epsilon_\Delta \left(1 + (1-f)\frac{\epsilon_\Delta}{3\epsilon_m}\right). \tag{3.7.2}$$

If the inclusions modifiy the dielectric function only slightly, $\epsilon_\Delta \ll \epsilon_m$, we can simplify the equation 3.7.2 to

$$\epsilon_{\text{eff}} \approx \epsilon_m + f\epsilon_\Delta. \tag{3.7.3}$$

This approximation is delicate since the dielectric function is complex. Therefore, the approximation is only valid in a limited frequency range that is dependent on the details of the complex dielectric function.

If the inclusion is much larger than the wavelength we have to consider an average dielectric function that can be calculated like a multilayer system. In the case the wave length is much smaller than the size of the inclusion and the thickness is smaller than the thickness of the inclusions, the transmittance is given by the mixture of two separate measurements

$$T = (1 - f)T_m + fT_i, \tag{3.7.4}$$

where T_m and T_i correspond to the transmittance of the pure medium and the pure inclusion.

Part II

Methods

Chapter 4

Measuring instruments

Most measurements have been performed on the Fourier Transform Infrared (FTIR) spectrometer, which covers a broad frequency range. Additionally, measurements at lower frequency were performed with the THz setup[1]. Measurements at higher frequencies were performed with the ellipsometer[2].

4.1 FTIR spectrometer

We have used a FTIR spectrometer from Bruker version 66v/s. With the measured reflectance and transmittance we can determine the complex dielectric function in a frequency range from 40-10000 cm^{-1}, see section 5.1 and 3.6. A huge advantage of Fourier spectroscopy is the broad frequency range, which can be measured within a relatively short time. Furthermore, it provides a high frequency resolution.

The beam size can be adjusted by an aperture from 0.5 mm to 12 mm. The beam is led to a beamsplitter, which reflects half of the beam to a fixed mirror and transmits the other half of the beam to a moving mirror, see figure 4.1. The fixed mirror and the moving mirror reflect the light back to the beamsplitter. Hence, half of the superposition of the beams is led to the sample for the actual measurement. The transmittance measurements are performed with vertical incidence of the beam on the sample. In the case of a reflectance measurement vertical incidence is impossible to measure. However, the sample is turned 90° and a reflectance unit is placed in the sample chamber of the spectrometer. The beam is led to the sample and hits the sample with an angle of 7° to the normal of the sample surface. By performing the reflectance measurement with an angle close to vertical incidence, the reflectance can be treated as the vertical reflectance, since $\sin(83^\circ) > 0.99$. After the reflection or transmission the mirrors in the spectrometer lead the beam to the detector. We are able to measure in the far-infrared (FIR) range, 40-700 cm^{-1} and the mid-infrared (MIR) range 500-10000 cm^{-1}.

---

[1] The THz measurements have been performed by Valeri Mehler and Malte Langenbach in the group of Prof. Grüninger at the II. Physical Institute at the University of Cologne.

[2] The ellipsometry data were obtained by Ignacio Vergara in the group of Prof. Grüninger at the II. Physical Institute at the University of Cologne.

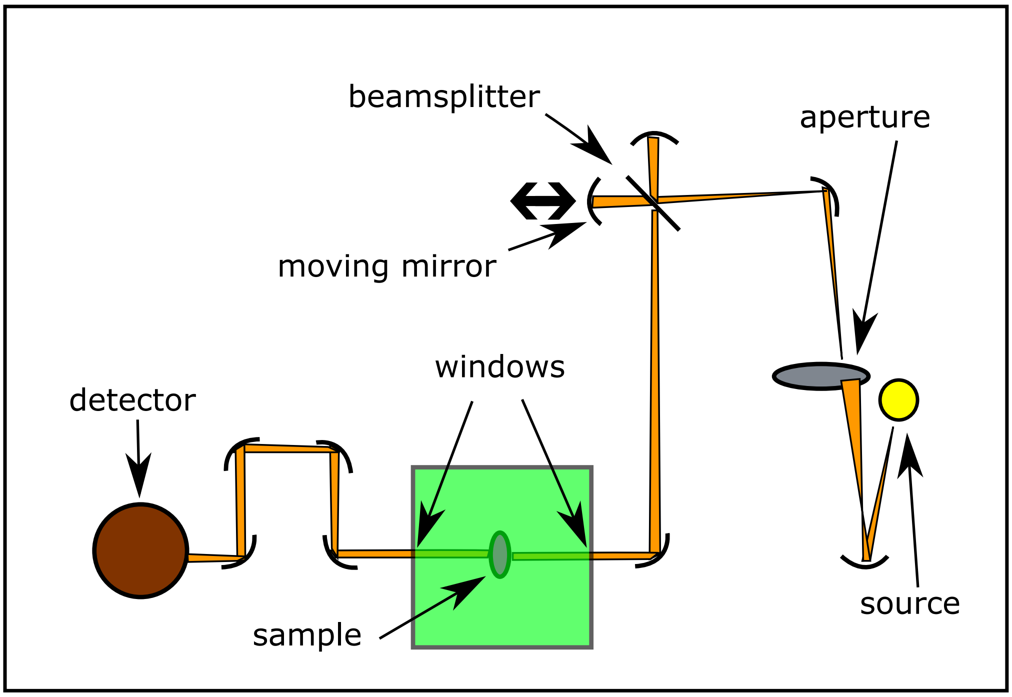

Figure 4.1: The most important components of the used FTIR spectrometer are sketched.

The instruments that are limiting the frequency range are the source, the beamsplitter, the windows, and the detector.

The FIR measurements have been performed with a mercury vapor discharge lamp ST 75 as source and a Mylar beamsplitter. The beamsplitter consists essentially of an uniform thick synthetic resin film, of polyethyleneterephthalate and polypropylene. This film is coated with germanium. Beamsplitter with film thicknesses ranging from 6-50 μm are available. Most measurements are performed with the Mylar 6 μm, because of lower loss and a larger period of the Fabry-Pérot interference fringes. Polyethylene windows are used, because of their low absorption in the FIR range. The temperature can be tuned from 4.2° K to 400° K, due to a cryostat from CryoVac which is cooled with liquid helium and a heater. It enables us to vary the temperature from 4.2° K to 400° K. The detector is a bolometer with a thermistor as detector element, which is cooled with liquid helium. The beam hitting the detector element causes a change in temperature and resistance. This change in resistance is converted to voltage and amplified.

The MIR measurements are performed with a tungsten lamp as source. The beamsplitter consist of free-standing KBr with a thin coating of Ge. The windows are as well made of KBr. The detector is a mercury cadmium telluride (MCT) detector. It converts the resistance change of the semiconductor with a narrow direct gap, due to incoming MIR light, to an electric signal.

In the end both methods send a voltage proportional to the detected intensity to the computer. Additionally, the computer receives the position of the moving mirror. The intensity as a function of the mirror position gives the interferogram. The sought-after quantity is the intensity as a function of frequency, the spectrum. Demonstrative, the mirror position gives the interference conditions for the frequencies, combined with the intensity for many mirror positions a great puzzle evolves. This puzzle can be solved in an elegant way by the Fourier transformation. Due to the finite resolution the discrete form of the Fourier transformation is needed to calculate the spectrum from the interferogram which is done by OPUS. To obtain the transmittance or the reflectance of the sample the spectrum has to be divided by a reference. The reference is the spectrum of a measurement under the same condition like the sample measurement, but with an empty sample holder for transmittance, respectively a gold mirror for the reflectance. For details on Fourier spectroscopy see,*e. g.*, [27].

4.2 THz spectrometer

The THz setup allows us to determine the transmittance and the phase in the frequency range from 3-50 cm^{-1}. The THz setup consists out of three NIR lasers. The wavelength of the lasers is about 781 nm. Two lasers are tuned to two slightly different frequencies. The wavelength difference is a few nanometers. Hence, the signal of the superimposed beams has a high frequency contribution and an envelope in the THz range. The photomixer is used as transmitter and acts as a low-pass filter, leaving only the THz signal. The third laser is used to correct the drift in the phase, mostly caused by thermal instabilities [28]. Furthermore, a magnetic field up to 8 T can be applied. For further details on the THz spectrometer see [28–30].

4.3 Ellipsometer

We can perform measurements with the ellipsometer starting at the upper frequency end of the mid-infrared range $\sim$ 1 eV up to 6.3 eV ($\sim$8066-50813 cm^{-1}). The ellipsometry is especially powerful to measure surface properties. The technique takes advantage of the change of the polarization by reflection. The complex dielectric function can be determined by the change in the absolute value of the reflectance and the drift of the polarization plane, determined by angle-resolved intensity measurements. This only works if the sample is homogenous on the length scale of the penetration depth. For inhomogeneous samples a model with reasonable assumptions is necessary to obtain the dielectric function of the layers. For a detailed description of ellipsometry see [31].

Chapter 5

Data analysis

5.1 Inverting transmittance and reflectance

The transmittance and the reflectance harbor all the necessary information to calculate the optical conductivity $\sigma_1(\omega)$. Therefore, it is possible to determine $\sigma_1(\omega)$ by inversion of the transmittance and the reflectance. The transmittance needs to be measurable for this purpose. Although, the transmittance shows Fabry-Pérot interference fringes that restrain the inversion of the optical spectra. However, we eliminate the effect of multiple reflections by removing the $\sin^2$ with a Fourier filter from the spectrum which leads to the spectrum for incoherent transmission. The two equations have been motivated in section 2.4. For a sample in vacuum the equation 2.4.3 and 2.4.4 simplify to

$$t = \frac{t^2 \exp(i\omega N d/c)}{1 - r^2 \exp(i2\omega N d/c)}, \tag{5.1.1}$$

and

$$r = \frac{r + r \exp(i2\omega N d/c)}{1 - r^2 \exp(i2\omega N d/c)}. \tag{5.1.2}$$

Since t^2 and r^2 are given by the measurement the only unknown quantity is the complex refractive index N. Hence, the κ and n, respectively the dielectric function, are determined by these equations without any further assumptions. A disadvantage compared to fitting the data with the help of oscillators is that it is impossible to calculate $\sigma_1(\omega)$ of multilayer systems with this method.

5.2 Modeling the transmittance and reflectance

The formulas for modeling the optical spectra are introduced in chapter 2 and 3. The fitting requires convenient starting parameters and some programming effort. Most of the programs have been written in MATLAB R2014a. A good alternative is RefFIT 1.2.95[1]. It

---

[1] RefFIT is a free software written by Alexey Kuzmenko.

is designed to model optical spectra of multilayer systems and fit them. Although, RefFIT cannot solve every problem, it is sufficient in most cases. A broad variety of oscillator types is available. Additionally, the Kramers-Kronig-constrained variational dielectric function enables the description of little deviations from a fit by many oscillators. This way every feature down to noise can be transferred from the spectrum to the dielectric function.
Most graphs of this thesis were designed using OriginPro 8.5G and Inkscape 0.91.

5.3 Analysis of Fabry-Pérot fringes

While fringes are causing problems when we want to calculate $\sigma_1(\omega)$ by inverting the optical spectra, they are as well the source of information. The condition for interference of the rays for a certain frequency depends on the thickness and the refractive index according to equation 2.4.5. Hence, we can determine the refractive index with the knowledge of the thickness and vice versa. However it is essential to determine the order of the fringes, which is not straight forward, since the data start at finite frequency, at which the first fringes usually cannot be observed. An estimation for the refractive index can be made by equation 2.4.7. Here, we assume that the refractive index exhibits negligible change between two fringes. The thickness is determined by a stamp with accuracy around ± $5\,\mu$m. We also tried to determine the thickness by the weight and the volume of the sample, but the error bar was much larger compared to the method with the stamp. The refractive index determined by the difference in frequency of neighboring maxima is a good estimate for flat regions of the refractive index, but when the refractive index changes significant between two maxima this method is not accurate.
The exact method takes more effort. It uses equation 2.4.5. The thickness of the sample is determined like described above. In the following a reasonable order for the maxima is chosen. For this purpose the overall shape of the refractive index is taken into account, as well as the refractive index determined by the difference of the maxima in frequency. Thereby, the limits for the order can be set. The next step requires a sample of the same crystal with different thickness. The ratio of the distance between two maxima at the same frequency range gives the thickness ratio of both samples. It is convenient to choose a thick sample for determining the thickness by the stamp, since an absolute error of roughly $5\,\mu$m results in a small relative error. This way the error from the first measurement becomes a systematical error. More important the relative error is the same for each sample. From the thickness ratio we can estimate the order of the maxima and calculate $n(\omega)$ for the second sample with the thickness of the second sample. The refractive index of the first and the second sample need to be exactly the same. We plot the refractive indexes for slight variations of the order for the first and second sample together. A few curves of the first sample will lie on top of the curves of the second sample. Unless the ratio of the thickness is not an integer, the number of curves on top of each other is small, but only these curves might give the correct refractive index. Usually, a third or even fourth sample thickness is needed to determine the correct curve for the refractive index. This curve fixes the order

of the maxima for each sample. In the end the refractive index is determined with a high accuracy by the fringes.

5.4 Determining the n from R

When the transmittance is zero no information about fringes is available. However, the complex refractive index is linked to the reflectance by equation 2.3.2. This means that we have two variables and only one equation. In many cases it is convenient to assume $\kappa \ll n$ and directly determine the refractive index from the reflectance. If this is not the case it is possible to model the refractive data by, *e.g.*, RefFIT. Thereby, the transmittance and the reflectance need to be reproduced. Furthermore, the refractive index needs to smoothly merge to the refractive index determined by the fringes.

Eventually, the complex refractive index can also be obtained by Kramers-Kronig analysis, see section 8.1.1.9.

Part III

Topological insulators

Chapter 6

Introduction to topological insulators

Topological insulators represent a novel, quantum state of matter. The topological nature of the bulk wave functions is manifested in peculiar edge or surface states. The main characteristics of topological insulators are introduced in the following.

6.1 Band inversion

The band structure of topological insulators is gapped, in analogy to ordinary insulators. Although, the strong SOC leads to a band inversion, which is the reversing of the order of the bands of an element in a crystal compared to the order in the crystal with artificially reduced SOC. Therefore, topological insulators consist of elements with large atomic number Z causing large SOC. An example for a topological insulator is $\mathrm{Bi_2Se_3}$. The band inversion observed between Bi and Se p orbitals is pictured by the calculation of their corresponding energies of the Se and Bi orbitals by Yan *et al.* [32] in figure 6.1. The calculations consider successively chemical bonding, crystal field splitting, and SOC. Owing to the inclusion of SOC in the last step, the p-orbital of Se is higher in energy than the p-band of Bi.

6.2 Chern number

Topology is a term primary used in mathematics. There it refers to the theory of the properties of a body which persist under continuous transformations. This theory is linked to topological insulators by the body of the wave function of the electronic states spanned in Hilbert space [33]. The wave functions can be distinguished by the topological invariant, called the Chern number $n \in \mathbb{Z}$. It groups the wave functions into classes, which are described by Hamiltonians $H(k)$ that can be smoothly transformed into each other. In particular, the transformation does not close or open an energy gap in the band structure.

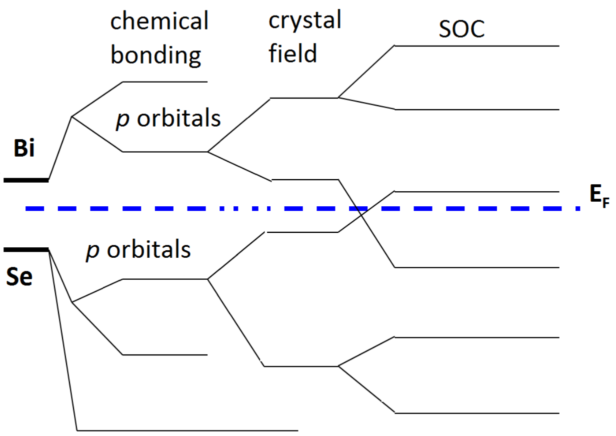

Figure 6.1: In three steps the effect of chemical bonding, crystal field splitting, and SOC are successively added to the atomic p orbitals. The last step results in an inversion of the orbital order. Figure is a modified version of figure 6a) in reference [32]`https://doi:10.1088/0034-4885/75/9/096501` {DOI}.

The Chern number n is defined by the total Berry flux in the Brillouin zone (BZ)

$$n_m = \frac{1}{2\pi} \int d^2k \, F_m, \tag{6.2.1}$$

where F_m is the curl of the Berry vector potential A_m

$$F_m = \nabla \cdot A_m. \tag{6.2.2}$$

Vacuum and the other ordinary insulators built the class of trivial insulators with the Chern number $n = 0$, whereas the topological insulators with $n \neq 0$ are named non-trivial topological insulators. Now, we considering the junction between two topological insulator. The energy gap for insulators with the same Chern number does not close when the band structure transforms into each other, as mentioned above. Although, transforming the band structure from a trivial insulator into the band structure of a non-trivial insulator leads to the closing of the energy gap at the interface. This is manifested in the rise of the surface state. The properties of the topologically surface states are the topic of the next section.

6.3 Topologically protected surface states

The dispersion relation of the surface states is given by the Dirac cone, see figure 6.2. It can be described in the vicinity of the Dirac point by

$$E(\mathbf{k}) = \pm\hbar v_F \cdot |\mathbf{k}|, \tag{6.3.1}$$

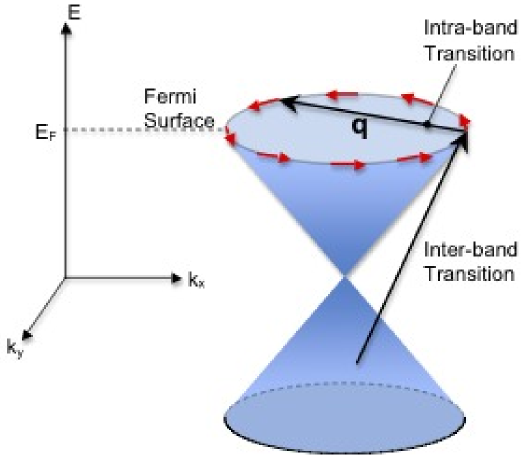

Figure 6.2: The Dirac cone describes the energy of the surface states as a function of the wave vectors k_x and k_y. The black arrows indicate the allowed electronic transitions in the absence of magnetic impurities, while the red arrows correspond to the spin direction. Figure has been taken from reference [35]. Copyright (2008) by Cambridge University Press

where v_F denotes the Fermi velocity and $\mathbf{k}$ the wave vector. We can easily find the relation between the Fermi energy E_F and the Fermi wave vector k_F, $E_F = \hbar v_F \cdot k_F$. Each state on the Dirac cone has a spin pointing tangential to the Dirac cone [34]. The dispersion relation locks the momentum to the spin in a way that an electron state with momentum along a certain direction presupposes a state with opposite momentum and spin, see figure 6.3. The spin-momentum locking causes the suppression of the backscattering at impurities, since a change of the momentum requires a change of the spin. Backscattering to the opposite k-vector is even forbidden, except at non-magnetic impurities.

Time-reversal symmetry requires that at the Γ point ($k = 0$) and the X point at the BZ boundary the states are degenerate, forming Kramers pairs [36]. Away from these points the degeneracy is lifted by SOC. Due to the linear dispersion relation the mass m in the relativistic energy momentum relation $E = \sqrt{m^2c^4 + p^2c^2}$ is zero. Therefore, the charge carriers are called massless Dirac fermions. However, the effective mass m^* of charge carriers at the Fermi level can be determined by the momentum for matter waves $m^* = \frac{\hbar k_F}{v_F}$.

6.3.1 Optical conductivity and conductance of surface states

In general two transitions are distinguished: the transition at the Fermi level from one state to another state, the so-called intra-band transition, and the transition from below the Dirac point to a state above the Dirac point. It is called inter-band transition. The inter-band transitions require at least twice the E_F with $E_F(k = 0)$ defined to zero. It has been predicted that for frequencies $\omega \leq 2E_F/\hbar$ this channel supplies an universal conductance [37, 38]

$$G_{inter} = \pi e^2/8h \approx 1.5 \cdot 10^{-5}\Omega^{-1}. \tag{6.3.2}$$

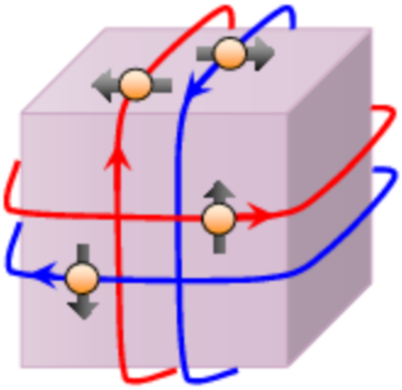

Figure 6.3: The cube represents a 3D topological insulator. The momentum of the electrons is indicated by the red and blue trajectories. The black arrows correspond to the spin directions. Figure has been taken from reference [36] url-https://dx.doi.org/10.7566/JPSJ.82.102001 {DOI}. Copyright (2013) by Journal of the Physical Society of Japan.

This conductance channel is available for each surface.

The intra-band transitions supply an additional conductance channel. The conductance of the channel is given by

$$G_{DC} = \frac{\pi e^2 n_{2D}}{m^* \gamma} = \frac{E_F}{4\pi\hbar}, \tag{6.3.3}$$

where n_{2D} represents the number of available states, m^* the effective mass, and γ the scattering rate. Since the Fermi energy determines the filling of the Dirac cone it also gives $\frac{n_{2D}}{m^*}$.

For graphene it is known that the spectral weight of the intra-band transitions is enhanced, by the spectral weight of the inter-band transitions that are forbidden by energy conservation [39–41]. The f-sum rule [42] implies the transfer of the spectral weight from the inter-band transition to the intra-band transition

$$2G_{inter}E_F = \int_0^\infty G_{intra}\hbar \, d\omega. \tag{6.3.4}$$

By solving the integral we determine the shifted spectral weight $D_{2D} = 4E_F G_{inter}/\hbar = \frac{e^2 E_F}{4\hbar^2}$. This shift is pictured in figure, 6.4.

G_{DC} is linked to D_{2D} by

$$G_{DC} = D_{2D}\frac{\tau}{\pi}. \tag{6.3.5}$$

Note, that the percentaged effect of the surface state on the transmittance is, to first order, independent of the thickness of the bulk. Since the optical spectrum is dominated by quantities which originate from the bulk, it is convenient to analyze $\sigma_1(\omega)$. Therefore, it is necessary to calculate the influence of the surface state on $\sigma_1(\omega)$ calculated by assuming no surface.

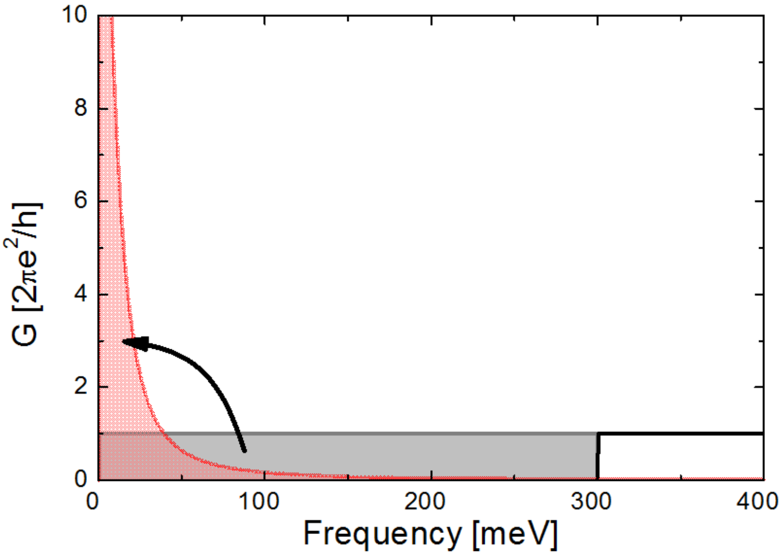

Figure 6.4: The spectral weight D of the inter-band transitions for the $E < E_F \approx 150\,meV$ (gray area) is shifted to the intra-band transitions (red area).

The conductance $G_{ss}(\omega)$ of the surface states results in the observation of an increase in $\sigma_1(\omega)$, since $\sigma_1(\omega)$ averages over $\sigma_{1,bulk}(\omega)$ and $\sigma_{1,ss}(\omega) = G_{ss}(\omega)/d$ with d the thickness of the topological insulator. Analog, the weight of the Drude peak caused by the surface state

$$D_{2D,ss} = \frac{\pi n_{2D} e^2}{m}, \tag{6.3.6}$$

causes a Drude weight for the whole topological insulator of

$$D_{3D} = D_{2D}/d = \frac{\pi n_{2D} e^2}{d\,m} = \pi \epsilon_0 \omega_p^2. \tag{6.3.7}$$

6.4 Compensated semiconductors

The first generation of 3D topological insulators have been unintentionally, strongly doped [34, 43–60]. Since reducing the conductivity is crucial for device fabrication and the observation of the surface state, the bulk conductivity is reduced by decreasing the density of the defects causing doping. However, reducing the bulk conductivity by decreasing the defect density is only efficient to a certain extend. Beyond this point the bulk resistivity can be increased by compensation [43, 61–65]. Compensation describes the addition of donors/acceptors to an acceptor/donor dominated semiconductor. The idea of compensation is to tune the Fermi level into the energy gap, since the donors and acceptors recombine, as shown in figure 6.5 [66]. These effects have already been investigated in the 70es mainly by Efros and Shklovskii [67–69]. Recently, the theory has been used to explain the enhanced conductivity, the activation energy, and the influence of deviations from perfect compensation in topological insulators [70–73].

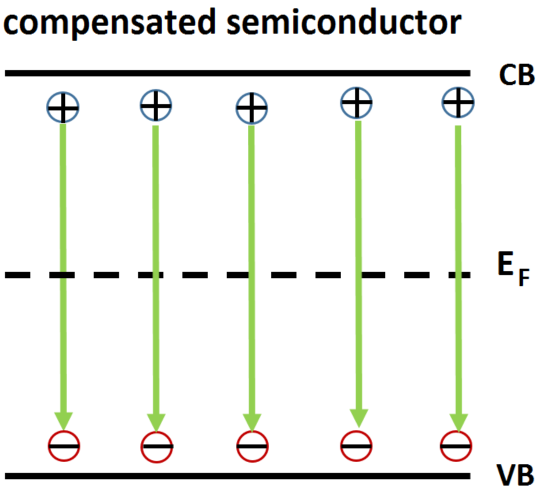

Figure 6.5: Simple idea of compensation in a semiconductor. Donors close to the conduction band (CB) give the electron to an acceptor valence band (VB). The process is indicated by green arrows. The result are positively charged donors and negatively charged acceptors. The doted line represents the Fermi energy, which is in the middle of the gap for perfect compensation.

6.4.1 Theoretical description in literature

In the following we will give a short summary of the existing theory based on the work of Efros, Shklovskii, and Skinner *et al.* [70–73].

6.4.1.1 Assumptions

The theory assumes a random distribution of donors and acceptors. The high dielectric constant ensures that the acceptors and the donors are close to the valence band and the conduction band, respectively, as can be shown by considering a hydrogen model [71]. Therefore, the donors and acceptors are treated as shallow defects. Furthermore, the charge carriers in the valence band and in the conduction band are neglected. Hence, only the low-energy physics is described, with $k_B T \ll \Delta$, with Δ the energy gap.

6.4.1.2 Formation of puddles

This model is used to explain the enhanced bulk conductivity in topological insulators [43]. Many donors give their electrons to acceptors. The result are charged, empty donors and charged, occupied acceptors. These charges are the reason why not all donors give their electrons to the acceptors. This scenario is described by a bent band structure. Since the Coulomb potential makes it energetically favorable to have an occupied donor or an empty acceptor. When the valence band or the conduction band crosses the chemical potential neutral defects are created in this region, which we call puddle. Randomly distributed charged defects imply that in a volume r^3 a charge $\sqrt{N_{def} \cdot r^3}$ is uncompensated. Thus

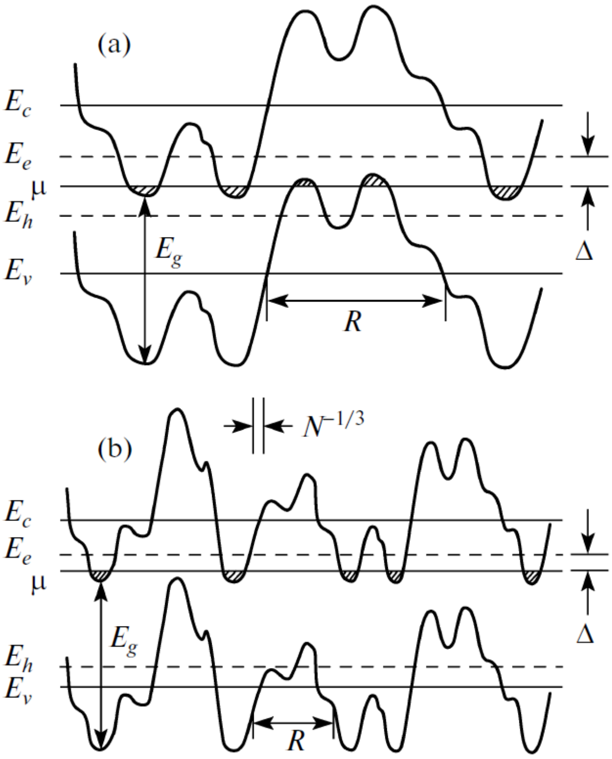

Figure 6.6: The potential fluctuations are sketched for perfect compensation a) and a n-type semiconductor with a compensation of 95 % b). The solid line between the conduction band, marked with E_C, and the valence band, marked with E_V, is the chemical potential μ. The shaded areas, where the conduction band and the valence band cross the chemical potential, are puddles with neutral dopants. R is the characteristic size of the potential fluctuations. The dashed line corresponds to the percolation levels. The figure has been taken from reference [73]`https://dx.doi.org/10.1134/S1063776113110150` {DOI}. Copyright (2013) by Pleiades Publishing, Inc.

the Coulomb potential $e^2\sqrt{N_{def}R^3}/(4\pi\epsilon_0\epsilon R) \propto \sqrt{r}$. Bulk puddles are created when the Coulomb potential exceeds half the energy gap. The puddle size R can be estimated to [71]

$$R = \frac{(\Delta/E_C)^2}{8\pi N_{def}^{-1/3}}, \tag{6.4.1}$$

where Δ denotes the energy gap, E_c the average Coulomb interaction between neighboring defects, and N_{def} the defect density. The resulting n-doped and p-doped regions are sketched in figure 6.6.

6.4.1.3 Activation energy

These potential fluctuations cause a percolation level for the electron and holes. The percolation level corresponds to the energy that is needed to move across the sample by utilizing the bending of the bands, see figure 6.6a). Since a charge carrier can move freely through

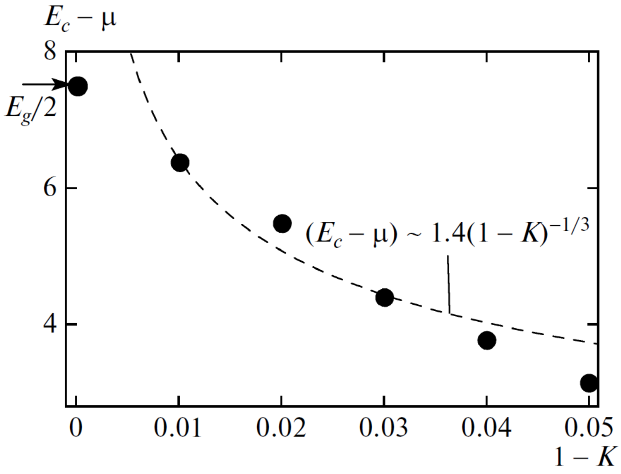

Figure 6.7: The numerical results for the activation energy is plotted for six different degrees of compensation. Dashed line is a prediction from theory assuming a single band [74]. The figure is taken from reference [73]`https://dx.doi.org/10.1134/S1063776113110150` {DOI}. Copyright (2013) by Pleiades Publishing, Inc.

the sample when the percolation level is reached, the activation energy is reduced to the difference of the chemical potential and the percolation level. The numerical calculations by Skinner *et al.* [71] yielded an activation energy $E_{\mathrm{act}} = 0.15\Delta$ for perfect compensation. The scenario with less than perfect compensation is discussed below in section 6.4.1.4.

6.4.1.4 Deviations from perfect compensation

The calculations have been extended to the experimental relevant regime with compensation below perfect, $K < 1$ with $K = N_D/N_A$ for the acceptor density N_A larger than the donor density N_D. The density of neutral defects increases as the compensation decreases. One consequence is the decrease of the amplitude of the potential fluctuations, because the random distribution of defects is screened by the additional, uncompensated defects. Along with the decreased amplitude of the potential fluctuation goes the reduction of the characteristic size of the potential fluctuations R. The figure 6.6 b) shows the potential fluctuation for less than perfect compensation. The chemical potential approaches the percolation level of the conduction band E_c, which means that the activation energy will decrease with decreasing compensation. The formula for the activation energy E_{act} given by Skinner *et al.* [71] is $E_{\mathrm{act}} = 0.3(E_C - \mu)$ for n-type semiconductors, where the dependence on the compensation is hidden in the chemical potential (for p-type semiconductors E_c is replaced by E_V). The dependence of the chemical potential on the compensation is plotted in figure 6.7.

6.4.1.5 Variable range hopping

Variable range hopping (VRH) describes tunneling of charge carriers from localized states to localized states, thereby increasing the conductivity. At 0 K the VRH does not contribute to the conductivity, since the tunneling probability is suppressed. With increasing temperature VRH strongly increases, before it saturates at high temperatures. According to Mott [75] the conductivity σ caused by VRH can be written as

$$\sigma = \sigma_0 \exp(-T_0/T)^{1/4}. \tag{6.4.2}$$

Note that Efros and Shklovskii claimed that the exponent is 1/2 instead of 1/4 at temperatures $T \ll e^4 a g_0/\epsilon^2$, with a the localization length of states with an energy close to the Fermi level, g_0 the density of states at the Fermi level, and ϵ the dielectric constant [71]. The reason for the deviation from Mott's law is the assumption by Mott that the density of states is constant at the Fermi level [75].

6.4.1.6 Modeling the density of states

The basis for quantitative results is a Hamiltonian, which captures the main energy contributions. It is given by

$$H = \sum_i \frac{E_g}{2} f_i n_i + \sum_{\langle ij \rangle} V(r_{ij}) q_i q_j, \tag{6.4.3}$$

where n_i is 0 or 1, depending on the number of electrons on the *ith* donor or acceptor. The binary variable is $f_i = 1$ for donors and $f_i = -1$ for acceptors. The net charge on the site i is given by $q_i = (f_i/2 - n_i + 1/2)$. The potential caused by the charge at the site j caused at the site i is given by $V(r_{ij}) = e^2/(4\pi\epsilon_0\epsilon(|\mathbf{r}_i - \mathbf{r}_j|^2 + a_B^2)^{1/2})$, with the short-distance cutoff a_B, which takes the finite extent of the wave function of the shallow dopants into account. This Hamiltonian is as well used for the calculations, see section 8.1.2.3. For computational details see [71]. One of the insights from the calculation of the ground state is that charge carriers in the ground state must satisfy the so called Efros-Shklovskii criterion [73]

$$\epsilon_j - \epsilon_i V(r_{ij}) > 0, \tag{6.4.4}$$

where ϵ corresponds to the single electron energy at the respective dopant. It is the reason for the Coulomb gap in the density of states (DOS), see figure 6.8. In other words the Coulomb gap is the consequence of the fact that a puddle is not filled completely to the chemical potential, since adding a charge decreases the attractive Coulomb interaction in the puddle. The calculated DOS for perfect compensation is symmetric and close to uniform. For a compensation of 95 % the DOS is strongly asymmetric. Assuming dominant n-type doping implies many donor states close to the Coulomb gap ($E > 0$) while the acceptor states are well separated from the Coulomb gap, close to the valence band, see figure 6.8. The small peak to the left of the Coulomb gap corresponds to empty donors. Furthermore, temperature-dependent, numerical simulations have been performed [73]. However, the influence of activated charge carriers on the potential fluctuation was not taken into account. Considering this feedback is the main conceptual improvement that the calculations provide

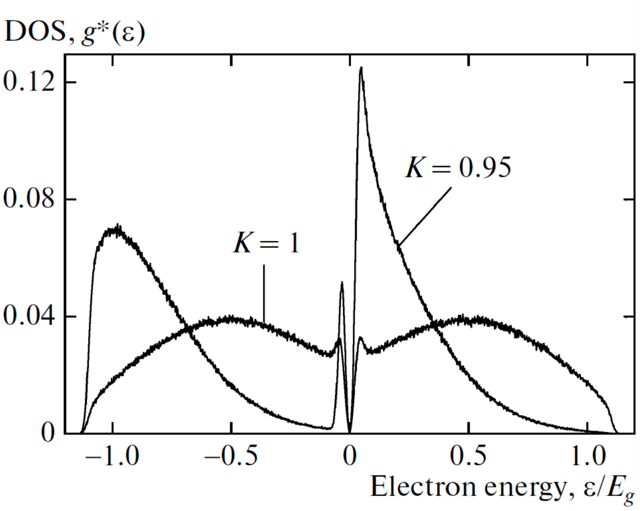

Figure 6.8: The single-electron DOS is plotted versus the energy scaled by the energy gap E_g. The DOS is symmetric concerning donors and acceptors for perfect compensation. For K=95 % a strong asymmetry is observed. For both levels of compensation the Coulomb gap is present at the chemical potential [73]`https://dx.doi.org/10.1134/S1063776113110150` {DOI}. Copyright (2013) by Pleiades Publishing, Inc.

[1]. The model will be discussed in section 8.1.2.

6.4.1.7 Optics below the gap

The potential fluctuations do not only cause puddles, but they also influence the optics directly below the gap. This was first realized by Shklovskii *et al.* [77]. In the previous section it was shown that an almost constant DOS in the gap is caused by the potential fluctuations for compensation close to perfect. Nevertheless, a gapless excitation is not possible, since the states are spatially separated. Therefore, it is necessary to tunnel a certain distance in order to realize an excitation with an energy smaller than the energy gap. This process is sketched in figure 6.9. Therefore, the matrix element for an excitation with a certain energy smaller than the gap depends on the DOS and on the tunneling probability.

Shklovskii *et al.* [77] introduced the energy deficit $\hbar\omega_\Delta$. It describes the energy mismatch between the incident energy and the energy gap. Shklovskii *et al.* [77] distinguish two regimes. One regime describes excitations with a small energy deficit $\hbar\omega_\Delta$, which requires only weak band bending. The other regime corresponds to excitations with a large energy deficit. The latter regime, is caused by impurity clusters, which bend the band strongly on a small length scale. Otherwise, the large spatial distance between states with an energy difference much smaller than the energy gap would suppress these excitations. However, in the vicinity of clusters the potential fluctuations enable transitions with a large energy

---

[1] The simulations have been carried out by Dr. Lux and Prof. Rosch of the Institute for Theoretical Physics at the University of Cologne [76]

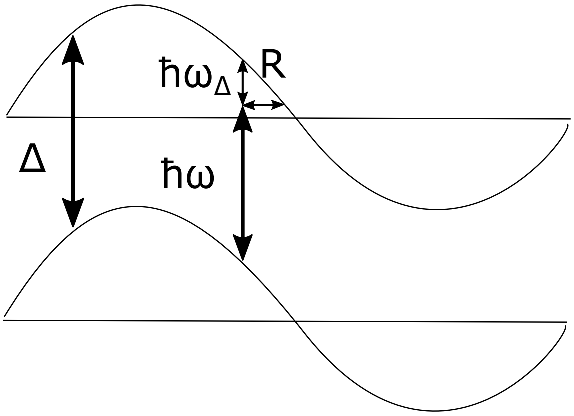

Figure 6.9: The potential fluctuations enable excitations with an energy $\hbar\omega$ which is smaller than the energy gap Δ by tunneling an distance R into a state with an energy deficit $\hbar\omega_\Delta$.

deficit. The formula describing the ratio of the absorption coefficient below the gap $\alpha(\omega_\Delta)$ and the absorption coefficient at the gap α_Δ is [77]

$$\ln\frac{\alpha(\omega_\Delta)}{\alpha(\Delta)} = -\sqrt{\frac{\hbar\omega_\Delta}{E_B}}\ln\left[\left(\frac{\hbar\omega_\Delta}{E_B}\right)^2\frac{1}{N_{def}a_B^3}\right], \tag{6.4.5}$$

where E_B stands for the ionization energy of an isolated dopant.

The second regime for excitations slightly beneath the energy gap relies on the smooth fluctuations of the Coulomb potential, which are statistically enhanced compared to the strong fluctuations on a short length scale. The excitation depends on the probability to have Z charge carriers in the volume R^3 that are supplying the electrical field to overcome the energy deficit and the tunneling probability across the distance R. The resulting ratio of the absorption coefficient below the gap and the absorption coefficient at the gap is given by [77]

$$\ln\frac{\alpha(\omega_\Delta)}{\alpha(\Delta)} = -\frac{2}{5}\sqrt{\pi}\left(\frac{\hbar\omega_\Delta}{E_B}\right)^{5/4}\frac{1}{(N_{def}a_0^3)^{1/2}}. \tag{6.4.6}$$

Note that both equations have been derived without considering the screening of the Coulomb potential by charge carriers. This might especially effect the equation 6.4.5 since large potential fluctuation are likely to be screened.

Chapter 7

Thin films of topologically insulating $(\mathrm{Bi}_x\mathrm{Sb}_{1-x})_2\mathrm{Te}_3$

Topological insulators exhibit exciting physics at the surface. However, in optical data and in transport data usually the bulk conductivity is dominant. In order to investigate the topologically protected surface state, it is reasonable to reduce the bulk conductance by investigating thin films. In transport measurements this lead to the observation of surface-dominated transport [43, 53, 78]. In optics the observation of the surface state has been reported as well [53, 79–81], but the proof of its topological nature is challenging. The intra-band transitions of the surface state are manifested in a Drude peak in $\sigma_1(\omega)$ [53, 79–81]. Additionally, the inter-band transitions are causing a constant conductance [53, 80], see section 6.3. This has been observed in optics only for graphene [39–41]. We perform thickness-dependent, optical measurements to obtain the contribution of the surface. The thickness-dependent data cannot prove directly the topological nature of the surface state, but the existence of the topological protected surface state in $\mathrm{Bi}_x\mathrm{Sb}_{1-x}\mathrm{Te}_3$ has been shown by ARPES [66]. The order of magnitude of the conductance, the Drude weight, and the scattering rate indicate whether the surface contribution comes from a trivial surface state or the topologically protected surface state.

In the following we report results on $\mathrm{Bi}_2\mathrm{Te}_3$ and on $(\mathrm{Bi}_{0.57}\mathrm{Sb}_{0.43})_2\mathrm{Te}_3$. $\mathrm{Bi}_2\mathrm{Te}_3$ is one of the first 3D topological insulators [34,82–84]. It has a low intrinsic charge carrier density at room temperature, due to the energy gap of about 150 meV [6,34,53,85]. However, unintentional n-type doping causes metallic behavior of the bulk. Therefore, we additionally investigate the compensated compound $(\mathrm{Bi}_{0.57}\mathrm{Sb}_{0.43})_2\mathrm{Te}_3$ with a very low charge carrier concentration in the bulk, see section 6.4.

7.1 Crystal structure and fundamental properties

$(\mathrm{Bi}_x\mathrm{Sb}_{1-x})_2\mathrm{Te}_3$ crystallizes in hexagonal quintuple layers, see figure 7.1a. Within the quintuple layers the atoms are bonded covalently [86]. Whereas quintuple layers are coupled

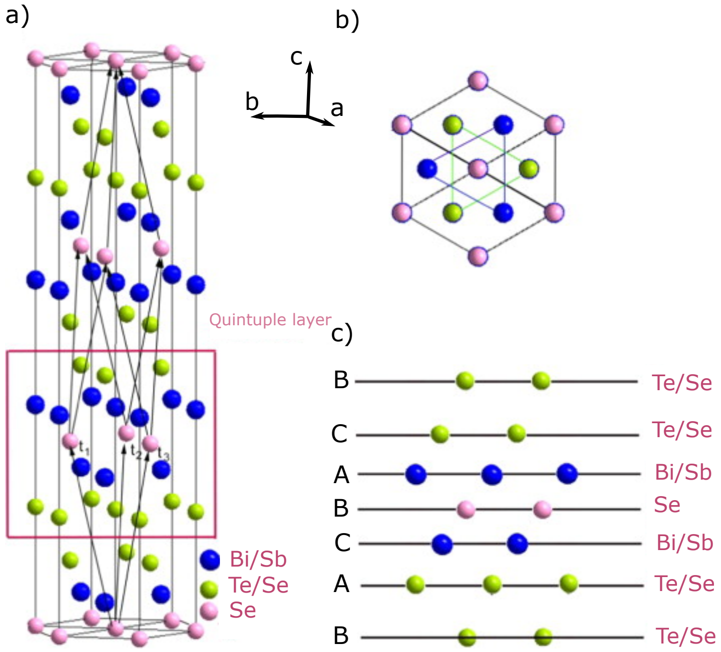

Figure 7.1: $BiSbTeSe_2$ crystal structure. $(Bi_xSb_{1-x})_2Te_3$ is obtained by substituting Se with Te and Bi_2Te_2 by additionally substituting Sb with Bi. a) 3D sketch of the crystal structure. One quintuple layer is marked by the rose box. b) 2D crystal structure resulting from the view along the c-axis. c) View along the a-axis. Emphasizing the ABC stacking. Figure is a modification of a figure in reference [82]`https://dx.doi.org/10.1016/j.pnsc.2012.11.011` {DOI}. Copyright (2012) by Chinese Materials Research Society.

weakly to each other by Van der Waals forces [86]. The stacking of the quintuple layers results in an ABC stacking, see figure 7.1. For Bi_2Te_3 the single layers are either composed exclusively of Bi atoms or Te atoms. For $(Bi_{0.57}Sb_{0.43})_2Te_3$ the Bi/Sb layer is composed of 57 % Bi and to 43 % Sb.

7.1.1 Phonon modes

We expect 12 optical phonon modes [87], $2A_u^1$, $2E_u$, $2A_g^1$, $2E_g$, where the E modes are doubly degenerate, see figure 7.2. The two E_u modes have a dipole moment which makes them infrared active. These have been observed in Bi_2Te_3 in reflectance measurements on single crystals at 15 K with eigenfrequencies $\omega_{0,1} = 48 \pm 2\,\mathrm{cm}^{-1}$ and $\omega_{0,2} = 98 \pm 3\,\mathrm{cm}^{-1}$ [87]. Similar values have been measured by neutron scattering [88], where the eigenfrequencies of the E_u modes at the Γ point have been observed at 77 K at 52±3 cm^{-1} and 101,5±1,5 cm^{-1}. First principle studies have shown that for thin films of Bi_2Te_3 and Bi_2Se_3 infrared active modes can become Raman active and vice versa [52, 89]. The potential in a thin film

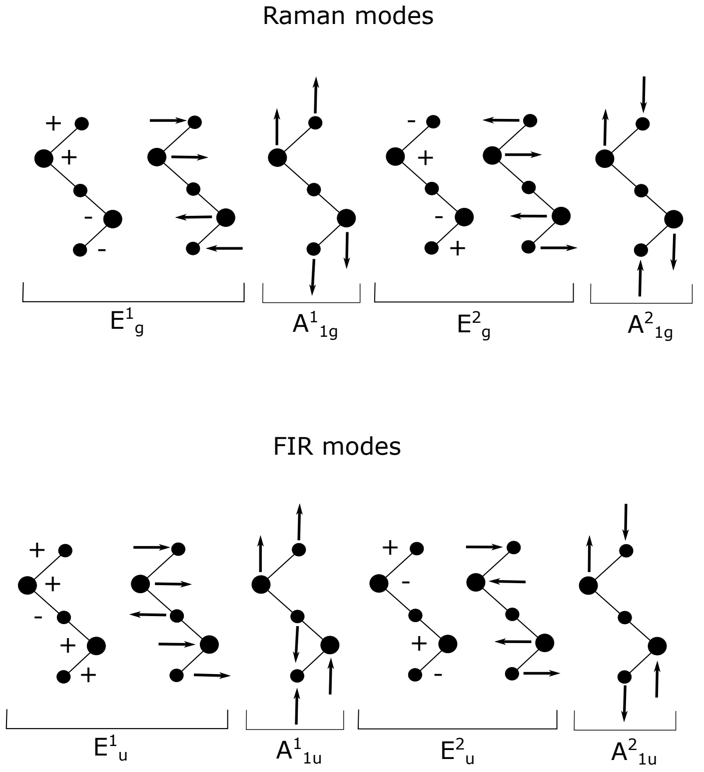

Figure 7.2: Upper sketch shows the Raman-active phonon modes of Bi_2Te_3. The arrows correspond to the direction of motion. Lower sketch shows the FIR modes. The superscripts 1 and 2 correspond to the low-frequency and high-frequency modes, respectively. Figure is a modified version of figure 2 in reference [87].

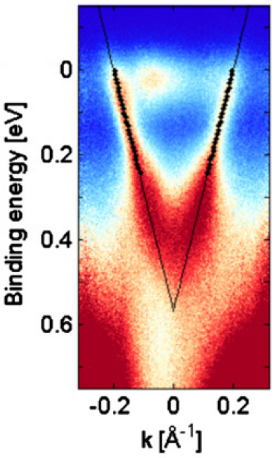

Figure 7.3: ARPES data on Bi_2Te_3. The color scale corresponds to density of states. The black line emphasizes the Dirac cone. Figure has been taken from reference [97].

is changing, *i.e.* a strong, anharmonic potential is found around the Bi atoms. Thus, the symmetry is broken and a finite dipole moment is induced. Additionally, the eigenfrequency of the phonon mode depends on the thickness of the film [90,91], due to the influence of the interface force constants. However, the eigenfrequency approaches the bulk value within the first ten quintuple-layers ($\approx 10\,\mathrm{nm}$) [91]. Therefore, we do not expect to see this effect.

7.1.2 Literature on the observation of the surface state

The pronounced Dirac cone in Bi-based topological insulators is evidence for the topologically non-trivial surface state. It has been widely studied in angle-resolved photoemission spectroscopy (ARPES), see figure 7.3 [34, 56, 66, 92–94]. However, it is difficult to detect the surface state by techniques that are less sensitive to the surface like transport or optical spectroscopy. The reason is its rather small conductance and the finite charge carrier density in the bulk. *Ab initio* density functional calculations of the band structure for Bi_2Te_3 [95] show that the Fermi level is close to the valence band of Bi_2Te_3 [34], see figure 7.4. Additionally, in ARPES data the bulk conduction band can be observed, which means that the investigated Bi_2Te_3 is *n*-type conducting in the bulk, see figure 7.3 [96]. In Bi_2Te_3, unintentional doping may give raise to both, *n*-type or *p*-type conductivity [36, 43]. IR experiments have failed to observe signatures that could distinctly identify the topologically protected surface state [51, 59]. Nevertheless, the observation of the topologically protected surface states with time-domain terahertz spectroscopy was reported on thin films of the related topological insulator Bi_2Se_3 by Aguilar *et al.* [81]. A Drude peak in the conductance, independent of the thickness, was reported, see figure 7.5. The peak was attributed to the Dirac fermions. The plot clearly shows that the absorption of the phonon scales with the thickness, while the Drude peak is independent of the thickness, which proofs its origin in the surface. One argument questioning the topologically protected nature is the large value

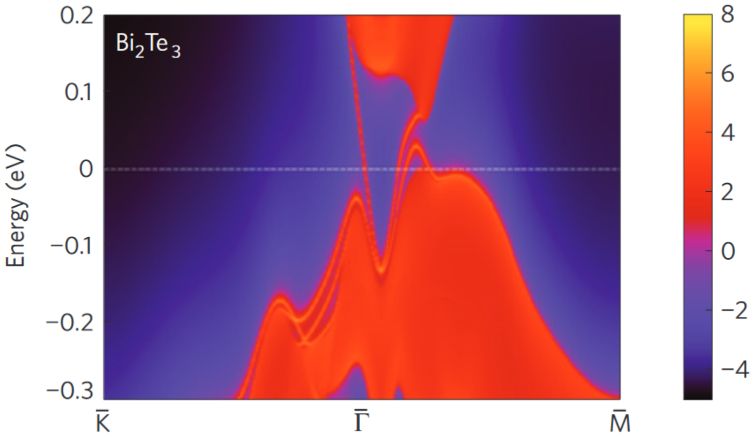

Figure 7.4: *Ab initio* density functional calculations of the band structure in Bi$_2$Te$_3$. White dashed line corresponds to the Fermi level. Figure has been taken from reference [34].

of the conductance compared to the expected values from theory, see section 6.3. The energy gap of about $\Delta \approx 300\,\mathrm{meV}$ gives the upper limit of the filling of the Dirac cone, for which the observed conductance originates in the surface only. However, the spectral weight of a Dirac cone, filled to this limit, is about five times smaller than the observed spectral weight. Additionally, a trivial surface state is observed for Bi$_2$Se$_3$, which coexists with the topologically protected surface state [47, 48, 50]. In contrast, for Bi$_2$Te$_3$ no trivial surface state is reported. In this sense, it is better suited to only investigate the topologically protected surface state by optical spectroscopy than Bi$_2$Se$_3$. Nevertheless, FTIR spectroscopy could not yet distinctly detect the topologically protected surface state of Bi$_2$Te$_3$ [51, 53]. Chapler *et al.* [53] report on $\sigma_1(\omega)$ of Bi$_2$Te$_3$ with a Drude-like feature, see figure 7.6. However, the weight is too large for its origin in the topologically protected surface state. Hence, Chapler *et al.* [53] conclude that it originates from bulk charge carriers.

We will report on thickness-dependent data from Bi$_2$Te$_3$. Additionally, we will report on data from the compensated topological insulator (Bi$_{0.57}$Sb$_{0.43}$)$_2$Te$_3$, which is known to have the highest resistivity in the (Bi$_{1-x}$Sb$_x$)$_2$Te$_3$ family [98].

7.2 Data and analysis for Bi$_2$Te$_3$

In order to detect the topologically protected surface state, we investigate Bi$_2$Te$_3$ films with a thickness of 14, 33, and 53 nm in the THz and FIR range. Our samples have been prepared by molecular-beam epitaxy (MBE)[1] on high-resistivity Si(111) wafers with a thickness of about 0.5 mm. A good surface quality was observed in atomic-force microscopy [97]. Steps of 1 nm were detected, which corresponds to the thickness of one quintuple layer.

---

[1] The samples have been fabricated by Dr. Mussler in the group of Prof. Grutzmacher at the Forschungszentrum Jülich

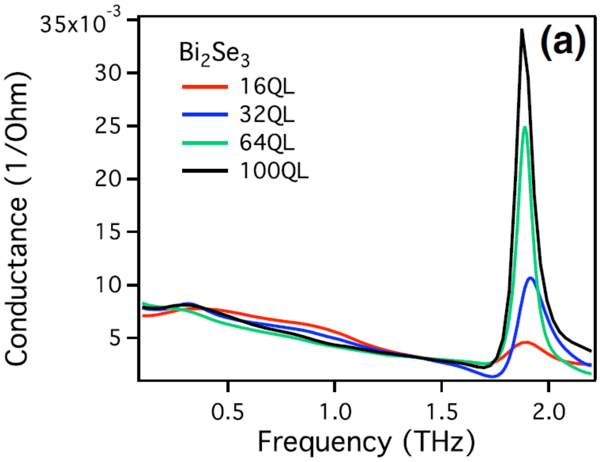

Figure 7.5: Conductance for Bi_2Se_3 thin films of different thickness as a function of frequency. Figure has been taken from reference [81].

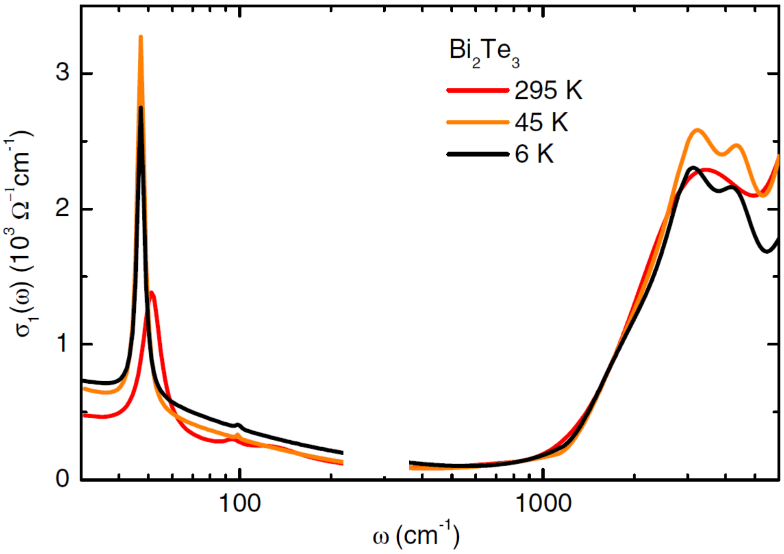

Figure 7.6: Temperature dependent $\sigma_1(\omega)$ of Bi_2Te_3. Figure has been taken from reference [53].

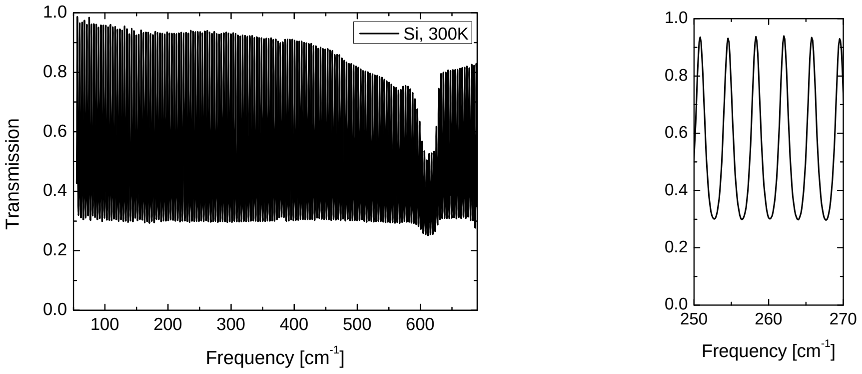

(a) (b)

Figure 7.7: a) transmittance of the silicon substrate at 300 K. a) Closeup of Fabry-Pérot fringes.

7.2.1 Characterizing the silicon substrate

We characterize the substrate in order to distinguish between features from the substrate and the topological insulator, see figure 7.7a. The transmittance of Si exhibits pronounced Fabry-Pérot fringes from multiple reflections within the substrate, see figure 7.7b. The maxima of the fringes reach almost unity for low frequencies even for 300 K. Accordingly, the substrate exhibits a low defect density.
The pronounced excitation just above 620 cm^{-1} (77 meV) is the well-known optical phonon of silicon [99].

7.2.2 Phonons in Bi$_2$Te$_3$

The transmittance of the 14 nm thick film of Bi$_2$Te$_3$ on the Si substrate is shown for 300 K and 5 K in figure 7.8. The data cover the range from 50 cm^{-1} to 680 cm^{-1} and were measured in the THz setup and the FTIR spectrometer, see section 4.2 and 4.1. We observe an excitation at about 50.4 cm^{-1} at 5 K. Richter *et al.* reported an infrared active phonon at 48±2 cm^{-1} (50±2 cm^{-1}) for 15 K (300 K) and for single crystals [87]. The feature broadens with increasing temperature, see figure 7.9. We conclude that the detected excitation is an optically active E_u phonon mode of Bi$_2$Te$_3$. This mode shows a very large oscillator strength of $\Delta\epsilon = 205$ [87] and thus leaves a clear signature even for such a small film thickness of $d = 14$ nm. The higher E_u mode is not visible in the data, due to the much smaller oscillator strength of $\Delta\epsilon$=1.5 [87].

The temperature-dependent transmittance in figure 7.9 reveals a shift of the phonon mode from 51.1 cm^{-1} at 5 K to 55.9 cm^{-1} at 300 K. The shift in the other samples is comparable, see table 7.1. At first sight, this temperature-induced hardening comes as a surprise. We expect a softening with increasing temperature due to the increased lattice parameters. However, strain caused by the lattice mismatch between Si and Bi$_2$Te$_3$ increases due to dif-

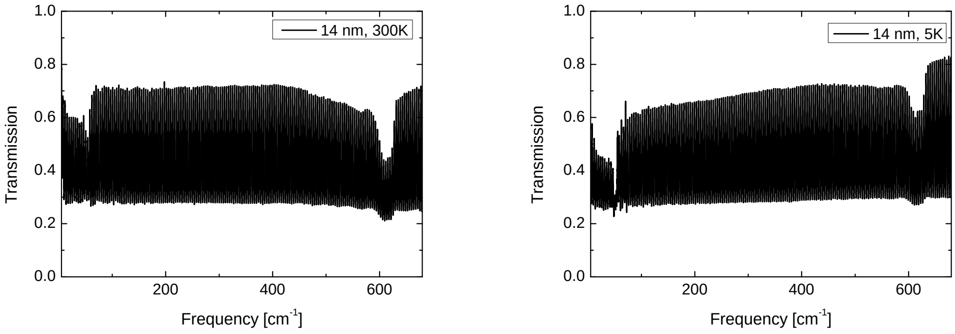

(a) (b)

Figure 7.8: Transmittance for a film of 14 nm thickness of Bi_2Te_3 on Si at 300 K (a) and 5 K (b). THz data and FIR data have been merged.

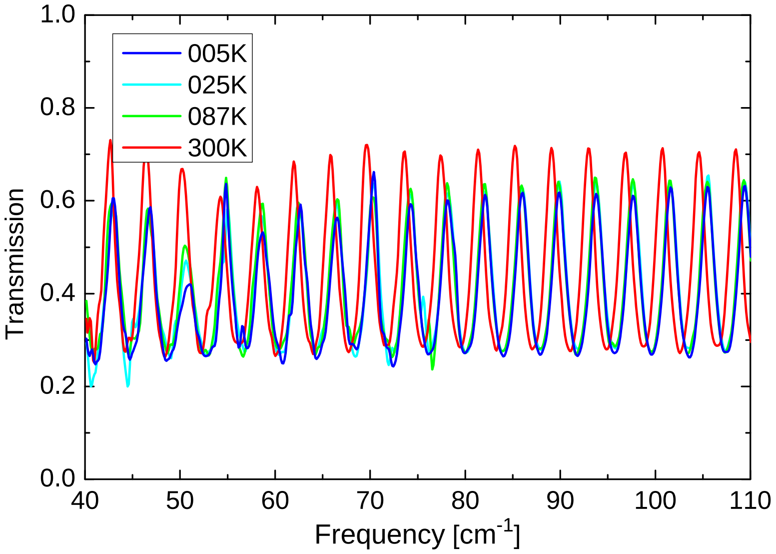

Figure 7.9: Closeup of the transmittance of 14 nm Bi_2Te_3 on Si in the phonon frequency range. The dip assigned to the phonon mode shifts to lower frequencies for lower temperatures.

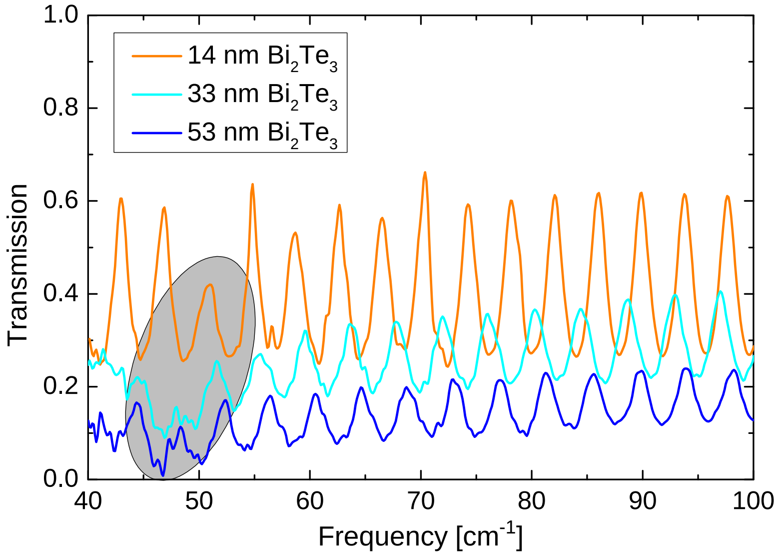

Figure 7.10: Transmittance of Bi_2Te_3 films on Si substrate for different thicknesses at 5 K. The dip assigned to the phonon mode (gray area) shifts to lower frequencies for larger thicknesses.

Thickness	14 nm	33 nm	53 nm
ω_0 5 K	51.0	46.7	46.3
ω_0 300 K	55.6	51.4	51.9

Table 7.1: table
Eigenfrequencies of the E_u phonon mode for 5 K and 300 K for different film thicknesses.

ferent thermal expansion coefficients. This leads to an increase of the eigenfrequency. This is accompanied by the observation of a similar shift depending on the thickness; the thicker a sample, the lower the frequency of the phonon, see figure 7.10. The reason is the release of strain within the sample. Therefore, the value of the eigenfrequency approaches the value of bulk Bi_2Te_3 of $48 \pm 2\,cm^{-1}$ at 15 K and $50 \pm 2\,cm^{-1}$ at 300 K [87] for large film thickness.

7.2.3 Looking for the surface state

The transmittance of Bi_2Te_3 on Si deviates from the transmittance of the pure substrate over a broad frequency range, compare figure 7.8 and 7.7a. We attribute the suppression to free charge carriers in Bi_2Te_3. The corresponding Drude peak may be caused either by doping of the bulk or by the Dirac fermions of the topologically-protected surface state. Additionally, the presence of inter-band transitions within the Dirac cone causes a constant suppression of the transmittance. The challenge is to distinguish the surface contributions from the bulk contributions. Therefore, we analyze the spectra of the 14, 33, and 53 nm thick films on Si. In order to obtain an overview of the thickness and temperature dependence, we plot the upper envelope of the transmittance, see figure 7.11. The envelope of the thick

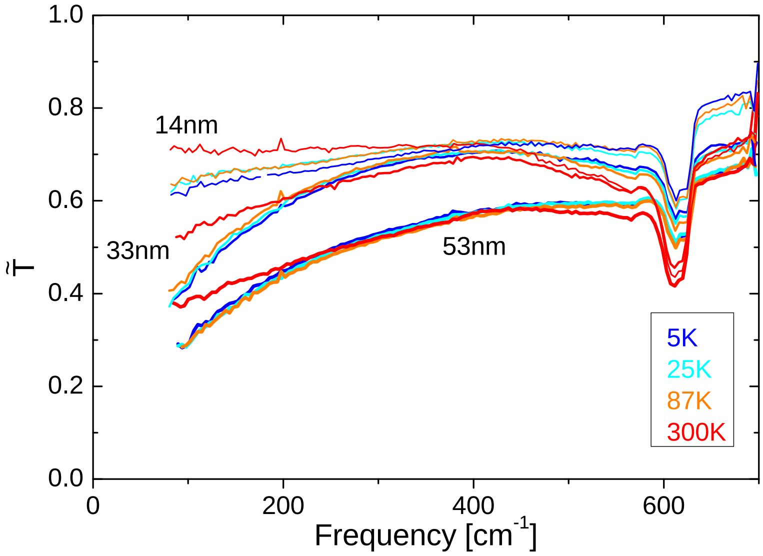

Figure 7.11: Temperature-dependent maxima of the transmittance of the 14, 33, and 53 nm thick films of Bi_2Te_3 on Si substrate.

sample is significantly more suppressed than the envelope of the thin sample. This proofs that the bulk properties are dominating or at least of importance. However, it does not proof the absence of a surface contribution. Remarkably, the envelope increases from 5 K to 300 K for each thickness. This is not related to an increased scattering rate, which would shift the spectral weight to higher frequencies, since above the Si phonon the transmittance is independent of temperature. It might be related to puddles, see section 6.4.1.2. An alternative could be the rise of a surface state with decreasing temperatures, hence the effect on the envelope should be independent of the thickness of the film. To quantify the thickness and temperature dependence we determine $\sigma_1(\omega)$ of the Bi_2Te_3 films by fitting a two-layer model to the transmittance from 40-500 cm^{-1}[2]. The parameters of the Si layer have been determined by the transmittance of Si only. For the Bi_2Te_3 film we assume three contributions: a phonon, a Drude peak, and an offset. We expect the size of the offset to be a sample dependent property and therefore use the same value for the 5 K and the 300 K fit. Its value is determined by the transmittance for 5 K at 450 cm^{-1}, since here neither the Drude peak nor the phonon of Si influence the transmittance. Even though the transmittance exhibits pronounced fringes, we can precisely fit the spectra, as the fit for the film thickness of 53 nm at 5 K shows, see figure 7.12. The resulting $\sigma_1(\omega)$ for the three samples at 5 K and 300 K are plotted in figure 7.13. It is striking that $\sigma_1(\omega)$ of the 33 nm thick sample is very similar to the 53 nm thick sample. Furthermore, the 14 nm thick sample has a larger offset. At 300 K the films have approximately the same σ_{DC}, while at 5 K the thickest sample has the highest σ_{DC}. A contribution from the surface would have the strongest effect on

---

[2] The fits are performed using RefFIT which is a free program written by Alexey Kuzmenko. It can be downloaded from https://sites.google.com/site/reffitprogram/. The program is designed to fit optical spectra of multi-layer systems.

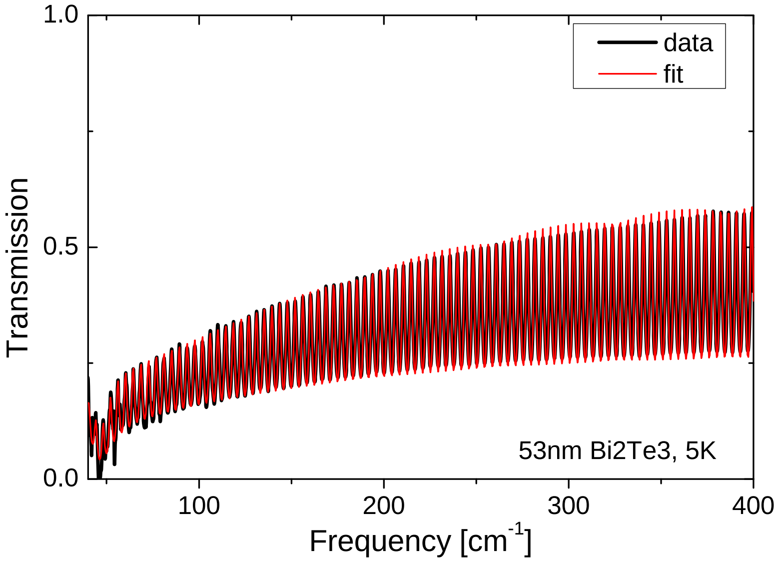

Figure 7.12: Black: The transmittance of the 53 nm thick film on Si substrate at 5 K. Red: Fit of a two-layer model takes a phonon, a Drude peak, and an offset for the Bi_2Te_3 into account.

$\sigma_1(\omega)$ of the thinnest sample. Therefore, we can rule out that the Drude peak mainly comes from surface states. We determine the spectral weight of the fitted oscillators and compare it to the spectral weight caused by intra-band excitations of a Dirac cone, with a filling of 150 meV, $D_{2D} \approx 1.1 \cdot 10^9\,(\Omega\,\mathrm{cm})^{-1}$, according to section 6.3.1. The spectral weight of the Drude peak, the offset, and the offset plus the Drude peak are plotted in 7.14a) for 300 K and in 7.14b) for 5 K. For both temperatures the spectral weight of the intra-band excitations is well below the spectral weight of the offset. Furthermore, each fit parameter is clearly increasing with increasing thickness. Actually, the parameters should be constant, but sample-dependent effects like surface roughness can cause deviations. Moreover, the surface roughness might be larger for thin films, since the crystal growth is more difficult for very few quintuple layers. This might explain the enhanced offset for the 14 nm thick sample.

So far we have no indication for a significant surface contribution and the spectral weight of the Drude peak and the offset exceeds the spectral weight of a pure surface contribution by intra-band excitations by far, similar to the previous reports in literature on Bi_2Te_3 [47,53]. However, the envelope of the transmittance showed an decrease with rising temperatures. In order to investigate whether this effect comes from the bulk or the surface, we have to isolate it. Therefore, we subtract $\sigma_1(300\,K)$ of the Drude peak from $\sigma_1(5\,K)$ of the Drude peak for all thicknesses. The resulting $\Delta\sigma_{1,Drude}(\omega)$ in figure 7.15 shows that in $\sigma_1(\omega)$ the excitations have approximately the same spectral weight D, as expected for a bulk contribution. Since the scattering rates differ for the three samples, we determine D, see figure 7.16. It is similar to the spectral weight of intra-band excitations, but the $D(d)$ extrapolates to the origin, which clearly shows that this contribution comes from the bulk.

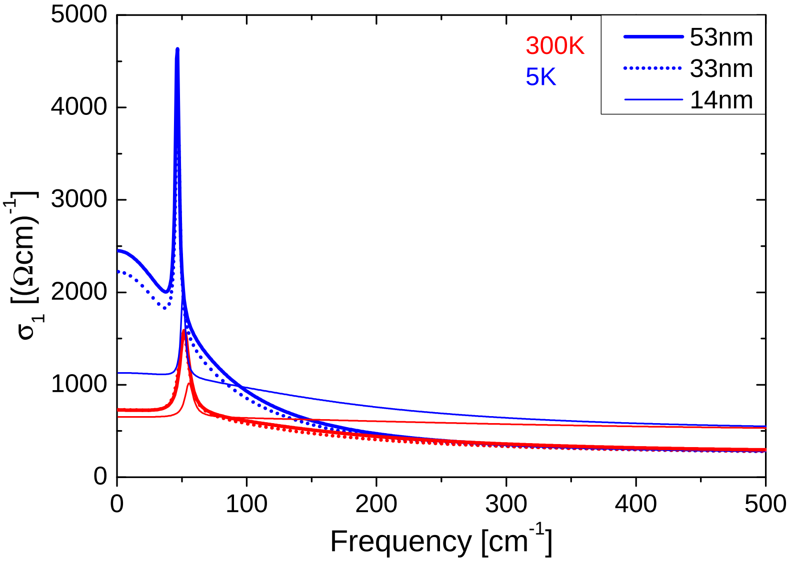

Figure 7.13: $\sigma_1(\omega)$ of the film determined from fits to the transmittance.

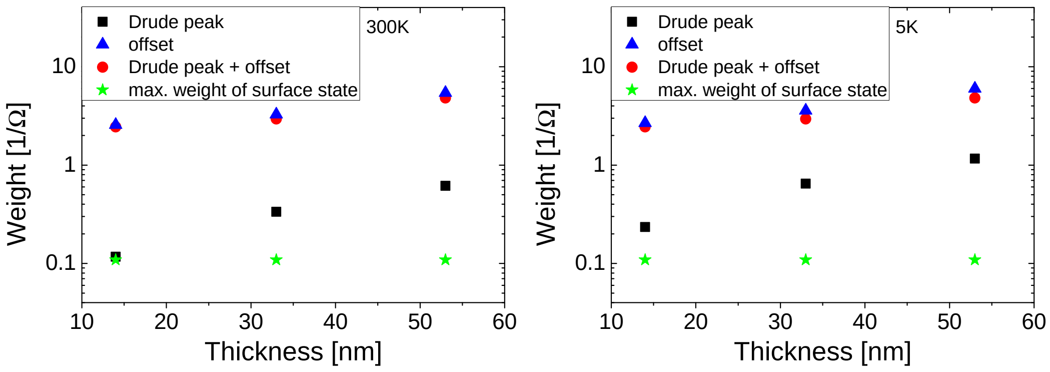

(a)

(b)

Figure 7.14: Spectral weight at 300 K (a) and 5 K (b) of the Drude peak (black squares), the spectral weight of the offset (blue triangles), the Drude weight plus the spectral weight of the offset (red circles), and the spectral weight of intra-band excitations of a Dirac cone filled to the $E_F = \Delta = 150\,\text{meV}$ (green stars).

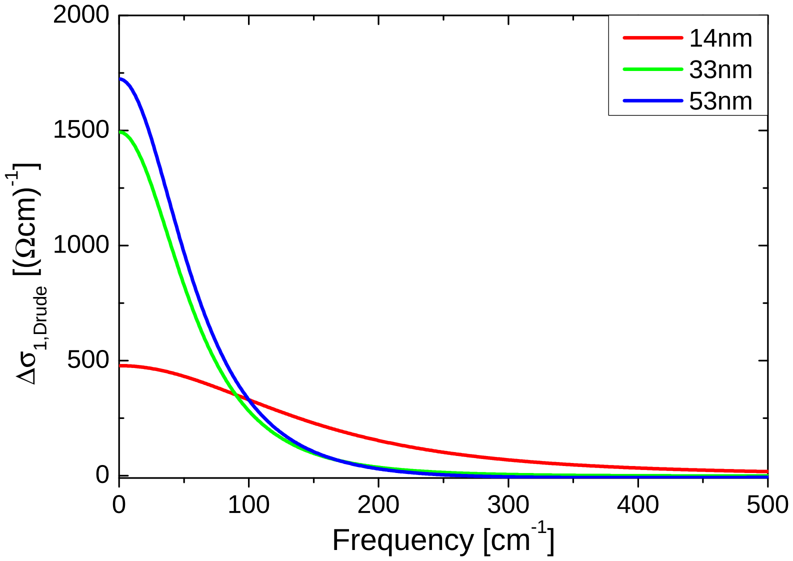

Figure 7.15: $\Delta\sigma_{1,Drude}(\omega)$ resulting from the subtraction of $\sigma_{1,Drude}(\omega)$ at 300 K from the $\sigma_{1,Drude}(\omega)$ at 5 K.

7.2.4 Conclusion

We report on thickness dependence and temperature dependence of the E_u^1 phonon mode, which we explain by stress. We determine $\sigma_1(\omega)$ for the films by fits and show that $\sigma_1(\omega)$ represents the bulk properties of the topological insulator, since we find neither evidence for a trivial, nor a topologically protected surface state. Nevertheless, the topologically protected surface state is known to exist in Bi_2Te_3, but it is likely to be covered by excitations of charge carriers in the bulk.

7.3 Thin film of compensated $(Bi_{0.57}Sb_{0.43})_2Te_3$

The charge carriers in the bulk can be reduced by compensation, according to section 6.4. Bi_2Te_3 is usually n-type. The topological insulator Sb_2Te_3 is p-type. Therefore, we can realize the transition from n-type to p-type conductivity for $(Bi_xSb_{1-x})_2Te_3$ by tuning the Bi-Sb ratio [66, 96, 98]. DC conductivity measurements performed by Weyrich *et al.* [98] showed this transition, see figure 7.17a. A maximal resistivity of about ρ=1.2 mΩcm was achieved for the composition $(Bi_{0.57}Sb_{0.43})_2Te_3$ [98], see figure 7.17b. We investigated a 28 nm thick film of $(Bi_{0.57}Sb_{0.43})_2Te_3$ on a Si substrate[3] in the THz setup[4] and in the FTIR spectrometer, see figure 7.18.

---

[3] The film was grown by Dr. Mussler by MBE at the Forschungszentrum Jülich

[4] The THz measurements have been performed by Valeri Mehler and Malte Langenbach

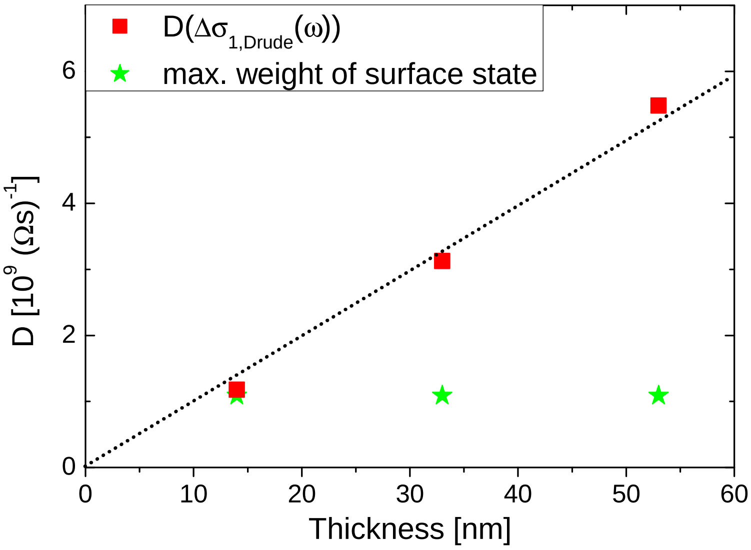

Figure 7.16: Red squares: The spectral weight of $\Delta\sigma_{1,Drude}(\omega)$. Green stars: The spectral weight of intra-band excitations of a Dirac cone filled to the $E_F = \Delta = 150\,\text{meV}$. The dashed line is beginning in the origin and fitted to the three data points.

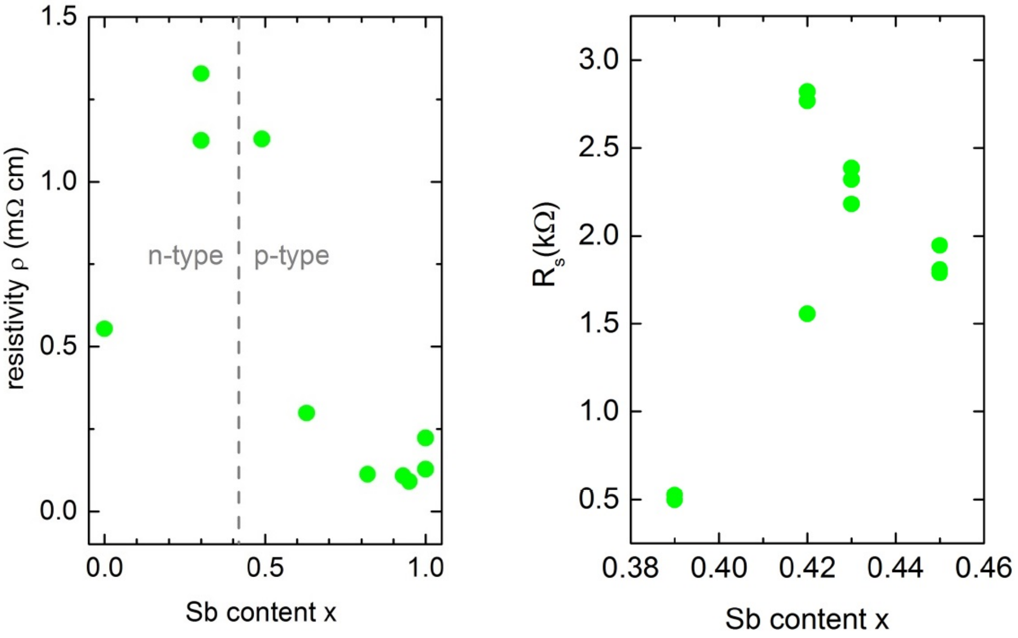

(a) (b)

Figure 7.17: A: Resistivity of $(\mathrm{Bi}_x\mathrm{Sb}_{1-x})_2\mathrm{Te}_3$ as function of the Sb content. The dashed line represents the transition from n-type to p-type conductivity. B: Resistance of $(\mathrm{Bi}_x\mathrm{Sb}_{1-x})_2\mathrm{Te}_3$ close to the transition from n-type to p-type conductivity. Reproduced from [98], `https://dx.doi.org/10.1088/0953-8984/28/49/495501` {DOI}, with the permission of AIP Publishing.

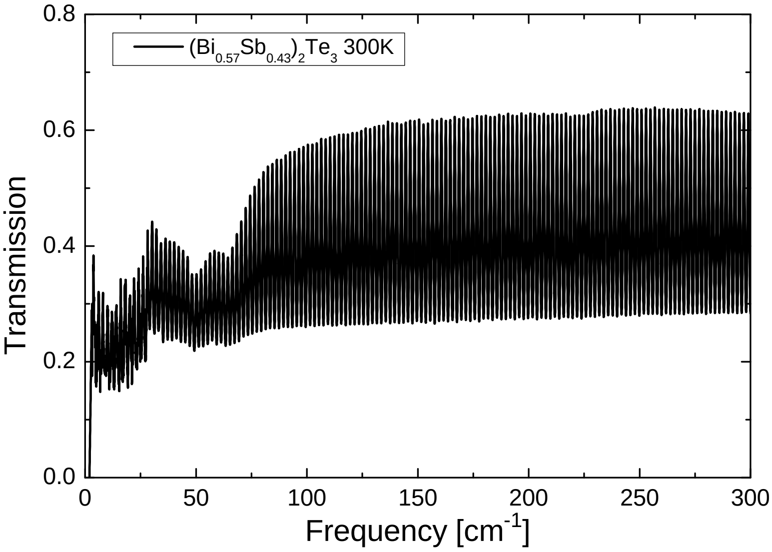

Figure 7.18: Transmittance of 28 nm $(\mathrm{Bi}_{0.57}\mathrm{Sb}_{0.43})_2\mathrm{Te}_3$ on Si at 300 K. The data were obtained by THz and FIR spectroscopy.

7.3.1 Room-temperature transmittance

7.3.1.1 Phonons

The transmittance is dominated by phonons at low frequencies. A closeup is shown in figure 7.19. In contrast to transmittance of $\mathrm{Bi}_2\mathrm{Te}_3$, we find three phonon modes. We extract the phonon eigenfrequencies $\omega_{0,1}$=35 cm^{-1}, $\omega_{0,2}$=48.9 cm^{-1}, and $\omega_{0,3}$=64.8 cm^{-1} by a fit[5]. The two latter modes correspond to the E_u^1 modes. The frequencies of the E_u^1 modes can be explained by the different masses of Bi and Sb. In the model for a free vibration without damping, the eigenfrequency is given by

$$\omega_0 = \sqrt{\frac{k}{m}}, \tag{7.3.1}$$

with k the force constant. Between the eigenfrequency of the same phonon with Bi and with Sb, we expect a factor of 1.31, since the eigenfrequencies depend on the inverse square root of the mass

$$\frac{m_{Bi}}{m_{Sb}} = \frac{208.98}{121.76} = 1.716 = (1.31)^2. \tag{7.3.2}$$

The ratio of the frequencies is 1.33, which is in excellent agreement considering the simple model. However, this means that we observe pure Bi and pure Sb modes, which could be explained by an inhomogeneous distribution of Bi and Sb in the sample or a superlattice. The lowest phonon mode at 35 cm^{-1} is associated with the E_g^1 mode which is Raman-active in $\mathrm{Bi}_2\mathrm{Te}_3$. The mode was measured for $\mathrm{Bi}_2\mathrm{Te}_3$ in Raman at 35 cm^{-1} [100]. In $\mathrm{Bi}_2\mathrm{Te}_3$ the E_g^1 mode has no dipole moment, since the two Bi layers within a quintuple layer vibrate in

---

[5] The fits have been performed using RefFIT

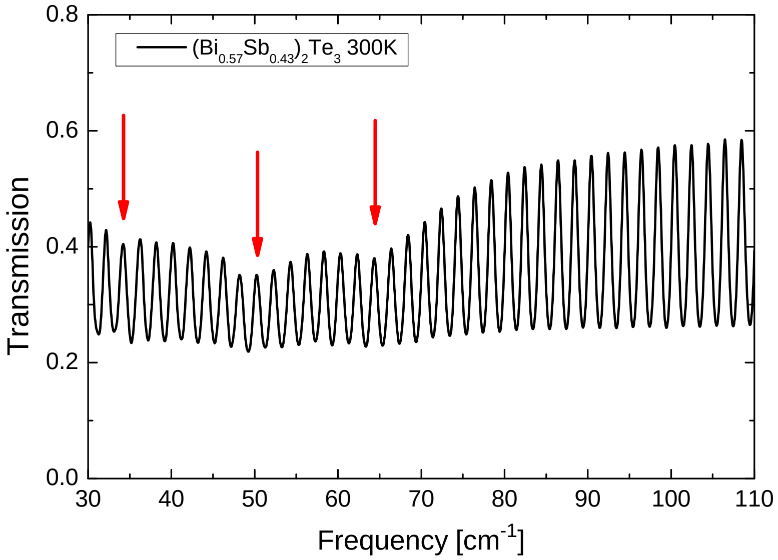

Figure 7.19: Closeup of the transmittance of $(\mathrm{Bi}_{0.57}\mathrm{Sb}_{0.43})_2\mathrm{Te}_3$ on Si at 300 K. The red arrows indicate the position of the phonon modes.

opposite direction, see figure 7.2. However, the mode becomes infrared active, if the sites are partially occupied by Bi or Sb.

7.3.1.2 Drude contribution of the substrate

At room temperature and low frequencies we find a Drude absorption feature besides the phonons, see figure 7.18. However, we only find from the transmittance of the substrate that the Drude peak originates from the Si substrate, see figure 7.20. Due to the low impedance of the substrate we are restricted to the low-temperature data which shows no Drude peak.

7.3.2 Surface state

The spectra from 39 K on are not influenced by the activated charge carriers in the substrate. Moreover, the spectra are independent of temperature, see figure 7.21. In the maxima, the transmittance reaches on average about 95 %. No Drude peak can be observed. Hence, the compensation successfully reduced the charge carrier density, resulting in an insulating bulk as desired for topological insulators.

We determine the expected suppression of the transmittance due to the Dirac fermions according to section 6.3.1. At first, we calculate the influence of the inter-band transition on the transmittance for the Fermi level at the Dirac point. The surface conductance of $G = 1.5 \cdot 10^{-5}\,\Omega^{-1}$, see equation 6.3.2, at both interfaces would result in a suppression of the transmittance by about 1 %. For $\hbar\omega \leq 2E_F$, the sum-rule describes the transfer of the spectral weight from the inter-band transitions to the Drude peak of intra-band transitions [39, 79]. The 2D Drude weight D_{2D} to explain a transmittance of 95 % can be calculated analog to the calculations for $\mathrm{Bi}_2\mathrm{Te}_3$ in section 7.2.3. We assume a minimal scattering

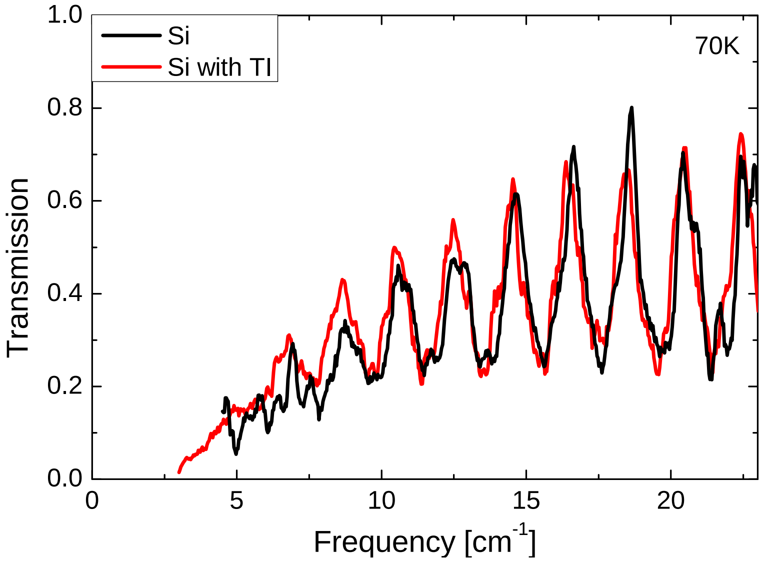

Figure 7.20: The transmittance for the substrate only and for the substrate with 28 nm of $(Bi_{0.57}Sb_{0.43})_2Te_3$ at 70 K.

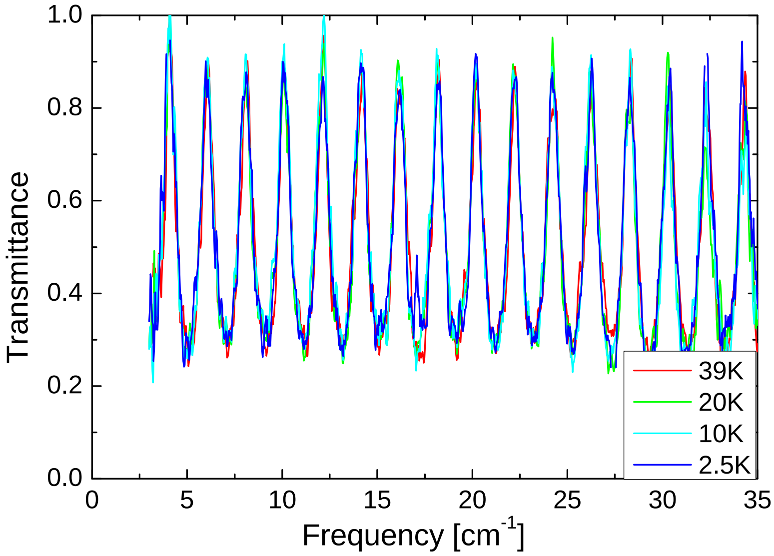

Figure 7.21: Temperature-dependent transmittance of $(Bi_{0.57}Sb_{0.43})_2Te_3$.

rate of $\gamma \geq 440\,\mathrm{cm}^{-1}$, since no increase of the conductivity in the measured frequency range is visible. According to equation 6.3.7, the minimal Drude weight explaining the suppression of 95 % corresponds to $\mathrm{D}_{2D} = 9.3{\cdot}10^8\ (\Omega\mathrm{s})^{-1}$. The energy gap in $(\mathrm{Bi}_x\mathrm{Sb}_{1-x})_2\mathrm{Te}_3$ is $\Delta \approx 200 - 250\,\mathrm{meV}$ [66]. Therefore, the Drude weight of the intra-band transitions for $\mathrm{E}_F \leq \Delta$ is $\mathrm{D}_{2D} = 1.8 - 2.3 \cdot 10^{10}(\Omega\mathrm{s})^{-1}$, according to equation 6.3.6.

In summary, the intra-band transitions can explain even the suppression of the transmittance to 95 %, while the inter-band transitions have too little spectral weight. Indeed, the intra-band excitations could explain a much stronger suppression. Therefore, the main result is that the spectral weight of bulk carriers and the intra-band excitations is minimized for $(\mathrm{Bi}_{0.57}\mathrm{Sb}_{0.43})_2\mathrm{Te}_3$, which is remarkable, since in literature Drude peaks with a spectral weight exceeding the spectral weight of the intra-band excitations are reported [53, 79–81].

7.3.3 Summary

We investigated a thin film of compensated topological insulator $(\mathrm{Bi}_{0.57}\mathrm{Sb}_{0.43})_2\mathrm{Te}_3$. Most remarkably, it shows no Drude peak coming from the bulk at low temperatures. The minimal suppression is in the order of magnitude which is expected from the topologically protected surface state, which makes the film an ideal topological insulator.

Chapter 8

Compensated topological insulators

The topological insulators Bi_2Te_3 and Bi_2Se_3 exhibit metallic behavior due to defect-induced charge carriers. Bi_2Se_3 is known for its n-type conductivity originating from Se vacancies acting as donors, while Bi_2Te_3 usually exhibits p-type conductivity due to antisite defects. By understanding the defect chemistry [36, 101, 102] the carrier density was reduced. The progress in device fabrication allowed the growth of bulk-insulating thin films of Bi_2Te_3 [55]. To reduce the bulk conductivity further the defects are compensated, *i.e.* $K \equiv N_A/N_D = 1$. This leads to insulating single crystals of $Bi_{2-x}Sb_xTe_{3-y}Se_y$, see figure 8.1. In $Bi_{2-x}Sb_xTe_{3-y}Se_y$ the charge carrier density is reduce by chalcogen order [43, 103, 104], see figure 7.1, forming Te/Se-Bi/Sb-Se-Bi/Sb-Te/Se quintuple layers. The Se vacancies are reduced by the two Bi/Sb layers trapping the Se layer, because of strong chemical bonding between Bi and Se in this position, making the Se layer less exposed to evaporation. Additionally, Bi/Te antisite defects are reduced due to strong bonding between the Bi/Sb layers and the Se layer which makes it energetically favorable for the Te and Se to occupy the Te/Se layer.

The compensation is achieved by variation of x and y, see figure 8.2. In addition, the variation offers the possibility to tune the energy of the Dirac point with respect to the Fermi energy E_F [105, 106], see figure 8.3. For $BiSbTeSe_2$ the Fermi level and the Dirac point nearly coincide. Therefore, we expect very little influence of the surface on the optical data obtained on single crystals, which makes this composition ideal for studying the bulk carrier dynamics. However, for thin films of $BiSbTeSe_2$ the surface is the dominant transport channel [78, 104, 107]. Nevertheless, σ_{DC} as function of temperature for $Bi_{2-x}Sb_xTe_{3-y}Se_y$ is puzzling, since it does not fall below 0.05-0.1 $(\Omega\text{cm})^{-1}$ [43, 103, 104, 107–114], which cannot be explained by the surface state.

Before we present the results on $Bi_{2-x}Sb_xTe_{3-y}Se_y$ for $x = 0.75, 0.5, 0.25$, and 0 and explain the influence of x on the properties of $Bi_{2-x}Sb_xTe_{3-y}Se_y$, we will discuss the results for $BiSbTeSe_2$ ($x = 1$). Thereby, we focus on the analysis of the optical data and the sim-

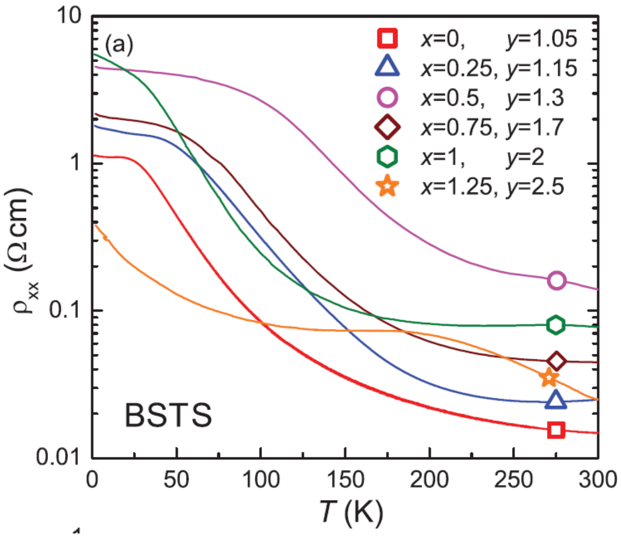

Figure 8.1: The resistivity ρ_{xx} is plotted on a logarithmic scale versus the temperature for optimized compositions. Figure has been taken from reference [43]`https://dx.doi.org/10.1103/PhysRevB.84.165311` {DOI}. Copyright by American Physical Society (2011).

ulation, explaining the observed phenomena. Note that the results and data on $BiSbTeSe_2$ along with the theory have partly been published [115,116].

8.1 $BiSbTeSe_2$

8.1.1 Optical properties

In order to determine $\sigma_1(\omega)$ we perform optical transmittance and reflectance measurements in the FIR and MIR ranges. To detect a possible surface contribution, we measured samples of different thickness. It is known that the resistivity is sample dependent and can vary up to a factor of three within the same composition [43]. Therefore, we investigated the same sample and successively cleave the sample to obtain samples of different thicknesses. We measured the thicknesses according to section 5.3 and obtained 183 μm (#1 a), 130 μm (#1 b), 102 μm (#1 c), and 2 μm (flake).

8.1.1.1 Transmittance

The transmittance $T(\omega)$ of sample # 1 is shown in figure 8.4. The transmittance for 300 K exceeds the noise level only between 830 to 1335 cm^{-1} and stays below 0.5 %. Upon cooling the transmittance increases. For 50 K it exceeds the noise level between 180 cm^{-1} and 2060 cm^{-1} and reaches values of up to 25 %. In the highly transparent range pronounced Fabry-Pérot fringes are present due to multiple reflections between the plane-parallel surfaces of the cleaved sample, see the right panel in figure 8.4. Most remarkably, the transmittance decreases strongly upon further cooling below 50 K. For 5 K the maximum transmittance

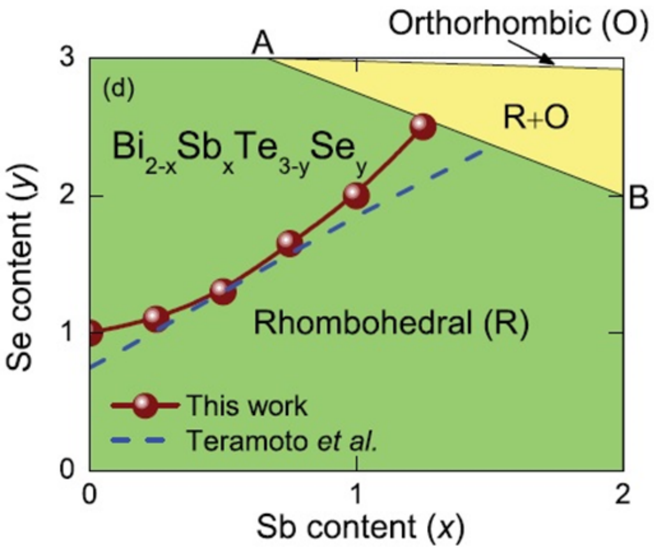

Figure 8.2: Compensated alloys of $Bi_{2-x}Sb_xTe_{3-y}Se_y$. Red points represent the samples with the highest resistivity as found by Ren *et al.* [43]. The size of the points represents the error on the composition. The dashed line is the result of a previous study by Teramoto *et al.* [117]. Figure has been taken from reference [43]`https://dx.doi.org/10.1103/PhysRevB.84.165311` {DOI}. Copyright by American Physical Society (2011).

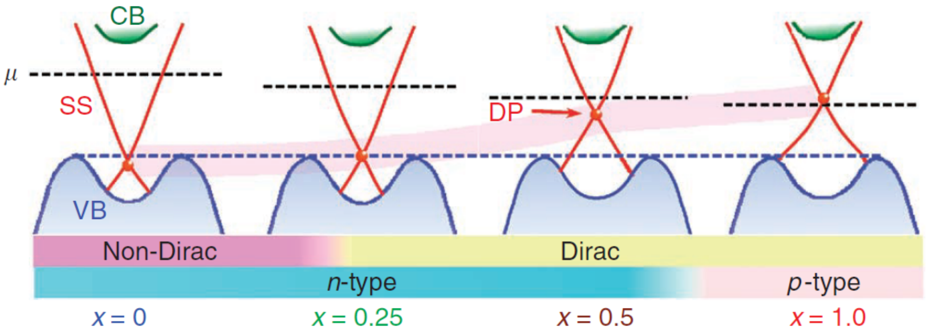

Figure 8.3: The Dirac cone located at the surface is plotted with respect to the conduction and valence band for different values of x in $Bi_{2-x}Sb_xTe_{3-y}Se_y$. The Dirac point is labeled with DP and the Fermi level corresponds to the upper dashed line. The figure has been taken from reference [105]`https://dx.doi.org/10.1038/ncomms1639` {DOI}. Copyright by Macmillan Publishers Limited (2012).

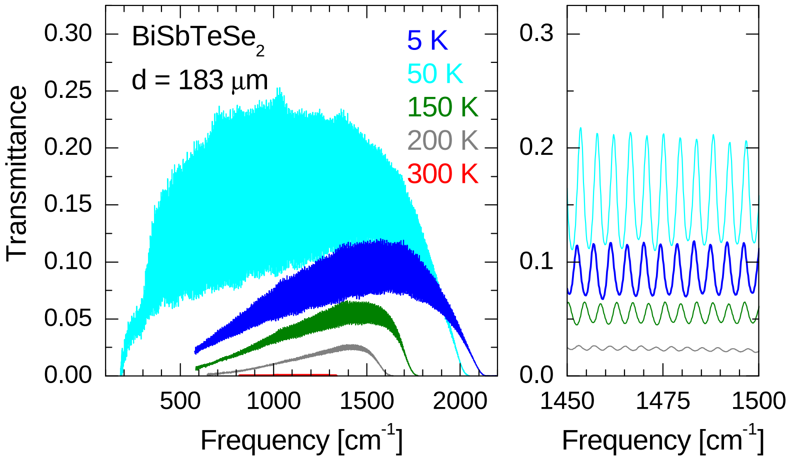

Figure 8.4: The transmittance of the 183 μm thick sample is plotted for different temperatures. The data at 50 K is plotted in the FIR range and the MIR range. For the other data only the MIR range is plotted. The right panel is a closeup of the data, picturing the Fabry-Pérot fringes. This figure has been published in [115]`https://dx.doi.org/10.1103/PhysRevB.93.245149` {DOI}. Copyright by American Physical Society (2016).

is 12 %, which is less than half of the value for 50 K. The low-frequency cut-off of the mid-infrared detector (MCT) limits the data set for 5 K and 150 K to 600 cm^{-1}. For the low-frequency measurements in the far-infrared range a bolometer was used. However, the transmittance can only be measured if the low-frequency intensity exceeds a certain value, which was the case for 50 K only.

8.1.1.2 Energy gap

The high-frequency cut-off is given by the energy gap. We plot the temperature-dependent value of the energy gap in figure 8.5. The gap decreases by almost 40 % from 2124 cm^{-1} (263 meV) at 5 K to 1302 cm^{-1} (161 meV) at 300 K. Such a strong temperature dependence of the gap is in agreement with band-structure calculations for binary compounds [54, 118]. Additionally, we plot two fits using the Varshni relation [119]

$$\Delta(T) = \Delta_0 - \frac{\alpha T^2}{T+\beta}, \tag{8.1.1}$$

where Δ_0 denotes the gap for 0 K, and α and β fitting parameters characteristic for the compound. The red, dashed line is a fit to all data points, while the green, dashed curve is a fit to the data from 100 K to 300 K. The latter fit is more accurate, due to a broad, temperature-dependent excitation directly below the energy gap. The theory of the excitation below the gap is discussed in section 6.4.1.7, while the influence on the data is discussed in section 8.2.4. The fit gives an energy gap at 5 K of 2183 $^{-1}$ (271 meV). We find $\alpha = 3.3\,(\mathrm{cm\,K})^{-1}$ and $\beta = 37.5$ K. This value for α is framed by $\alpha = 0.77\,(\mathrm{cm\,K})^{-1}$ reported

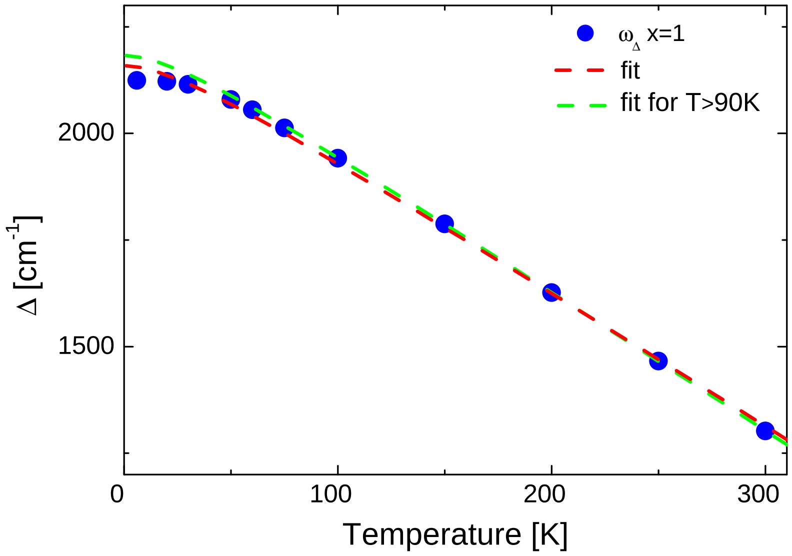

Figure 8.5: Energy gap Δ as function of temperature. Varshni fit on $\Delta(T)$ of the 102 μm thick sample yields Δ_0. The two different fits take a different temperature range into account.

for Bi$_2$Te$_3$ [120], $\alpha = 1.6\ (\mathrm{cm\,K})^{-1}$ [121], and $\alpha = 2.0\,(\mathrm{cm\,K})^{-1}$ [59] reported for Bi$_2$Se$_3$, and $\alpha = 5.6\,(\mathrm{cm\,K})^{-1}$ for Sb$_2$Se$_3$ [121].

In order to perform a quantitative analysis it is convenient to determine $\sigma_1(\omega)$. Therefore, it is necessary to determine the reflectance.

8.1.1.3 Reflectance

The reflectance in the transparent range is determined by the Fabry-Pérot fringes as described in section 5.3 and 5.4. Therefore, at first the temperature-dependent refractive index is determined, see figure 8.6. The refractive index $n(\omega)$ increases at high frequencies due to interband excitations. The main contribution comes from excitations across the band gap which shifts to lower frequencies with rising temperature. At frequencies below about 1000 cm^{-1} the decrease of $n(\omega)$ is caused by phonons and free or localized charge carriers. Similar to the transmittance, $n(\omega)$ shows a non-monotonic temperature dependence below 1000 cm^{-1}, with a maximum of $n(\omega)$ at about 40 K. From the refractive index we can determine the reflectance directly, because the absorption in the transparent range is small, see section 2.3.

We are interested in the reflectance of a semi-infinite sample in the FIR and MIR ranges to determine $\sigma_1(\omega)$. Therefore, we measured the reflectance of a single crystal with a thickness of 1100 μm. However, the low $\sigma_1(\omega)$ causes additional intensity from reflections on the backside of the sample, increasing the reflectance in the transparent range, see figure 8.7. The discrepancy in the transparent frequency range is the largest for 50 K, for which we expect the highest transmittance. The reflectance from the fringes was determined by the transmittance of a 102 μm thick sample which has a much larger transparent range than the

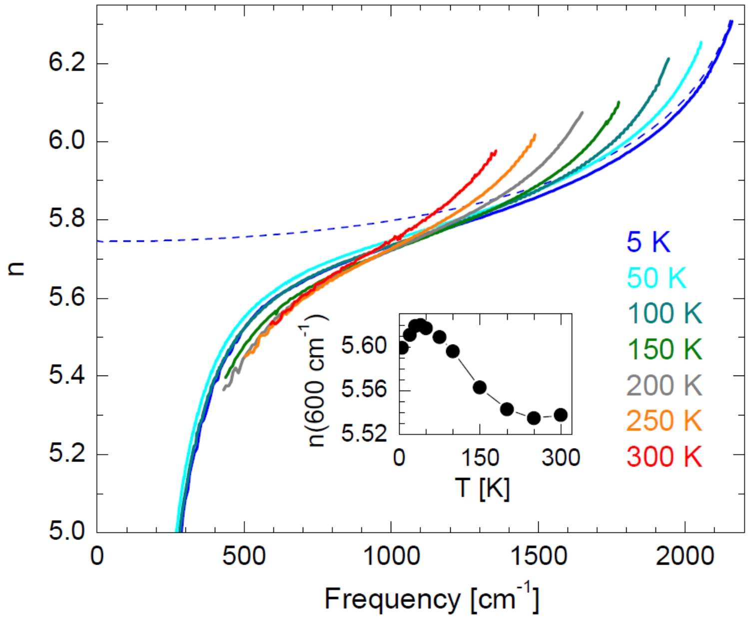

Figure 8.6: The refractive index n(ω) obtained in the transparent frequency range of the 102 μm thick sample from the positions of the interference fringes. At 5 K, $n(\omega)$ extrapolates to about 5.75 below the gap (dashed line) after subtracting the low-frequency contributions of phonons and after subtracting a Drude peak for the free charge carriers. Inset: Non-monotonic temperature dependence of $n(\omega)$ at 600 cm^{-1}.

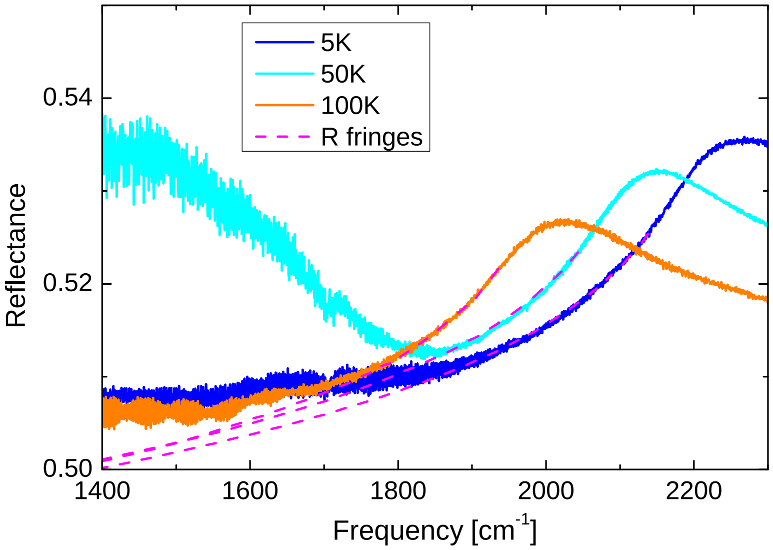

Figure 8.7: Reflectance of the 1100 μm thick sample is plotted for different temperatures together with the reflectance calculated from the fringes (dashed pink line).

1100 μm thick sample. Therefore, both reflectance have a large overlap in frequency. The agreement of both near the gap emphasizes the minor role of absorption for the reflectance in the transparent frequency range.

The measured transmittance supplemented with the reflectance from the fringes allows us to determine $\sigma_1(\omega)$ in the transparent frequency range. In order to obtain $\sigma_1(\omega)$ in the whole frequency range, we need the reflectance from 0 to ∞ to perform a Kramers-Kronig analysis. At high frequencies ($> 7500\,\mathrm{cm}^{-1}$) the reflectance measured by Fourier spectroscopy is supplemented by the reflectance determined by ellipsometry, see figure 8.8. The ellipsometry data were obtained using a rotating analyzer ellipsometer (Woollam VASE) equipped with a retarder between polarizer and sample. The measurements have been performed at room temperature in the photon-energy range of 0.75 eV to 5.5 eV (6050 cm^{-1} to 44360 cm^{-1}) for three different incidence angles (60°, 70°, and 80°)[1].

The reflectance for even higher frequencies ($> 44360\,\mathrm{cm}^{-1}$) has been extrapolated by a model including Drude, Lorentz, and Tauc-Lorentz oscillators which fits to the measured optical data and to the reflectance of Bi$_2$Te$_{1.8}$Se$_{1.2}$ above the ellipsometry range reported by Greenaway *et al.* [122].

At low frequencies the reflectance is dominated by phonon modes. We expect two phonon modes with E_u symmetry for a measurement with polarization parallel to the cleaved plane [87]. In Bi$_2$Te$_3$ these modes have been observed at 48 cm^{-1} and 98 cm^{-1}, in Bi$_2$Se$_3$ at 61 cm^{-1} and 134 cm^{-1} [87]. In BiSbTeSe$_2$ the modes have been measured at 62 cm^{-1} and 120 cm^{-1} [79]. The mode lower in energy is much stronger than the one higher in energy. Therefore, high reflectance is observed at about 50 cm^{-1} and a weak absorption feature at

---

[1] The ellipsometry data were obtained by Ignacio Vergara in the group of Prof. Grüninger at the II. Physical Institute at the University of Cologne.

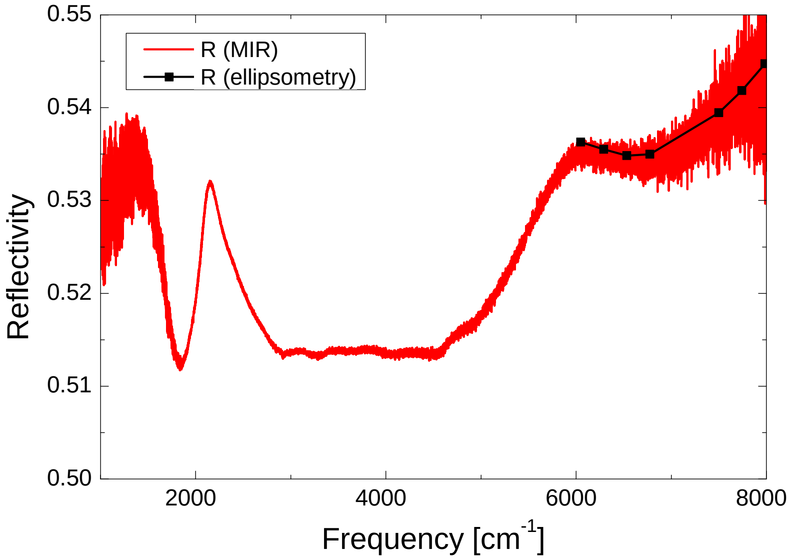

Figure 8.8: The reflectance at 40 K obtained in the MIR range (red curve) and the reflectance obtained by ellipsometry (black curve).

about 120 cm^{-1}, attributed to the weaker phonon mode, see figure 8.9. Similar interpretations of the reflectance have been reported for Bi_2Te_2Se [123–125]. However, the absorption features are sharper in Bi_2Te_2Se, which we attribute to the absence of Bi/Sb disorder and strongly reduced Te/Se disorder.

We use the observed phonons and the Drude peak to model the reflectance to zero frequency. On the resulting reflectance, a Kramers-Kronig analysis is performed. The resulting $\sigma(\omega)$ is part of the discussion in the following chapter.

8.1.1.4 Optical conductivity

We determine $\sigma_1(\omega)$ in order to obtain a quantity independent of the thickness. We are interested in the physics in the FIR and MIR ranges. Inversion gives $\sigma_1(\omega)$ in the transparent frequency range, see section 5.1, while a Kramer-Kronig analysis is needed to obtain $\sigma_1(\omega)$ above the gap, see section 3.6. An overview of $\sigma_1(\omega)$ in the transparent frequency range is plotted in figure 8.10. At high frequencies a steep increase of $\sigma_1(\omega)$ limits the data, which is caused by excitations across the energy gap. The gap decreases strongly with rising temperature as discussed in section 8.1.1.1. The main focus is drawn to the low-frequency $\sigma_1(\omega)$ and especially its temperature dependence. At 50 K the Drude peak is absent and $\sigma_1(\omega)$ is as low as $0.3\,(\Omega\text{cm})^{-1}$. Most remarkably, upon further cooling the Drude peak appears again.

8.1.1.5 Fit of $\sigma_1(\omega)$

We fit $\sigma_1(\omega)$ using RefFIT. Our fit takes into account a background, a phonon at 124 cm^{-1} and a multi-phonon at 350 cm^{-1}, in agreement with the results of Reijnders *et al.* [125]

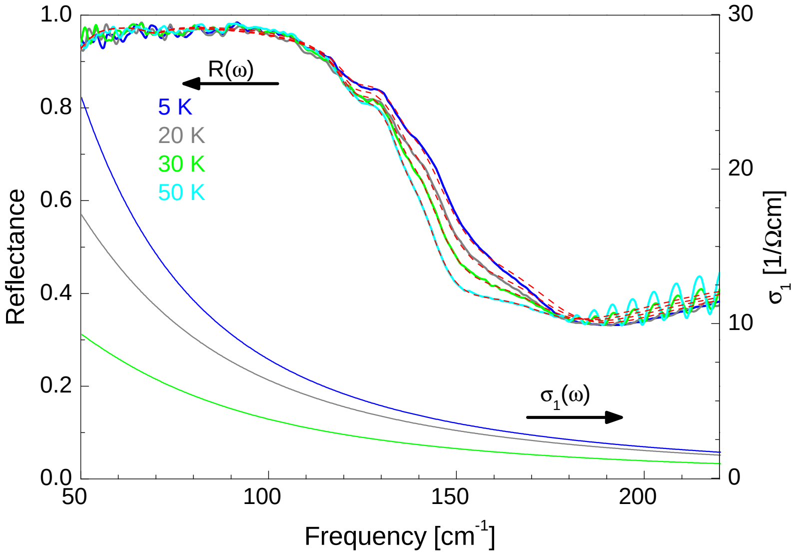

Figure 8.9: Left axis: Low-temperature reflectance compared with fits (red dashed lines). First, the data for 50 K was fitted. Then, the shift of the reflectance edge upon decreasing temperature is described by adding a single oscillator with an eigenfrequency of 20 cm^{-1}, while the parameters of the other oscillators are kept fixed. The contribution of the additional oscillator to $\sigma_1(\omega)$ is shown in the lower part of the figure (right axis).

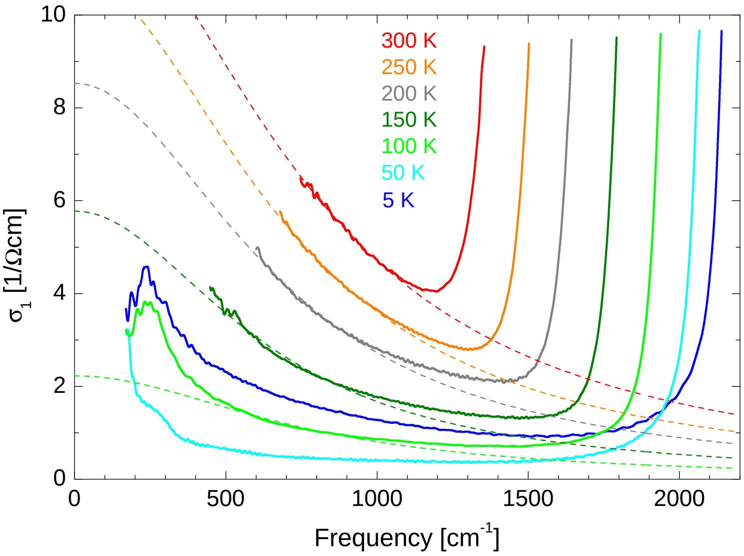

Figure 8.10: Temperature-dependent $\sigma_1(\omega)$ of BiSbTeSe$_2$ for a thickness of 102 μm (solid lines). The Drude peak has been extrapolated to zero frequency (dashed lines). Figure is based on [115]`https://dx.doi.org/10.1103/PhysRevB.93.245149` {DOI}. Copyright by American Physical Society (2016).

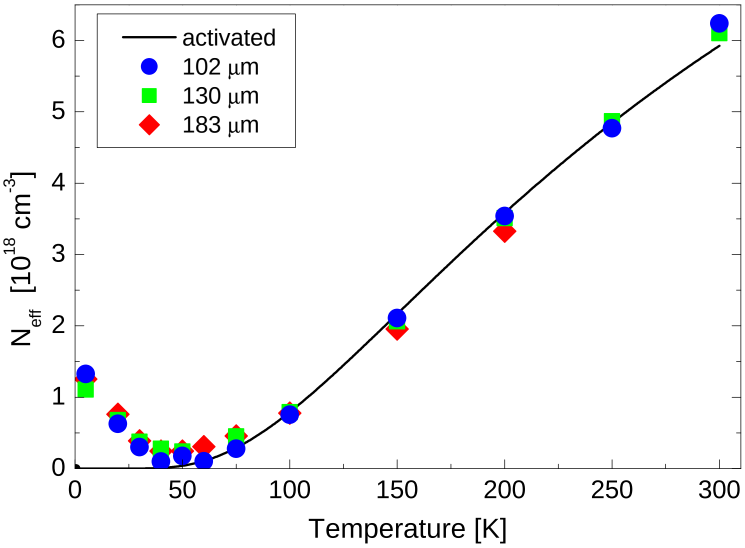

Figure 8.11: Effective charge carrier density is plotted versus temperature for three different thicknesses. The effective charge carrier density is obtained by the plasma frequency from a fit of the Drude peak. The solid line represents the activated behavior. This figure has been published in [115]`https://dx.doi.org/10.1103/PhysRevB.93.245149` {DOI}. Copyright by American Physical Society (2016).

and Post *et al.* [79]. We attribute the background to uncertainties in the amplitude of the transmittance and surface roughness. Furthermore, an oscillator for the gap and a Drude peak is included. The width of the Drude peak is nearly independent of temperature. We obtain a scattering rate of $1/\tau \approx 1.4 \cdot 10^{14}\,s^{-1}$. In order to obtain the charge carrier density related to the Drude peak we need the effective mass which can be estimated with the scattering rate and the mobility $\mu = e\tau/m^* = 62\,\mathrm{cm}^2/\mathrm{Vs}$ determined in transport measurements at 300 K on a piece of the same crystal to $m^*/m_e \approx 0.2$. A value for the effective mass has not been reported to our knowledge, but in Bi_2Se_3 the cyclotron mass of the bulk conduction band was determined to m_e^*=0.14-0.24 m_e [49].

8.1.1.6 Drude peak

The unusual temperature dependence is manifested in the spectral weight of the Drude peak. The Drude peak plus the background is plotted in figure 8.10. From the plasma frequency ω_p of the Drude peak and the effective mass we can calculate the effective charge carrier density N_{eff} according to equation 3.1.4. The resulting N_{eff} is plotted in figure 8.11. This figure emphasizes the non-monotonic temperature behavior. At 40-50 K a minimal charge carrier density contributes to $\sigma_1(\omega)$. Towards lower temperatures the charge carrier density rises. For increasing temperatures the charge carriers are thermally activated and the charge carrier density rises.

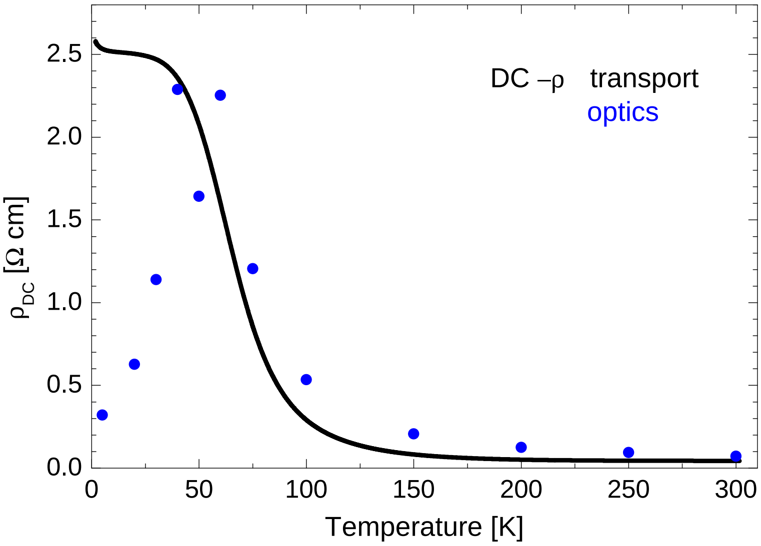

Figure 8.12: Blue circles: temperature-dependent DC conductivity of sample # 1 c extrapolated from a Drude fit to $\sigma_1(\omega)$. Black line: temperature dependent DC conductivity measured in transport. Both measurements have been performed on pieces of the same crystal. This figure is based on in [115]`https://dx.doi.org/10.1103/PhysRevB.93.245149` {DOI}. Copyright by American Physical Society (2016).

8.1.1.7 Puddles

From figure 8.1 we know that the DC conductivity does not show a non-monotonic behavior. For a direct comparison we plot the DC resistivity and the inverse of the extrapolated DC conductivity $\sigma_1(0)^{-1}$ together, see figure 8.12. This figure is adapted from [115].

At temperatures above 50 K the data are in good agreement. Below 50 K a striking discrepancy is present. The DC resistivity saturates at about 2.5 Ωcm, while the $\sigma_1(0)^{-1}$ decreases to values close to the resistivity at 150 K. This contradiction between transport conductivity and optical conductivity can only be resolved if the low-frequency spectral weight below 50 K in $\sigma_1(\omega)$ originates from localized charge carriers that do not contribute to the DC conductivity. In the present case, these localized carriers form so-called charge puddles. Consequently, the peak we described as Drude peak earlier is no Drude peak. It must have a maximum at finite frequencies, since a Drude peak would contribute to the DC conductivity. However, for frequencies above a cutoff frequency ω_c given by the Thouless energy $\hbar\omega_T$, the contribution from the puddles is indistinguishable from the contribution from free charge carriers. The Thouless energy is given by the time scale on which a charged carrier diffuses through a puddle $\omega_c = D/L^2$, with D the diffusion constant and L the characteristic puddle size. The diffusion constant can be estimated to $D \approx 2\,cm^2/s$ with the Einstein relation [126]

$$D = \mu k_B T/e, \tag{8.1.2}$$

with the mobility $\mu = 62\,cm^2/Vs$ at 300 K. With a puddle size larger than 100 μm [116] we

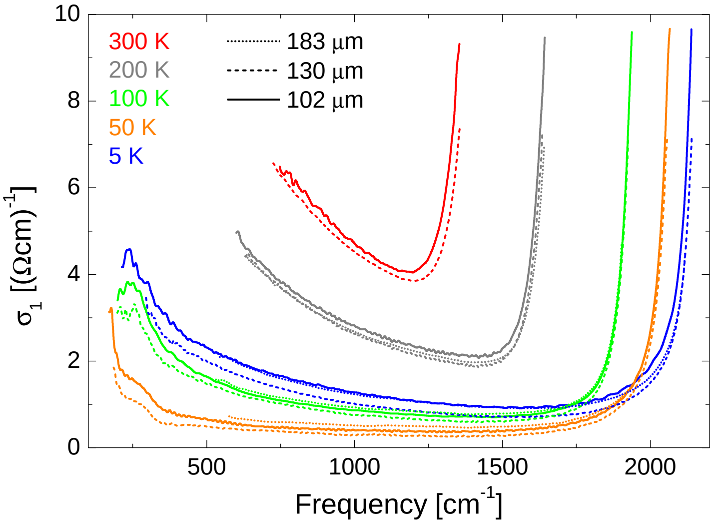

Figure 8.13: $\sigma_1(\omega)$ of BiSbTeSe$_2$ # 1. $\sigma_1(\omega)$ is plotted from 5 K to 300 K. The data is obtained for three different thicknesses: 183 μm (dotted line), 130 μm (dashed line), and 102 μm (solid line). This figure is adapted from [115]`https://dx.doi.org/10.1103/PhysRevB.93.245149` {DOI}. Copyright by American Physical Society (2016).

find $\omega_c/2\pi c \leq 0.1$ cm^{-1}. Hence, ω_c is more than three orders of magnitude smaller than the frequency range investigated by us. Therefore, we can describe the puddles with a Drude peak, especially the plasma frequency of the Drude peak yields the correct N_{eff}.
If the investigated frequency range is close or below the cutoff frequency the puddle contribution needs to be described by a Lorentzian oscillator. However, a Lorentzian oscillator could not take the different puddles sizes into account. Therefore, a distribution of Lorentzian oscillators might describe the puddles contributions in the vicinity of the cutoff frequency.

8.1.1.8 Thickness dependence

It has been reported that at low temperatures the surface state is enhanced [127, 128]. Since the Dirac point is close to the Fermi level the density of states is tiny and we expect no surface contribution in $\sigma_1(\omega)$. Additionally, a surface contribution could not explain the discrepancy between optics and transport. However, to ensure that we are not sensitive to surface effects, we perform thickness-dependent measurements. The resulting $\sigma_1(\omega)$, neglecting any surface contribution for the thicknesses 102, 130, and 183 μm, are plotted in figure 8.13.

If the surface state influences $\sigma_1(\omega)$, we expect an increase of $\sigma_1(\omega)$ with decreasing thickness, due to the high mobility of the surface state. Especially, the spectral weight of the Drude peak at low temperatures would increase with decreasing sample thickness. Certainly, the thinnest sample (#1 c) does not exhibit the highest $\sigma_1(\omega)$. Rather the thickest sample (#1 a) has the highest $\sigma_1(\omega)$. However, the ratio of $\sigma_1(\omega)$ of sample (#1 c) and sample (#1 a) $\sigma_{102}/\sigma_{183}$ lies between 0.99-1.05 below 1500 cm^{-1}. The deviations between the $\sigma_1(\omega)$ can be attributed to uncertainties in the absolute value of the transmittance or in the thickness. Consequently, the physics determining $\sigma_1(\omega)$ arises from the bulk.

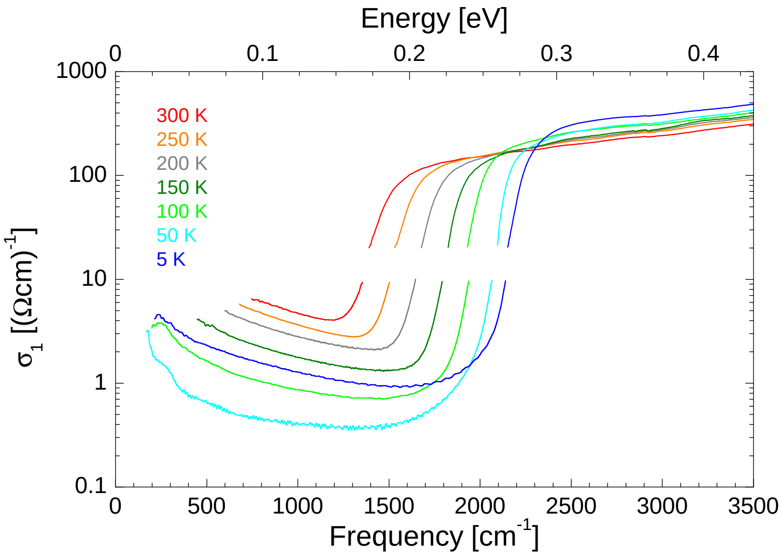

Figure 8.14: $\sigma_1(\omega)$ from inversion of reflectance and transmittance is plotted temperature-dependent. The results from Kramers-Kronig analysis are plotted as dashed lines.

8.1.1.9 Kramers-Kronig analysis

Since we know that the $\sigma_1(\omega)$ is given by the bulk properties we can perform a Kramers-Kronig analysis according to section 3.6. The Kramers-Kronig analysis enables us to obtain $\sigma_1(\omega)$ above the onset of excitations across the gap. However, the transparent range with low values of $\sigma_1(\omega)$ is not described as precisely by Kramers-Kronig analysis as by inversion. Therefore, $\sigma_1(\omega)$ obtained by both methods does not overlap, see figure 8.14. In contrast to the inversion, the Kramers-Kronig analysis is prone to errors in the reflectance. This is emphasized by the comparison of our results to the $\sigma_1(\omega)$ obtained by Kramers-Kronig analysis by Post *et al.* [79] in figure 8.15. Besides the deviations in the absolute value, the main deviation is in the shape of the energy gap. Post *et al.* [79] have reported two gaps at low temperatures. Such an erroneous two-gap structure might arise in $\sigma_1(\omega)$ calculated by Kramers-Kronig analysis from the increase of the reflectance in the transparent range (even for single crystals with 1100 μm, see figure 8.7). We have determined the reflectance of a semi-infinite sample from the refractive index, which was determined from the fringes in the transmittance of a thin sample. In combination with the reflectance of the 1100 μm thick sample we can rule out an increase of the reflectance in the transparent range below the energy gap. The error in the reflectance decreases with decreasing transmittance, which would explain why the erroneous two-gap structure disappears for 300 K.

8.1.1.10 Flake

In order to extend the frequency range in which we determine $\sigma_1(\omega)$ from inversion at the gap, we prepare a sample with a thickness of 2 μm. It was not possible to exfoliate this sample from the adhesive tape and glue it to the sample holder. Therefore, we had to

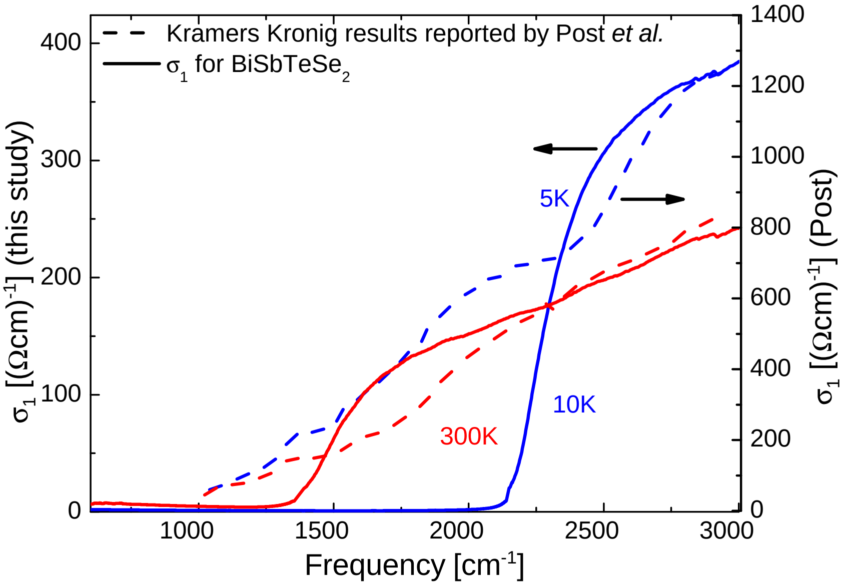

Figure 8.15: $\sigma_1(\omega)$ for 300 K (red) and 5 K respectively 10 K (blue). Our $\sigma_1(\omega)$ (solid line) is based on the inversion of the transmittance and the reflectance combined with Kramers-Kronig results. The $\sigma_1(\omega)$ (dotted line) reported by Post *et al.* was calculated by Kramers-Kronig analysis [79].

measure the transmittance of the flake on top of the tape. Additionally, we measured the transmittance of the tape only and found that the tape is characterized by many sharp absorption features in the MIR range. We divided the spectrum of the flake on top of tape by the spectrum of tape only and cut off the features in the spectrum which appeared due to the absorption in the tape, see figure 8.16. Thereby, we neglected multiple reflections within the tape, which is possible due to the low refractive index of the tape.

In contrast to the analysis based on inversion of transmittance and reflectance for the large single crystals we cannot apply a Fourier filter to the transmittance of the flake, since the fringe period extends over a frequency range comparable to the frequency range over which the transmittance drops at the gap. Therefore, we invert the transmittance including the fringes. Hence, $\sigma_1(\omega)$ exhibits dips corresponding to the fringes. However, we are only interested in $\sigma_1(\omega)$ at the gap; here, the fringes are suppressed and $\sigma_1(\omega)$ is not influenced by the fringes above $100\,(\Omega\mathrm{cm})^{-1}$, see figure 8.17.

The comparison of $\sigma_1(\omega)$ of the thin sample with $\sigma_1(\omega)$ calculated by Kramers-Kronig analysis emphasizes that the reflectance was determined correctly by us. Especially, we find no indication of a second gap.

8.1.2 Simulation

In the following we will explain the non-monotonic temperature dependence by defects in the crystal that are randomly distributed causing n-doped and p-doped regions, called puddles. These considerations are based on a simple, classical, electrostatic, model in combination

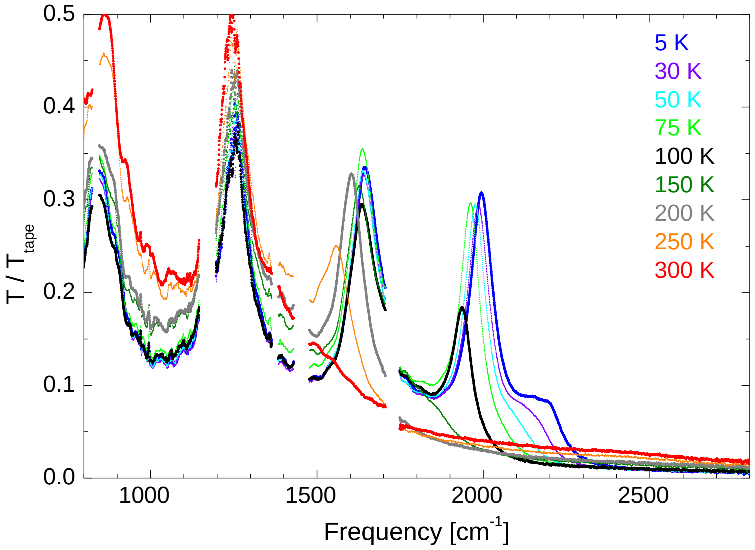

Figure 8.16: Transmittance of the BiSbTeSe$_2$ flake on tape normalized by the transmittance of the tape. The resulting ratio is plotted in the MIR range for nine temperatures between 5 K and 300 K. Frequency ranges with strong absorption in the tape have been cut off the spectra.

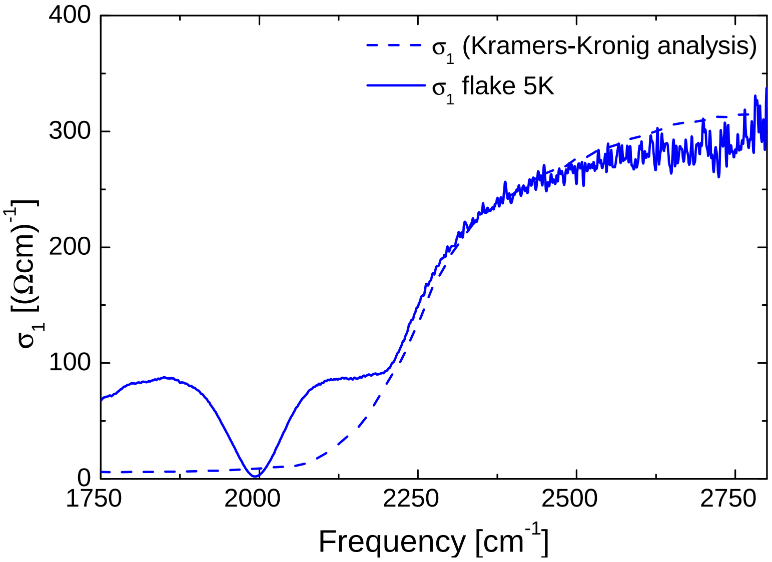

Figure 8.17: $\sigma_1(\omega)$ calculated by the inversion of the transmittance of the BiSbTeSe$_2$ flake for 5 K and $\sigma_1(\omega)$ calculated by Kramers-Kronig analysis from the reflectance of semi-infinite BiSbTeSe$_2$ is plotted in the MIR range (solid line). The dashed line is $\sigma_1(\omega)$ which results out of the Kramers-Kronig analysis.

with Monte Carlo simulations for the temperature dependence[2].
The simulations are related to a theory by Efros, Skinner, and Shklovskii *et al.* introduced in section 6.4 [69–72]. It describes the crystal as a semiconductor with randomly distributed, shallow defects that are donors and/or acceptors. The density of donors is N_D and the density of acceptors is N_A. The defect density is given by $N_{def} = \frac{N_A+N_D}{2}$. We focus on the scenario with compensation close to perfect, $K = N_D/N_A \approx 1$, since the values of x and y of the alloys of $\mathrm{Bi}_{2-x}\mathrm{Sb}_x\mathrm{Te}_{3-y}\mathrm{Se}_y$ are chosen in such a way that the resistivity is maximized.

8.1.2.1 Hydrogen model

The dielectric function of $\mathrm{BiSbTeSe}_2$ is very large for low frequencies, $\epsilon(\omega = 0) \approx 200$ [87]. The donors and acceptors can be depicted in the hydrogen model with a small binding energy $E_b = R_y \frac{m^*}{m}\frac{1}{\epsilon^2} \approx 0.007\,\mathrm{meV} \approx 2 \cdot 10^{-5}\Delta$. Their energy levels will be close to the valence band, respectively the conduction band. Hence, the donors and acceptors are shallow. Thus the static ions go along with localized electrons in a sphere with a radius of r=10 nm which is much larger than the lattice constant $a \approx 0.5$ nm.

8.1.2.2 Anisotropy of $\epsilon(\omega = 0)$

The dielectric function exhibits an anisotropy due to a strongly polarizable phonon mode. However, we have only access to $\epsilon_{\perp c}$ and no values of $\epsilon_{\parallel c}$ have been reported for $\mathrm{Bi}_{2-x}\mathrm{Sb}_x\mathrm{Te}_{3-y}\mathrm{Se}_y$. From reflectance data we find $\epsilon_{\perp c} \approx 230$, see figure A.31 in the appendix. For $\mathrm{Bi_2Se_3}$ the ratio of $\epsilon_{\parallel c}/\epsilon_{\parallel c} \approx 6.5$ can be estimated based on references [52, 59, 87, 123]. For $\mathrm{Bi_2Te_3}$ the ratio of $\epsilon_{\parallel c}/\epsilon_{\parallel c} \approx 3.9$ was reported [87]. Considering, a similar ratio in $\mathrm{Bi}_{2-x}\mathrm{Sb}_x\mathrm{Te}_{3-y}\mathrm{Se}_y$ we obtain $\epsilon_{\parallel c} = 35 - 60$. Therefore, we find the average value $\epsilon_{avg} = \sqrt[3]{\epsilon_{\perp c}^2 \epsilon_{\parallel c}} \approx$123 to 147. However, for the theory we stay closer to the value determined by our measurement for $\epsilon_{\perp c}$ and use $\epsilon = 200$. Note that the qualitative results do not depend on the exact value of ϵ, but the quantitative results a large error bar has to be consider.

8.1.2.3 The Hamiltonian

To obtain the ground state it is necessary to minimize the energy of the system, which is given by the Hamiltonian

$$\hat{H} = \sum_i \Delta f_i n_i + \frac{1}{2}\sum_{i,j} V_{r_i - r_j} q_i q_j, \tag{8.1.3}$$

where $n_i = 0, 1$ stands for the number of electrons on the i-th donor or acceptor. The factor f_i equals -1 for an occupied acceptor, because the energy level is $\Delta/2$ below the Fermi energy and f_i equals 1 for an occupied donor, because the energy level is $\Delta/2$ above the Fermi energy. The second term consists of the sum over the Coulomb potential $V_{r_i - r_j}$

---

[2] The simulations that are the basis of the chapter have been carried out by Dr. Lux and Prof. Rosch of the Institute for Theoretical Physics at the University of Cologne [76]

between two defects i and j, which are separated by the distance $r_i - r_j$. Because of the large ϵ two positive charged acceptors close to each other would arrange its electrons in a way that the distance of the core area would be larger than the defect distance. Additionally, quantum mechanical corrections need to be considered if the defects are close to each other. Therefore, a maximal Coulomb energy between two defects was taken into account by a short-distance cutoff a_B. The Coulomb potential is then given by $V_{r_i - r_j} = e^2/(4\pi\epsilon_0\epsilon(|r_i - r_j|^2 + a_B^2)^{1/2})$. The cutoff was set to $a_B = 2/N_{def}^{1/3}$, which is twice the average distance between dopants $d_{def} = 2/N_{def}^{1/3}$. Note that the results of the simulation do not depend on the exact value of the cutoff. The factor q denotes the sign of the charge. An occupied donor and an empty acceptor are charge neutral and have $q = 0$, while an empty donor has $q = 1$ and a filled acceptor has $q = -1$.

In summary the energy of the system is given by only two contributions; the energy difference between the level of the dopants and the Fermi level, plus the Coulomb energy of the charged defects. Charge carriers in the valence or conduction band are not taken into account. This approach is justified, since the density of states in the conduction band is much smaller than the density of states of the defects.

We are aware of the fact that this model is a strong simplification, but is has shown to capture the main features of the data. Additionally, it is simple enough to perform temperature-dependent simulations with reasonable effort.

8.1.2.4 Ground state

The melt of the topological insulators is annealed to 850 K, thus the number of activated charge carriers is large enough to screen the Coulomb potential and ensure a random distribution of the defects in the crystal [43]. After distributing $m/2$ donors and $m/2$ acceptors randomly $2^m/\sqrt{m}$ configurations, concerning their occupation, are possible [76]. In principle the energy of each configuration needs to be calculated and the lowest in energy is the configuration of the ground state. However, with a trick invented by Efros and Shklovskii a pseudo-ground state can be determined [70, 71]. The method tracks the pseudo-ground state by pairwise exchange of electrons from an occupied and an unoccupied site. When the minimal energy is reached a configuration with lower energy can only be reached by an exchange of two pairs at the same time. The state with the lowest energy taking two pair exchanges into account could be lowered by three pair exchanges and so forth. However, the ground state found by pairwise exchange has almost the identical energy as the real ground state and can be derived with significantly less effort.

8.1.2.5 Simulating finite temperatures

To our knowledge, the temperature dependence of the model has not been investigated thus far. Finite temperatures can be simulated by Monte Carlo simulation. The finite temperature basically allows configurations with energies above the energy of the pseudo-ground state. The simulations can only be performed with a ratio of Δ/E_c up to 25, while

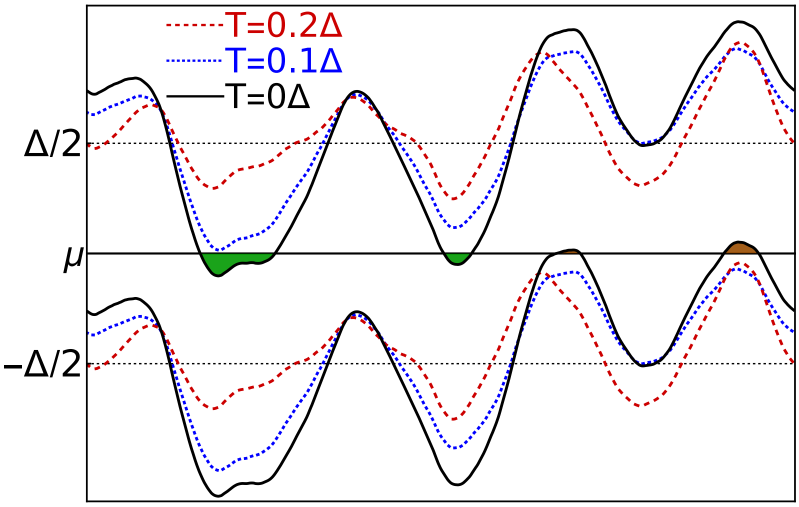

Figure 8.18: The valence band and the conduction band exhibit spatial fluctuations due to randomly distributed defects. In the regions where the fluctuations are larger than $\Delta/2$ neutral defects are created. Neutral donors are marked green while the brown areas correspond to neutral acceptors. The solid black line represents the ground state configuration for T=0 K. The blue dotted line corresponds to T=0.1Δ. The red dashed line corresponds to T=0.2Δ. Figure has been taken from reference [115]`https://dx.doi.org/10.1103/PhysRevB.93.245149` {DOI}. Copyright by American Physical Society (2016).

the experimental ratio for BiSbTeSe_2 lies at about 100. The experimental range cannot be simulated due to finite-size effects or extremely long simulation times, due to an increased system size. Further details concerning the implementation are given in the Ph.D. thesis of Jonathan Lux [76].

8.1.2.6 Microscopic picture

Before the analysis of the results of the calculations, we take a look at the general behavior of the dopants in compensated semiconductors. We are looking for a mechanism that causes an increase of $\sigma_1(\omega)$ at low temperatures. If we start from a system with randomly distributed charge-neutral acceptors and donors many electrons from the donors will go to the acceptors since the electrons and holes occupying the dopants are weakly bound. The energy gained in this process is the energy gap Δ, since the dopants are shallow. However, this process produces an acceptor with a negative charge and a donor with a positive charge. The average charge fluctuations in a system of the size $V = R^3$ are $Q \propto \sqrt{V} \propto \sqrt{R^3}$. The potential a charged dopant feels is $\Phi(R) \propto Q_R/R \propto \sqrt{R}$. The potential increases with the system size. Thus, after many donors gave an electron to an acceptor a region with increased donor density will exhibit a large positive charge. At one point it will be energetically favorable to have a neutral donor in this region. This happens when the Coulomb potential bends the donor states below the Fermi level, see figure 8.18. In a region with a large acceptor density the Coulomb potential will rise above the Fermi level, causing neutral acceptors. In the end, the ground state is described by neutral and charged dopants. The neutral dopants have a

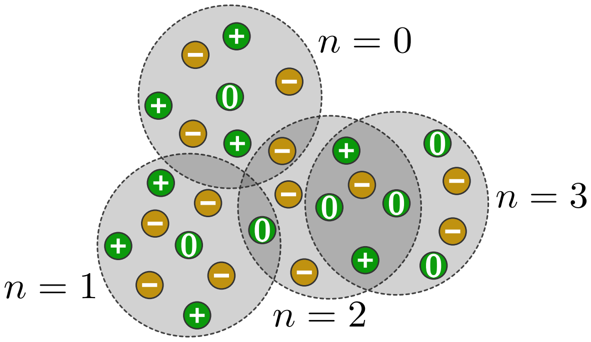

Figure 8.19: This sketch illustrates the counting mechanism used to determine the formation of puddles. The charge of the defect is described by 0, +, and -. The brown circles are donors and the green circles are acceptors. For each neutral defect the neutral defects are counted in a sphere around the initial neutral defect. The spheres are indicated by the gray circles. Figure has been taken from reference [115]`https://dx.doi.org/10.1103/PhysRevB.93.245149` {DOI}. Copyright by American Physical Society (2016).

weakly bound hole or electron. These holes and electrons are delocalized across many sites. In a region with many weakly bound holes or electrons the wave functions will overlap. We state that these regions can be described by free charges confined to the region where the dopants level crosses the Fermi level. Many neutral acceptors build hole puddles and many neutral donors build electron puddles. With increasing temperature the thermal energy causes a high probability for configurations in which dopants outside of puddles become neutral. Thereby they screen the Coulomb potential causing a reduction of puddles which explains the evaporation of puddles with rising temperature.

How many defects are located in puddles depends on the ratio of the Coulomb potential and the energy gap. The number of neutral dopants is increased if the Coulomb energy $E_c = e^2/(4\pi\epsilon_0\epsilon d_{def})$ is large, while the number of charged dopants is increased if the gap Δ is large. The ratio E_c/Δ is crucial for the emergence of puddles.

8.1.2.7 Finding puddles in the simulations

We will now focus on the quantitative analysis of the simulations. One important task is finding the puddles. Therefore, we count the neutral neighbors for each neutral dopant, see figure 8.19. The neutral neighbors are the neutral dopants within a sphere of the radius $r_0 = 1.42\, d_{def}$. Therefore, 12 dopants of the same type are on average in the sphere, which is the number of nearest neighbors for close-packed spheres. We name neutral dopants a part of a puddle if the dopants have at least four neutral neighbors.

8.1.2.8 Temperature dependence of puddles

The distribution of neutral dopants as a function of the number of neutral neighbors for different temperatures is plotted in figure 8.20. It is striking that the percentage of neutral dopants with a single neutral neighbor goes to zero for low temperatures, while the percent-

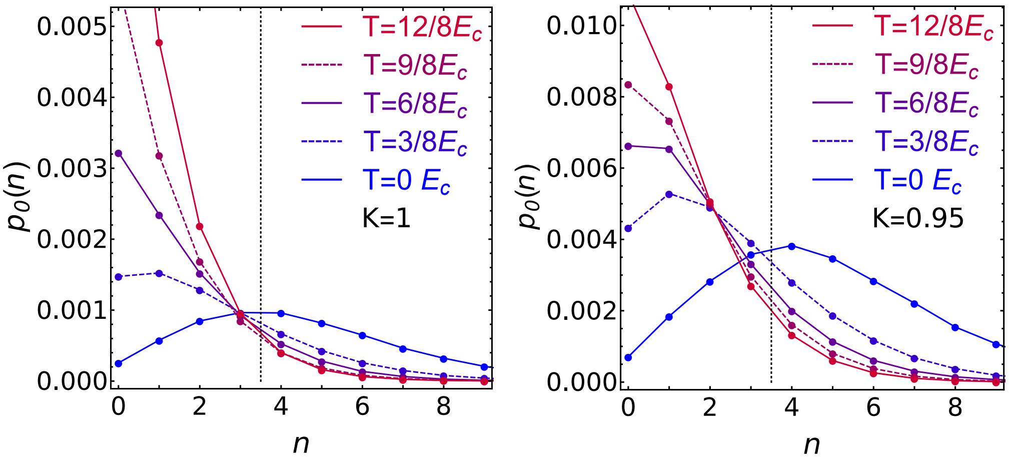

Figure 8.20: The number of neutral dopants with n neutral neighbors normalized by the total number of dopants is plotted versus the number of neutral neighbors n. The curves have been calculated for different temperatures. For the left figure perfect compensation is considered, while the right figure gives $p_0(n)$ for $K = 0.95$. The dotted line represents the value of n from where the neutral donor is called part of a puddle. For both levels of compensation a maximum at finite values for the number of neutral dopants in the sphere is present at zero temperature. This behavior is associated with the formation of puddles at low temperatures. Figure has been taken from reference [115]`https://dx.doi.org/10.1103/PhysRevB.93.245149` {DOI}. Copyright by American Physical Society (2016).

age of neutral dopants with many neutral neighbors increases with decreasing temperature. The total number of charge carriers in puddles is the sum over all dopants with more than three neutral neighbors, which corresponds to the integral over the curve in figure 8.20 from n=3.5. In figure 8.21 the charge carriers in puddles are plotted as a function of temperature. The calculations do not depend on the ratio of E_c/Δ except for perfect compensation. We can clearly see a non-monotonic temperature dependence. Similar to the observation in the data we find a minimum at finite temperatures. Note that the total number of neutral charge carriers increases with temperature. At first glance, this contradicts the temperature dependence of the puddles, but since the puddles only occupy a small fraction of the volume, the neutral dopants are created mostly outside of the puddles, as the increase of the area beneath the curves with temperature in figure 8.20 shows. These thermally activated charge carriers screen the fluctuations of the Coulomb potential. Eventually, this leads to a reduction of the charge carriers in the puddles with increasing temperature. The single neutral dopants do not create a Drude peak, since they follow the physics of a hydrogen atom. In contrast, a cluster of neutral dopants forms a puddle, which causes a Drude-like peak.

In figure 8.21 we see that the temperature at which the puddles disappear is almost independent of the compensation. Note that the increase at high temperatures is due to the activation of charge carriers across the energy gap. The onset of this increase depends on the

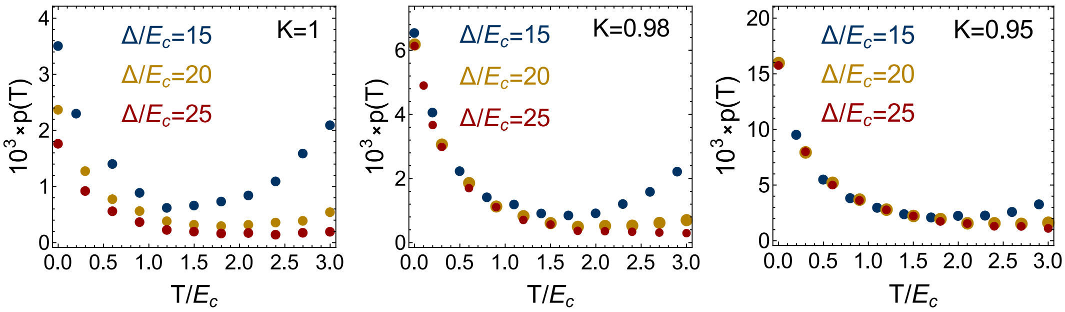

Figure 8.21: The fraction of the dopants with four or more neutral neighbors is plotted as function of the temperature normalized by E$_C$. The simulations have been performed for Δ/E$_C$=15, 20, and 25. The curves for K=0.98 and K=0.95 with different ratio of Δ/E$_C$ vary only for high temperatures. However, we do not claim to describe the activated behavior by these plots correctly. Figure has been taken from reference [115]`https://dx.doi.org/10.1103/PhysRevB.93.245149` {DOI}. Copyright by American Physical Society (2016).

energy gap Δ and therefore, on Δ/E_c. Since this value is smaller than in the experiment, in order to achieve reasonable computational time, the increase at high temperature is not described correctly.

The compensation has a big impact on the percentage of dopants forming puddles, since a mismatch between donors and acceptors implies many neutral dopants. At T=0 K reducing the compensation causes a linear increase of the percentage of dopants in puddles, see figure 8.22. Although, close to perfect compensation the percentage of dopants in puddles approaches a constant. This constant depends on the ratio Δ/E_c.

8.1.2.9 Defect density

The effective charge carrier density determined from the Drude-like peak at low temperatures is proportional to the percentage of defects in puddles, $N_{\text{eff}}(T) \propto p(T)$. The temperature scale, on which the percentage of charge carriers in puddles $p(T)$ reaches a minimum is approximately E_c/k_B, as shown in figure 8.21. Consequently, we can determine E_c/k_B from the temperature scale on which puddles evaporate from $N_{\text{eff}}(T)$. Thereby, we determine the defect density since it is directly proportional to the mean Coulomb potential

$$E_c = e^2/(4\pi\epsilon_0\epsilon d_{def}) = e^2/(4\pi\epsilon_0\epsilon N_{def}^{-1/3}). \tag{8.1.4}$$

In summary, we determine N_{def} by the temperature dependence of the puddles, which enables us to determine K from $N_{\text{eff}}(T=0)$.

8.1.3 Applying the theory

In the following the theory presented above will be used to determine several quantities from the data of sample #1 of BiSbTeSe$_2$.

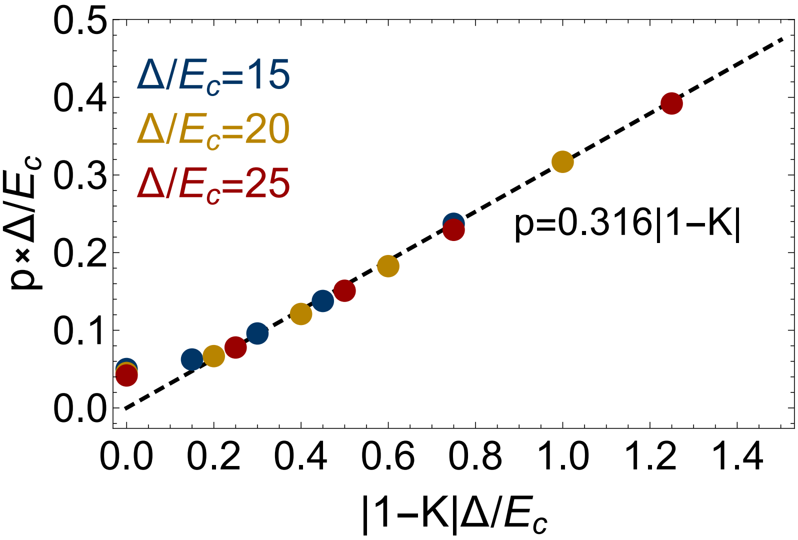

Figure 8.22: The fraction of dopants in puddles times the ratio of Δ/E_C is plotted for different ratios of Δ/E_C as function of the compensation, explicitly as function of $|1-K|\Delta/\mathrm{E}_C$. The data follow the formula $p = 0.316|1-K|$, except close to perfect compensation. For perfect compensation the part of dopants in puddles approaches a constant value, which depends slightly on the ratio pf Δ/E_C. figure has been taken from reference [115]`https://dx.doi.org/10.1103/PhysRevB.93.245149` {DOI}. Copyright by American Physical Society (2016).

8.1.3.1 Defect density and compensation

In the case of BiSbTeSe$_2$, E_c/k_B is about 30-40 K, see figure 8.11. This translates with equation 8.1.4 into a defect density $N_{def} = 4.6 - 11 \cdot 10^{19}\,\mathrm{cm}^{-3}$. This value is comparable with defect densities in uncompensated topological insulators [44,45]. The ratio of the energy gap Δ and the Coulomb energy E_c is about $\Delta/E_c = 75 - 100$. With $p \cdot N_{def} = N_{\mathrm{eff}} \cdot \frac{m_e^*}{m_e}$ we find a $p = 0.3 - 0.6\,\%$ for the sample #1 of BiSbTeSe$_2$. This yields $p \cdot \Delta/E_c = 0.25 - 0.46$, which means that the linear range with $p = 0.316|1-K|$ is reached, see figure 8.22. Hence, the compensation is $K = 98.1 - 99.2\,\%$.

8.1.3.2 Activation energy

The analysis of the charge carrier density as a function of temperature enables us to determine the activation energy. The spectral weight of the Drude peak above 50 K determines the number of activated charge carriers. For a semiconductor without doping we expect

$$N_{\mathrm{eff}} \propto \exp -\frac{\Delta}{2k_B T}. \tag{8.1.5}$$

In section 8.1.1.6 we have determined the effective charge carrier densities of sample # 1. In the low-temperature range the puddle formation dominates the effective charge carrier density. From about 50 K we can observe activated behavior. The formula for the activation energy (equation 8.1.5) can be written as

$$ln(N_{\text{eff}}) = -\frac{E_A}{2k_BT} + ln(c), \tag{8.1.6}$$

with c a constant. The slope of the effective charge carrier density versus the inverse temperature corresponds to the activation energy divided by the Boltzmann constant, see figure 8.23.

We replaced the energy gap by the activation energy, because for compensated semiconductors it is known that the activation energy is smaller than $\Delta/2$, see section 6.4.1.3 [71]. Numerical calculations yields an activation energy $E_A \approx 0.15\Delta$ [71]. DC measurements on these compounds have confirmed that the activation energy is much smaller than the energy gap [43].

We face two main difficulties while determining the activation energy. Usually, the activation energy is determined over a temperature range of at least the order of E_A/k_B. In the temperature range below 50 K or 150 K, depending on the compound, the temperature dependence is dominated by the dynamics of puddles, which leaves a small temperature range for the investigation of the activation energy. Measuring up to much higher temperatures is not reasonable, since the samples will change their properties. The second problem is that the activation energy is temperature dependent, because the disorder potential is smoothed by activated charge carriers. For very high temperatures the activation energy will approach the intrinsic energy gap.

In conclusion, the exact values for the activation energy need to be treated with caution.

The fit to the charge carrier density as a function of the inverse temperature of the sample #1 is plotted in figure 8.23 for the three different thicknesses. We observe an activation energy of 26 meV. A similar result was reported for temperature-dependent transport measurements, where the activation energy was determined to E_A=22 meV [43]. This is approximately 0.11 Δ, which is fairly close to the 0.15 Δ predicted by theory, considering the problems discussed above. The agreement with theory, respectively the low value of the activation energy, emphasizes the role of disorder in the samples.

8.1.3.3 BiSbTeSe$_2$ samples # 2-3

Here, we summarize the optical properties from the thick sample # 2 from which the reflectance was obtained and the optical properties of sample # 3 which was characterized for scanning tunneling microscopy (STM) [3], see section 8.1.6.

For sample # 2 we find the defect density of $N_{def} = 4.6 - 11 \cdot 10^{19}\,\text{cm}^{-3}$, as for sample # 1. In contrast, we find a larger defect density for sample # 3 with $N_{def} = 1 - 4 \cdot 10^{20}\,\text{cm}^{-3}$. This finding is based on the discrepancy in the temperature dependence of the puddles which is displayed in figure 8.24. The offset in the defect density for sample # 3 is related to the distinctness of the minimum of the puddle contribution in temperature, which is sample

---

[3] The STM measurements were performed by T. Knispel and Dr. W. Jolie in the group of Prof. Michely from the II. Institute of Physics at the University of Cologne [116]

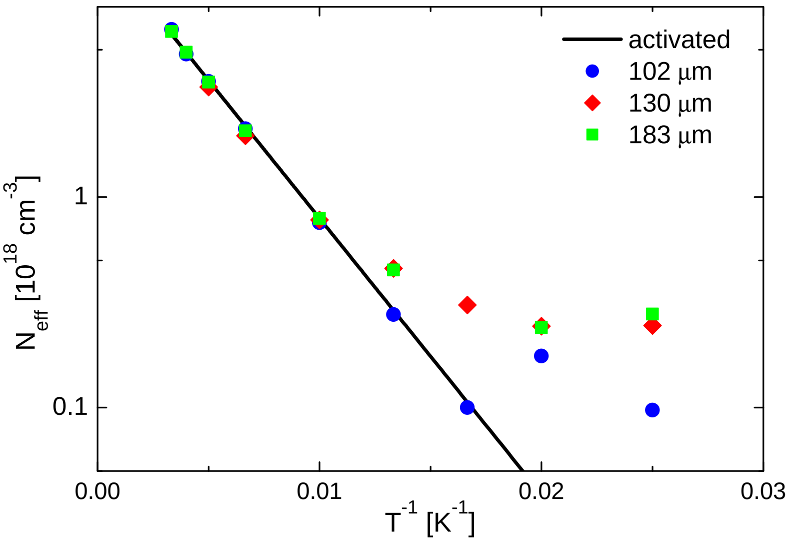

Figure 8.23: The effective charge carrier densities for three different thicknesses of sample# 1 are plotted versus the inverse temperature. For high temperatures the activation energy can be determined by a fit (black line).

dependent.

With the defect density we calculate the compensation for sample # 2 to $K = 98.5 - 99.5\,\%$ and for sample # 3 to $K = 98 - 100\,\%$.

The activation energy could only be determined on the data of sample # 3, because $\sigma_1(\omega)$ of sample # 2 above 100 K was not accessible due to the large thickness. The activation energy of sample # 3 is with E_A=22 meV slightly smaller than for sample # 1.

8.1.4 Effective medium approach

We attribute the Drude peak at low temperatures to charge carriers confined in spatial regions. This raises the question whether the inhomogeneity has to be considered for the analysis. The puddles in $\mathrm{Bi}_{2-x}\mathrm{Sb}_x\mathrm{Te}_{3-y}\mathrm{Se}_y$ have a characteristic length scale in the order of hundred nanometers to a few micrometer, according to equation 6.4.1. The wavelength for frequencies below 1000 cm^{-1} is larger than 10 μm. Accordingly, the dielectric function changes on the length scale of the wave length. Therefore, it is appropriate to use an effective medium approach to describe the response of the medium.

The effective medium approach describes the response of an inhomogeneous medium to an electromagnetic field as a function of frequency. It gives the effective dielectric function $\epsilon_{eff}(\nu)$. Here, we use the Maxwell Garnett approximation, which reads [129]

$$\left(\frac{\epsilon_{\mathrm{eff}} - \epsilon_{bulk}}{\epsilon_{\mathrm{eff}} + \epsilon_{bulk}}\right) = f\left(\frac{\epsilon_{pudd} - \epsilon_{bulk}}{\epsilon_{pudd} + \epsilon_{bulk}}\right). \tag{8.1.7}$$

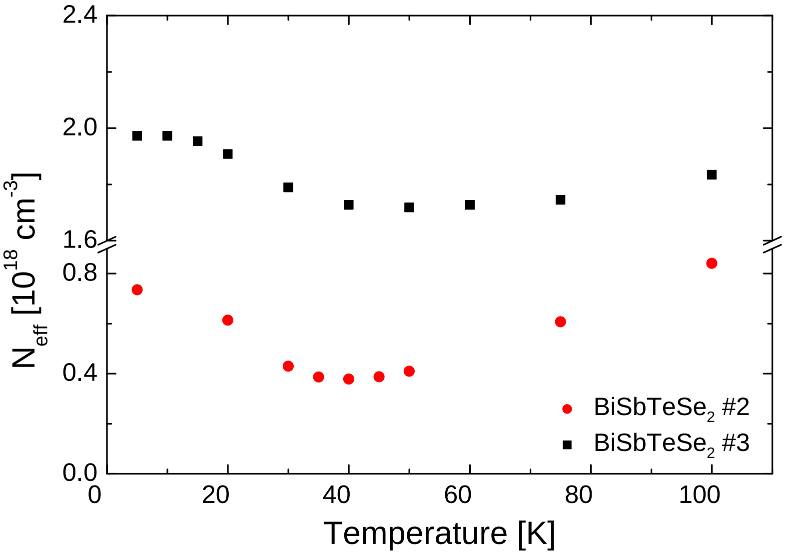

Figure 8.24: N_{eff} as function of temperature for sample # 2 (red circles) and sample # 3 (black squares). For a better comparison a break is inserted in the N_{eff} axis from 0.9 to 1.6.

The dielectric functions in the bulk and in the puddles are given by ϵ_{bulk} and ϵ_{pudd}. The factor f gives the volume filling fraction of puddles inside the medium. Solving the equation for ϵ_{eff} yields

$$\epsilon_{\mathrm{eff}} = \epsilon_{bulk} \frac{2\epsilon_{bulk} + \epsilon_{pudd} + 2f(\epsilon_{pudd} - \epsilon_{bulk})}{2\epsilon_{bulk} + \epsilon_{pudd} + f(\epsilon_{pudd} - \epsilon_{bulk})}. \tag{8.1.8}$$

We assume that the dielectric function within the puddles differs from the bulk dielectric function only by an additive Drude term ϵ_D

$$\epsilon_{pudd} = \epsilon_{bulk} + \epsilon_D. \tag{8.1.9}$$

Replacing ϵ_{pudd} by equation 8.1.9 in equation 8.1.8 yields

$$\epsilon_{\mathrm{eff}} = \epsilon_{bulk} + f\epsilon_D \left(1 + (1-f)\frac{\epsilon_D}{3\epsilon_{bulk}}\right)^{-1}. \tag{8.1.10}$$

The static dielectric function of BiSbTeSe$_2$ is about $\epsilon(\omega = 0) = 200$. In the frequency range above the phonons and below the energy gap the dielectric function is still large, with values of $\epsilon \approx 35$. Since the Drude contribution of the puddles is rather small, we can make the assumption $\epsilon_D \ll 3\epsilon_{bulk}$. This assumption simplifies equation 8.1.10 to

$$\epsilon_{\mathrm{eff}} \approx \epsilon_{bulk} + f\epsilon_{pudd}. \tag{8.1.11}$$

This approximation has been used so far for the analysis of the density of charge carriers in the puddles, see figure 8.11.

Besides giving reasons for a simplified approach, we used the full formula, equation 8.1.8, to

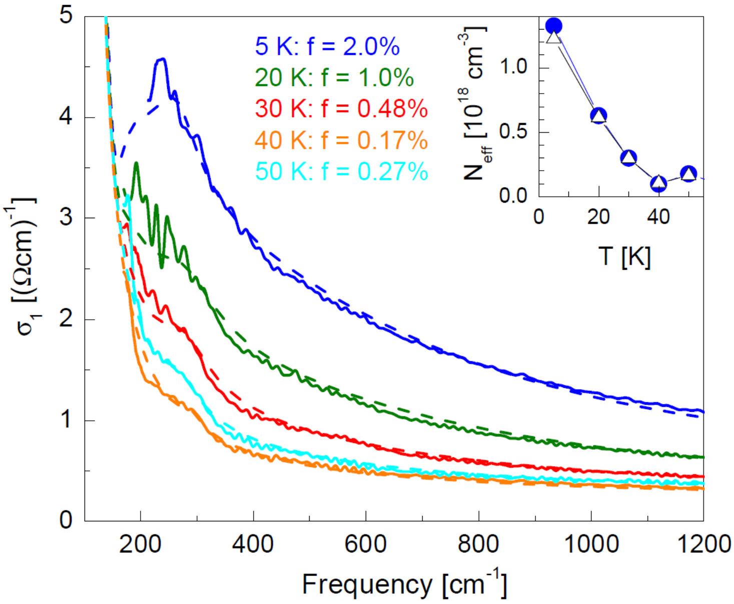

Figure 8.25: $\sigma_1(\omega)$ for sample # 1 102 μm is plotted as a function of frequency. The data is shown in low temperature limit from 5 K-50 K. For each temperature a fit considering the effective medium approach is performed. The results are plotted as dashed lines. The filling factors obtained by the fit are listed in the left inset. The right inset compares the effective charge carrier density obtained by the fit (open triangles) to the effective charge carrier density which was extracted by fitting a model assuming a homogenous sample (blue circles). The values are in excellent agreement for different temperatures. This figure is based on [115]`https://dx.doi.org/10.1103/PhysRevB.93.245149` {DOI}. Copyright by American Physical Society (2016).

fit $\sigma_1(\omega)$. The resulting fits are plotted in figure 8.25. The effective charge carrier density is almost the same as for the simple scenario, see inset in figure 8.25. Nevertheless, from the fit we obtain the filling f as a function of temperature. At 5 K we find a filling of $f \approx 2\%$, which decrease down to 0.2% for 40 K.

We conclude that in the case of a weak Drude term on top of a large dielectric function the effective medium theory is not needed to calculate the charge carrier densities from the Drude peak.

8.1.5 Foot below the gap

The gap of a semiconductor without defects becomes broader with increasing temperature due to thermally activated phonons. In contrast to the behavior of a clean semiconductor we find a sharpening of $\sigma_1(\omega)$ at the gap with increasing temperature, see figure 8.26. However, Shklovskii *et al.* predicted a broadening of the gap for compensated semiconductors with shallow dopants, since the potential fluctuations cause an almost constant DOS within the gap, see section 6.4.1.7. With rising temperature the thermal screening causes a reduction of the Coulomb fluctuations. Therefore, the energy gap approaches the energy gap of a "clean"

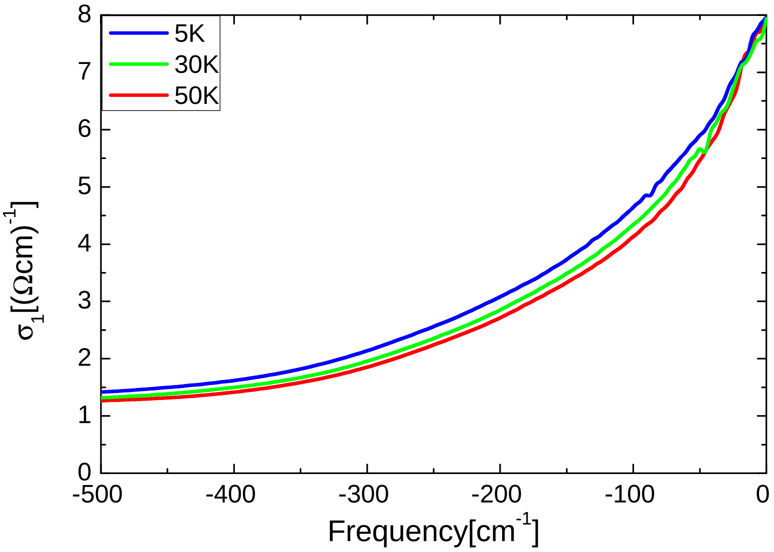

Figure 8.26: $\sigma_1(\omega)$ at the gap for 5 K, 30 K, and 50 K. Each shifted by the respective value of the estimated gap Δ(T).

semiconductor for increasing temperatures, including the thermal broadening. In the work of Skinner *et al.* [71] the absorption closely below gap was given by the equation 6.4.6. For sample # 3 of BiSbTeSe$_2$ with $N_{def} = 1 - 4 \cdot 10^{20}\,\mathrm{cm}^{-3}$, a_0=50 nm, and E_B=0.3 meV we find

$$ln \frac{\alpha(\hbar\omega_\Delta)}{\alpha(\Delta)} = -\beta_0 \left(\frac{\hbar\omega_\Delta}{1\,meV}\right)^{5/4}, \tag{8.1.12}$$

with β_0=0.015-0.03. In order to fit the gap it is necessary to subtract the Drude peak of the puddles from $\sigma_1(\omega)$. The result with the fit is plotted in figure 8.27. The data can be described well with an β_0=0.01. This is in reasonable agreement with the expected value of β_0=0.015-0.03, considering the uncertainties on the inserted quantities.

8.1.6 Surface puddles

As mentioned above the sample # 3 was characterized for STM measurements[4]. The goal of our investigation was to determine the influence of the bulk potential fluctuations on the surface state, especially the filling of the Dirac cone. STM measurements are perfectly suited for this purpose, since they grant insight into the density of states at the surface, including the potential fluctuations at the surface. The STM data revealed surface potential fluctuations on a length scale of 40-50 nm with an amplitude of 8-14 meV, which is much smaller than in the bulk, where it exceeds half the energy gap. The potential fluctuation are expected to be smaller than the bulk fluctuations, since the surface state supplies a gapless screening channel. However, the potential fluctuations are even smaller than expected from theory [73], which indicates an influence of the bulk screening on the screening at the surface.

---

[4] The STM measurements were performed by T. Knispel and Dr. W. Jolie in the group of Prof. Michely from the II. Institute of Physics at the University of Cologne [116]

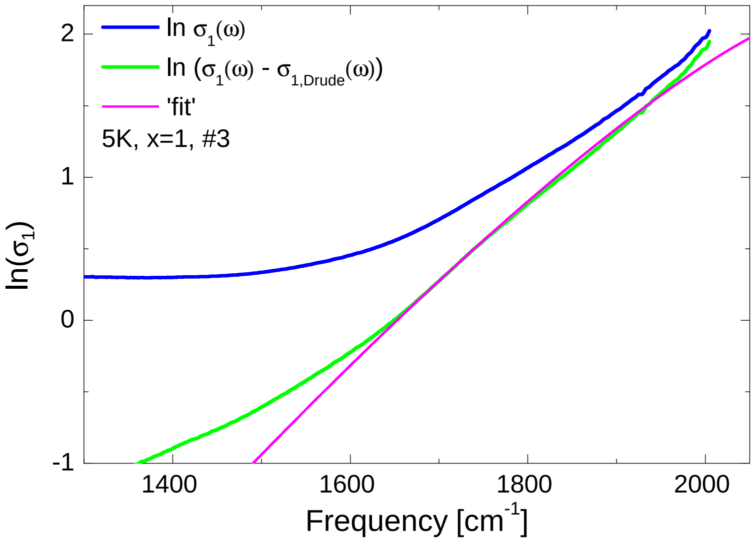

Figure 8.27: Blue curve $\ln \sigma_1(\omega)$ at the gap for 5 K. Green curve: $\ln \sigma_1(\omega)$ after subtracting the Drude peak and a small constant background. Magenta: theory, see equation 8.1.12, using a gap of 260 meV.

Details are published by Knispel *et al.* [116].

8.1.7 Summary

We have investigated BiSbTeSe_2 which has the highest DC resistivity of the $\text{Bi}_{2-x}\text{Sb}_x\text{Te}_{3-y}\text{Se}_y$ family at low temperatures [43]. It is characterized by the average Fermi level close to the Dirac point, see figure 8.3. The optical conductivity granted us insight to the carrier dynamics that are not accessible by DC transport measurements.

Our results reveal the formation of charge puddles in this almost perfectly compensated topological insulator at low temperatures. The puddles evaporate on a temperature scale of 30-40 K. This non-monotonic temperature dependence of the average carrier density in puddles is well described by the numerical simulations[5], which are based on the Efros-Shklovskii theory [69–72] which describes disordered Coulomb systems by shallow donors and acceptors interacting by long-ranged Coulomb interactions. With rising temperature the activated charge carriers efficiently screen the potential fluctuations, causing a reduction of the potential fluctuations and thereby the evaporation of the puddles. The formation and the evaporation of puddles observed in the experiment agree well with the numerical simulations. In particular, the temperature scale and the optical weight agree semiquantitatively. The formations of puddles is important for all compensated semiconductors. Furthermore, the puddle formation plays an important role for other materials with vanishing density of electronic states, such as Dirac matter in two or three dimensions, like graphene [130] or Weyl semimetals. For the latter, long-range potential fluctuations cause the difference

---

[5] The simulations have been carried out by Dr. Lux and Prof. Rosch of the Institute for Theoretical Physics at the University of Cologne [76]

between Weyl semimetals and real metals to blur [131–133]. The band bending and the puddle formation need to be considered for the observation of the heavily sought after chiral anomaly in Weyl semimetals, since the observation requires the Fermi level to be close to the Dirac point.

The puddles formation is a direct proof of spatial fluctuations of the Fermi level in the sample. The fluctuations imply that it is difficult to increase the bulk resistivity further by perfect compensation. However, the puddles cause a localization of charge carriers, especially for deviations from perfect compensation, which increases the DC resistivity. The surface state in topological insulators screens the potential fluctuations close to the surface. Therefore, studying the puddle formation as function of sample thickness promises interesting insights. Understanding the puddle formation further and controlling it may turn out to be the next step to reduce the bulk conductivity further.

x	# 1	# 2	# 3	# 4
0	$31\,\mu$m	$76\,\mu$m	$210\,\mu$m	
0.25	$89\,\mu$m	$27\,\mu$m		
0.5	$555\,\mu$m	$149\,\mu$m	$138\,\mu$m	$126\,\mu$m
0.75	$257\,\mu$m	$76\,\mu$m		
1	$183\,\mu$m, $130\,\mu$m, $102\,\mu$m	$1100\,\mu$m	$135\,\mu$m	$2\,\mu$m

Table 8.1: The thicknesses of the samples of the different compounds.

8.2 $Bi_{2-x}Sb_xTe_{3-y}Se_y$

In this chapter we will present the results on the topological insulators of the family $Bi_{2-x}Sb_xTe_{3-y}Se_y$ with $0 \leq x < 1$. We will reveal the presence of puddles in all compounds and discuss the x dependence of properties like the defect density and the compensation.
The analysis of the optical data is performed analogous as far as possible to the analysis of $BiSbTeSe_2$ in the previous chapter, see section 8.1.3. The thickness of the samples we report on for each compound are listed in table 8.1

A temperature-dependent $\sigma_1(\omega)$ for each compound is plotted in figure 8.28. The small constant background and the size of the Drude peak at low temperatures are the properties of $\sigma_1(\omega)$ that are sample dependent for the same x. The striking differences for different x are the size of the energy gap and the low-temperature behavior of the Drude peak.

8.2.1 Energy gap

Experimentally, there are different possibilities to determine the energy gap. Often, $\sigma_1(\omega)$ is obtained via Kramers-Kronig analysis of reflectance data, and the gap is estimated by extrapolating the data to $\sigma_1(\omega) = 0$. In comparison, the transmittance is more sensitive to small values of $\sigma_1(\omega)$ but limited at large $\sigma_1(\omega)$. Therefore, the transmittance allows us to determine the very onset of excitation across the gap. This is straightforward if the slope of $\sigma_1(\omega)$ is particularly large. This is the case for $x = 0.75$, see figure 8.28a. We use $\sigma_1(\omega_\Delta) = 6\,(\Omega\text{cm})^{-1}$ to define the value of the gap ω_Δ. Due to the steep increase of $\sigma_1(\omega)$ for $x = 0.75$, the value of ω_Δ hardly depends on the choice of the constant, *i.e.* very similar results are obtained for choosing, *e.g.*, $\sigma_1(\omega_\Delta) = 10\,(\Omega\text{cm})^{-1}$. However, this is not the case for the more gradual increase of $\sigma_1(\omega)$ for $x = 0.5$. The consequences of this will be discussed below.
The x dependence of the energy gap ω_Δ is plotted in figure 8.29a. Note that we subtracted the background for the analysis, in order to compare the absolute values of $\sigma_1(\omega)$ at the gap. We find that from $BiSbTeSe_2$ ($x = 1$) to Bi_2Te_2Se ($x = 0$) the energy gap, more precisely $\omega_\Delta(5K)$, constantly increases from about $2120\,\text{cm}^{-1}$ to $2850\,\text{cm}^{-1}$. The results for $x = 0.5$ deviates from a smooth trend as a function of x.
Additionally, we compare the temperature behavior of the different compounds in figure

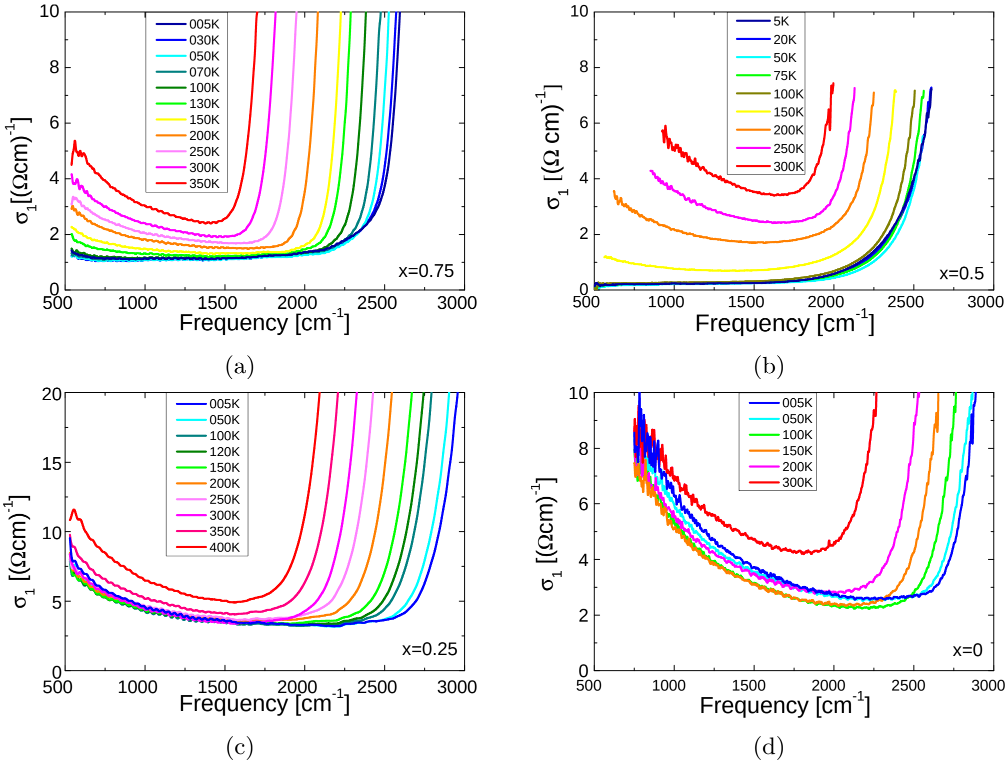

Figure 8.28: $\sigma_1(\omega)$ for different temperatures for (a) $x = 0.75$, (b) $x = 0.5$, (c) $x = 0.25$, and (d) $x = 0$.

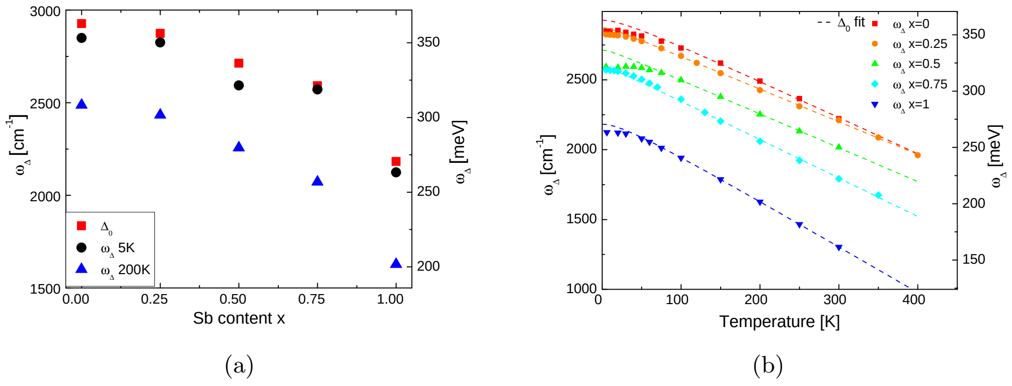

Figure 8.29: (a) The energy gap ω_Δ represented by $\sigma_1(\omega_\Delta)=6\,(\Omega\mathrm{cm})^{-1}$ at 5 K and 200 K depending on x. Additionally, Δ_0 from the fit as function of x (b) Temperature dependent $\sigma_1(\omega)$ and the fit using the Varshni relation.

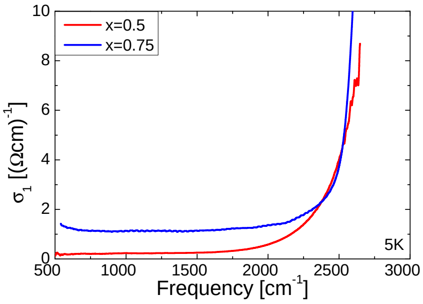

Figure 8.30: $\sigma_1(\omega)$ at 5 K for $x = 0.75$ and $x = 0.5$ to the noise level.

8.29b. Above about 75 K, the temperature dependence is very similar for all compounds. However, at low temperatures the range in which the gap is roughly constant is different in different data sets. This is striking for $x = 0.5$ and $x = 0.75$. While $x = 0.75$ exhibits a constant gap over approximately 50 K, the gap of $x = 0.5$ is decreasing already for 30 K. This is emphasized by the fit to the ω_Δ for temperatures larger than 90 K using the Varshni relation [119], see equation 8.1.1. The fits suggest that the gap is slightly underestimated for all compounds.

The plot of Δ_0 in figure 8.29a shows a smooth variation as function of x. The differences between Δ_0 and ω_Δ are attributed to the finite slope at $\sigma_1(\omega_\Delta) = 6\,(\Omega\mathrm{cm})^{-1}$ and to the existence of a weak absorption feature in the vicinity of the gap at low temperatures, a "foot" below the gap. This foot is particularly pronounced for $x = 0.5$, explaining the large difference between $\omega(\Delta)$ and Δ_0.

Microscopically, this foot can be attributed to the absorption for energies slightly smaller than the gap which is possible due to strong band bending and tunneling, as discussed in section 6.4.1.7. Its dependence on x will be discussed in section 8.2.4. Since the band bending is reduced with rising temperature, we plot the values of ω_Δ for 200 K. In agreement with $\Delta_0(x)$ we find a smooth dependence on x for $\omega_\Delta(200K)$ which emphasizes the role of the foot below the gap for low temperatures.

We compare the results on the size of the gap for $x = 0.5$ as function of temperature to the results reported by Post *et al.* [79], see figure 8.31. The size of the gap at 300 K is in good agreement with Δ slightly above 2000 cm^{-1}. At 5 K Post *et al.* [79] report a gap of $\Delta \approx 2742\,\mathrm{cm}^{-1}$ (340 meV) confirming the value of Δ_0=2713 cm^{-1} (336 meV) observed by us while the ω_Δ=2593 cm^{-1} (321 meV) is 120 cm^{-1} (15 meV) smaller.

For $x = 1$ we compare our results to the "larger" gap reported by Post *et al.* [79], since we claim that the "smaller" gap is an artifact of the Kramers-Kronig analysis, see section 8.1.1.4. Post *et al.* report on $\Delta \approx 1774\,\mathrm{cm}^{-1}$ (220 meV) at 5 K while we find Δ_0=2182 cm^{-1} (271 meV). At 300 K our Δ_0=1303 cm^{-1} (162 meV) is in better agreement with the $\Delta \approx 1210\,\mathrm{cm}^{-1}$ (150 meV) reported by Post *et al.* [79]. This finding emphasizes that the Kramers-Kronig result by Post *et al.* is influenced by the transparency which increases for low temperatures.

Greenaway *et al.* reported for $x = 0$ Δ =2400 cm^{-1} [122] at room temperature. The room-

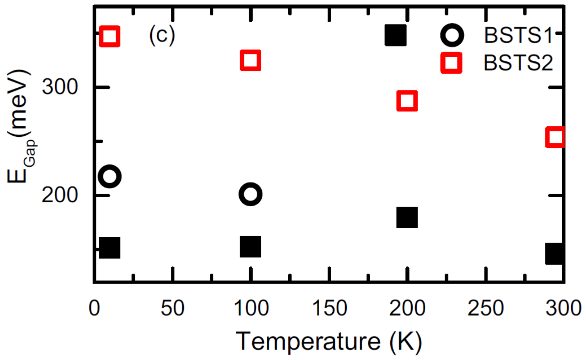

Figure 8.31: Energy gap as function of temperature as reported by Post *et al.* [79]. BSTS1 corresponds to $x = 1$, BSTS2 corresponds to $x = 0.5$. The open circles and the filled squares in black represent the "two" gaps. The figure is a reprint of figure 2 c of [79]`https://dx.doi.org/10.1103/PhysRevB.91.165202` {DOI}. Copyright by American Physical Society (2015).

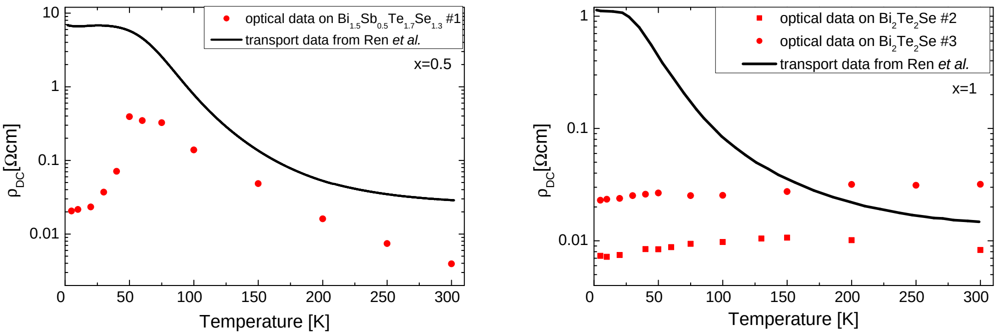

(a) (b)

Figure 8.32: Comparison of the DC conductivity obtained by transport measurements by Ren *et al.* [43] and by extrapolation of the Drude peak in optics as function of temperature for $x = 0.5$ (a) and $x = 0$ (b).

temperature gap reported by Akrap *et al.* [124] is Δ=2420 cm^{-1} (300 meV). However, they report as well on $\Delta \approx 2300\,\text{cm}^{-1}$ (285 meV) determined by using a Tauc-Lorentz model. We find Δ_0=2230 cm^{-1} (276 meV) in reasonable agreement with the gap determined by using a Tauc-Lorentz model reported by Akrap *et al.* [124].

In summary, the energy gap of $Bi_{2-x}Sb_xTe_{3-y}Se_y$ increases from $x = 1$ to $x = 0$. The temperature dependence is comparable. The shape of $\sigma_1(\omega)$ in the vicinity of the energy gap depends on the compounds.

8.2.2 Effective charge carrier density

For $x = 0.75$ and $x = 0.5$, the physics is qualitatively similar to the case $x = 1$, see figure 8.33. The low-frequency weight at low temperatures comes from puddles, too, as shown for $x = 0.5$ by the comparison of the DC conductivity extrapolated from $\sigma_1(\omega)$ and

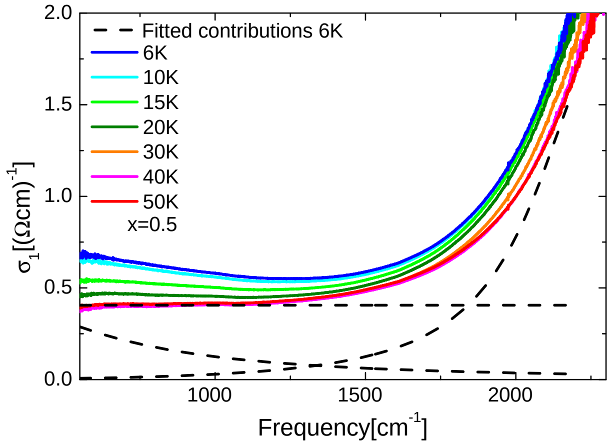

Figure 8.33: $\sigma_1(\omega)$ of sample # 1 for $x = 0.5$ for different temperatures. The different contributions are plotted as dashed lines.

the DC conductivity obtained in transport measurements, see figure 8.32a. But there are quantitative differences, *e.g.* the puddle contribution is weaker. For $x = 1$, we determined $\sigma_1(\omega)$ from the smoothed transmittance (Fourier filtered to average the Fabry-Pérot fringes). For the thinner samples of $x = 0.5$ (# 2) and $x = 0.75$ (# 2) the temperature dependence of $\sigma_1(\omega)$ at low temperatures is tiny, the changes are close to the noise level, see appendix figure A.33. However, the fringe amplitude offers a very sensitive way to determine the absorption strength. Figure 8.34 shows the temperature dependence of the fringe amplitude for $x = 0.5$. A non-monotonic behavior is obvious.
Assuming that the scattering rate is independent of temperature, as observed for $x = 1$, we can use the fringe amplitude to determine the Drude weight. The result is shown in figure 8.37c.
Furthermore, we performed a similar analysis on the data for $x = 1$, see figure 8.35. The result agrees with the one described above obtained by a fit to $\sigma_1(\omega)$, see figure 8.36. The deviations in N_{eff} are originating from a different scattering rate. The scattering cannot be determined precisely by the transmittance, since a perfect fit across the whole frequency range is hindered by the fringes, whereas the smooth $\sigma_1(\omega)$ gives the scattering rate precisely. A disadvantage of determining the N_{eff} by the fringes is that this method is only applicable to transmittance that show clear fringes, unlike the transmittance for 150 or 200 K, see inset 8.35.

Like for $x = 1$, we determine E_c by comparison of the theoretical curve $p(T)$, see figure 8.21, to $N_{\text{eff}}(T)$, see section 8.1.3.1. The small spectral weight of the Drude-like peak makes the determination of the exact values of $N_{\text{eff}}(T)$ difficult. Therefore, we do not claim to observe a sample dependence of E_c for $x = 0.25$ or $x = 0.5$, but determine a sample independent range which is in agreement with N_{eff} for both samples within the error bars. The temperature scale on which the puddles evaporate for the samples # 1 and # 2 with $x = 0.5$ is 20-25 K (E_c=1.7-2.2 meV), see inset figure 8.37c. The defect density is

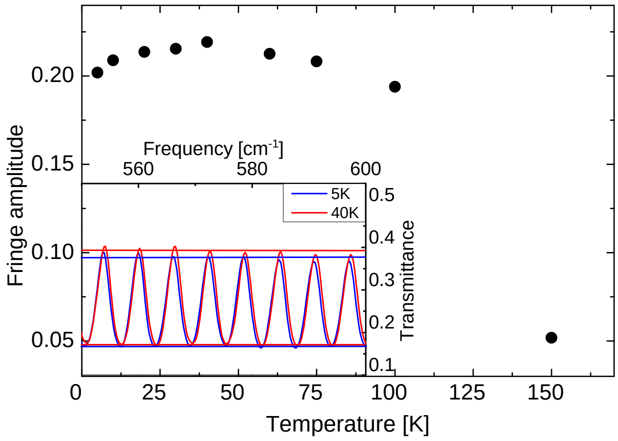

Figure 8.34: The amplitude of the fringes averaged over ten oscillations as function of temperature for sample # 4 with $x = 0.5$. Inset: transmittance for 5 K and 40 K. The bars represent the average extrema.

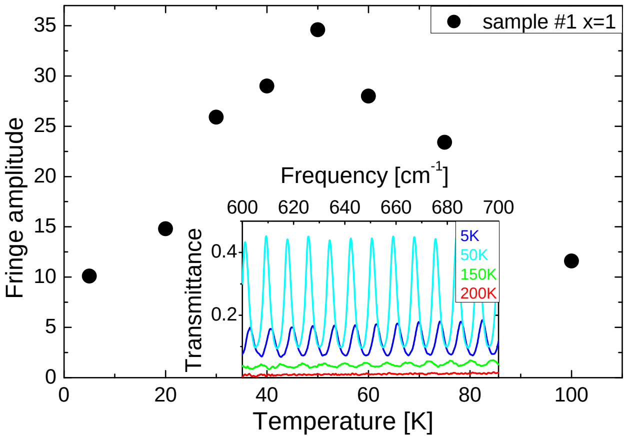

Figure 8.35: The averaged amplitude from 600-700 cm^{-1} Inset: Transmittance in the analyzed frequency range.

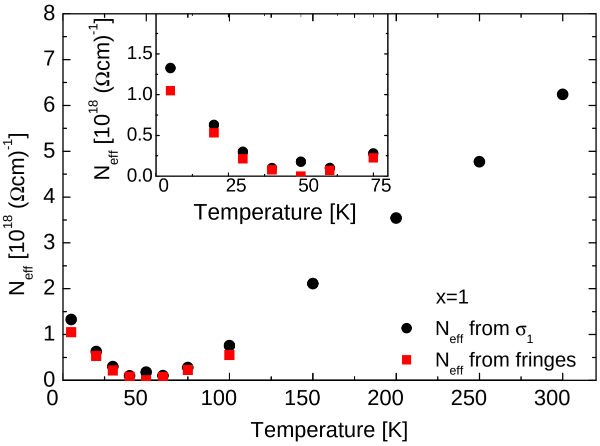

Figure 8.36: N_{eff} of sample # 1 with $x = 1$ obtained by $\sigma_1(\omega)$ (black dots) and N_{eff} obtained by the fringe amplitude (red squares). Inset: Closeup of the low-frequency range.

$N_{def} = 1.4 - 2.7 \cdot 10^{19}\,\text{cm}^{-1}$. For $x = 0.75$ the temperature-dependent Drude weight vanishes between 15-20 K (E_c=1.3-1.7 meV), see inset figure 8.37b. This results in a defect density of $N_{def} = 0.6 - 1.4 \cdot 10^{19}\,\text{cm}^{-3}$.

For $x = 0$ and $x = 0.25$ we find little temperature dependence of the Drude weight of $\sigma_1(\omega)$, see figure 8.37e and 8.37d. The optical data for $x = 0$ presented in this chapter are measured on sample # 2. To reveal the sample dependence of the absolute value, the results for sample# 3 are plotted, too. Additionally, for $x = 0$ the presence of puddles is shown by the discrepancy at low temperatures of the DC conductivity obtained by transport and the DC conductivity extrapolated from optical data, see figure 8.32b. The difference at high temperatures might be due to uncertainties in the measurement or due to the fact that the data is not obtained on the identical sample.

The activated behavior cannot be observed by optics in the measured temperature range for both compositions, because the puddle contribution dominates the low-frequency range and activated carriers are suppressed due to the enhanced gap and reduced potential fluctuations. For $x = 0$ and $x = 0.25$ the temperature scale on which puddles evaporate and activated charge carriers become important strongly overlaps. A temperature scale of 150 K would already result in a defect density two orders of magnitude larger than observed for $x > 0.25$. Neither is there a reason for such an increase in the defect density, nor is the resulting defect density in agreement with the Drude weight of the puddles. The Drude weight would need to be much larger even for perfect compensation. We attribute the deviations between theory and experiment to a compensation far from perfect which is not described by the theory, see section 8.2.3.

The defect densities for $x = 0.5 - 1$ are plotted in figure 8.38a. We observe very small defect densities for $x = 0.5$ and $x = 0.75$. We explain this with less order in the atom layers for $x = 1$, which has a ratio of Bi to Sb of 1:1 in the Bi/Sb and a ratio of Te to Se of 1:1 in the Te/Se layer. For $x = 0.75$ the ratio is 5:3 in the Bi/Sb layer and 13:7 in the Te/Se layer.

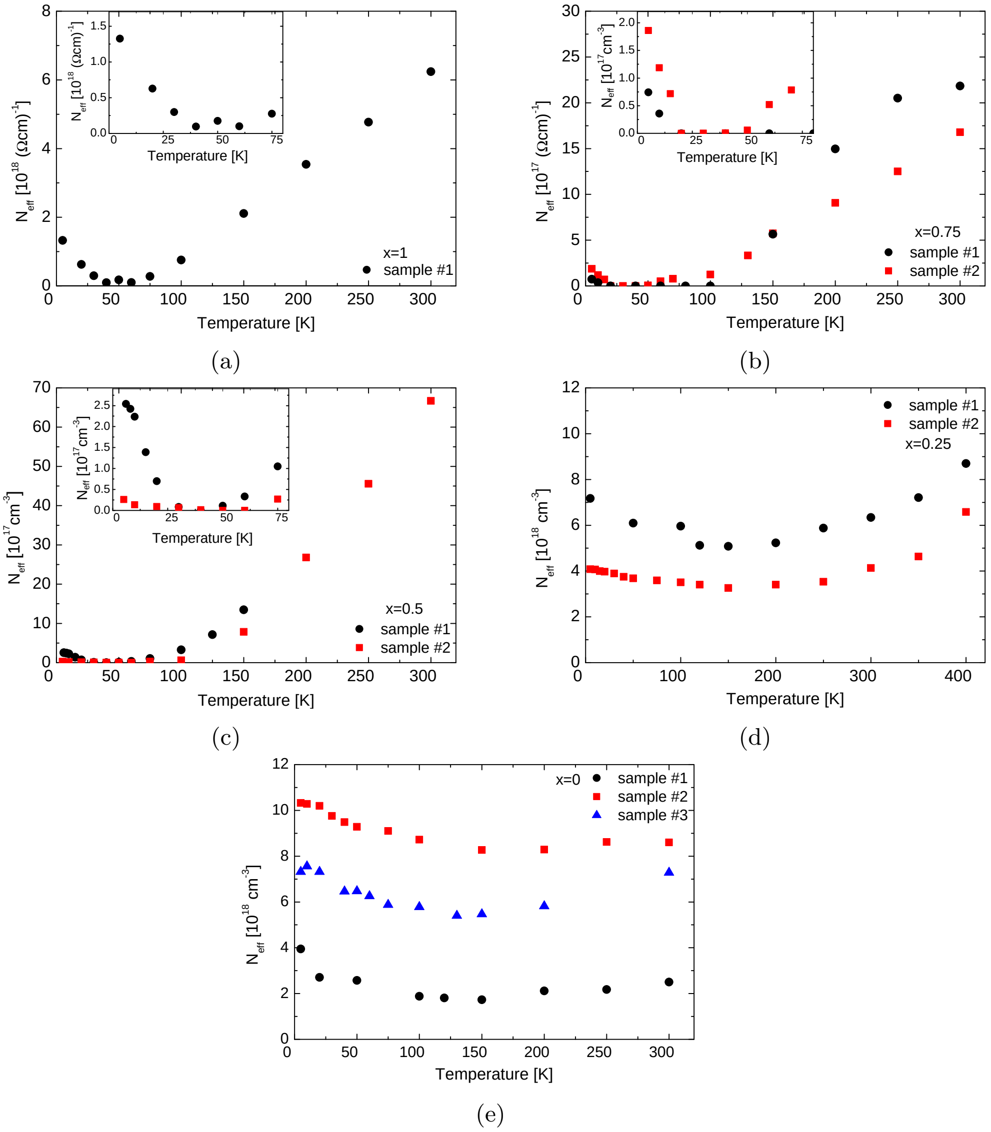

(a) (b) (c) (d) (e)

Figure 8.37: N_{eff} density for each x. Inset: N_{eff} at low temperatures.

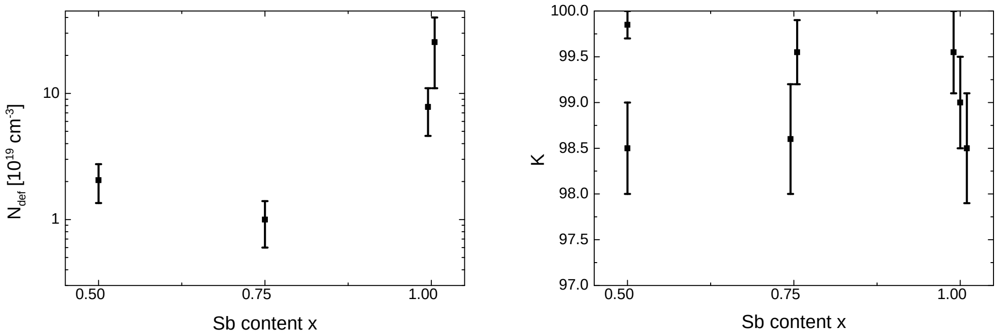

(a) (b)

Figure 8.38: Defect density (A) and compensation (B) as function of x

For $x = 0.5$ the ratio is 3:1 in the Bi/Sb layer and 17:3 in the Te/Se layer. In the limit of $x = 0$ each layer of the quintuple layer is occupied by only one atom type. In a naive picture antisite defects and vacancies are causing less distortion in a layer with randomly placed atoms of different types than in the same layer with only one atom type, making defects energetically more favorable for $x = 1$.

8.2.3 Compensation

For sample # 1 with $x = 0.75$ we find K=99.2-99.9 % and for sample # 2 we find K=98.0-99.2 %. For $x = 0.5$ the compensation is perfect within the error bars. The compensation for sample # 1 with $x = 0.5$ is determined to 98-99 %, while sample # 3 has K=99.7-100 %. The values for the compensation as function of x are plotted in figure 8.38b. It emphasizes that for the three compounds with $x = 0.5$, $x = 0.75$, and $x = 1$ perfect compensation can be reached.

For $x = 0.25$ and $x = 0$, we cannot determine the compensation, because we cannot determine the defect density, as discussed above. However, we know from ARPES data reported by Arakane *et al.* [105] that the Fermi level shifts towards the conduction band for decreasing x, see figure 8.3. This clearly shows that compensation is far from perfect for $x = 0$.

We expect that for $x = 0.25$ and $x = 0$ the large density of uncompensated defects are causing puddles that are dominating the Drude weight even above $T = \frac{E_c}{k_B}$. The theoretical calculations have not shown a dependence of the temperature scale on which the puddles evaporate on the compensation for K between 95 % and 100 %, see figure 8.21, but it is plain to see that below a certain compensation a large amount of neutral charge carriers must be localized in puddles. The reason is that a neutral defect needs four neutral defects out of the twelve next neighbors to be called part of a puddle, see section 8.1.2.7. Hence, if the compensation drops below $K = 50\%$ a neutral dopant will have in average four neutral neighbors. Therefore, we expect at least 50 % of the defects in puddles, independent of temperature (neglecting excitations into the conduction band).

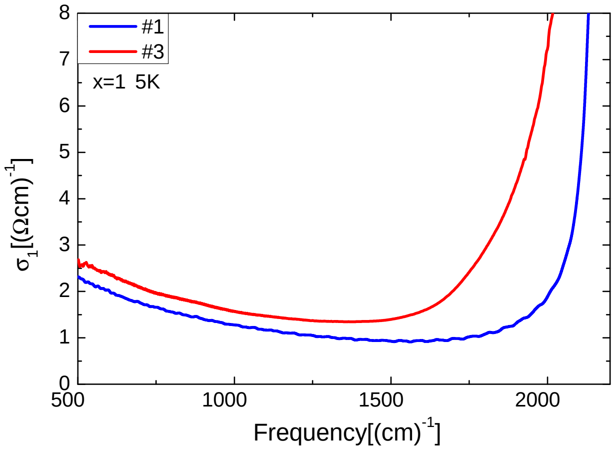

Figure 8.39: $\sigma_1(\omega)$ for sample # 1 and # 3 for $x = 1$.

In conclusion, the temperature dependence of the Drude weight cannot be described by our model, which we attribute to a compensation far from perfect. For $x \geq 0.5$ theory and experiment are in good agreement and we find excellent compensation.

8.2.4 Coulomb fluctuations

According to the theory by Shklovskii *et al.* [77] described in section 6.4.1.7, a smeared out line shape of $\sigma_1(\omega)$ at the gap is associated with strong Coulomb fluctuations. The Coulomb fluctuations are increasing with increasing defect density. Therefore, we expect an increase of the foot below the gap for an increasing defect density. In order to avoid effects from a change of compensation, we compare $\sigma_1(\omega)$ at the gap of two samples with $x = 1$ and a similar compensation. For sample # 1 we find $K = 97.9 - 99.1\,\%$ and for sample # 3 $K = 98 - 100\,\%$. The main difference between both samples is the defect density, which is $4.6 - 11 \cdot 10^{19}\,\mathrm{cm}^{-3}$ for sample # 1 and $1 - 4 \cdot 10^{20}\,\mathrm{cm}^{-3}$ for sample # 3.

We find a much sharper increase of $\sigma_1(\omega)$ at the gap for sample # 1, see figure 8.39. As expected the sharp $\sigma_1(\omega)$ at the gap can be associated with smaller potential fluctuations caused by a smaller defect density.

Additionally, we investigate the influence of the compensation on the shape of $\sigma_1(\omega)$ at the gap. Perfect compensation goes along with many charged defects, while worse compensation means less charged defects. The determined compensations are between $K = 98 - 100\,\%$, hence the density of charged defects differs only by $1 - 2\,\%$ for these samples. Therefore, we expect little difference for different compensations on the shape of $\sigma_1(\omega)$ at the gap.

We compare $\sigma_1(\omega)$ at 5 K for $x = 0.75$ of sample # 1 with $K = 99.2 - 99.9\,\%$ and sample # 2 with $K = 98.0 - 99.2\,\%$, see figure 8.40a. Furthermore, we compare $\sigma_1(\omega)$ at 5 K for $x = 0.5$ of sample # 1 with $K = 98 - 99\,\%$ and sample # 2 with $K = 99.7 - 100\,\%$, see figure 8.40b. In both cases we observe that the sample with a compensation closer to perfect has the sharper shape of $\sigma_1(\omega)$ at the gap. This contradicts the expectation. However, the error bars on the defect density are huge compared to the deviations of the compensation,

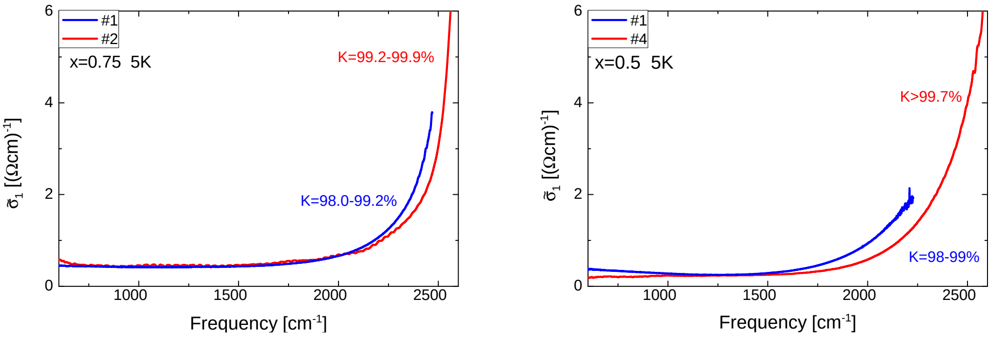

(a) (b)

Figure 8.40: $\sigma_1(\omega)$ shifted to the same offset for $x = 0.75$ (A) and $x = 0.5$ (B).

i.e. the defect density lies between $\mathrm{N}_{def} = 0.6 \cdot 10^{19}\,\mathrm{cm}^{-1}$ and $\mathrm{N}_{def} = 1.4 \cdot 10^{19}\,\mathrm{cm}^{-1}$ for $x = 0.75$, which is directly proportional to the charge carrier density, while the compensation lies between $K = 98\,\%$ and $K = 100\,\%$. Therefore, it is likely that the shape of $\sigma_1(\omega)$ at the gap is dominated in both cases by differences in the defect density in the low percent range, which can not be resolved by the temperature dependence of N_{eff}.

So far, we have compared the shape of $\sigma_1(\omega)$ at the gap only for the same value of x, which means that the influence of the gap was not investigated, yet. A small energy gap limits the potential fluctuations and especially the steepness of the Coulomb potential. Therefore, the matrix element for the excitation of an electron-hole pair with the energy deficit $\hbar\omega_\Delta$ is reduced. Hence, we expect a large gap to cause a large foot below the gap. In order to test the dependence of $\sigma_1(\omega)$ on the compensation, the defect density, and the energy gap, we plot $\sigma_1(\omega)$ of the thinnest sample for each x, see figure 8.41 and figure 8.42. For $x = 0$ and $x = 0.25$ the foot below the gap is small. This is in agreement with the small defect density and the compensation far from perfect for these compounds. However, the smallest foot below the gap is observed for $x = 1$ which has a compensation close to perfect, the highest defect density, and the smallest energy gap. For $x = 0.75$ and $x = 0.5$ the compensation is close to perfect, the defect density is decreased and the energy gap is larger. The foot increases and reaches a maximum for $x = 0.5$.

The increasing energy gap is the main reason for the increase of the foot from $x = 1$ to $x = 0.5$.

For $x = 0.25$ and $x = 0$ the energy gap is even larger, but the energy gap is only limiting potential fluctuations and not causing them. The compensation far from perfect and the small defect density cause a smaller density of charged defects and therefore smaller potential fluctuations.

In contrast to $\sigma_1(\omega)$ of an uncompensated semiconductor $\sigma_1(\omega)$ becomes sharper at the gap with increasing temperature, if large potential fluctuations are present like for $x = 0.5$, see figure 8.43. Band bending is reduced with increasing temperature, see figure 8.18, thus the foot below the gap is reduced with increasing temperature, see figure 8.43. This leads to the sharpening of the line shape of $\sigma_1(\omega)$ at the gap with increasing temperature. At temper-

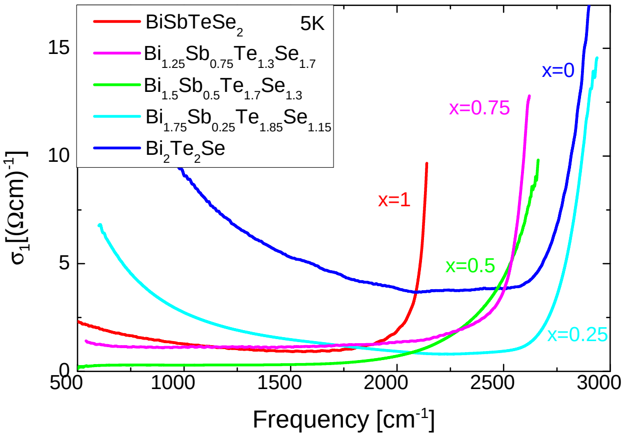

Figure 8.41: $\sigma_1(\omega)$ of the thinnest sample of each compound.

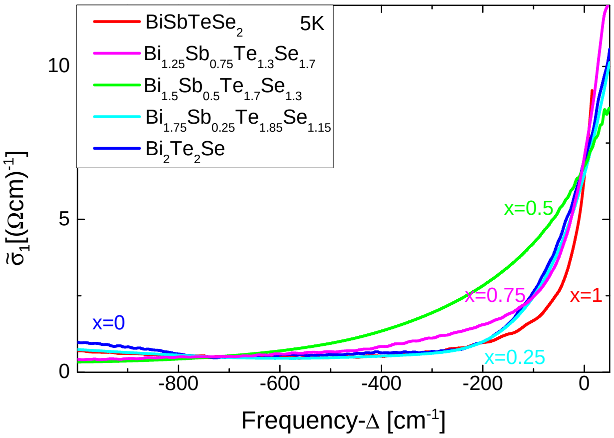

Figure 8.42: $\sigma_1(\omega)$ shifted by the gap of each compound. An offset was subtracted from $\sigma_1(\omega)$ to match the minimal offset of $x = 0.5$.

atures above about 75 K the thermal broadening becomes dominant and the temperature dependence of $\sigma_1(\omega)$ at the gap is that of an uncompensated semiconductor.
In summary, the x dependence and the temperature dependence show that the foot below the gap is caused by charged defects and limited by the energy gap.

8.3 Summary

We report on the experimental verification of charge puddles and reveal the highly non-monotonic temperature dependence of $\sigma_1(\omega)$ in almost perfectly compensated BiSbTeSe$_2$. The compensation reduces not only $\sigma_1(\omega)$ to values of $0.3\,(\Omega\mathrm{cm})^{-1}$, but it gives as well rise to potential fluctuation and eventually to puddles which cause the non-monotonic temperature dependence of $\sigma_1(\omega)$. Furthermore, the potential fluctuation cause a reduced activation energy. In order to explain the dynamics of puddles, we performed Monte Carlo simulations,

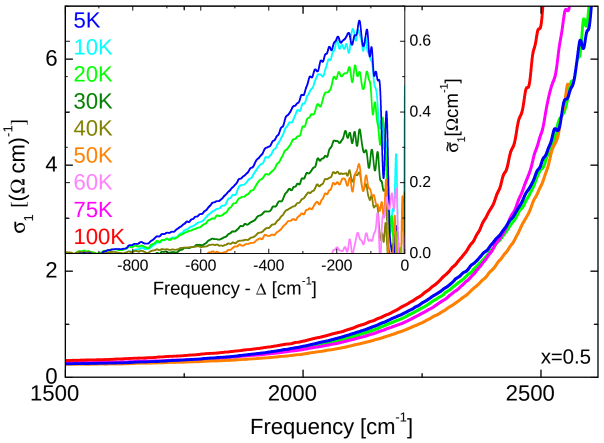

Figure 8.43: $\sigma_1(\omega)$ of sample #2($x = 0.5$) from 5 K to 100 K at the gap. Inset: The data was shifted on top of each other at $\sigma_1(\omega_\Delta)$=6 Ωcm^{-1} in frequency. Subsequently, the shifted $\sigma_1(\omega)$ for 75 K was subtracted from all $\sigma_1(\omega)$, since it exhibits the smallest foot below the gap.

in collaboration with the group of Prof. Rosch of the Institute for Theoretical Physics at the University of Cologne, based on a simple, classical, electrostatic model as discussed by Skinner, Chen, and Shklovskii [71]. The simulations were able to reveal the formation of puddles in a compensated semiconductor and especially to model the temperature dependence of the puddles. Additionally, the simulations allowed us to deduce N_{def} and K from the optical data. We identified a foot below the gap, predicted by Shklovskii *et al.* [77], which causes a sharpening of the gap with rising temperature before the thermal broadening of the gap becomes dominant.

We have investigated many samples of the $\mathrm{Bi}_{2-x}\mathrm{Sb}_x\mathrm{Te}_{3-y}\mathrm{Se}_y$ family for $x \leq 1$ and showed the importance of potential fluctuations for all sample. In particular, we found puddles in every sample. We observed an increase of Δ for decreasing x. The simulations were able to describe the physics of $x = 0.75$ and $x = 0.5$, while the physics caused by the deviations of the compensation from $K = 100\,\%$ are too large for $x = 0.25$ and $x = 0$ to be described by the simulations. For $x \geq 0.5$ we have found excellent compensation which is sample dependent, while N_{def} is mostly sample independent. N_{def} is considerably reduced for $x = 0.5$ and $x = 0.75$ compared to $x = 1$. By comparing the foot below the gap we were able to estimate the potential fluctuation. We found that the potential fluctuations for $x \geq 0.5$, are limited by Δ. Hence, causing the largest foot below the gap for $x = 0.5$. In contrast, for $x = 0.25$ and $x = 0$ the screening of uncompensated defects causes only a small foot below the gap. The optical data represents a broad overview of the compensated topological insulators $\mathrm{Bi}_{2-x}\mathrm{Sb}_x\mathrm{Te}_{3-y}\mathrm{Se}_y$ in the light of the revealed charge puddles.

Part IV

Spin-orbit-entangled Mott insulators

Chapter 9

Introduction to spin-orbit-entangled Mott insulators

In this chapter we will sketch how to derive the eigenstates for d^5 spin-orbit-entangled Mott insulators and discuss the excitations. In general the Hamiltonian including the cubic crystal field, the trigonal crystal field, the Coulomb repulsion, the Hund's exchange and the spin-orbit coupling has to be solved. This takes a lot of effort and can usually be done numerically, only. However, we can often solve the problem by considering certain limits. The limits relevant for $4d/5d$ materials, investigated by us, are discussed below.

9.1 Mott insulators

For the large majority of crystalline solids, electronic correlations can be neglected. The electronic structure of such compounds and many other properties can be described in a single-electron picture which takes the periodic potential of the crystal into account. The result is the band theory, giving the allowed energies as function of the electron wave vector. A standard band insulator or a semiconductor exhibits an energy gap between full and empty bands. In contrast, a metal exhibits partly filled bands, which allows a change of the wave vector without overcoming an energy gap. Each band consists of 2N states for electrons, with N the number of atoms. Hence, the number of electrons per unit cell needs to be even to form an insulator in the band picture. However, many compounds, especially transition metals, are known to exhibit insulating behavior even though their unit cell harbors an odd number of electrons. These insulators are called Mott insulators. The band theory does not apply to these compounds, because the electrons are localized to the atoms due to electron correlations, which will be discussed in the following chapter in detail.

9.1.1 Magnetic properties of Mott insulators

The localization of an electron on site goes along with the localization of a spin, respectively magnetic momentum. Hence, Mott insulators are strong magnets. In the simple case of one localized electron per site on a square lattice with 180° metal-ligand-metal bonding geometry, the electrons on neighboring sites interact antiferromagnetically via superexchange. The reason is virtual hopping between neighboring sites, which is forbidden for parallel spins. However, for doped Mott insulators it may be favorable to order ferromagnetically to gain kinetic energy of the dopants [134]. Furthermore, doped Mott insulators can even exhibit superconductivity.
The following chapter is for the most part based on the work of S. Sugano, Y. Tanabe, H. Kimura [135], D. Khomskii [134], G. L. Stamokostas and G. A. Fiete [136], and Perkins *et al.* [137].

9.2 Hubbard model

In a simple picture, the interactions causing the localization are described in the Hubbard model [1]. The Hamilton operator $\hat{H}$ for the Hubbard model is defined as

$$\hat{H} = U \sum_{i} c^{\dagger}_{i\uparrow} c_{i\uparrow} c^{\dagger}_{i\downarrow} c_{i\downarrow} - t \sum_{\langle ij \rangle, \sigma} (c^{\dagger}_{i\sigma} c_{j\sigma} + c^{\dagger}_{j\sigma} c_{i\sigma}). \tag{9.2.1}$$

The quantity U is the on-site Coulomb repulsion between two electrons. The quantity t is the overlap integral between electrons on neighboring sites. The c_i is the annihilation operator of an electron on the site i and $c^{\dagger}_i$ corresponds to a creation operator of an electron on the site i. If t is large the band width is increased and thus the kinetic energy is lowered for a partially filled band. Hence, the electrons prefer to stay on site for $U \gg t$ which leads to insulating behavior. In summary, this model describes the insulating behavior of compounds which are supposed to be metallic according to band theory by electron-electron interactions.

9.3 From spherical harmonics to the $j = 1/2$ groundstate

The large Coulomb repulsion ensures that we can consider only d^5 states when determining the ground state, *i.e.*, we examine an insulator. By neglecting any other energy contribution the eigenstates of the d orbitals are energetically degenerate, given by the spherical harmonics

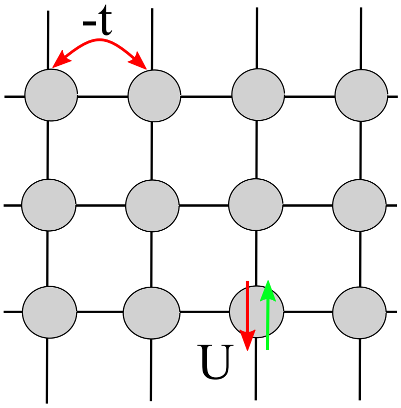

Figure 9.1: Hopping to the neighbor site is described by the overlap integral t. The Coulomb repulsion is U.

Y_l^m with the orbital momentum $l = 2$ [134],

$$d_{yz} = -\frac{1}{i\sqrt{2}}(Y_2^1 + Y_2^{-1}), \tag{9.3.1}$$

$$d_{zx} = -\frac{1}{i\sqrt{2}}(Y_2^1 - Y_2^{-1}), \tag{9.3.2}$$

$$d_{xy} = \frac{1}{i\sqrt{2}}(Y_2^2 + Y_2^{-2}), \tag{9.3.3}$$

$$d_{3z^2-r^2} = Y_2^0, \tag{9.3.4}$$

$$d_{x^2-y^2} = \frac{1}{\sqrt{2}}(Y_2^2 + Y_2^{-2}). \tag{9.3.5}$$

The shape of the orbital wave functions is plotted in figure 9.2.

9.3.1 Cubic crystal field

In a cubic crystal field the degeneracy of the eigenstates is lifted. The Crystal Field Theory was developed by John H. van Vleck in 1932 to describe the optical and electrical properties of transition metals [138]. The material-dependent constant $10Dq$ is giving the cubic crystal field splitting for d orbitals. This theory is relevant for the d and f electrons. The electrons of the neighboring atoms interact with the d and f electrons causing a contraction or elongation of the orbitals depending on the exact lattice geometry, which breaks rotational symmetry, see figure 9.2. Therefore, the d orbitals have different energies according to their geometry. A prominent example is the splitting of the d orbitals in a cubic crystal field, caused by, *e.g.*, an octahedron of ligands surrounding a metal ion. In cubic symmetry the d orbital splits into the t_{2g} states d_{yz}, d_{zx}, and d_{xy} and the e_g states $d_{3z^2-r^2}$, $d_{x^2-y^2}$. The crystal field splitting $10Dq$, which is larger than the trigonal crystal field or the SOC in the 4d^5 and $5d^5$ compounds. Therefore, the other energy contributions can often be treated perturbatively on the five electrons in the t_{2g} level.

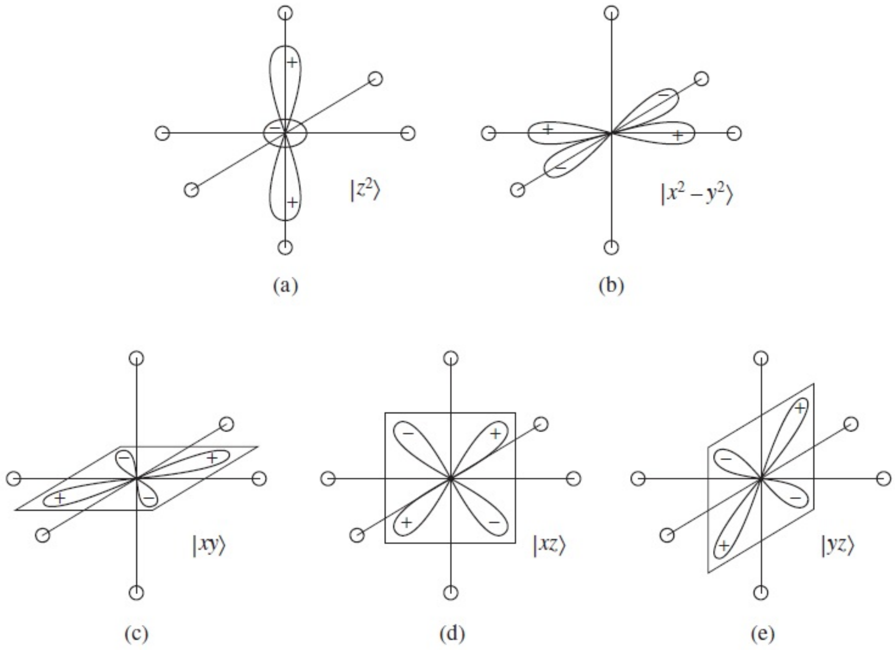

(a) (b)

(c) (d) (e)

Figure 9.2: Shape of the probability distribution of the d orbitals. In the presence of a cubic crystal field a) and b) correspond to the e_g orbital and c),d), and e) to the t_{2g} orbital. Figure has been taken from reference [134]. Copyright by Cambridge University Press.

9.3.2 Trigonal crystal field

The degeneracy of the t_{2g} level is lifted by a trigonal crystal field, see figure 9.3. The distortion reduces or increases the Coulomb potential on the different level, thereby splitting them into the a_{1g} doublet and the e_g^{π} quartet. For details see appendix V.

9.3.3 Spin-orbit coupling

The SOC describes, as the name implies, the interaction of the spin with the orbital angular momentum. If it is the only energy contribution considered in a certain energy level, it builds electronic states or multiplets with well-defined angular momentum $\mathbf{j}$ from states with orbital angular momentum $\mathbf{l}$ and spin angular momentum $\mathbf{s}$. The Hamiltonian writes

$$\hat{H}_{SO} = \sum_i \xi_i \mathbf{l}_i \cdot \mathbf{s}_i, \tag{9.3.6}$$

where ξ is the partial SOC constant and the sum goes over all electrons. In general one can distinguish between LS coupling, for which the total spin angular momentum $\mathbf{S}$ and the total orbital momentum $\mathbf{L}$ couple to the total angular momentum $\mathbf{J}$, and the jj coupling, for which each spin interacts with the orbital momentum before adding up to the total angular momentum $\mathbf{J}$, see section 9.3.3.2 and 9.3.3.1. For the $4d/5d$ transition metals investigated in this thesis the LS coupling dominant [137, 139–144].

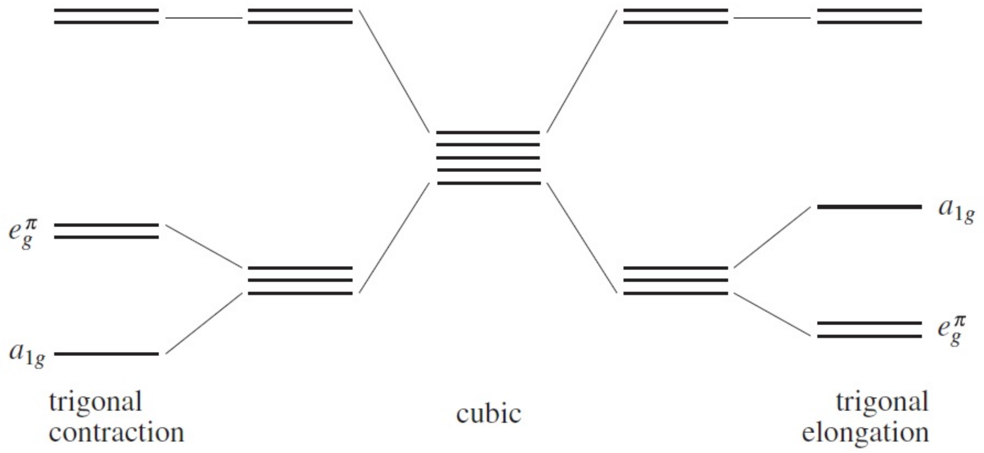

Figure 9.3: Cubic crystal field splits the d level into a e_g level and a t_{2g} level. Trigonal crystal field splits the t_{2g} level into a a_{1g} and a e_g^π levels. The energy of the a_{1g} (e_g^π) level is higher than the energy of the e_g^π (a_{1g}) level for trigonal elongation (contraction). The figure has been taken from Khomskii [134]. Copyright by Cambridge University Press.

9.3.3.1 jj coupling

The jj coupling applies to very heavy atoms like the $4f$ and $5f$ elements. For these elements the spin-orbit interaction of the individual electron overcomes the Coulomb interaction between them. Therefore, each electron forms a total angular momentum by adding its l_i and s_i, $j_i = l_i + s_i$. Finally, the total angular momenta are summed to form $\mathbf{J} = \sum_i \mathbf{j}_i$.

9.3.3.2 LS coupling

The LS coupling applies to all atoms in which the Coulomb interaction of the electrons is larger than the SOC for a single electron. The Hamilton operator for LS coupling can be written as

$$\hat{H}_{LS} = \lambda \mathbf{L} \cdot \mathbf{S}, \tag{9.3.7}$$

with λ the coupling constant. By considering that ξ_i is constant within a shell, λ is defined by equation 9.3.6 to

$$\lambda = \pm \frac{\xi}{2S}, \tag{9.3.8}$$

where the plus sign refers to less than half-filled shells and the minus sign refers to more than half-filled shells. Hence, the value and the sign of λ depend on the valence and the spin state of the ion, in contrast to the atomic value of ξ which is always positive. Hence, $\lambda > 0$ for shells filled less than half and $\lambda < 0$ for shells filled more than half. The energy of the electron state caused by LS coupling according to equation 9.3.7 can be calculated to

$$\hat{H}_{LS} = \lambda \mathbf{L} \cdot \mathbf{S} = \frac{\lambda}{2}(\mathbf{J}^2 - \mathbf{L}^2 - \mathbf{S}^2) = \frac{\lambda}{2} \cdot (J(J+1) - L(L+1) - S(S+1)). \tag{9.3.9}$$

The value of J can vary between $J = L+S, L+S-1, ..., |L-S|$. For dominant LS coupling the electron configuration, implying L and S, are given by Hund's rules.

9.3.3.3 Hund's rules

The classification of the ground state for certain electron configurations is an important aspect of solid state physics. The Hund's rules determine the filling of the corresponding atomic levels [145]. The rules apply to compounds with dominant LS coupling.

9.3.3.4 First Hund's rule

The total spin angular momentum of a shell will be maximized. Therefore, the first electrons in a shell will have the same spin angular momentum until the filling exceeds half the states.

9.3.3.5 Second Hund's rule

The second Hund's rule states that the total orbital angular momentum will be maximized. This means if the occupation according to the first Hund's rule leaves freedom for the orbital angular momentum, which is the case if the shell is not completely or half-filled, the states with large orbital angular momentum pointing in the same direction will be filled at first.

9.3.3.6 Third Hund's rule

The total angular momentum $\mathbf{J}$ is minimized if the shell is less than half-filled whereas it is maximized for a shell filled more than half. For a half-filled shell $\mathbf{J} = \mathbf{L} + \mathbf{S}$ gives the same result as $\mathbf{J} = |\mathbf{L} + \mathbf{S}|$, because the total orbital angular momentum is zero.

9.3.3.7 Hund's exchange

The Hund's exchange can be written in the mean-field approximation as

$$\hat{H}_H^{MF} = -J_H \sum 1/2 + 2S^z_{i\alpha} S^z_{i\beta}, \tag{9.3.10}$$

with J_H the Hund's exchange constant and $S^z_{i\alpha}$ the z-component of the spin of the electron at the site i with α and β referring to the orbital quantum number l_z.

9.3.4 LS coupling in t_{2g}

In the following we determine the ground state of the $4d^5$ and $5d^5$ state by considering only LS coupling in the t_{2g} level. We will apply the Hund's rules to obtain the electron configuration in the ground state. However, when, *e.g.*, the trigonal crystal field comes into play, the Hund's rules do not apply without loss of generality. In this case the Hamiltonian has to be solved, which we will sketch for LS coupling only.

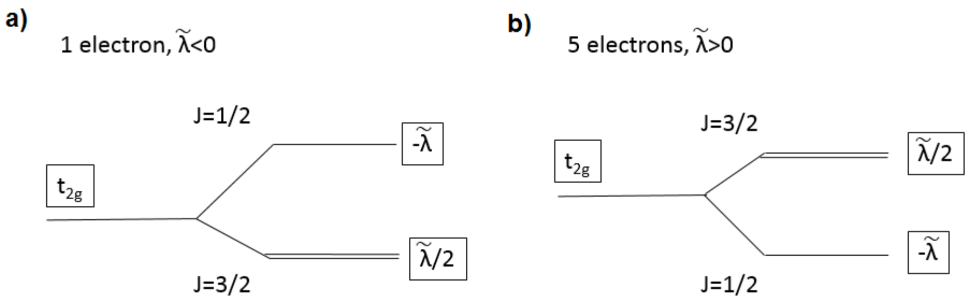

Figure 9.4: The energy levels for the eigenstates for one electron (a) and one hole (b) in the t_{2g} orbital under LS coupling.

9.3.4.1 Hund's rules in the t_{2g}

The orbital angular momentum l is not a good quantum number in the t_{2g} level. Therefore, it is convenient to characterize the t_{2g} states by the effective orbital angular momentum $\tilde{l}$ [134]. This yields the Hamiltonian for the t_{2g} level

$$\hat{H}_{SO}(t_{2g}) = \tilde{\lambda} \cdot \tilde{\mathbf{l}}\mathbf{S}, \tag{9.3.11}$$

with $\tilde{\lambda}$ the effective coupling constant. It has been shown that $\tilde{\lambda}$ is proportional to λ but with opposite sign [146]. Consequently, Hund's third rule changes to: for a shell less than half-filled $\tilde{\mathbf{J}}$ is maximized, while for a shell filled more than half the minimal $\tilde{\mathbf{J}}$ is favorable. For one electron in the t_{2g} level, $\tilde{L} = 1$ and $S = 1/2$, we find the total degeneracy of $(2\tilde{L} + 1)(2S + 1) = 6$. The SOC splits these states into a quartet with $\tilde{J} = \tilde{L} + S = 3/2$ and a doublet with $\tilde{J} = \tilde{L} - S = 1/2$. By considering $\tilde{\lambda} \propto -\lambda$ we find the quartet with $\tilde{J} = 3/2$ at $\tilde{\lambda}/2$ lying lower in energy than the doublet $\tilde{J} = 1/2$ at $-\tilde{\lambda}$, see figure 9.4a). The description is similar with one hole, respectively five electrons, in the t_{2g} shell, but $\tilde{\lambda}$ changes sign, since the shell is filled more than half. Accordingly, the single-hole state with $\tilde{J} = 3/2$ lies above the doublet with $\tilde{J} = 1/2$, see figure 9.4b).

9.3.5 Solving the Hamiltonian for LS coupling

The d^5 scenario with LS coupling is as simple as only one electron in the d orbital, since we can switch to the hole picture and do not have to consider electron-electron interactions or Hund's exchange. Hence, the Hamilton operator for SOC $\hat{H}_{ls}$ in the hole picture is

$$\hat{H}_{ls} = \lambda(\hat{l}_x\hat{s}_x + \hat{l}_y\hat{s}_y + \hat{l}_z\hat{s}_z). \tag{9.3.12}$$

The orbital wave functions, d_{xy}, d_{xz}, d_{yz} of the undistorted atom are chosen as the basis. The orbital angular momentum operators are $\hat{l}_x$, $\hat{l}_y$, and $\hat{l}_z$. Each of the operators is a 3 × 3 matrix. Its components are the orbital angular momenta of the orbitals in the basis of the three different orbitals. These three matrices are multiplied by the three spin matrices. After multiplying the matrices the three 6 × 6 matrices are added. The result is the full Hamilton operator

$$\hat{H}_{ls} = \begin{pmatrix} 0 & 0 & i & 0 & 0 & -1 \\ 0 & 0 & 0 & -i & 1 & 0 \\ -i & 0 & 0 & 0 & 0 & i \\ 0 & i & 0 & 0 & i & 0 \\ 0 & 1 & 0 & -i & 0 & 0 \\ -1 & 0 & -i & 0 & 0 & 0 \end{pmatrix} \times \frac{\lambda}{2}. \tag{9.3.13}$$

The basis **b** for this matrix is

$$\mathbf{b} = \begin{pmatrix} d_{yz}\uparrow & d_{yz}\downarrow & d_{xz}\uparrow & d_{xz}\downarrow & d_{xy}\uparrow & d_{xy}\downarrow \end{pmatrix}, \tag{9.3.14}$$

where the arrows denote the spin-up and spin-down state. The matrix can be separated due to Kramers degeneracy into two 3 × 3 matrices, each for one spin direction. The result are the two matrices

$$\hat{H}_1 = \begin{pmatrix} 0 & i & -1 \\ -i & 0 & i \\ -1 & -i & 0 \end{pmatrix} \times \frac{\lambda}{2}, \ \hat{H}_2 = \begin{pmatrix} 0 & -i & 1 \\ i & 0 & i \\ 1 & -i & 0 \end{pmatrix} \times \frac{\lambda}{2}. \tag{9.3.15}$$

To calculate the eigenstates, we perform a basis transformation. A smart choice is (t_+, t_-, z) with $t_\pm = \mp\frac{1}{\sqrt{2}}(d_{yz} \pm i d_{xz})$. The Hamilton in the new basis is given by,

$$\hat{H}' = \begin{pmatrix} t_+^* \\ t_-^* \\ z^* \end{pmatrix} \cdot \hat{H} \cdot \begin{pmatrix} t_+ & t_- & z \end{pmatrix} = \begin{pmatrix} -1 & 0 & 0 \\ 0 & 1 & -\sqrt{2} \\ 0 & -\sqrt{2} & 0 \end{pmatrix} \times \frac{\lambda}{2}. \tag{9.3.16}$$

To determine the eigenvalues, the determinant of the matrix is set to zero, yielding the eigenvalues $\lambda_{1/2} = -1$ and $\lambda_3 = 2$. The vectors that solve the equation $\hat{H}_{1/2}\mathbf{E}_i = \lambda_i \mathbf{E}_i$ are the eigenstates. For each Hamiltonian we determine three eigenstates

$$\begin{gathered} E_1 = |t_+\uparrow\rangle, \ E_2 = |t_-\downarrow\rangle, \ E_3 = \frac{1}{\sqrt{3}}|t_-\uparrow\rangle + \sqrt{\frac{2}{3}}|z\downarrow\rangle, \ E_4 = \frac{1}{\sqrt{3}}|t_+\downarrow\rangle + \sqrt{\frac{2}{3}}|z\uparrow\rangle, \\ E_5 = -\sqrt{\frac{2}{3}}|t_-\uparrow\rangle + \frac{1}{\sqrt{3}}|z\downarrow\rangle, \ E_6 = \sqrt{\frac{2}{3}}|t_+\downarrow\rangle - \frac{1}{\sqrt{3}}|z\uparrow\rangle. \end{gathered} \tag{9.3.17}$$

E_1 to E_4 have the energy $-\frac{\lambda}{2}$, while E_5 and E_6 have the energy λ. Two of the orbital wavefunctions are plotted in figure 9.5. The eigenstates in this basis correspond to the typically used eigenstates $|j, \ j_z\rangle$

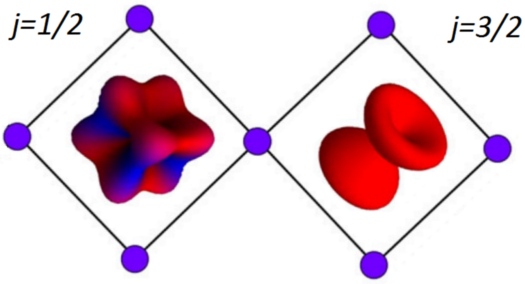

Figure 9.5: The orbital wave function of a $j = 1/2$ state on the left and a $j = 3/2$ state on the right. The color corresponds to the spin distribution. The figure is a modified version of figure 1 in reference [147]`https://doi.org/10.1103/PhysRevLett.116.106401` {DOI}. Copyright by American Physical Society (2016). Copyright by American Physical Society (2016).

$$\Psi_1 = \frac{1}{\sqrt{2}}(-|d_{yz}\uparrow\rangle - i|d_{xz}\uparrow\rangle) = |3/2,\ 3/2\rangle \tag{9.3.18}$$

$$\Psi_2 = \frac{1}{\sqrt{2}}(|d_{yz}\downarrow\rangle - i|d_{xz}\downarrow\rangle) = |3/2,\ -3/2\rangle \tag{9.3.19}$$

$$\Psi_3 = \frac{1}{\sqrt{3}}(\frac{1}{\sqrt{2}}(|d_{yz}\downarrow\rangle - i|d_{xz}\downarrow\rangle) + \sqrt{2}|d_{xy}\uparrow\rangle) = |3/2,\ 1/2\rangle \tag{9.3.20}$$

$$\Psi_4 = \frac{1}{\sqrt{3}}(\frac{1}{\sqrt{2}}(-|d_{yz}\uparrow\rangle - i|d_{xz}\uparrow\rangle) + \sqrt{2}|d_{xy}\downarrow\rangle) = |3/2,\ -1/2\rangle \tag{9.3.21}$$

$$\Psi_5 = \frac{1}{\sqrt{3}}(-|d_{yz}\downarrow\rangle + i|d_{xz}\downarrow\rangle + |d_{xy}\uparrow\rangle) = |1/2,\ 1/2\rangle \tag{9.3.22}$$

$$\Psi_6 = \frac{1}{\sqrt{3}}(-|d_{yz}\uparrow\rangle + i|d_{xz}\uparrow\rangle + |d_{xy}\downarrow\rangle) = |1/2,\ -1/2\rangle. \tag{9.3.23}$$

The Hamilton $\hat{H}_{t2g}$ in the basis $|j,\ j_z\rangle$

$$\begin{pmatrix} |1/2,\ \ 1/2\rangle^* \\ |1/2,-1/2\rangle^* \\ |3/2,\ \ 3/2\rangle^* \\ |3/2,-3/2\rangle^* \\ |3/2,\ \ 1/2\rangle^* \\ |3/2,-1/2\rangle^* \end{pmatrix} \hat{H}_{t2g} \begin{pmatrix} |1/2,\ \ 1/2\rangle \\ |1/2,-1/2\rangle \\ |3/2,\ \ 3/2\rangle \\ |3/2,-3/2\rangle \\ |3/2,\ \ 1/2\rangle \\ |3/2,-1/2\rangle \end{pmatrix}^{-1} = \begin{pmatrix} 1 & 0 & 0 & 0 & 0 & 0 \\ 0 & 1 & 0 & 0 & 0 & 0 \\ 0 & 0 & -\frac{1}{2} & 0 & 0 & 0 \\ 0 & 0 & 0 & -\frac{1}{2} & 0 & 0 \\ 0 & 0 & 0 & 0 & -\frac{1}{2} & 0 \\ 0 & 0 & 0 & 0 & 0 & -\frac{1}{2} \end{pmatrix} \lambda. \tag{9.3.24}$$

In summary, the ground state for one hole in the t_{2g} orbitals is described by $j_{\text{eff}} = 1/2$ and in the excited state by $j_{\text{eff}} = 3/2$. Hence, the five-electron ground state exhibits a local $j_{eff} = 1/2$ moment and an excited state exhibits a local $j_{\text{eff}} = 3/2$ moment. The transition from the hole picture to the electron picture is discussed in detail below.

9.3.6 Hole picture and electron picture

When we switch from one-hole picture to five-electron picture in the t_{2g} level we have to be careful. The hole states are described by $|j,\ j_z\rangle$. In the ground state with $j_{\text{eff}} = 1/2$ the wave function of the single hole can be described by either $|1/2, 1/2\rangle$ or $|1/2, -1/2\rangle$. In the excited state $j_{\text{eff}} = 3/2$ the wave function of the hole can be described by one of the orbital wave functions $|3/2, 3/2\rangle$, $|3/2, 1/2\rangle$, $|3/2, -1/2\rangle$, or $|3/2, -3/2\rangle$. In the ground state $j_{\text{eff}} = 1/2$ the d^5 configuration can as well be described by the five electrons. However, the electrons do not occupy the single-hole states, but single-electron states which are described by $|l_z,\ s_z\rangle$, $|\pm1, \pm1/2\rangle$, $|\mp1, \pm1/2\rangle$, $|0, \pm1/2\rangle$, which have no energy difference. However, this is not analog to filling the single-hole levels with electrons and describe the $j_{\text{eff}} = 1/2$ ground state by four electrons in the $j_{\text{eff}} = 3/2$ state and one electron in the $j_{\text{eff}} = 1/2$. First off all the $|j,\ j_z\rangle$ states are single-holes states, therefore they can only be occupied by holes. Additionally, the filling of these levels by electrons suggests that for d^1 to d^6 configurations the states are identical, which is clearly not the case, due to Hund's exchange and electron-electron interaction. One could argue that the filling of single-hole states by electrons is only possible in the d^5 configuration, but this is wrong as well, because the single-hole states have an energy difference of $3/2\lambda$. By filling the single-hole states, the d^5 state would be described by four electrons occupying the energetically favorable states $|3/2, 3/2\rangle$, $|3/2, 1/2\rangle$, $|3/2, -1/2\rangle$, and $|3/2, -3/2\rangle$ and one electron in the energetically unfavorable states either $|1/2, 1/2\rangle$ or $|1/2, -1/2\rangle$. Actually, this picture is often used, *e.g.*, when the insulating behavior of the spin-orbit-entangled Mott insulator is explained. But it actually is wrong. The d^5 state consists of a linear combination of $|l_z,\ s_z\rangle$ states. These states have no energy difference. However, the linear combination of states with L and S summing up to $j_{\text{eff}} = 1/2$ is lower in energy than the linear combination yielding $j_{\text{eff}} = 3/2$.

For the d^4 configuration the physics can be described in the hole picture as well, although we cannot avoid the electron-electron interaction or the hole-hole interaction, respectively. In return the idea of filling two-hole states by electrons becomes more absurd. A brief sketch of the calculations can be found in the appendix V, for details see [137]

9.3.7 Hopping

Now, we apply the gained information concerning the eigenstates to calculate the hopping between d^5 ions in edge sharing octahedra of ligands. This situation is characterized by one hole in the t_{2g}. The Heisenberg exchange is proportional to the square of the hopping integral t divided by the on site Coulomb repulsion U. The hopping integral corresponds to the overlap of the wave functions, lowering the kinetic energy. We consider three exchange paths for the ions in edge sharing octahedra. The most obvious is the direct exchange from ion to ion, see figure 9.6. However, this exchange path is strongly suppressed due to the large distance of the ions, going along with a small overlap integral of the electronic wave functions of both ions. The second and third exchange path are mirror symmetric. They couple the ions via p_z orbital of the ligands in between the two ions. These paths are favored,

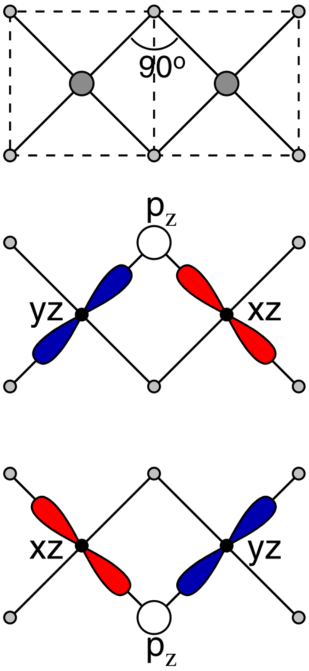

Figure 9.6: Edge-sharing octahedra form 90°-bonds. The orbitals along the bond direction coupling via the Ir atoms O atoms. The two different paths are shown in the middle and lower sketch. Figure has been taken from reference [148]. `https://doi.org/10.1103/PhysRevLett.102.017205` {DOI}. Copyright by American Physical Society (2009).

since the d_{yz} and d_{xz} orbitals, which are partly occupied by the hole in the $j_{\text{eff}} = 1/2$ ground state, extend along these directions, see figure 9.6. From the first atom hopping via the d_{yz} orbital to the d_{xz} orbital of the second atom is likely due to the overlap with the p_z orbital of the ligand. The same probability has the hopping via the d_{xz} orbital of the first atom to the d_{yz} orbital of the second atom, see figure 9.6. However, the paths interfere destructively for the $j_{\text{eff}} = 1/2$ ground state. The mathematical formulation of this problem can be made by determining the hopping matrix. At first we determine the hopping amplitude for the hopping of one hole to the next neighbor ions t_{eff}. The amplitude is the product of the amplitude for hopping to the ligand and from there to the second ion. With the charge transfer gap Δ_{CT} the effective hopping amplitude can be approximated as

$$t_{\text{eff}} = \frac{t^2}{\Delta_{CT}}. \tag{9.3.25}$$

The symmetry of the orbitals that are involved in the hopping process are taken into account by the hopping operator $\hat{T}$ connecting neighboring ion and ligand orbitals. The transfer matrix from the state γ to the state γ' via the ligand p_z orbital can be written as

$$\tau_z^{\gamma,\gamma'} =_{\gamma} \langle J, J_z|\hat{T}|p_z\rangle\langle p_z|\hat{T}|J, J_z\rangle_{\gamma'}. \tag{9.3.26}$$

In the following we will explicitly calculate the hopping between the d^5 ground state $\langle 1/2,\ 1/2| = -\frac{1}{\sqrt{3}}\left(\langle d_{yz},\downarrow| - i\langle d_{xz},\downarrow| + \langle d_{xy},\uparrow|\right)$ via the ligand p_z orbital, see figure 9.6. For the upper path in figure 9.6 the transfer matrix $\tau_1^{1,1}$ can be written as

$$\tau_{z,1}^{1,1} = \frac{-1}{\sqrt{3}}\langle d_{yz}|\hat{T}|p_z\rangle \frac{i}{\sqrt{3}}\langle p_z|\hat{T}|d_{xz}\rangle = \frac{-i}{3}. \tag{9.3.27}$$

To obtain the hopping matrix element we need to multiply the result with the effective hopping amplitude, but at first we need to consider the second path via the lower oxygen atom. The transfer matrix for the second path can be written as

$$\tau_{z,2}^{1,1} = \frac{-i}{\sqrt{3}}\langle d_{xz}|\hat{T}|p_z\rangle \frac{-1}{\sqrt{3}}\langle p_z|\hat{T}|d_{yz}\rangle = \frac{i}{3}. \tag{9.3.28}$$

The matrix element $\hat{J}^{1,1}$ describing the hopping between the ions in the groundstate $\langle \Phi_1| = -\frac{1}{\sqrt{3}}\left(\langle d_{yz},\downarrow| - i\langle d_{xz},\downarrow| + \langle d_{xy},\uparrow|\right)$ with

$$\hat{J}^{1,1} = t_{\text{eff}}\left(\tau_{z,1}^{1,1} + \tau_{z,2}^{1,1}\right) = 0. \tag{9.3.29}$$

This result means that the hopping from the $j = 1/2$ state into the $j = 1/2$ state via the two oxygen atoms is forbidden since both paths cancel. Therefore, the Heisenberg interaction has vanished, which is sought-after for realizing the Kitaev model, see section 9.3.8.

The other elements of the hopping matrix $\hat{J}$ can be calculated in the same way. The result is given by

$$\hat{J} = t_{\text{eff}} \cdot -\frac{2i}{\sqrt{6}} \begin{pmatrix} 0 & 0 & 0 & 0 & 0 & 1 \\ 0 & 0 & 1 & 0 & 0 & 0 \\ 0 & -1 & 0 & 0 & \frac{1}{\sqrt{2}} & 0 \\ 0 & 0 & 0 & 0 & 0 & \frac{1}{\sqrt{2}} \\ 0 & 0 & -\frac{1}{\sqrt{2}} & 0 & 0 & 0 \\ -1 & 0 & 0 & -\frac{1}{\sqrt{2}} & 0 & 0 \end{pmatrix} A_1, \tag{9.3.30}$$

where $A_1 = (|1/2, 1/2\rangle,\ |1/2, -1/2\rangle,\ |3/2, 3/2\rangle,\ |3/2, 1/2\rangle,\ |3/2, -1/2\rangle,\ |3/2, -3/2\rangle)$. In summary a d^5 insulator with strong SOC and edge-sharing octahedra exhibits hopping only between certain states. Namely, hopping between the states $|1/2, 1/2\rangle$ and $|3/2, -3/2\rangle$ and between $|3/2, -3/2\rangle$ and $|3/2, 1/2\rangle$. Additionally, hopping from $|1/2, -1/2\rangle$ to $|3/2, 3/2\rangle$ to $|3/2, -1/2\rangle$ and vice versa is allowed.

In conclusion, we have calculated the eigenstates in the presence of cubic crystal field, trigonal crystal field, and SOC, which enables us to judge depending on the values of the corresponding energy contributions whether the $j_{\text{eff}} = 1/2$ and the $j_{\text{eff}} = 3/2$ picture is a good approximation. Furthermore, we estimated the influence of deviations from the $j_{\text{eff}} = 1/2$ and the $j_{\text{eff}} = 3/2$ states on their energy separation. These calculations show that coupling of the $j_{\text{eff}} = 1/2$ and the $j_{\text{eff}} = 3/2$ is the dominant hopping process. Hence, a double spin-orbit excitation can be excited by hopping, while Heisenberg exchange is forbidden, see figure 9.7.

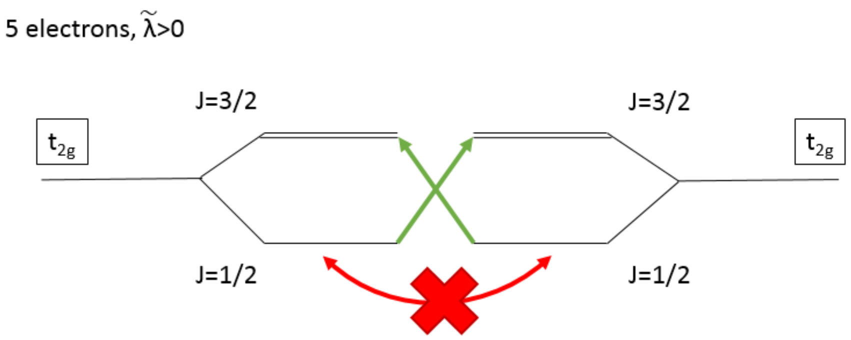

Figure 9.7: Double spin-orbit exciton caused by hopping (green arrows), while the Heisenberg exchange is forbidden (red arrow).

9.3.8 Kitaev coupling

The basis for Kitaev materials are bond-directional interactions, which are Ising like. In 2005 Khaliullin described the macroscopic foundations for bond-directional interaction [149], before in 2009 Khaliullin and Jackeli linked these bond-directional interactions with the Kitaev model [150] and suggested A_2BO_3 (where A and B are alkali and transition metal ions, respectively), as promising candidates for realizing the Kitaev model [148]. They realized that the orientation of neighboring octahedra is important to describe the exchange of the local moment of the metal ion, classified by the B-O-B bond geometry. The single bond for corner sharing octahedra is referred to as 180° bond, while the edge sharing octahedra exhibit 90° bonds. The 180° bond geometry is characterized by Heisenberg exchange. In contrast to the 90° bond geometry, for which the symmetric Heisenberg term is suppressed, due to destructive interference of the two exchange paths. In the absence of the Heisenberg exchange the dominant coupling becomes a directional, Ising-type coupling, based on Hund's rule [148, 149]. Its strength is given by

$$-\frac{8t^2 J_H}{3U^2} S_1^\gamma S_2^\gamma, \tag{9.3.31}$$

where $\gamma = x, y, z$ is the single spin component of the spin matrix S_i at the site i.

The Hamiltonian obtained by *ab initio* calculations, describes the coupling of $j_{\text{eff}} = 1/2$ moments by considering, besides the Kitaev coupling, isotropic Heisenberg coupling and off-diagonal exchange [151, 152].

9.3.8.1 Pure Kitaev model

In the pure Kitaev model only the Kitaev coupling is present. In this case, the bond directional interactions cannot be simultaneously satisfied, leading to a strong exchange frustration, see figure 9.8. This frustration ends up in a gapless quantum spin-liquid for the ground state. In case the Kitaev coupling along one bond direction is dominant, the ground

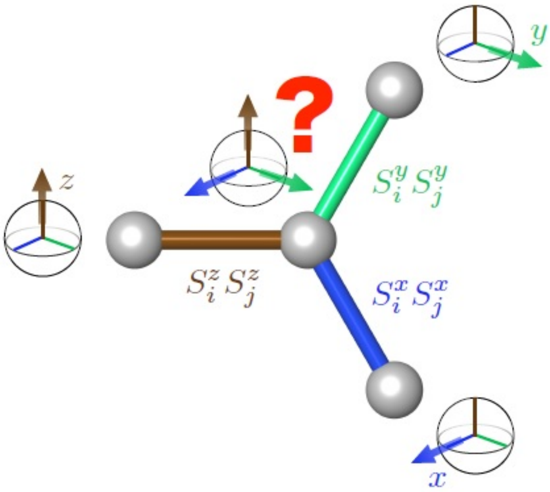

Figure 9.8: The different spin components couple via different bonds (indicated by the colors of the bonds), leaving the spin frustrated, which builds the basis for Kitaev coupling. Figure has been taken from reference [153]. Copyright by Macmillan Publishers Limited (2015)

state becomes a gapped quantum spin-liquid. Furthermore, the Kitaev model is exactly, analytically solvable [150], which reveals the existence of Majorana fermions in the Kitaev model. A detailed review on Kitaev physics has been published by Prof. Trebst [153].

9.3.8.2 Heisenberg-Kitaev model

Closer to the experimental situation is the Heisenberg-Kitaev model, since it considers Heisenberg exchange, which is present as soon as the $j_{\mathrm{eff}} = 1/2$ states are not pure. It exhibits frustrated local moments as well. However, besides the spin-liquid phases around the pure Kitaev limit, the model exhibits four phases, depending on the relative coupling strength $K = \cos\phi$, for Kitaev coupling and $J = \sin\phi$ for Heisenberg exchange, see figure 9.9.

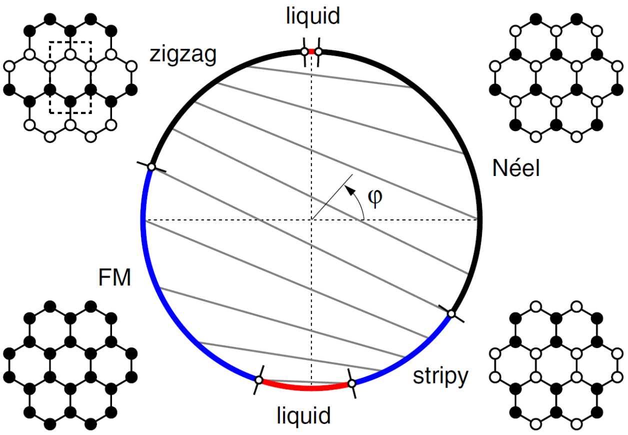

Figure 9.9: Phase diagram of the Kitaev Heisenberg model with the coupling strength $K = \cos\phi$, for Kitaev coupling and $J = \sin\phi$ for Heisenberg exchange. Figure has been taken from reference [154]`https://doi.org/10.1103/PhysRevLett.110.097204` {DOI}. Copyright by American Physical Society (2013).

Chapter 10

Results on spin-orbit-entangled Mott insulators

Two candidates for realizing the Kitaev model are investigated in this chapter, $\alpha-\mathrm{RuCl}_3$ and $\mathrm{Na}_2\mathrm{IrO}_3$, see section 9.3.8. For both materials the existence of the local $j_{\mathrm{eff}} = 1/2$ ground state is questioned. We investigate the optical spectrum and identify different excitations, thereby gaining insight into the underlying physics. In $\alpha-\mathrm{RuCl}_3$ we proof the local $j_{\mathrm{eff}} = 1/2$ moments by observation of the spin-orbit exciton. Furthermore, we reveal double and triple spin-orbit excitons. In $\mathrm{Na}_2\mathrm{IrO}_3$ we find evidence for the local $j_{\mathrm{eff}} = 1/2$ scenario by obtaining the strong suppression of the lowest electron-hole excitation. Additionally, we obtain signatures in the optical data of a controversially discussed peak obtained by RIXS.

10.1 $4d^5$ Mott insulator α-RuCl$_3$

The single crystal α-RuCl$_3$[1] is build of weakly bound layers of edge-sharing RuCl$_6$ octahedra with central Ru^{+3} ions on an almost perfect honeycomb lattice, see figure 10.1. Transport measurements in 1971 suggested that this material is a conventional semiconductor [156]. However in 1996 data obtained by optical spectroscopy indicated the formation of a Mott insulator [157]. Eventually, in 2014 Plumb *et al.* claimed that SOC plays an important role for the electronic structures in α-RuCl$_3$ [142]. $\alpha-\mathrm{RuCl}_3$ has been predicted to be a promising candidate for realizing the Kitaev model forming a spin-liquid in the ground state [148], for details on Kitaev physics see section 9.3.8. The SOC in $4d$ material is weaker than in $5d$ materials like $\mathrm{Na}_2\mathrm{IrO}_3$, although its symmetry is close to cubic [155, 158, 159], causing little mixing between the $j_{\mathrm{eff}} = 1/2$ and the $j_{\mathrm{eff}} = 3/2$ state, which is essential for realizing the spin-liquid. However, $\alpha-\mathrm{RuCl}_3$ exhibits at low temperature zigzag magnetic order, see figure 10.2 [155, 158, 160, 161]. Nevertheless, this material shows signatures of a spin-liquid,

---

[1] The single crystals of α-RuCl$_3$ investigated in this thesis have been synthesized by Prof. Dr. Becker-Bohatý and Prof. Dr. Bohatý of the Institute of Geology and Mineralogy, Section of Crystallography, University of Cologne

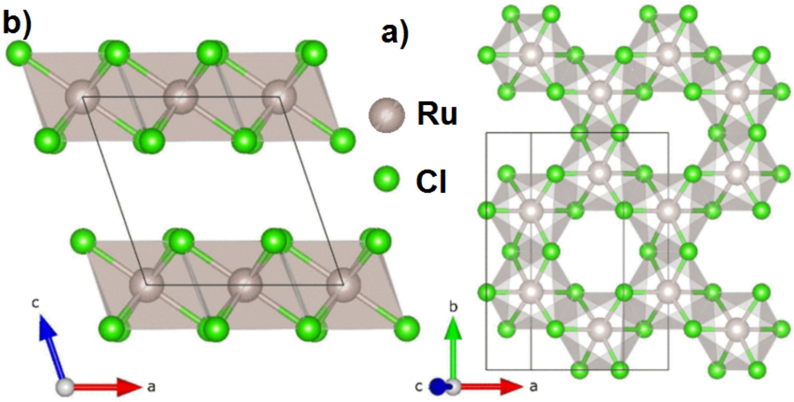

Figure 10.1: Crystal structure of $\alpha-$RuCl$_3$ along two different directions. Figure has been taken from reference [155]`https://doi.org/10.1103/PhysRevB.92.235119` {DOI}. Copyright by American Physical Society (2015).

such as a broad continuum of magnetic excitations identified in Raman scattering [143] and inelastic neutron scattering measurements [161]. When a magnetic field is applied $\alpha-$RuCl$_3$ undergoes several phase transitions [155, 162, 163]. Lately, the high-field phase in which no magnetic ordering is present has attracted great attention [155, 162–164]. Furthermore, $\alpha-$RuCl$_3$ exhibits a structural phase transition around 150 K from monoclinic at high-temperature to a rhombohedral at low-temperatures, with a strong hysteresis [162, 165, 166]. A controversially discussed alternative to a ground state defined by local j_{eff} moments are quasi-molecular orbitals [167, 168]. According to this scenario the electrons delocalize over the hexagon. However, Kim *et al.* state, based on numerically exact diagonalization analysis of the three-band Hubbard model, that in α-RuCl$_3$ the strength of the SOC together with the Coulomb repulsion causes the formation of local $j_{\text{eff}} = 1/2$ moments [168]. This is supported by the large Coulomb repulsion estimated by photoemission and inverse photoemission spectroscopies [144, 169]. Additionally, the magnetic moment of $2.2\,\mu_B$ determined by Curie-Weiss fits to the magnetic susceptibility supports the scenario of local $j_{\text{eff}} = 1/2$ moments [170].

However, it is not clear how large the mixing of the $j_{\text{eff}} = 1/2$ and the $j_{\text{eff}} = 3/2$ states is and whether it is sufficiently small to realize the Kitaev physics. In this context the observation of the spin-orbit exciton plays an important role, since it reveals the mixing of $j_{\text{eff}} = 1/2$ and $j_{\text{eff}} = 3/2$ states.

In order to determine the trigonal splitting it is essential to determine the SOC strength λ. In literature different values for λ have been reported. Even the size of the charge-transfer gap is under discussion with estimates ranging from 0.2 to 1.2 eV [142, 144, 156, 157, 171, 172]. Lately, the excitation located at 1.2 eV with an onset at 1 eV has been widely accepted as charge-transfer gap due to optical spectroscopy [171], electron energy loss spectroscopy [144], ARPES [172], and numerically exact diagonalization analysis of the three-band Hubbard model [168].

The atomic SOC strength is $\lambda \approx 150$ meV for ruthenium [173, 174]. The observation of the

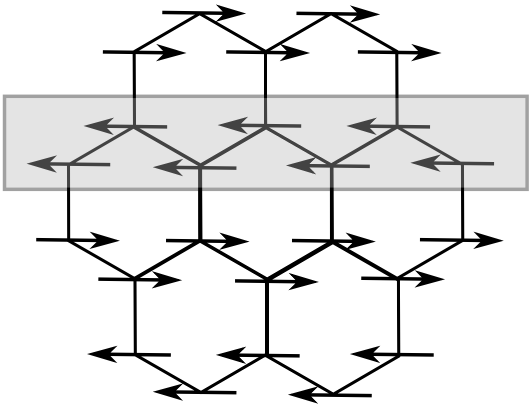

Figure 10.2: The orientation of local moment in zigzag order. The gray area marks the neighboring atoms with same orientation of the local moments.

spin-orbit exciton by Raman spectroscopy has been claimed by Sandilands *et al.* [171] at an energy of $E_{SO} \approx 145\,\text{meV}$, see figure 10.3a. Since it appears at $3/2\lambda$, see section 9.3.3, for $\Delta_{\text{tri}} = 0$, it implies $\lambda \approx 97\,\text{meV}$. However, the spin-orbit exciton couples to phonons [147], hence a broader peak is expected. Furthermore, this interpretation contradicts the quantum chemistry calculations by Yadav *et al.* [175], who estimated the spin-orbit exciton at 195 and 234 meV, considering a small trigonal crystal field. In neutron scattering data an excitation at $195\pm11\,\text{meV}$ was observed, which was also attributed to the spin-orbit exciton by Banerjee *et al.* [62], see figure 10.3b. This value matches the lower value reported by Yadav *et al.* [175]. Nevertheless, the upper excitation at 234 meV was not reported and the fit is questionable. It results in $\lambda = 130\,\text{meV}$. Furthermore, Sandilands *et al.* report on absorptions from $200 - 800\,\text{meV}$ which have as well been observed in optical spectroscopy data by Plumb *et al.* [142], see inset of figure 10.4. Plumb *et al.* [142] and Sandilands *et al.* [171] attribute the absorption to excitations from the t_{2g} to the e_g levels. A similar interpretation has been given by Reschke *et al.* on the basis of optical reflectance and transmittance data on $\alpha-$RuCl$_3$ [165]. These interpretations of the data imply a strong mixing between the t_{2g} and the e_g levels, due to the small distance in energy, which means that Kitaev coupling is not dominant. However, quantum chemistry calculations by Yadav *et al.* have predicted that the excitations from the t_{2g} to the e_g levels cost more than 1.3 eV.

10.1.1 Optical data on single-crystalline α-RuCl$_3$

In the following we will present our transmission data on single-crystalline α-RuCl$_3$ and attribute the excitations between 200-800 meV to the single, double, and triple spin-orbit exciton.

Our measurements are preformed on single crystals with a typical area of $1 \times 1\,\text{mm}$. The

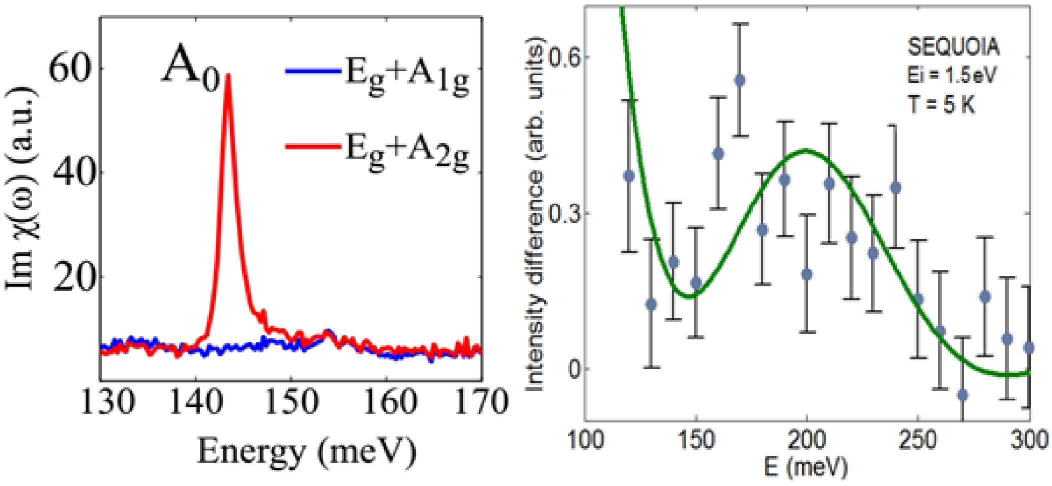

(a)

(b)

Figure 10.3: A) Raman susceptibility Im(χ) versus energy for two polarization channels at 10 K. Figure has been taken from reference [171]`https://doi.org/10.1103/PhysRevB.93.075144` {DOI}. Copyright by American Physical Society (2016). B) Intensity difference between data integrated over the ranges $Q = [2.5, 4.0]$ Å and $[4.5, 6.0]$ Å versus energy determined by inelastic neutron scattering at 5 K. The green line is a fit taking a background plus a Gaussian peak centered at 195±11 meV with a width of 48±6 meV into account. Figure has been taken from reference [161]`https://doi.org/10.1038/NMAT4604` {DOI}. Copyright by Macmillan Publishers Limited (2016).

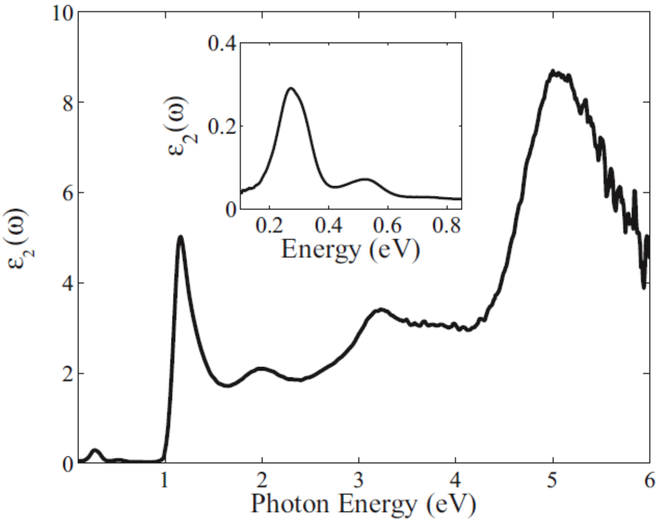

Figure 10.4: Imaginary part of the dielectric function, ϵ_2, versus the energy determined by optical spectroscopy. The inset shows a closeup of the spectrum at the supposed spin-orbit exciton. Figure has been taken from reference [142]`https://doi.org/10.1103/PhysRevB.90.041112` {DOI}. Copyright by American Physical Society (2014).

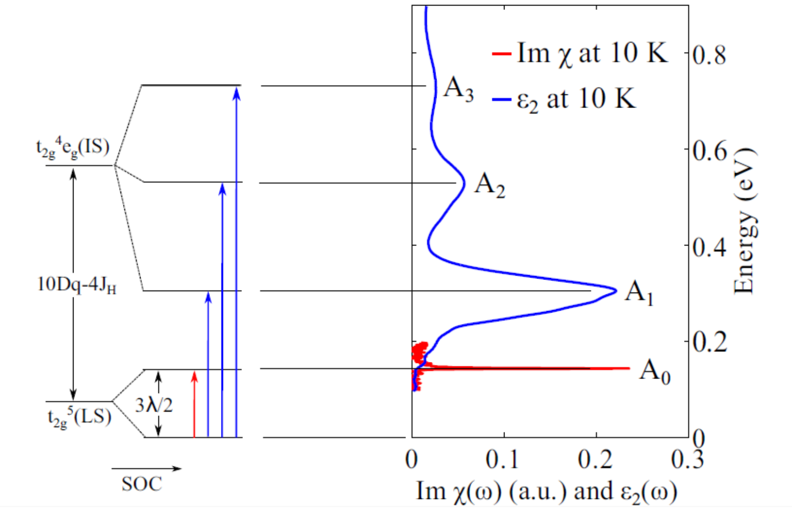

Figure 10.5: Orbital excitations in $\alpha-$RuCl$_3$ according to Sandilands *et al.*. At the left the energy of the spin configurations is sketched. The levels are matched to the energy of the absorptions observed with optical spectroscopy, which is plotted versus ϵ_2. Additionally, the energy of the Raman mode versus susceptibility Im(χ) is plotted. Figure has been taken from reference [171]`https://doi.org/10.1103/PhysRevB.93.075144` {DOI}. Copyright by American Physical Society (2016).

transmittance measurements are performed on a single crystal of the thickness 28 μm[2].

10.1.1.1 Raman mode at 145 meV

The Raman mode, reported as spin-orbit exciton by Sandilands *et al.* [171], vanishes with increasing temperature, see figure 10.6[3]. This temperature dependence is not expected for the spin-orbit exciton. The temperature dependence suggests that the excitation is related to an impurity level.

10.1.1.2 Fourier spectroscopy on α-RuCl$_3$

In order to determine the origin of the absorptions between 200 − 800 meV, we performed temperature-dependent transmittance measurements in the MIR range, see figure 10.7.

10.1.1.3 Reflectance

To directly compare the data to the spectra reported in literature we determine the dielectric constant $\epsilon(\omega)$ from the inversion of the reflectance and transmittance, see section 5.1. The size of the crystal hinders us from measuring the reflectance. Even, much larger and thicker crystals do not allow to measure a reasonable reflectance, as data reported by Reschke *et*

---

[2] The crystals have been synthesized by Prof. Dr. Becker-Bohatý and Prof. Dr. Bohatý of the Institute of Geology and Mineralogy, Section of Crystallography, University of Cologne

[3] The Raman data was measured by S. Kaul and Dr. Köthe in the group of Prof. v. Loosdrecht in the Department of Physics of the University of Cologne.

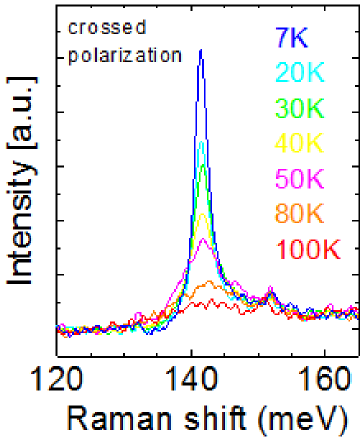

Figure 10.6: Temperature-dependent intensity versus Raman shift[4].

al. [165] show, see figure 10.8. In the frequency range above the phonon, where the refractive index approaches a constant, the reflectance for 5 K is supposed to be about 60 % of the reflectance at 120 K. This translates to a change of the refractive index by about 70 %. However, this can hardly be explained and our transmittance data show that it is wrong. Therefore, we determine the reflectance from the fringes in the transmittance, see inset in figure 10.7.

10.1.1.4 Refractive index

The determined temperature-dependent refractive index is plotted in figure 10.9. The refractive index changes in the measured frequency range up to 2 % as function of temperature, which strongly contradicts the change of the reflectance of 40 % reported by Reschke *et al.* [165]. A close view reveals a bisection in the refractive index between $n(T)$ for $T \leq 150\,\mathrm{K}$ and $T > 150\,\mathrm{K}$. This is manifested in the position of the maxima, see inset figure 10.7. It coincides with the observed structural phase transition [162, 165, 166]. With the refractive index we can determine the reflectance in the transparent frequency range precisely and with that $\sigma_1(\omega)$, respectively, $\epsilon_2(\omega)$.

10.1.1.5 Temperature-dependent spectral weight

The resulting $\sigma_1(\omega)$ and $\epsilon_2(\omega)$ are plotted in figure 10.10a and 10.10b. The three peaks reported by Sandilands *et al.* are present in our spectrum as well. The temperature dependence shows that the weight of the first peak increases with temperature which indicates a phonon-assisted process. Therefore, $\sigma_1(\omega)$ of the peak can be separated into $\sigma_1'(\omega - \omega_0)$, for the excitation plus the creation of a phonon, and $\sigma_1''(\omega + \omega_0)$, for the excitation plus the absorption of a phonon, with ω_0 the eigenfrequency of the phonon. The probability for

---

[4] The Raman data was measured by S. Kaul and Dr. Köthe in the group of Prof. v. Loosdrecht in the Department of Physics of the University of Cologne.

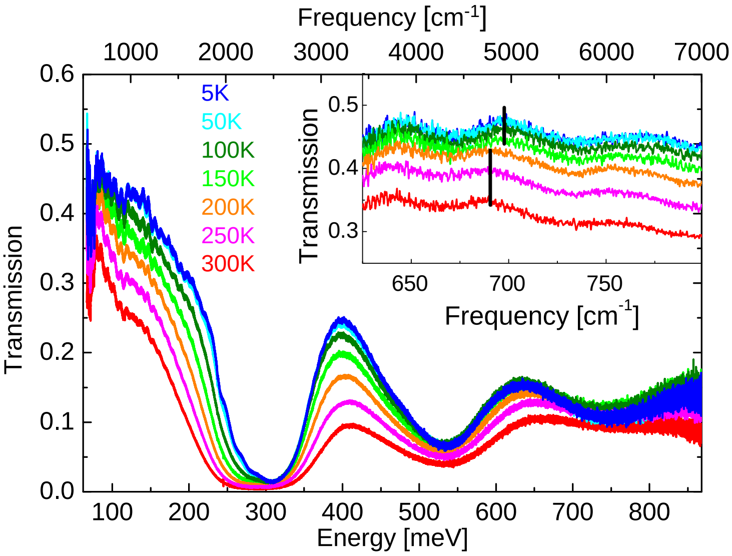

Figure 10.7: Temperature-dependent transmittance of the 28 μm thick $\alpha-$RuCl$_3$ sample. Inset: Closeup of the temperature-dependent transmittance. Black bars approximately represent the position of the maxima.

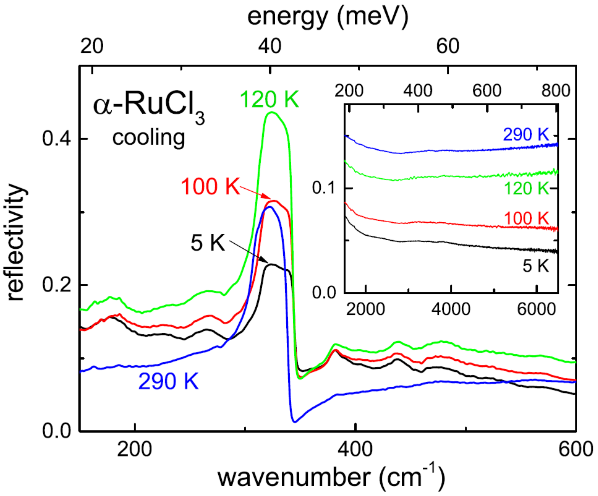

Figure 10.8: Temperature-dependent reflectance of $\alpha-$RuCl$_3$ reported by Reschke *et al.* Inset shows reflectance from 1500 cm^{-1} to 6500 cm^{-1}. Figure is a reprint of Fig. 1 in reference [165]`https://doi.org/10.1103/PhysRevB.96.165120` {DOI}. Copyright by American Physical Society (2017).

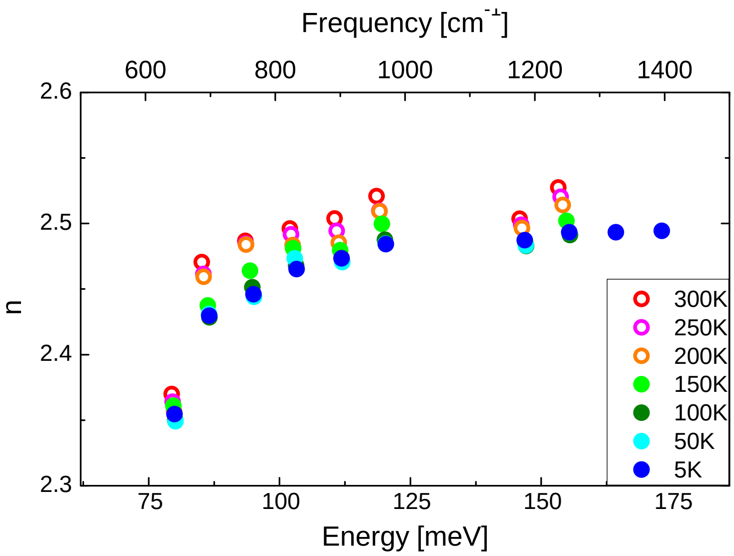

Figure 10.9: Temperature-dependent refractive index determined from the fringes in the transmittance.

each process depends on the occupation number of the phonons $\langle n(T)\rangle$ which is given by the Bose-Einstein distribution

$$\langle n(T)\rangle = \frac{1}{\exp \hbar\omega_0/k_B T - 1}. \tag{10.1.1}$$

The probability for the excitation in combination with the creation of a phonon is increasing with $\langle n(T)\rangle + 1$, while the probability in combination with the absorption of a phonon is increasing with $\langle n(T)\rangle$ [176, 177]. Therefore, the temperature dependence of the spectral weight can be written as

$$\int \sigma_1(\omega)\, d\omega = A + B \coth(\hbar\omega_0/2k_B T), \tag{10.1.2}$$

where A and B are fitting constants, in agreement with reference [171, 178]. We find a phonon energy for the first peak of 25 meV and for the second peak of 40 meV, while the third peak is almost independent of temperature, see figure 10.11. Both energies are in the typical energy range for phonons in $\alpha-$RuCl$_3$, see figure 10.12.

10.1.2 Spin-orbit exciton

We find the maxima of the three peaks below the charge transfer gap for 300 K at about $E_1 = 270\, meV$, $E_2 = 529\, meV$, and $E_3 = 741\, meV$. By taking the phonon energies into account, we find that the three peaks are separated by about 250 meV. The first excitation is at $\approx 250 + 25$ meV, the second excitation at $\approx 2 \cdot 250 + 40$ meV, and the third excitation at $\approx 3 \cdot 250$ meV. We can exclude that these peaks correspond to excitations from the t_{2g}

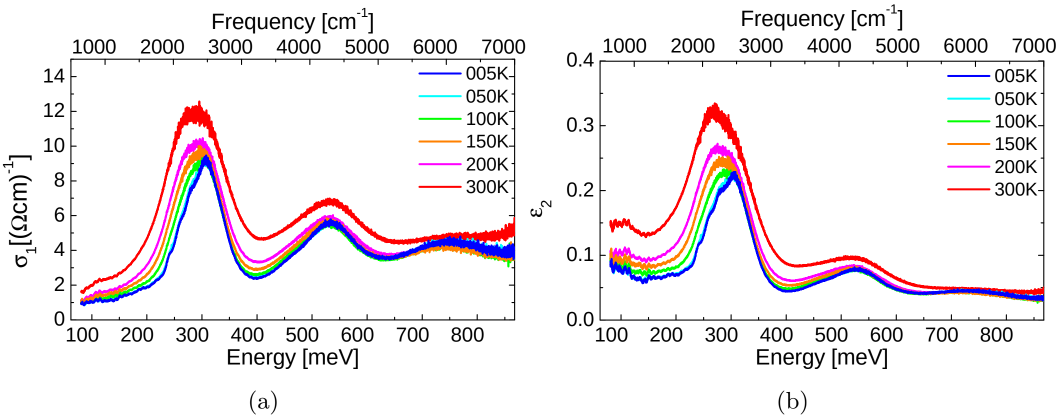

Figure 10.10: a) Temperature dependent $\sigma_1(\omega)$ b) Same data plotted as ϵ_2.

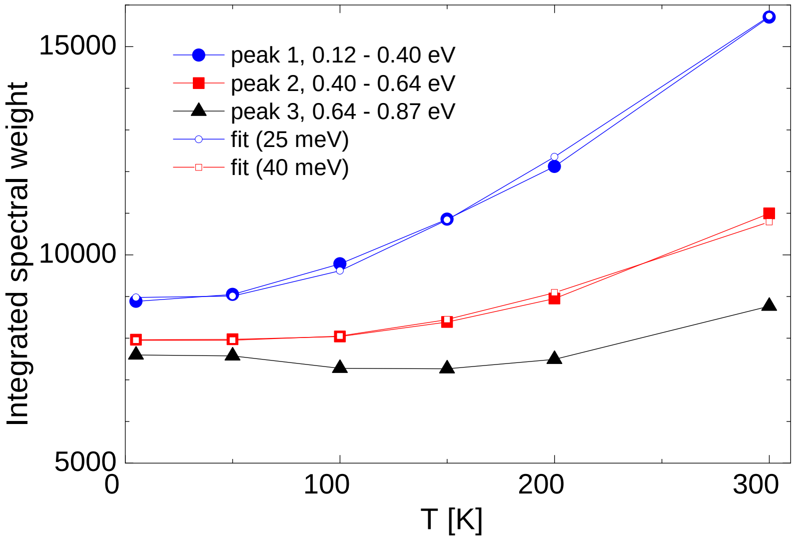

Figure 10.11: Spectral weight of the three peaks as function of temperature. From the fit to the spectral weight (line with open symbols) of the first (second) peak a phonon energy of 25 meV (40 meV) is obtained. The third peak hardly shows a temperature-dependent spectral weight.

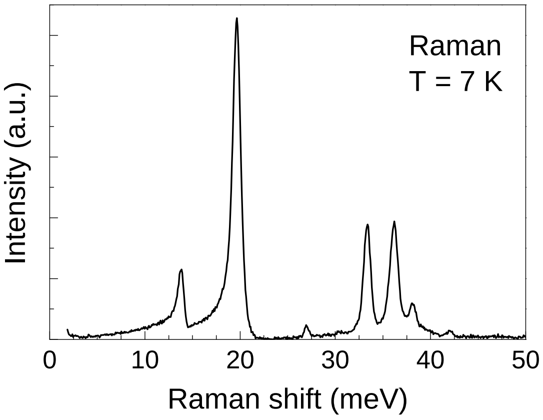

Figure 10.12: Raman spectrum of $\alpha-\mathrm{RuCl}_3$ at 7 K showing phonon modes.

into the e_g levels, since these excitations are expected for energies above 1.3 eV, see section 10.1. Additionally, we pointed out, that the excitation at 145 meV is not the spin-orbit exciton and addressing the spin-orbit exciton to the neutron data is questionable [161]. Furthermore, magnetic excitations are located below 15 meV [179] and phonons are located below 70 meV [165]. Therefore, the only possible explanation for the excitations are orbital excitations in the t_{2g} level. In the presence of dominant SOC theses intra-band excitations correspond to the spin-orbit exciton. We claim that the three excitations correspond to single, double, and triple spin-orbit excitons. This interpretation raises the questions, why we can see these excitations and why the weight of the higher order spin-orbit excitons is that large compared to the first-order spin-orbit exciton?

10.1.2.1 Symmetry breaking

Phonons are needed to break the symmetry of the $d-d$ excitation which is parity forbidden. The phonon energies differ, since for the single spin-orbit exciton the symmetry needs to be broken on-site, while the double spin-orbit exciton needs the breaking of the symmetry on the bond, see figure 10.13. Note that the different temperature dependence cannot be explain if these excitations were excitations into the e_g level. The triple spin-orbit exciton has no center of inversion. Hence, no phonon is needed to break the symmetry, which explains the temperature-independent weight and the position in energy at $3 \cdot 250$ meV.

10.1.2.2 Relative spectral weight

Compared to the spectral weight of the first-order peak, the spectral weight of the second-order peak is large, see figure 10.10a. The first-order process depends on the on-site coupling of the $j_\mathrm{eff} = 1/2$ and $j_\mathrm{eff} = 3/2$ state, while the second-order process depends on the inter-

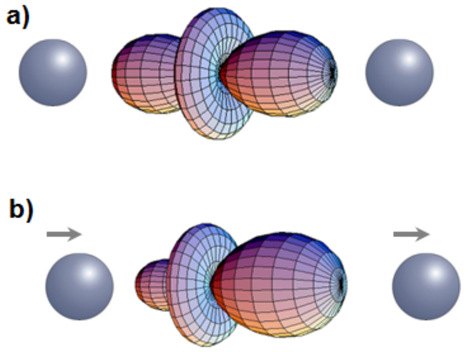

Figure 10.13: Electron density of a $d_{3z^2-r^2}$ orbital in the absence a) and in the presence b) of a phonon. Figure has been taken from reference [174] with permission from *The Royal Society of Chemistry*. Copyright by Wiley-VCH (2000).

site coupling of the $j_{\text{eff}} = 1/2$ and $j_{\text{eff}} = 3/2$ state. Since the Heisenberg interaction is absent for pure $j_{\text{eff}} = 1/2$ moments, see section 9.3, the coupling of the $j_{\text{eff}} = 1/2$ and $j_{\text{eff}} = 3/2$ is the dominant inter-site coupling. Considering the coupling to different phonon modes and the on-site, respectively the inter-site, character of the excitation, a similar spectral weight for the single spin-orbit exciton and the double spin-orbit exciton is reasonable. A similar process for which large weight has been reported, is the bi-magnon plus phonon in cuprates [180, 181]. The bi-magnon excitation has no dipole moment, just like the double spin-orbit excitation. Therefore, both excitations require a phonon to break the symmetry.

To even observe the triple spin-orbit exciton is rare. However, it has such a large weight, because it is not forbidden by parity. Therefore, it does not need a phonon and additionally in $\alpha-$RuCl$_3$ the coupling to the second-nearest neighbor is very large. Winter *et al.* report on an overlap integral to the second-nearest neighbor of $t_{2n} = 60\,\text{meV}$, which is large compared to the $t_{nn} = 160\,\text{meV}$ for the nearest neighbor [182].

10.1.2.3 Raman mode

The interpretation of the three peaks as spin-orbit excitations contradicts the observation of the Raman mode at 145 meV [171]. Nevertheless, the spin-orbit excitation should be visible in the Raman spectrum, as well. Indeed, we find a mode 25 meV below the spin-orbit exciton observed by Fourier-spectroscopy, which is phonon assisted ($E_{ph} = 25\,\text{meV}$), see figure 10.14. Thereby a self-contained picture of the excitations between the phonon and the charge gap has been given.

10.1.3 Trigonal distortion

After determining the nature of the excitations in $\epsilon_2(\omega)$, we can investigate the spin-orbit exciton, in order to estimate the trigonal splitting of the $j_{\text{eff}} = 3/2$ level, see section V. Thereby, we focus on the first peak, since it has the largest spectral weight and the influence

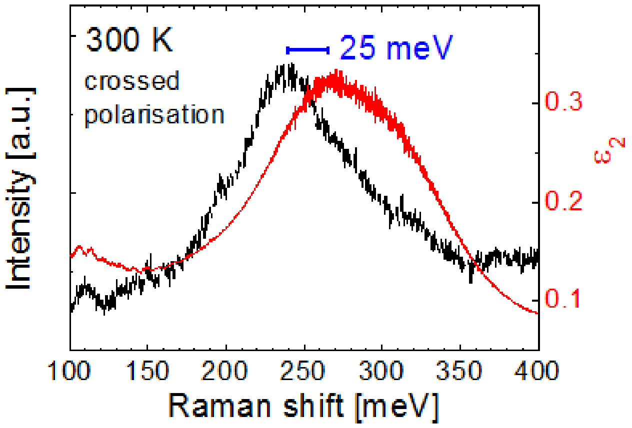

Figure 10.14: Black curve: Raman intensity versus energy at 300 K. Red curve: $\epsilon_2(\omega)$ of the single phonon-assisted spin-orbit exciton.

of the trigonal distortion for multiple spin-orbit excitons becomes more complicated.

10.1.3.1 Fit

At 5 K sidebands at the low-frequency edge of the peak appear. From a fit to $\sigma_1(\omega)$ we can determine the energy difference between the sidebands to 19 meV. At 19 meV no magnon mode is expected, [179] hence the sidebands originate in strong coupling to phonons, described by the Franck-Condon line shape, see section 3.5. However, the whole peak cannot be fitted by a single Franck-Condon oscillator. Therefore, we assume a split spin-orbit exciton. Since sidebands are absent we use an additional Lorentz oscillator to describe the line shape, see figure 10.16. We can achieve good fits with peak positions $E_1 = 288 \pm 6\,\text{meV}$ and $E_2 = 312 \pm 6\,\text{meV}$, yielding a separation of 27 meV of the two peaks. Note, that these energies include the excitation of a phonon with the energy of approximately 25 meV.

10.1.3.2 From the splitting to the trigonal distortion

The trigonal distortion and the SOC strength are determined by the peak positions of the split $j_{\text{eff}} = 3/2$ level, see equations A.20 in the appendix. From the peak positions we determine $\lambda_{\text{eff}} = 182 \pm 4\,\text{meV}$ and $\Delta_{\text{tri}} \approx 38 \pm 4\,\text{meV}$. The resulting energy levels of the split t_{2g} level for $\lambda_{\text{eff}} = 182 \pm 4\,\text{meV}$ as function of the trigonal distortion are plotted in figure 10.17a and the two excitation energies as function of the trigonal distortion in figure 10.17b.

The value of $\lambda = 182\,\text{meV}$ is surprisingly large compared to literature values which range from 97 to 130 meV [142, 161, 171]. However, these values are not reliable, see section 10.1. In the following we will explain why $\lambda_{\text{eff}} = 182\,\text{meV}$ is reasonable.

First of all, we determine the effective value of λ, due to the finite mixing of the e_g level into the $j_{\text{eff}} = 3/2$ level, which causes the $j_{\text{eff}} = 3/2$ level and the e_g level to repel each other. For details on the mixing t_{2g} states and e_g states without trigonal distortion see

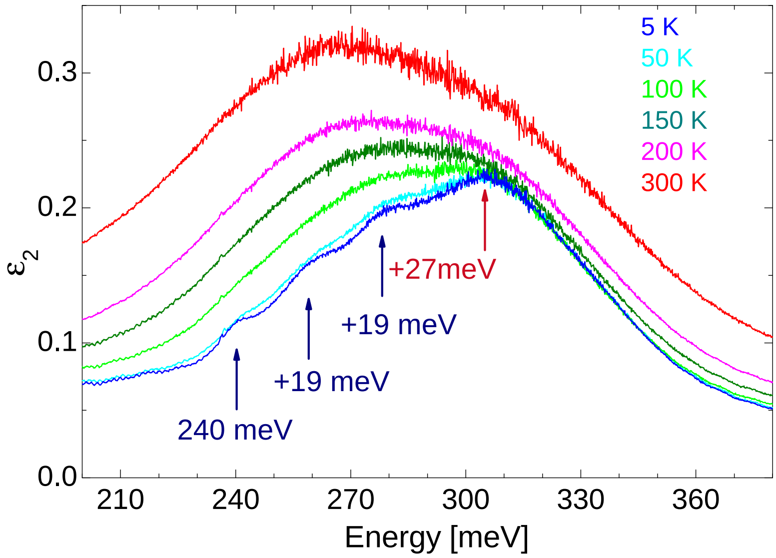

Figure 10.15: Temperature-dependent $\epsilon_2(\omega)$. Sidebands at 5 K are indicated by blue arrows. Red arrow represents the absolute maximum at 5 K.

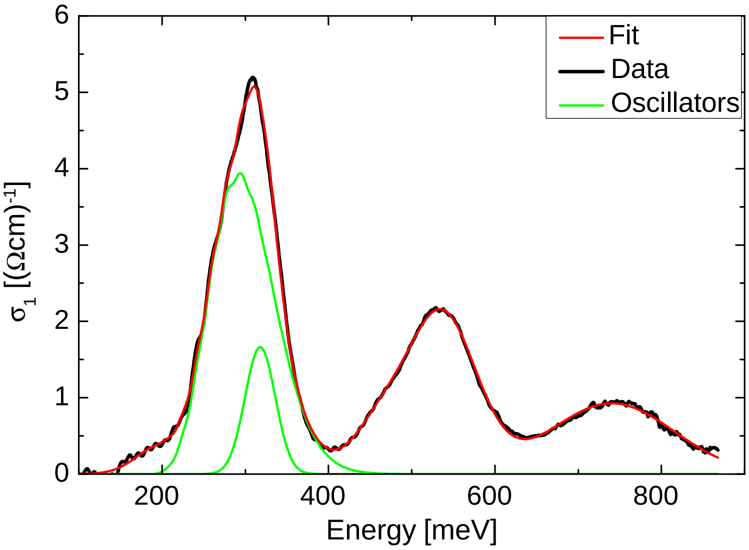

Figure 10.16: Fit (red curve) to $\sigma_1(\omega)$ (black curve) assuming two oscillators for the spin-orbit exciton (green curves).

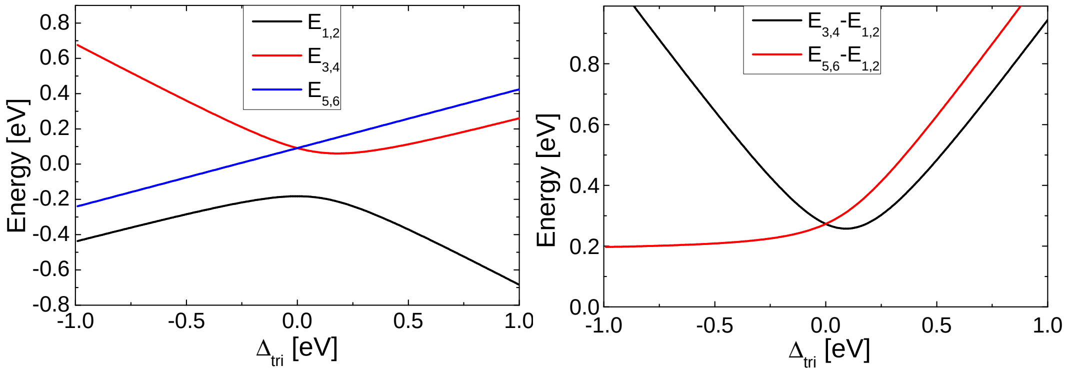

(a) (b)

Figure 10.17: a) Energies of the eigenstates of the t_{2g} orbital for $\lambda = 160\,\text{meV}$ as function of the trigonal crystal field. b) Excitation energies as function of the trigonal crystal field.

appendix V. For $10Dq \approx 2.1\,\text{eV}$ [144], and $\lambda' = 163\,\text{meV}$, we find $\lambda_{\text{eff}}/\lambda' \approx 1.10$, see figure A.34, which results in the observed $\lambda_{\text{eff}} = 182\,\text{meV}$. Hence, the e_g admixture enhances the splitting between $j_{\text{eff}} = 1/2$ and $j_{\text{eff}} = 3/2$.

Furthermore, in other ruthenates such large values of the SOC strength are reported as well. For Sr_2RuO_4 and Ca_2RuO_4, described in the picture of local $j_{\text{eff}} = 1/2$ moments, the SOC strength of $\lambda = 200\,\text{meV}$ has been reported on the basis of RIXS data [183]. Additionally, ARPES data on Sr_2RuO_4 suggest a SOC strength of $130 \pm 30\,\text{meV}$ [184]. Admittedly, both compounds are Ru^{4+} in contrast to $\alpha-RuCl_3$ with Ru^{3+} which increases the SOC strength by about 10% [174]. Furthermore, the Cl octahedron decreases the SOC strength compared to the O octahedron due to the larger degree of covalency in the chemical bonds of the former (relativistic nephelauxetic effect [185]). Both effect need to be taken into account when comparing the SOC strength of Sr_2RuO_4 and $\alpha-RuCl_3$. For Sr_2IrO_4 and $IrCl_3$ the ratio of the SOC strength has been determined by x-ray absorption spectroscopy to $\lambda_{O,4+}/\lambda_{Cl,3+} \approx 1.2$ [186]. This ratio is supposed to be robust against replacing Ir by Ru. Indeed, it is in good agreement with the ratio of the SOC strength for Sr_2RuO_4 $\lambda_{O,4+} = 200\,\text{meV}$ [183] and the SOC strength for $\alpha-RuCl_3$ reported by us, $\lambda = 183\,\text{meV}$, of $\lambda_{O,4+}/\lambda_{Cl,3+} = 1.1$.

10.1.4 Summary

The excitations below 1 eV in $\alpha-RuCl_3$ are controversially discussed. The three peaks between 200 meV to 800 meV have been interpreted as excitations from the t_{2g} levels into the e_g levels [142, 171]. Furthermore, Sandilands *et al.* interpreted the Raman mode at 145 meV as spin-orbit exciton. We were able to proof both interpretations wrong by the combination of our MIR transmittance data and the temperature-dependent Raman data from the group of Prof. v. Loosdrecht. The disappearance of the excitation at 145 meV in the Raman data points to an excitation related to impurities. Excitations from the t_{2g} levels into the e_g levels below 1 eV would imply a strong mixing of the t_{2g} and e_g states, thereby

Kitaev physics could not be realized in $\alpha-$RuCl$_3$. However, we proof that the three peaks are multiple spin-orbit excitations coupling to phonons by the precise determination of ϵ_2 by the transmittance measurements, which emphasizes the $j = 1/2$ nature of the groundstate. The coupling to phonons can be observed by the temperature-dependent spectral weight and phonon sidebands. The observation of multiple spin-orbit excitations and their relative weight is motivated by considering the exchange paths and the orbitals involved in the exchange. From a fit to the first peak we determine an estimate of the trigonal splitting $\Delta_{\mathrm{tri}} \approx 38\,\mathrm{meV}$ and $\lambda = 182\,\mathrm{meV}$. The small trigonal splitting and the large SOC strength make $\alpha-$RuCl$_3$ an excellent candidate for the realization of the Kitaev model.

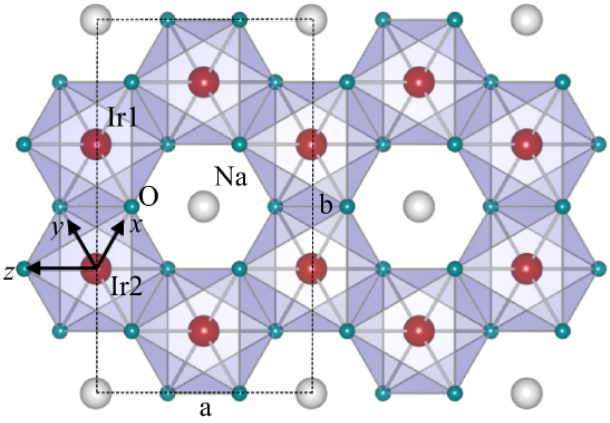

Figure 10.18: Crystal structure of Na_2IrO_3 with oxygen (green circle) octahedra surrounding the Ir (red circle). Figure has been taken from reference [187]`https://doi.org/10.1088/1367-2630/16/1/013056` {DOI}. Copyright by American Physical Society (2017).

10.2 Na_2IrO_3

In 2009 Na_2IrO_3 was proposed by Jackeli and Khaliullin [148] as a candidate for realizing the Kitaev model by the coupling of local $j_{\mathrm{eff}} = 1/2$ moments on a honeycomb lattice. Within the next year it was synthesized by Gegenwart *et al.* [188]. The crystal structure consists of hexagons of Ir atoms, each in an O octahedron, see figure 10.18. The IrO_6 octahedra of equal size form almost perfect 90° Ir-O-Ir bonds [189].
The temperature-dependent magnetic susceptibility data above 300 K show Curie-Weiss behavior with an effective momentum of $\mu_{\mathrm{eff}} = 1.82\,\mu_B$, indicating the predominant $j_{\mathrm{eff}} = 1/2$ character of the local moments [188,190]. Although, the SOC strength is much larger than the trigonal crystal-field splitting, the spin-liquid ground state is not realized in Na_2IrO_3. Instead, magnetic order develops at around 15 K [188,190], see figure 10.19. The magnetic ordering was determined by x-ray magnetic scattering [191] and neutron scattering [192] to be zigzag type.

The insulating gap of Na_2IrO_3 was determined to $\Delta = 340$ meV by reflectance and angle-integrated photoelectron spectroscopy at 130 K by Comin *et al.* [141]. Additionally, an excitation at about 420 meV was observed [140,193,194]. Gretarsson *et al.* [193] claim that it is an excitonic bound state due to long-range Coulomb interaction [194]. However, Khaliullin *et al.* claim that the peak originates from intersite hopping and concluded that it is the result of the coupling between the spin-orbit exciton and the *e*-*h* continuum [140]. In $\sigma_1(\omega)$ reported by Comin *et al.* this peak was not visible [141] which can be explained by selection rules, see figure 10.20. In contrast, several $d^5 - d^5$ to $d^4 - d^6$ transitions are visible in $\sigma_1(\omega)$, well below the charge-transfer excitations between the Ir $5d$ and O $2p$ orbitals starting from 2.5 eV [139,141,195]. However the number of excitations is under discussion. While Sohn *et al.* [139] report on five peaks, lately, Hermann *et al.* [195] fit $\sigma_1(\omega)$ with only three peaks.

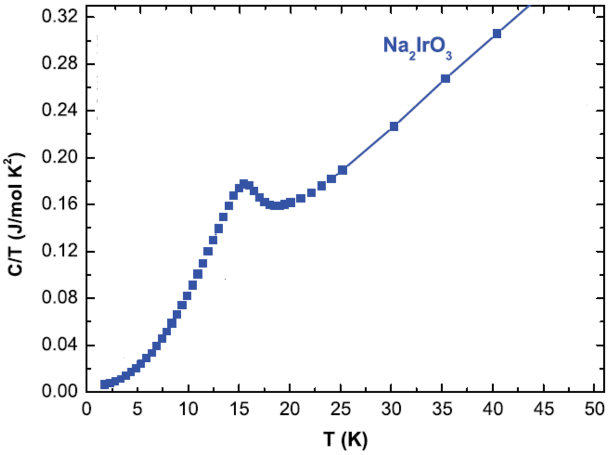

Figure 10.19: Heat capacity C of Na_2IrO_3 divided by temperature. Figure is a modified version of figure 1 from reference [190]`https://doi.org/10.1103/PhysRevLett.108.127203` {DOI}. Copyright by American Physical Society (2012).

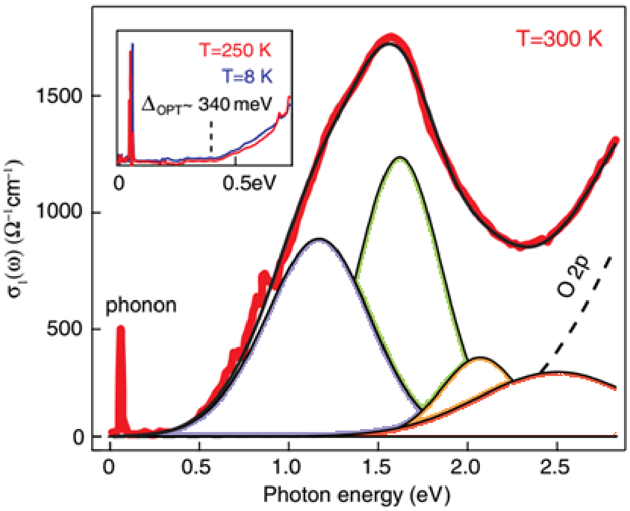

Figure 10.20: $\sigma_1(\omega)$ (red line) with the e-h continuum (black line) and its individual excitations from the simultaneous fit of ARPES and optical data. Inset: The onset of the $d^5 - d^5$ to $d^4 - d^6$ excitations. Figure is a modified version of figure 3 in reference [141]`https://doi.org/10.1103/PhysRevLett.109.266406` {DOI}. Copyright by American Physical Society (2012).

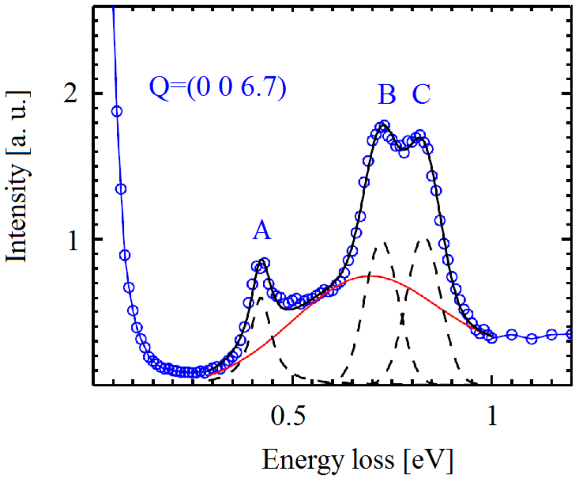

Figure 10.21: RIXS spectrum of a single crystal of Na_2IrO_3. The data is fitted with a broad peak (red line) for the *e*-*h* continuum and three Lorenz oscillators (dashed black line). The peaks B and C correspond to the split spin-orbit exciton, while Gretarsson *et al.* attribute the peak A to an excitonic bound state. Figure is a modified version of figure 1 in reference [193]`https://doi.org/10.1103/PhysRevB.87.220407` {DOI}. Copyright by American Physical Society (2013).

The advantage of the $5d^5$ transition-metal compound Na_2IrO_3 over the $4d^5$ transition-metal compound α-$RuCl_3$, concerning the realization of local $j_{\mathrm{eff}} = 1/2$ moments, is the enhanced SOC strength of $\lambda \approx 400 - 500$ meV [196, 197]. The scenario of local $j_{\mathrm{eff}} = 1/2$ moments is supported by resonant inelastic x-ray scattering (RIXS) measurements, which suggest a small trigonal distortion and a splitting of 110 meV based on the observation of the spin-orbit exciton at about 700 − 800 meV [193, 198], see figure 10.21. This scenario is supported by the branching ratio reported by x-ray absorption spectroscopy [186]. Nevertheless, it was suggested to describe Na_2IrO_3 by quasi-molecular orbitals (QMOs) extending over the Ir hexagon, see figure 10.22 [167, 199, 200]. Foyevtsova *et al.* [200] claim that the QMO scenario satisfyingly describes the peaks in RIXS and the branching ratio in x-ray spectroscopy, which are often interpreted as signatures of the local $j_{\mathrm{eff}} = 1/2$ scenario.However, theory predicts a large difference in $\sigma_1(\omega)$ depending on the nature of the ground state, see figure 10.23 [140, 199]. The reported values of $\sigma_1(\omega)$ in this frequency range determined by combining reflectance and ellipsometry measurements disagree on the spectral weight, see figure 10.24 [139, 141]. The mixing of $j_{\mathrm{eff}} = 1/2$ and $j_{\mathrm{eff}} = 3/2$ states can be caused by trigonal distortion of the oxygen octahedra, which goes along with a splitting of the $j_{\mathrm{eff}} = 3/2$ states, see section V. Optical transmittance measurements are ideally suited to determine the $\sigma_1(\omega)$ and therefore reveal whether the QMO or the local $j_{\mathrm{eff}} = 1/2$ scenario applies to Na_2IrO_3.

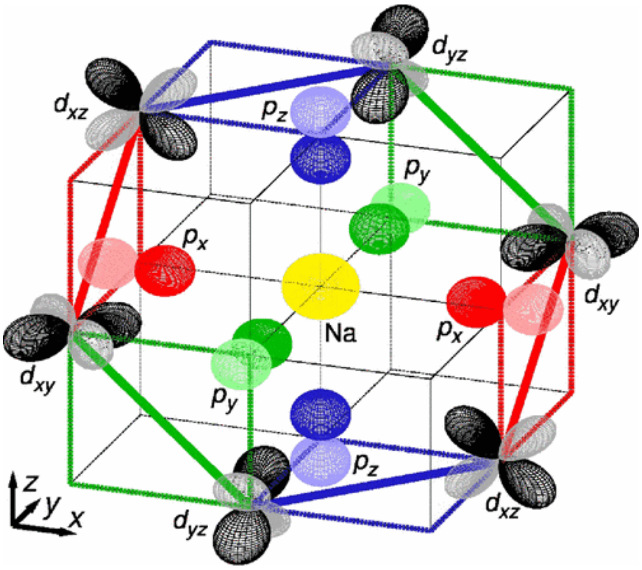

Figure 10.22: QMO scenario: Crystal structure with the orbital wave functions of the atoms involved in the hexagonal QMO. Figure has been taken from reference [167]`https://doi.org/10.1103/PhysRevLett.109.197201` {DOI}. Copyright by American Physical Society (2012).

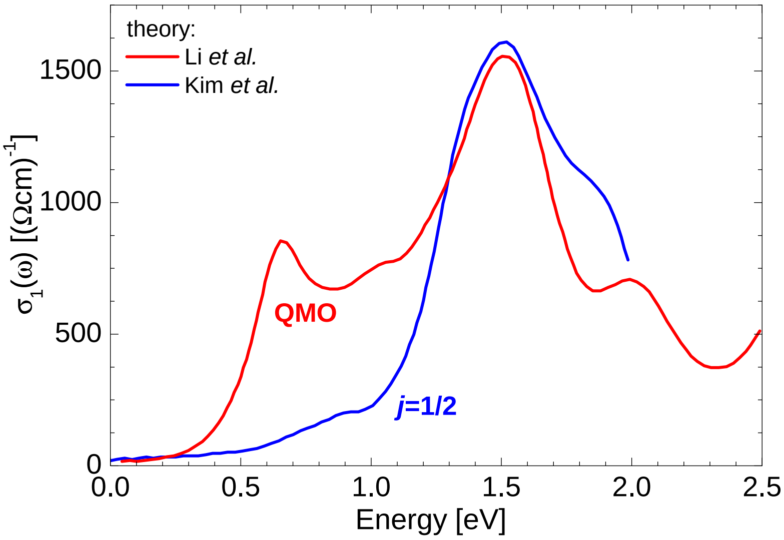

Figure 10.23: The theoretical $\sigma_1(\omega)$ for Na_2IrO_3 calculated by Kim *et al.* [140] (blue line) for local $j_{\text{eff}} = 1/2$ moments and Li *et al.* (red line) for QMO [199].

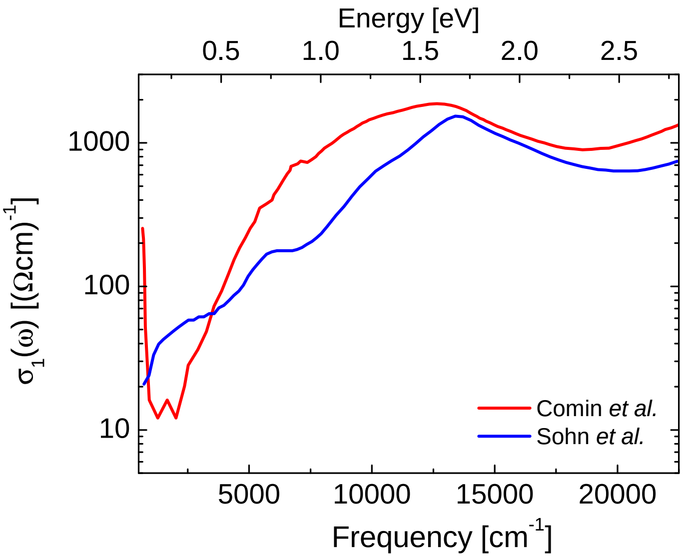

Figure 10.24: The $\sigma_1(\omega)$ reported by Comin *et al.* [141] and Sohn *et al.* [139].

In the following we report on $\sigma_1(\omega)$ determined on single crystals of Na_2IrO_3[5] from infrared transmittance measurements in the vicinity of the gap. In the range of 300 to 700 meV we find $\sigma_1(\omega)$ to be about an order of magnitude smaller than reported [139, 141]. This result strongly contradicts the QMO scenario and supports the local $j_{\text{eff}} = 1/2$ moments scenario. Additionally, we report on an excitation at 450 meV at low temperatures that coincides with a peak observed in RIXS [193]. The temperature dependence suggests that the peak originates in the coupling of electron-hole excitations with the spin-orbit exciton, which further supports the local $j_{\text{eff}} = 1/2$ moments scenario.

10.2.1 Determining $\sigma_1(\omega)$

We performed temperature-dependent MIR reflectance and transmittance measurements on single crystals of Na_2IrO_3. We are able to determine $\sigma_1(\omega)$ over a broad frequency range on which it changes by almost two orders of magnitude by performing transmittance measurements on crystals with thicknesses varying from 12.7 to 133 μm, see figure 10.25. We need to expose the samples for a short time to air in order to mount the sample in the cryostat, therefore we study the sample properties as function of time exposed to air, see appendix V. The reflectance is measured on a 140 μm thick crystal. Since the crystal has a finite transmittance, we apply a Fourier filter in the transparent range, see figure 10.25.

The $\sigma_1(\omega)$ is plotted in figure 10.26. At low frequencies $\sigma_1(\omega)$ is dominated by phonons like reported by Hermann *et al.* [195]. At about 1000 cm^{-1} we observe a peak which we attributed to multi-phonon absorptions. At high frequencies $\sigma_1(\omega)$ reveals the onset of

---

[5] The single crystals of Na_2IrO_3 investigated in this thesis have been synthesized by Prof. Dr. Becker-Bohatý and Prof. Dr. Bohatý of the Institute of Geology and Mineralogy, Section of Crystallography, University of Cologne

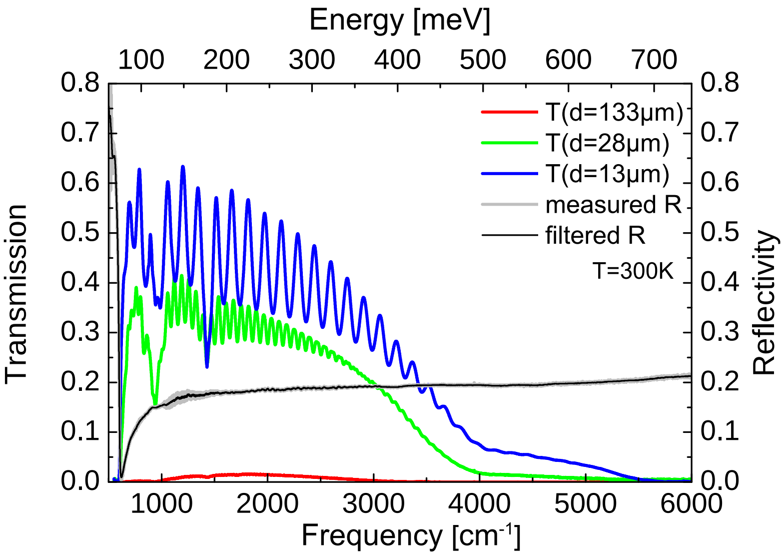

Figure 10.25: The transmittance for different thicknesses (left axis) and the measured reflectance merged with the reflectance from the fringes (right axis) for 300 K.

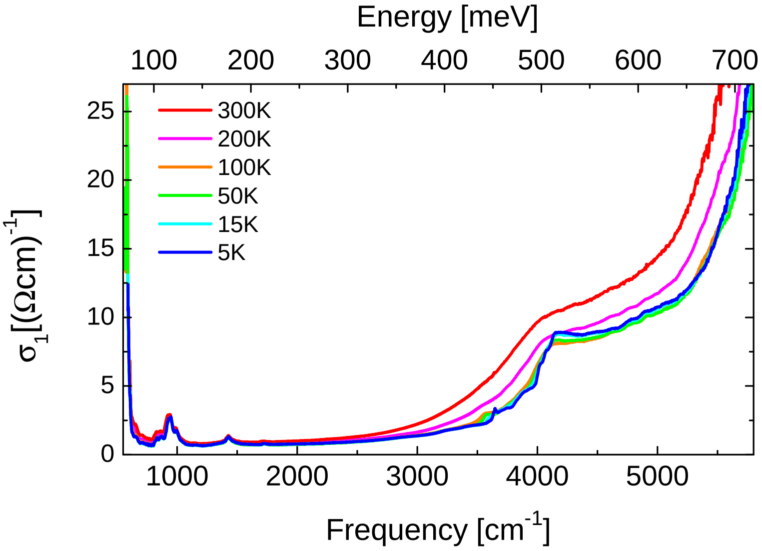

Figure 10.26: The merged temperature-dependent $\sigma_1(\omega)$ of samples of different thicknesses.

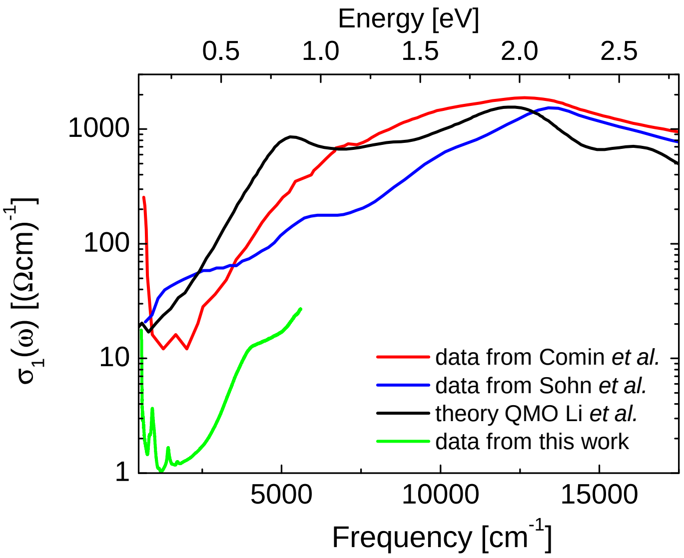

Figure 10.27: The $\sigma_1(\omega)$ reported by Comin *et al.* [141] and Sohn *et al.* [139], as well as the predicted $\sigma_1(\omega)$ for the QMO scenario by Li *et al.* [199] compared to our data.

excitations across the gap between 440 meV and 450 meV for 5 K. This is contradicting the reported gap of 340 meV by Comin *et al.* [141]. Note that they have performed their measurements at 130 K. At the gap several temperature-dependent features can be observed, which are discussed in section 10.2.3.

10.2.2 Quasi-molecular orbitals or local j_{eff} moments

In the frequency range of the lowest electron-hole excitation we find $\sigma_1(\omega) \approx 10\,(\Omega cm)^{-1}$. This is about one order of magnitude below $\sigma_1(\omega)$ in this frequency range reported in literature [139,141]. More importantly, it is about two orders of magnitude below the values predicted for the QMO scenario [199], see figure 10.27.

The alternative scenario of local $j_{\mathrm{eff}} = 1/2$ moments is investigated by Kim *et al.* [140] using the exact diagonalization method on a four-site Ir cluster. They calculate the lowest electron-hole excitation starting from local d^5 configuration on sites in the ground states. The excited state is characterized by a d^4 and a d^6 configuration on neighboring sites. The d^6 configuration is trivial, while the d^4 configuration can be realized for three different energies, see section V. Kim *et al.* find that the excitation of the lowest d^4 multiplet, located below about 1 eV, is strongly suppressed, due to the small hopping matrix element [140]. Hence, the low spectral weight strongly supports the local $j_{\mathrm{eff}} = 1/2$ scenario. Additionally, it suggests little mixing between the t_{2g} and the e_g states, since the mixing would increase the hopping matrix element.

In case the lowest electron-hole excitation is not forbidden, but lies higher in energy than expected by theory, the high energy features and the gap cannot be explained consistently. The dominant peak in $\sigma_1(\omega)$ at 1.5 eV, found in experiment and theory [139,141,199], implies

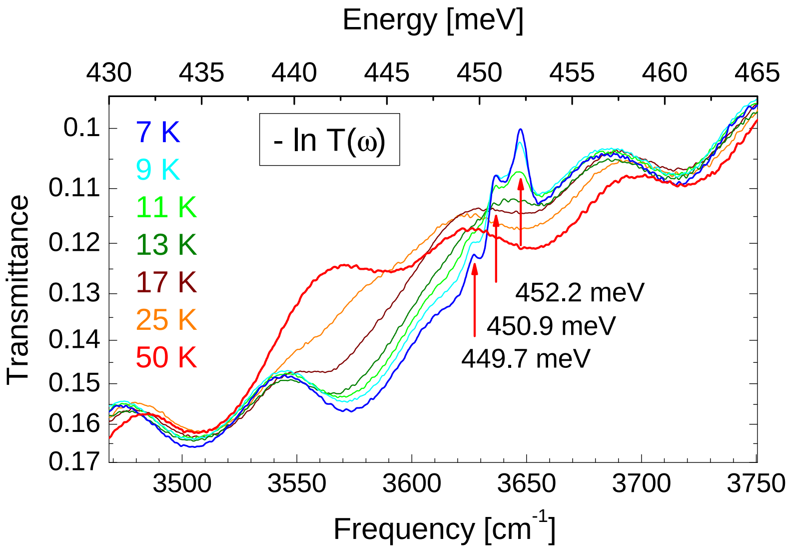

Figure 10.28: The temperature-dependent $ln(T)$ at the onset of the d^5-d^5 to d^4-d^6 excitations with magnon sidebands. The large period is originating from Fabry-Pérot fringes which cannot be filtered without affecting the structure of the magnon sidebands.

the lowest electron-hole excitation at about 0.5 meV [201]. Additionally, the origin of the features around 450 meV can hardly be explained if they are below the lowest electron-hole excitation.

In summary, the low spectral weight for the lowest interband excitation strongly supports the scenario of local $j_{\mathrm{eff}} = 1/2$ moments.

10.2.3 Excitations at the gap

The temperature-dependent $\sigma_1(\omega)$ exhibits several features close to the gap, see figure 10.26.

In agreement with Sohn *et al.* and in contrast to Hermann *et al.* we can clearly confirm the existence of the lowest d^5-d^5 to d^4-d^6 excitations at about 500 meV. Additionally, we find systematical fluctuations of the spectral weight of $\sigma_1(\omega)$ in the vicinity of the electron-hole excitation. If we assume local $\mathrm{j_{eff}}$=1/2 moments in the ground state the spectral weight of the d^5-d^5 to d^4-d^6 excitation depends on the orbital and magnetic correlations, which depends on temperature and can explain the systematical increase and decrease of $\sigma_1(\omega)$. At 450 meV and temperatures below roughly 15 K three peaks rise in the transmittance, see figure 10.28. The excitations are equally separated by about 1.2 meV, which is too low in energy for phonons. The periodicity and the energy range suggests that these excitations are magnon sidebands [193, 202].

We determine the transition temperature from the amplitude of the peaks, see figure 10.29. It roughly agrees with the magnetic transition reported by Singh and Gegenwart *et al.* at 15 K [188]. To which excitations these sidebands belong is speculative.

We conjecture that the sidebands are related to a RIXS peak reported by Gretarsson *et*

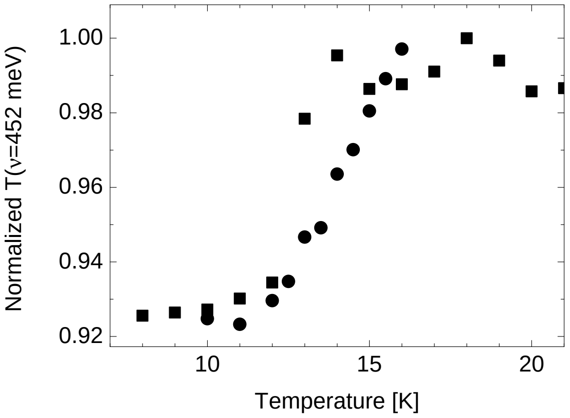

Figure 10.29: The normalized transmittance at the peak of the magnon sideband at $\omega = 452\,\text{meV}$. The black circles are determined from the transmittance of the $12.7\,\mu\text{m}$ thick sample while the black squares are determined from the transmittance of the $15\,\mu\text{m}$ thick sample.

al. [198], see figure 10.21. The position in energy of both features roughly coincides. However A. Revelli *et al.*[6] could show that the position of the RIXS peak and the onset of the gap coincides exactly within the error of 5 meV on the frequency resolution of the RIXS data. The nature of this peak is discussed controversially [140,147,198,203]. Plotnikova *et al.* [147] claim that it is an excitonic bound state (in $\mathrm{Sr_2IrO_4}$), while Kim *et al.* [140] claim that the peak is due to the coupling of the spin-orbit exciton to the electron-hole continuum. The latter involves magnetic excitation wherefore the magnon sidebands might point towards this interpretation.

10.2.4 Summary

We perform transmittance measurements to determine $\sigma_1(\omega)$ precisely. In order to determine $\sigma_1(\omega)$ in a broad frequency range, we measure samples of different thicknesses. From the transmittance of the thinnest samples we gain insight in $\sigma_1(\omega)$ beyond the gap at 450 meV. $\sigma_1(\omega)$ in the vicinity of the energy gap is particularly interesting, since it reveals the underlying microscopic physics. In contrast, to the quasi-molecular orbital scenario, the weight of the lowest electron-hole is strongly suppressed in the local $j_{\text{eff}} = 1/2$ scenario. We report on extremely low spectral weight for the lowest electron-hole excitation compared to literature. The theory which is consistent with this finding is based on local $j_{\text{eff}} = 1/2$ moments forming the ground state.

Furthermore, the low-temperature transmittance at the gap enables us to determine the magnetic-ordering temperature by the observation of magnon sidebands. The magnon sidebands coincide with a RIXS peak, which can be attributed to the coupling of the spin-orbit exciton and the electron-hole continuum.

---

[6] The data have been measured at the ERSF by Revelli *et al.* in the framework of his ongoing PhD thesis

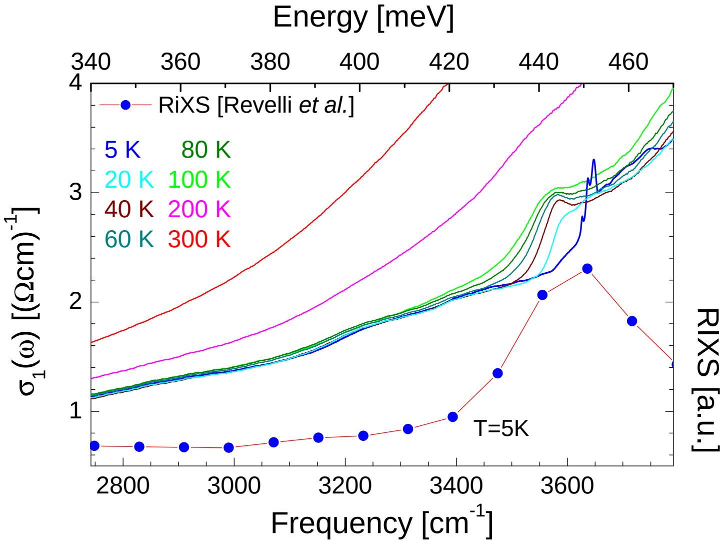

Figure 10.30: Temperature dependent $\sigma_1(\omega)$ in the vicinity of the magnon sidebands. RIXS data (blue circles) measured in the frame work of A. Revellis PhD project (5 K).

Our transmittance measurements giving $\sigma_1(\omega)$ are strong evidence for the local $j_{\mathrm{eff}} = 1/2$ scenario in $\mathrm{Na_2IrO_3}$.

Part V

Appendix

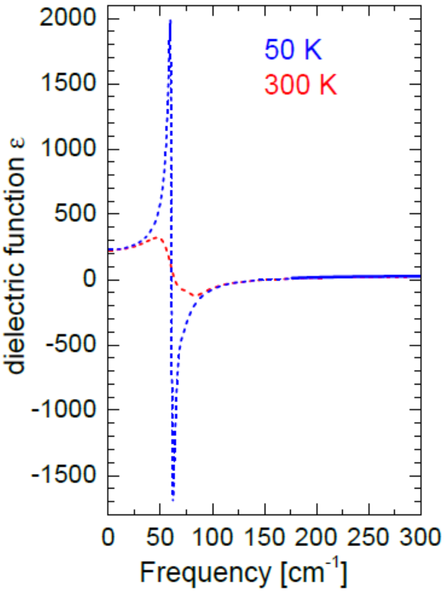

Figure A.31: Dashed lines represents the real part of the dielectric function $\epsilon(\omega)$ determined from the Drude-Lorentz fits of the reflectance. The Reststrahlenband carries a huge oscillator strength yielding $\epsilon(\omega = 0) = 230$. Solid lines show $\epsilon(\omega)$ calculated from the fringes. Image has been taken from [115]`https://dx.doi.org/10.1103/PhysRevB.93.245149` {DOI}. Copyright by American Physical Society (2016).

Real part of the dielectric function

The real part of the dielectric function was determined from reflectivity measurements, see figure A.31. Around 50 cm^{-1} the dielectric function is dominated by a strong phonon mode. This mode is mainly responsible for the large value of the real part of the dielectric function at low frequencies. Therefore, the size of the puddles is enhanced.

Fits to the transmittance of Bi_2Te_3 films on silicon

The fits to the transmission have been performed to clarify whether, the measurements are dominated by the bulk or the surface character, see figure A.32. Therefore, we fitted a bulk-only model to the transmittance spectra for different thicknesses. The fits described the data reasonably for 14 nm, 33 nm, and 53 nm, while the transmittance for 9 nm deviates.

$\sigma_1(\omega)$ of $Bi_{15}Sb_{05}Te_{17}Se_{13}$ sample # 4

The smoothed transmittance was used to determine $\sigma_1(\omega)$ by inversion. However, at low temperatures it was necessary to obtain $\sigma_1(\omega)$ by the amplitude of the fringes, since $\sigma_1(\omega)$ determined by inversion could not dissolve the differences in $\sigma_1(\omega)$, see figure A.33

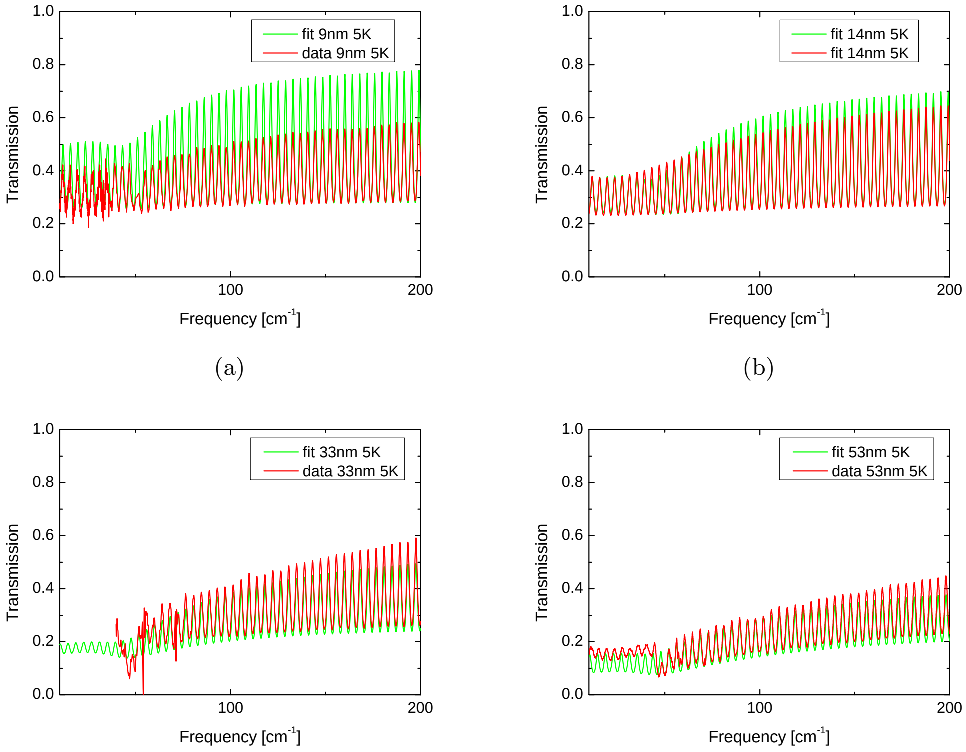

(a) (b)

(c) (d)

Figure A.32: The bulk only fit (red line) simultaneously fitted to the transmittance (green line) at 5 K of the four films.

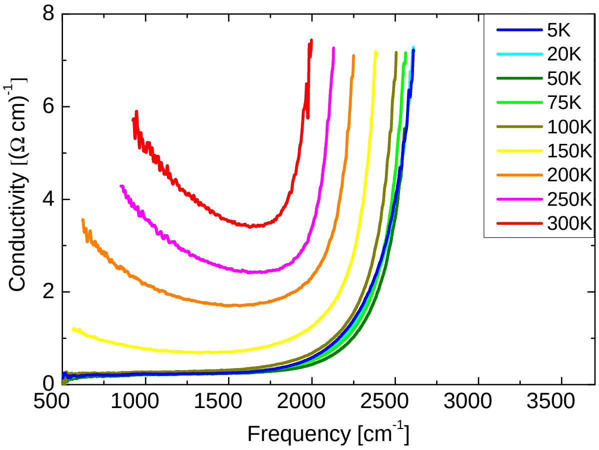

Figure A.33: Optically conductivity of $Bi_{15}Sb_{05}Te_{17}Se_{13}$ sample # 4

d^4 d^6 excitations

The hopping between sites causes d^4 states and trivial d^6 states. In the following we derive the states of a d^4 ion. We need not only to consider the SOC and the crystal field, but also the Hund's coupling constant J_H and the Coulomb repulsion U. The Hamiltonian without trigonal crystal field and SOC, following Perkins [137], has the form

$$\begin{aligned}\hat{H} = U_1 \sum_{i,\alpha} n_{i\alpha\uparrow} n_{i\alpha\downarrow} + \frac{1}{2}\left(U_2 - J_H\right) \sum_{i,\sigma,\alpha\neq\alpha'} n_{i\alpha\sigma} n_{i\alpha'\sigma} + U_2 \sum_{i,\alpha\neq\alpha'} n_{i\alpha\uparrow} n_{i\alpha'\downarrow} \\ + J_H \sum_{i,\alpha\neq\alpha'} a^\dagger_{i\alpha\uparrow} a^\dagger_{i\alpha\downarrow} a_{i\alpha'\downarrow} a^\dagger_{i\alpha\downarrow} a_{i\alpha'\uparrow} - J_H \sum_{i,\alpha\neq\alpha'} a^\dagger_{i\alpha\uparrow} a_{i\alpha\downarrow} a^\dagger_{i\alpha'\downarrow} a_{i\alpha'\downarrow},\end{aligned} \tag{A.1}$$

with $n_{i\alpha,\sigma} = a^\dagger_{i\alpha\sigma} a_{i\alpha\sigma}$, while $a_{i\alpha\sigma}$ is the annihilation hole operator and $a^\dagger_{i\alpha\sigma}$ is the creation hole operator. U_1 and U_2 are the Coulomb repulsion among electrons in the same and in different t_{2g} orbitals. The i refers to the site, while α refers to the type of the orbital (d_{xy}, d_{yz}, d_{xz}). The spin is taken into account by σ. The resulting energy eigenvalues for the two hole states are

$$E^{2h}_{(1)} = 6U_2 - J_H, \tag{A.2}$$

$$E^{2h}_{(2)} = 6U_2 + J_H, \tag{A.3}$$

$$E^{2h}_{(3)} = 6U_2 + 4J_H. \tag{A.4}$$

These are the three eigenvalues for the 15 states that are available for the two holes. d^5 states have an energy of $E(d^5) = 10U_2$. By adding one electron to the five electrons the energy increases by $5U_2$, to $E(d^6) = 15U_2$. With these energies the energies for an excitation from $d^5 d^5$ to $d^4 d^6$ can be calculated, similar to the $d^1 d^1$ to $d^0 d^2$ excitations [204]. The three possible energies for the transition are

$$E_{1,2,3} = E_{1,2,3}\left(d^4\right) + E\left(d^6\right) - 2E\left(d^5\right). \tag{A.5}$$

In the presence of a trigonal crystal field or SOC these contributions need to be added to the Hamiltonian. The resulting eigenstates are a mixture of the 15 eigenstates for the purely cubic crystal field without SOC. For details see Kim *et al.* [140].

Mixing of the t_{2g} and e_g levels

To calculate the mixing we have to consider the Hamiltonian with crystal field, SOC, and all ten states. After this step the procedure is in general the same as for the 3 × 3 Hamiltonian for SOC only, see section 9.3.5. The Hamiltonian can be transformed into another basis by a basis transformation

$$\mathbf{b}^* \cdot \hat{H} \cdot \mathbf{b} = \hat{H}'. \tag{A.6}$$

In the next step the Hamiltonian needs to be diagonalized to obtain the eigenvalues and the eigenstates. The e_g level is not affected by the SOC, since its orbital angular momentum is quenched, but the t_{2g} level splits into two levels with the energy

$$E_{1/2} = \frac{1}{2}(10Dq - \lambda/2) \pm \frac{1}{2}\sqrt{(10Dq - \lambda/2)^2 + 2 \cdot 10Dq\lambda + 6\lambda^2}, \tag{A.7}$$

with $10Dq$ the crystal field splitting. Here we focus on the eigenstates with small deviations from the pure $j_{\text{eff}} = 1/2$ states and $j_{\text{eff}} = 3/2$ states, which are the states given by E_1. The corresponding eigenstates for E_1 are

$$\left(-\frac{1}{\sqrt{2}}|d_{yz}\uparrow\rangle - \frac{i}{\sqrt{2}}|d_{xz}\uparrow\rangle - i\gamma_1|d_{3z^2-r^2}\downarrow\rangle\right)/\sqrt{1+\gamma_1^2} \tag{A.8}$$

$$\left(\frac{1}{\sqrt{2}}|d_{yz}\downarrow\rangle - \frac{i}{\sqrt{2}}|d_{xz}\downarrow\rangle - i\gamma_1|d_{3z^2-r^2}\uparrow\rangle\right)/\sqrt{1+\gamma_1^2} \tag{A.9}$$

$$\left(-\frac{1}{\sqrt{6}}|d_{yz}\downarrow\rangle - \frac{i}{\sqrt{6}}|d_{xz}\downarrow\rangle + \sqrt{\frac{2}{3}}|d_{xy}\uparrow\rangle - i\gamma_1|d_{x^2-y^2}\uparrow\rangle\right)/\sqrt{1+\gamma_1^2} \tag{A.10}$$

$$\left(\frac{1}{\sqrt{6}}|d_{yz}\uparrow\rangle - \frac{i}{\sqrt{6}}|d_{xz}\uparrow\rangle + \sqrt{\frac{2}{3}}|d_{xy}\downarrow\rangle + i\gamma_1|d_{x^2-y^2}\downarrow\rangle\right)/\sqrt{1+\gamma_1^2}, \tag{A.11}$$

with $\gamma_1 = \frac{\sqrt{2}}{3}(1/2 + E_1/\lambda)$. As a result, the quartet with $j_{\text{eff}} = 3/2$ has an e_g character [136, 137, 140, 205, 206]. The mixing can be approximated by $\sqrt{\frac{3}{2}\frac{\lambda}{(\lambda/2+\Delta)}}$ [136]. Therefore, the $j_{\text{eff}} = 3/2$ states and the e_g states repel each other. We plot in figure A.34 the energy of the eigenstates as a function of the ratio of the crystal field energy and the SOC constant λ. From the plot it is clear to see that the energy difference between the $j_{\text{eff}} = 1/2$ and the $j_{\text{eff}} = 3/2$ is enhanced so that the excitation energy for the spin-orbit exciton is enhanced.

d^5 with trigonal crystal field

We consider a large cubic crystal field and trigonal distortion (neglecting SOC). This distortion is along the [111] direction of the cubic coordinate system of highest symmetry. Therefore, it is reasonable to set the z-axis along the [111]-direction [140]. The Hamilton operator consists of a term for the cubic crystal field $\hat{H}_c$ and one for the trigonal distortion along the z-direction $\hat{H}_t$. By solving the Hamiltonian five eigenstates can be found, according to Kim *et al.* [140]. The eigenstates, for a coordinate system and α chosen like in figure

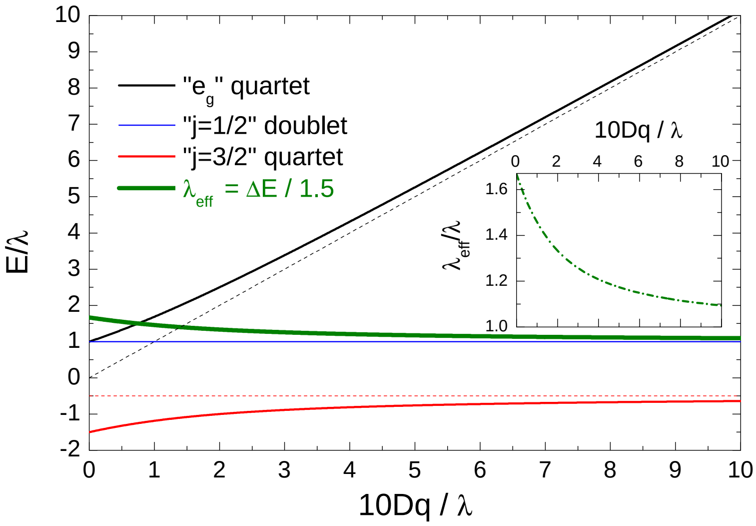

Figure A.34: The energy of the e_g level (black line), $j_{\text{eff}} = 1/2$ level (blue line), and the $j_{\text{eff}} = 3/2$ level (red line) divided by the SOC constant are plotted versus the cubic crystal field strength 10Dq divided by the SOC constant. The green line represents the energy splitting between the $j_{\text{eff}} = 1/2$ level and the $j_{\text{eff}} = 3/2$ level. Inset: Splitting between the $j_{\text{eff}} = 1/2$ level and the $j_{\text{eff}} = 3/2$ level as function of the cubic crystal field strength 10Dq divided by the SOC constant.

A.35, have the form

$$|e_g^{\pi-}\rangle = \cos\alpha|d_{xy}\rangle - \sin\alpha|d_{yz}\rangle \tag{A.12}$$

$$|e_g^{\pi+}\rangle = \cos\alpha|d_{x^2-y^2}\rangle - \sin\alpha|d_{zx}\rangle \tag{A.13}$$

$$|a_{1g}\rangle = |z^2\rangle \tag{A.14}$$

$$|e_g^{-}\rangle = \cos\alpha|d_{yz}\rangle - \sin\alpha|d_{xy}\rangle \tag{A.15}$$

$$|e_g^{+}\rangle = \cos\alpha|d_{zx}\rangle + \sin\alpha|d_{x^2-y^2}\rangle. \tag{A.16}$$

The two latest levels can be attributed to the e_g levels. The t_{2g} level is split into two e_g^π states and an a_{1g} level. If the splitting is Δ_{tri} the single a_{1g} level must be shifted by $\pm 2/3\Delta_{\text{tri}}$ and the two e_g^π states are shifted by $\mp 1/3\Delta_{\text{tri}}$, see figure 9.3. For a contraction along the z-axis the a_{1g} level is the lowest in energy and the e_g^π states are Δ_{tri} above. If the octahedron is elongated along the z-direction the splitting will be reversed.

Trigonal crystal field and spin-orbit coupling

We investigated the influence of SOC in the presence of a cubic crystal field and the influence of a trigonal distortion in the presence of a cubic crystal field on the eigenstates. In both cases the triplet state, created by the cubic crystal field, splits into a singlet and a doublet, see figure 9.3. The Hamiltonians for both problems are different, hence it is obvious that

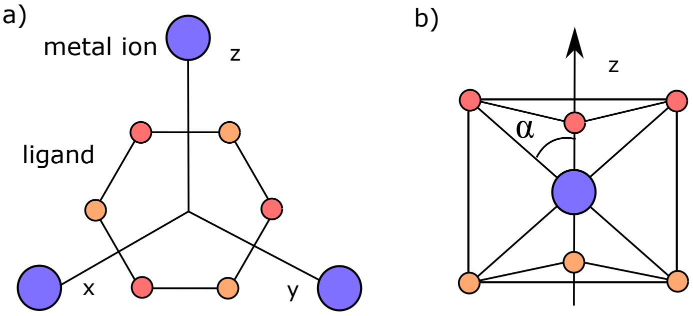

Figure A.35: a) Top view of edge-sharing octahedron. X, Y, and Z represent directions of nearest-neighboring metal ion sites. b) The compression of the octahedron is quantified by the angle α.

the eigenstates are different. We expect a splitting of the triplet into three singlets in the presence of a trigonal crystal field and SOC. For the exact solution the 10 × 10 matrix with all d^5 states needs to be diagonalized. We determine the Hamiltonian for the t_{2g} states in the presence of a large cubic crystal field, following Sizyuk *et al.* [206]. The Hamiltonian has the form

$$\hat{H}_{\lambda,\Delta} = \lambda \hat{s} \cdot \hat{l} + \Delta_{\mathrm{tri}} \left(-2|a_{1g}\rangle\langle a_{1g}| + |e_g^+\rangle\langle e_g^+| + |e_g^-\rangle\langle e_g^-| \right). \tag{A.17}$$

Explicitly the Hamiltonian can be written in the basis

$$\mathbf{b} = \begin{pmatrix} |1/2, \;\; 1/2\rangle \\ |1/2, -1/2\rangle \\ |3/2, \;\; 3/2\rangle \\ |3/2, \;\; 1/2\rangle \\ |3/2, -1/2\rangle \\ |3/2, -3/2\rangle \end{pmatrix}, \tag{A.18}$$

to

$$\hat{H}_{\lambda,\Delta_{\mathrm{tri}}} = \begin{pmatrix} -\lambda & 0 & -\frac{(1-i)\Delta_{\mathrm{tri}}}{3\sqrt{6}} & 0 & \frac{(1+i)\Delta_{\mathrm{tri}}}{3\sqrt{2}} & \frac{i\Delta_{\mathrm{tri}}}{3}\sqrt{\frac{2}{3}} \\ 0 & -\lambda & \frac{i\Delta_{\mathrm{tri}}}{3}\sqrt{\frac{2}{3}} & \frac{(1-i)\Delta_{\mathrm{tri}}}{3\sqrt{2}} & 0 & -\frac{(1+i)\Delta_{\mathrm{tri}}}{3\sqrt{6}} \\ -\frac{(1+i)\Delta_{\mathrm{tri}}}{3\sqrt{6}} & -\frac{i\Delta_{\mathrm{tri}}}{3}\sqrt{\frac{2}{3}} & \frac{\lambda}{2} & \frac{(1+i)\Delta_{\mathrm{tri}}}{3\sqrt{3}} & \frac{i\Delta_{\mathrm{tri}}}{3\sqrt{3}} & 0 \\ 0 & \frac{(1+i)\Delta_{\mathrm{tri}}}{3\sqrt{2}} & \frac{(1-i)\Delta_{\mathrm{tri}}}{3\sqrt{3}} & \frac{\lambda}{2} & 0 & \frac{i\Delta_{\mathrm{tri}}}{3\sqrt{3}} \\ \frac{(1-i)\Delta_{\mathrm{tri}}}{3\sqrt{2}} & 0 & -\frac{i\Delta_{\mathrm{tri}}}{3\sqrt{3}} & 0 & \frac{\lambda}{2} & -\frac{(1-i)\Delta_{\mathrm{tri}}}{3\sqrt{3}} \\ -\frac{i\Delta_{\mathrm{tri}}}{3}\sqrt{\frac{2}{3}} & -\frac{(1-i)\Delta_{\mathrm{tri}}}{3\sqrt{6}} & 0 & -\frac{i\Delta_{\mathrm{tri}}}{3\sqrt{3}} & -\frac{(1-i)\Delta_{\mathrm{tri}}}{3\sqrt{3}} & \frac{\lambda}{2} \end{pmatrix}. \tag{A.19}$$

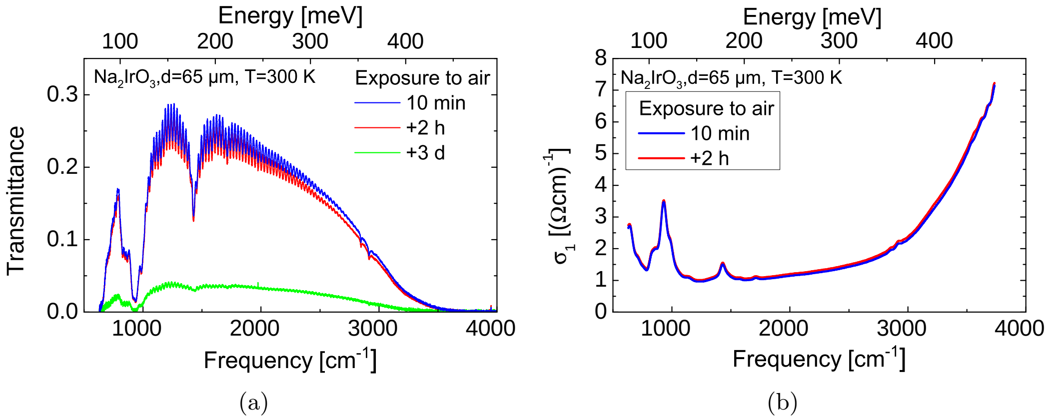

Figure A.36: a) The transmitted intensity of the same Na_2IrO_3 crystal at 300 K after different times of exposure to air. b) $\sigma_1(\omega)$ of the same sample after 10 min in air and additional 2 h in air.

The three, resulting singlets have the three energies

$$E_{1,2} = -\frac{\Delta_{\text{tri}}}{6} - \frac{\lambda}{4} - \frac{1}{2}\sqrt{2\lambda^2 + \left(\Delta_{\text{tri}} - \frac{\lambda}{2}\right)^2} \tag{A.20}$$

$$E_{3,4} = -\frac{\Delta_{\text{tri}}}{6} - \frac{\lambda}{4} + \frac{1}{2}\sqrt{2\lambda^2 + \left(\Delta_{\text{tri}} - \frac{\lambda}{2}\right)^2} \tag{A.21}$$

$$E_{5,6} = \frac{\Delta_{\text{tri}}}{3} + \frac{\lambda}{2}. \tag{A.22}$$

These relations enable us to calculate the energy splitting depending on the trigonal distortion and the SOC strength, see section 10.1.3.2.

Aging in air

For our measurements it is unavoidable to expose the sample to air for at least ten minutes. Since Na_2IrO_3 is known to react with air, we investigate the influence of the time exposed to air on the transmitted intensity. We expose the 65 μm thick sample after the measurement 2 h to air and measure the transmitted intensity. Then we expose the sample to air for three days and measure the transmitted intensity again, see figure A.36a. The results confirms that Na_2IrO_3 is sensitive to air and long exposure to air destroys the sample. However, the transmitted intensity is already changing by 5 % due to an exposure of 2 h, which means that it is crucial to minimize the time in air. The change of 5 % is not critical for our results, since $\sigma_1(\omega)$ only changes at most by $0.05\,(\Omega cm)^{-1}$, see figure A.36b. Note that the low values of $\sigma_1(\omega)$ would become even lower without exposure to air.

Bibliography

[1] John Hubbard. Electron correlations in narrow energy bands. *The Royal Society*, **276**:238, (1963).

[2] W. W.-Krempa, G. Chen, Y. B. Kim, and L. Balents. Correlated quantum phenomena in the strong spin-orbit regime. *Annual Review Condensed Matter Physics*, **5**:57, (2014).

[3] C. L. Kane and E. J. Mele. Quantum spin hall effect in graphene. *Physical Review Letters*, **95**:226801, (2005).

[4] C. L. Kane and E. J. Mele. Z_2 topological order and the quantum spin hall effect. *Physical Review Letters*, **95**:146802, (2005).

[5] M. König1, S. Wiedmann, C. Brüne, A. Roth, H. Buhmann, L. W. Molenkamp, X.-L. Qi, and S.-C. Zhang. Quantum spin hall insulator state in hgte quantum wells. *Science*, **318**:766, (2007).

[6] M. Z. Hasan and C. L. Kane. Colloquium: Topological insulators. *Review of Modern Physics*, **82**:3045, (2010).

[7] X.-L. Qi and S.-C. Zhang. Topological insulators and superconductors. *Reviews of modern physics*, **83**:1057, (2011).

[8] M. Z. Hasan and J. E. Moore. Three-dimensional topological insulators. *Annual Review of Condensed Matter Physics*, **2**:55–78, (2011).

[9] L. Balents. Spin liquids in frustrated magnets. *Nature*, **464**:199, (2010).

[10] L. Savary and L. Balents. Quantum spin liquids: a review. *Reports on Progress in Physics*, **80**:016502, (2017).

[11] Walter Greiner. *Quantum Mechanics: An Introduction.* Springer, (2001).

[12] Axelfoley. Polariton, wikipedia, (2017). Online; accessed 18-August-2017.

[13] Z. Q. Qiu and S. D. Bader. Surface magneto-optic kerr effect. *Review of Scientific Instruments*, **71**:1423, (1999).

[14] C. C. Katsidis and D. I. Siapkas. General transfer-matrix method for optical multilayer systems with coherent, partially coherent, and incoherent interference. *Applied Optics*, **41**:3978, (2002).

[15] George Grüner Martin Dressel. *Electrodynamics of Solids.* Cambridge University Press, 2 edition, (2003).

[16] G. S. Jenkins, D. C. Schmadel, and H. D. Drew. Simultaneous measurement of circular dichroism and faraday rotation at terahertz frequencies utilizing electric field sensitive detection via polarization modulation. *Review of Scientific Instruments*, **81**:083903, (2010).

[17] V. A. Volkov and S. A. Mikhailov. Quantization of the faraday effect in systems with a quantum hall effect. *JETP Letter*, **41**:475, (1985).

[18] G. E. Jellison and F. A. Modine. Parameterization of the optical functions of amorphous materials in the interband region. *Applied Physics Letters*, **69**:371, (1996).

[19] U. Fano. Effects of configuration interaction on intensities and phase shifts. *Physical Review*, **124**:1866, (1961).

[20] Andrea Damascelli. *Optical Spectroscopy of Quantum Spin Systems.* PhD thesis, University of Groningen, (1999).

[21] E. Condon. A theory of intensity distribution in band systems. *Physical Review*, **28**:1182, (1926).

[22] J. Franck and E. G. Dymond. Elementary processes of photochemical reactions. *Transactions of the Faraday Society*, **21**:536, (1926).

[23] M. Fox. *Optical Properties of Solids.* Oxford master series in condensed matter physics. Oxford University Press, 2 edition, 2010.

[24] F. Ansbacher. über die berechnung von franck-condon-integralen. *Zeitschrift für naturforschung*, **14a**:889, (1959).

[25] Frenzie23. Franck condon diagram, wikipedia, (2014). Online; accessed 04-April-2018.

[26] R. de L. Kronig. *On the theory of dispersion of X-rays*, volume 6. Journal of the Optical Society of America, 12 edition, (1926).

[27] P. Griffiths and J. A. de Hasseth. *Fourier Transform Infrared Spectrometry.* Wiley-Blackwell, 2 edition, (2007).

[28] K. Thirunavukkuarasu, M. Langenbach, A. Roggenbuck, E. Vidal, H. Schmitz, J. Hemberger, and M. Grüninger. Self-normalizing phase measurement in multimode terahertz spectroscopy based on photomixing of three lasers. *Applied Physics Letters*, **106**:031111, (2014).

[29] A. J. Deninger, T. Göbel, D. Schönherr, T. Kinder, A. Roggenbuck, M. Köberle, F. Lison, T. Müller-Wirts, and P. Meissner. Precisely tunable continuous-wave terahertz source with interferometric frequency control. *Review of Scientific Instruments*, **79**:044702, (2008).

[30] A. Roggenbuck, K. Thirunavukkuarasu, H. Schmitz, J. Marx, A. Deninger, I. C. Mayorga, R. Güsten, J. Hemberger, and M. Grüninger. Using a fiber stretcher as a fast phase modulator in a continuous wave terahertz spectrometer. *Journal of the Optical Society of America B*, **29**:614, (2012).

[31] M. Schubert. *Infrared Ellipsometry on Semiconductor Layer Structures.* Springer Tracts in Modern Physics. Springer, 1 edition, 2004.

[32] B. Yan and S.-C. Zhang. Topological materials. *Reports on Progress in Physics*, **75**:096501, (2012).

[33] J. E. Moore and L. Balents. Topological invariants of time-reversal-invariant band structures. *Physical Review Letters B*, **75**:121306, (2007).

[34] H. Zhang, C.-X. Liu, X.-L. Qi, X. Dai, Z. Fang, and S.-C. Zhang. Topological insulators in Bi_2Se_3, Bi_2Te_3 and Sb_2Te_3 with a single dirac cone on the surface. *Nature Physics*, **5**:438, (2009).

[35] M. El-Batanouny and F. Wooten. *Symmetry and Condensed Matter Physics: A Computational Approach.* Cambridge University Press, (2008).

[36] Y. Ando. Topological insulator materials. *Journal of the Physical Society of Japan*, **82**:102001, (2013).

[37] D. Schmeltzer and A. Saxena. Interference effects for $t^2 = -1$ time reversal invariant topological insulators: Surface optical and raman conductivity. *Physical Review B*, **88**:035140, (2013).

[38] Z. Li and J. P. Carbotte. Hexagonal warping on optical conductivity of surface states in topological insulator Bi_2Te_3. *Physical Review B*, **87**:155416, (2013).

[39] V. P. Gusynin, S. G. Sharapov, and J. P. Carbotte. Sum rules for the optical and hall conductivity in graphene. *Physical Review B*, **75**:165407, (2007).

[40] L. A. Falkovsky and S. S. Pershoguba. Optical far-infrared properties of a graphene monolayer and multilayer. *Physical Review B*, **76**:153410, (2007).

[41] E. J. Nicol and J. B. Carbotte. Optical conductivity of bilayer graphene with and without an asymmetry gap. *Physical Review B*, **77**:155409, (2008).

[42] D. N. Basov, Richard D. Averitt, D. v. d. Marel, M. Dressel, and K. Haule. Electrodynamics of correlated electron materials. *Reviews of modern Physics*, **83**:471, (2011).

[43] Z. Ren, A. A. Taskin, S. Sasaki, K. Segawa, and Y. Ando. Optimizing $Bi_{2-x}Sb_xTe_{3-y}Se_y$ solid solutions to approach the intrinsic topological insulator regime. *Physical Review B*, **84**:077144, (2011).

[44] K. Eto, Z. Ren, A. A. Taskin, K. Segawa, and Y. Ando. Angular-dependent oscillations of the magnetoresistance in Bi_2Se_3 due to the three-dimensional bulk fermi surface. *Physical Review B*, **81**:195309, (2010).

[45] J. G. Analytis, J.-H. Chu, Y. Chen, F. Corredor, R. D. McDonald, Z. X. Shen, and I. R. Fisher. Bulk fermi surface coexistence with dirac surface state in Bi_2Se_3: A comparison of photoemission and shubnikovde haas measurements. *Physical Review B*, **81**:205407, (2010).

[46] W. Zhang, R. Yu, H.-J. Zhang, X. Dai, and Z. Fang. First-principles studies of the three-dimensional strong topological insulators Bi_2Te_3, Bi_2Se_3 and Sb_2Te_3. *New Journal of Physics*, **12**:065013, (2010).

[47] M. Bianchi, D. Guan, S. Bao, J. Mi, B. B. Iversen, P. D.C. King, and P. Hofmann. Coexistence of the topological state and a two-dimensional electron gas on the surface of Bi_2Se_3. *Nature Communications*, **1**:128, (2010).

[48] M. Bianchi, R. C. Hatch, J. Mi, B. B. Iversen, and P. Hofmann. Simultaneous quantization of bulk conduction and valence states through adsorption of nonmagnetic impurities on Bi_2Se_3. *Physical Review Letters*, **107**:086802, (2011).

[49] K. Eto, Z. Ren, A. A. Taskin, K. Segawa, and Y. Ando. Angular-dependent oscillations of the magnetoresistance in Bi_2Se_3 due to the three-dimensional bulk fermi surface. *Physical Review B*, **81**(195309), (2010).

[50] P. D. C. King, R. C. Hatch, M. Bianchi, R. Ovsyannikov, C. Lupulescu, G. Landolt, B. Slomski, J. H. Dil, D. Guan, J. L. Mi, E. D. L. Rienks, J. Fink, A. Lindblad, S. Svensson, S. Bao, G. Balakrishnan, B. B. Iversen, J. Osterwalder, W. Eberhardt, F. Baumberger, and P. Hofmann. Large tunable rashba spin splitting of a two-dimensional electron gas in Bi_2Se_3. *Physical Review B*, **107**:096802, (2011).

[51] S. V. Dordevic, M. S. Wolf, N. Stojilovic, H. Lei, and C. Petrovic3. Signatures of charge inhomogeneities in the infrared spectra of topological insulators Bi_2Se_3, Bi_2Te_3 and Sb_2Te_3. *Journal of Physics: Condensed Matter*, **25**:075501, (2013).

[52] Wei Cheng and Shang-Fen Ren. Phonons of single quintuple Bi_2Te_3 and Bi_2Se_3 films and bulk materials. *Physical Review B*, **83**:094301, (2011).

[53] B. C. Chapler, K. W. Post, A. R. Richardella, J. S. Lee, J. Tao, N. Samarth, and D. N. Basov. Infrared electrodynamics and ferromagnetism in the topological semiconductors Bi_2Te_3 and mn-doped Bi_2Te_3. *Physical Review B*, **89**:235308, (2014).

[54] M. Michiardi, I. Aguilera, M. Bianchi, V. E. d. Carvalho, L. O. Ladeira, N. G. Teixeira, E. A. Soares, C. Friedrich, S. Blügel, and P. Hofmann. Bulk band structure of Bi_2Te_3. *Physical Review B*, **90**:075105, (2014).

[55] K. Hoefer, C. Becker, D. Rata, J. Swanson, P. Thalmeier, and L. H. Tjeng. Intrinsic conduction through topological surface states of insulating Bi_2Te_3 epitaxial thin films. *Proceedings of the National Academy of Sciences*, **111**:14979, (2014).

[56] Y. L. Chen, J. G. Analytis, J.-H. Chu, Z. K. Liu, S.-K. Mo, X. L. Qi, H. J. Zhang, D. H. Lu, X. Dai, Z. Fang, S. C. Zhang, I. R. Fisher, Z. Hussain, and Z.-X. She. Experimental realization of a three-dimensional topological insulator, Bi_2Te_3. *Science*, **325**:178, (2009).

[57] G. Wang, X.G. Zhu, Y.Y. Sun, Y.Y. Li, T. Zhang, J. Wen, X. Chen, K. He, L.L. Wang, X.C. Ma, J.F. Jia, S. B. Zhang, and Q.K. Xue. Topological insulator thin films of Bi_2Te_3 with controlled electronic structure. *Advanced Materials*, **23**:2929, (2011).

[58] Z. Aabdin, M. Winkler, D. Bessas, J. König, N. Peranio, O. Eibl, R. Hermann, and H. Böttner. Sb_2Te_3 and Bi_2Te_3 thin films grown by room-temperature mbe. *Journal of Electronic Materials*, **41**(1493), (2012).

[59] A. D. LaForge, A. Frenzel, B. C. Pursley, T. Lin, X. Liu, J. Shi, and D. N. Basov. Optical characterization of Bi_2Se_3 in a magnetic field: Infrared evidence for magnetoelectric coupling in a topological insulator material. *Physical Review B*, **81**:125120, (2010).

[60] L. He, F. Xiu, Y. Wang, A. V. Fedorov, G. Huang, X. Kou, M. Lang, W. P. Beyermann, J. Zou, and K. L. Wang1. Epitaxial growth of Bi_2Se_3 topological insulator thin films on si (111). *Journal of Applied Physics*, **109**:103702, (2011).

[61] C. W. Rischau, A. Ubaldini, E. Giannini, and C. J. v. d. Beek. Charge puddles in a completely compensated topological insulator. *New Journal of Physics*, **18**:073024, (2016).

[62] A. Banerjee, A. Sundaresh, K. Majhi, R. Ganesan1, and P. S. Anil Kumar. Accessing rashba states in electrostatically gated topological insulator devices. *Applied Physics Letters*, **109**:232408, (2016).

[63] H. Plank, S. N. Danilov, V. V. Bel'kov, V. A. Shalygin, J. Kampmeier, M. Lanius, G. Mussler, D. Grützmacher, and S. D. Ganichev. Opto-electronic characterization of three dimensional topological insulators. *Journal of applied physics*, **120**:165301, (2016).

[64] T. Chen and B. Skinner. Enhancement of hopping conductivity by spontaneous fractal ordering of low-energy sites. *Applied Physics Letters*, **94**:085146, (2016).

[65] E. P. Amaladass, T. R. Devidas, S. Sharma, and A. Mani. Quantum coherence phenomenon in disordered $\mathrm{Bi_2seTe_2}$ topological single crystal: effect of annealing. *Journal of Physics: Condensed Matter*, **29**(17):175602, (2016).

[66] J. Zhang, C.-Z. Chang, Z. Zhang, J. Wen, X. Feng, K. Li, M. Liu, K. He, L. Wang, X. Chen, Q.-K. Xue, X. Ma, and Y. Wang. Band structure engineering in $\mathrm{(Bi_{1-x}Sb_x)_2Te_3}$ ternary topological insulators. *Nature Communications*, **2**:1588, (2011).

[67] A. L. Efros and B. I. Shklovskii. Coulomb gap and low temperature conductivity of disordered systems. *Journal of Physics C: Solid State Physics*, **8**:49, (1975).

[68] A. L. Efros. Coulomb gap in disordered systems. *Journal of Physics C: Solid State Physics*, **9**(11):2021, (1975).

[69] B. I. Shklovskii A. L. Efros, N. V. Lien. Impurity band structure in lightly doped semiconductors. *Journal of Physics C: Solid State Physics*, **12**:1869, (1979).

[70] Alex L Efros Boris Isaakovich Shklovskii. *Electronic properties of doped semiconductors*, volume 45. Springer Science & Business Media, (2013).

[71] B. Skinner, T. Chen, and B. I. Shklovskii. Why is the bulk resistivity of topological insulators so small? *Physical Review Letters*, **109**, (2012).

[72] B. Skinner, T. Chen, and B. I. Shklovskii. Effects of bulk charged impurities on the bulk and surface transport in three-dimensional topological insulators. *Journal of Experimental and Theoretical Physics*, **117**:579, (2013).

[73] B. Skinner, T. Chen, and B. I. Shklovskii. Effects of bulk charged impurities on the bulk and surface transport in three-dimensional topological insulators. *Journal of Experimental and Theoretical Physics*, **117**:579, (2013).

[74] B. I. Shklovskii A. L. Efros. *Electronic Properties of Doped Semiconductors.* Springer Series in Solid-State Sciences, (1984).

[75] N. F. Mott. Conduction in non-crystalline materials. *The Philosophical Magazine: A Journal of Theoretical Experimental and Applied Physics*, **19**:835, (1969).

[76] Jonathan Lux. *Fluctuations in and out of equilibrium: Thermalization, quantum measurements and Coulomb disorder.* PhD thesis, Univercity of Cologne, 5 (2016).

[77] B. I. Shklovskii and A. L. Efros. Interband absorption of light in strongly doped semiconductors. *Soviet Physics Jetp*, **32**, (1971).

[78] Yang Xu. Observation of topological surface state quantum hall effect in an intrinsic three-dimensional topological insulator. *Nature Physics*, **10**:956, (2014).

[79] K. W. Post, Y. S. Lee, B. C. Chapler, A. A. Schafgans, Mario Novak, A. A. Taskin, Kouji Segawa, and M. D. Goldflam. Infrared probe of the bulk insulating response in $Bi_{2-x}Sb_xTe_{3-y}Se_y$ topological insulator alloys. *Physical Review B*, **91**:165202, (2015).

[80] K.W. Post, B. C. Chapler, 1 J. S. Wu M. K. Liu, H. T. Stinson, M. D. Goldflam, A. R. Richardella, and J. S. Lee. Sum-Rule constraints on the surface state conductance of topological insulators. *Physical Review B*, **115**:116804, (2015).

[81] R. V. Aguilar, A.V. Stier, W. Liu, L. S. Bilbro, D. K. George, N. Bansal, L. Wu, J. Cerne, A. G. Markelz, S. Oh, and N. P. Armitage. Terahertz response and colossal kerr rotation from the surface states of the topological insulator Bi_2Se_3. *Physical Review Letters*, **108**:087403, (2012).

[82] Z.-G. Chen, G. Han, L. Yang, L. Cheng, and J. Zou. Nanostructured thermoelectric materials current research and future challenge. *Progress in Natural Science: Materials International*, **22**:535, (2012).

[83] Y. Xia, D. Qian, D. Hsieh, L. Wray, A. Pal, H. Lin, A. Bansil, D. Grauer, Y. S. Hor, R. J. Cava, and M. Z. Hasan. Observation of a large-gap topological-insulator class with a single dirac cone on the surface. *Nature Physics Letters*, **5**:398, (2009).

[84] Joel E. Moore. The birth of topological insulators. *Nature*, **464**:194, (2010).

[85] M. Schulz O. Madelung, U. Rössler. *Non-Tetrahedrally Bonded Elements and Binary Compounds I*, volume 41c of *Group III Condensed Matter.* Springer, (1998).

[86] Thomas P. Debies. X-ray photoelectron spectra and electronic structure of Bi_2x_3 (x=o, s, se, te). *Chemical Physics*, **20**:277, (1977).

[87] W. Richter, H. Köhler, and C. R. Becker. A raman and far-infrared investigation of phonons in the rhomobohedral v_2-vi_3 compounds. *basic solid state physics*, **84**:619, (1977).

[88] R.Scherm, G.Dolling, R.Ritter, E.Schedler, W.Teuchert, and V.Wagner. A variable curvature analyser crystal for three-axis spectrometers. *Nuclear Instruments and Methods*, **143**:77, (1977).

[89] A. F. Zurhelle, V. L. Deringer, R. P Stoffel, and R. Dronskowski. Ab initio lattice dynamics and thermochemistry of layered bismuth telluride Bi_2Te_3. *Journal of Physics: Condensed Matter*, **28**:115401, (2016).

[90] X. Luo, Y. Zhao, J. Zhang, M. Toh, C. Kloc, Q. Xiong, and S. Y. Quek. Effects of lower symmetry and dimensionality on raman spectra in two-dimensional wSe_2. *Physical Review B*, **88**:195313, (2013).

[91] Y. Zhao, X. Luo, J. Zhang, Wu, X. Bai, M. Wang, J. Jia, H. Peng, Z. Liu, S. Y. Quek, and Q. Xiong. Interlayer vibrational modes in few-quintuple-layer Bi_2Te_3 and

two-dimensional crystals: Raman spectroscopy and first-principles studies. *Physical Review B*, **90**:245428, (2014).

[92] D. Hsieh, Y. Xia, D. Qian, L. Wray, F. Meier, J. H. Dil, J. Osterwalder, L. Patthey, A. V. Fedorov, H. Lin, A. Bansil, D. Grauer, Y. S. Hor, R. J. Cava, and M. Z. Hasan. Observation of time-reversal-protected single-dirac-cone topological-insulator states in Bi_2Te_3 and Sb_2Te_3. *Physical Review Letters*, **103**:146401, (2009).

[93] D. Hsieh, Y. Xia, D. Qian, L. Wray, J. H. Dil, F. Meier, J. Osterwalder, L. Patthey, J. G. Checkelsky, N. P. Ong, A. V. Fedorov, H. Lin, A. Bansil, D. Grauer, Y. S. Hor, R. J. Cava, and M. Z. Hasan. A tunable topological insulator in the spin helical dirac transport regime. *Nature*, **460**:1101, (2009).

[94] Y. Takagaki, A. Giussani, K. Perumal, R. Calarco, and K.-J. Friedland. Robust topological surface states in Sb_2Te_3 layers as seen from the weak antilocalization effect. *Physical Review Letters B*, **86**:125137, (2012).

[95] J. P. Perdew, K. Burke, and M. Ernzerhof. Generalized gradient approximation made simple. *Physical Review Letters*, **77**:3865, (1996).

[96] D. Kong, Y. Chen, J.J. Cha, Q. Zhang, J. G. Analytis, K. Lai, Z. Liu, S. S. Hong, K. J. Koski, S. K. Mo, Z. Hussain, I. R. Fisher, Z. X. Shen, and Y. Cui. Ambipolar field effect in the ternary topological insulator $(Bi_xSb_{(1x)}Te_3$ by composition tuning. *Nature Nanotechnology*, **6**:705, (2011).

[97] L. Plucinski, G. Mussler, J. Krumrain, A. Herdt, S. Suga, D. Grützmacher, and C. M. Schneider. Robust surface electronic properties of topological insulators: Bi_2Te_3 films grown by molecular beam epitaxy. *Applied Physics Letters*, **98**:222503, (2011).

[98] C. Weyrich, M. Drögeler, J. Kampmeier, M. Eschbach, G. Mussler, T. Merzenich, T. Stoica, I. E. Batov, J. Schubert, L. Plucinski, B. Beschoten, C. M. Schneider, C. Stampfer, D. Grützmacher, and T. Schäpers. Growth, characterization, and transport properties of ternary $(Bi_{1-x}Sb_x)_2Te_3$ topological insulator layers. *Journal of physics: Condensed matter*, **28**:495501, (2016).

[99] G. Dolling and R. A. Cowley. The thermodynamic and optical properties of germanium, silicon, diamond and gallium arsemide. *Proceedings of the Physical Society*, **88**:463, (1966).

[100] K.H. Unkelbach. *Nachweis optisch aktiver Gitterschwingungen und optische Eigenschaften von Antimontellurid*. PhD thesis, RWTH Aachen, (1973).

[101] R. J. Cava, Huiwen Ji, M. K. Fuccillo, Q. D. Gibson, and Y. S. Hor. Crystal structure and chemistry of topological insulators. *Journal of Materials Chemistry C*, **1**:3176, (2013).

[102] D. O. Scanlon, P. D. C. King, R. P. Singh, A. d. l. Torre, S. M. Walker, G. Balakrishnan, F. Baumberger, and C. R. A. Catlow. Controlling bulk conductivity in topological insulators: Key role of anti-site defects. *Advanced Materials*, **24**:2154, (2012).

[103] Z. Ren, A. A. Taskin, S. Sasaki, K. Segawa, and Y. Ando. Large bulk resistivity and surface quantum oscillations in the topological insulator Bi_2Te_2se. *Physical Review B*, **82**:241306, (2010).

[104] A. A. Taskin, Z. Ren, S. Sasaki, K. Segawa, and Y. Ando. Observation of dirac holes and electrons in a topological insulator. *Physical Review Letters*, :016801, (2011).

[105] T. Arakane, T. Sato, S. Souma, K. Kosaka, K. Nakayama, M. Komatsu, T. Takahashi, Z. Ren, K. Segawa, and Y. Ando. Tunable dirac cone in the topological insulator $Bi_{2-x}Sb_xTe_{3-y}Se_y$. *Nature Communication*, **3**:636, (2012).

[106] M. Neupane, S.-Y. Xu, L. A. Wray, A. Petersen, R. Shankar, N. Alidoust, Chang Liu, A. Fedorov, H. Ji, J. M. Allred, Y. S. Hor, T.-R. Chang, H.-T. Jeng, H. Lin, A. Bansil, R. J. Cava, and M. Z. Hasan1. Topological surface states and dirac point tuning in ternary topological insulators. *Physical Review B*, **85**:235406, (2012).

[107] Y. Pan, D. Wu, J.R. Angevaare, H. Luigjes, E. Frantzeskakis, N. de Jong, E. van Heumen, T.V. Bay, B. Zwartsenberg, Y.K. Huang, M. Snelder, A. Brinkman, M.S. Golden, and A. de Visser. Low carrier concentration crystals of the topological insulator $Bi_{2-x}Sb_xTe_{3-y}Se_y$ a magnetotransport study. *New Journal of Physics*, **16**:123035, (2014).

[108] S. Jia, H. Beidenkopf, I. Drozdov, M. K. Fuccillo, J. Seo, J. Xiong, N. P. Ong, A. Yazdani, and R. J. Cava. Defects and high bulk resistivities in the Bi-rich tetradymite topological insulator $Bi_{2+x}Te_{2-x}$se. *Physical Review B*, **86**:165119, (2012).

[109] S. K. Kushwaha, Q. D. Gibson, J. Xiong, I. Pletikosic, A. P. Weber, A. V. Fedorov, N. P. Ong, T. Valla, and R. J. Cava. Comparison of Sn-doped and nonstoichiometric vertical-Bridgmangrown crystals of the topological insulator Bi_2Te_2se. *Journal of Applied Physics*, **115**:143708, (2014).

[110] A. Akrap, A. Ubaldini, E. Giannini, and L. Forro. $Bi_2Te_{3-x}Se_x$ series studied by resistivity and thermopower. *Europhysics Letters*, **107**:57008, (2014).

[111] C. Shekhar, C. E. ViolBarbosa, B. Yan, S. Ouardi, W. Schnelle, G. H. Fecher, and C. Felser. Evidence of surface transport and weak antilocalization in a single crystal of the Bi_2Te_2se topological insulator. *Physical Review B*, **90**:165140, (2014).

[112] Z. Ren, A. A. Taskin, S. Sasaki, K. Segawa, and Y. Ando. Fermi level tuning and a large activation gap achieved in the topological insulator Bi_2Te_2se by Sn doping. *Physical Review B*, **85**:155301, (2012).

[113] J. Xiong, Y. Luo, S. Jia Y. Khoo, R. J. Cava, and N. P. Ong. High-field shubnikovde haas oscillations in the topological insulator Bi_2Te_2se. *Physical Review B*, **86**:045314, (2012).

[114] J. Xiong, A. C. Petersen, D. Qu, R. J. Cava, and N. P. Ong. Quantum oscillations in a topological insulator Bi_2Te_2se with large bulk resistivity (6ωcm). *Physica E: Low-dimensional Systems and Nanostructures*, **44**:917, (2012).

[115] N. Borgwardt, I. Vergara J. Lux, Z. Wang, A. A. Taskin, K. Segawa, P. H. M. v. Loosdrecht, Y. Ando, A. Rosch, and M. Grüninger. Self-organized charge puddles in a three-dimensional topological material. *Physical Review B*, **93**:245149, (2016).

[116] T. Knispel, W. Jolie, N. Borgwardt, J. Lux, Zhiwei Wang, Yoichi Ando, A. Rosch, T. Michely, and M. Grüninger. Charge puddles in the bulk and on the surface of the topological insulator $BiSbTeSe_2$ studied by scanning tunneling microscopy and optical spectroscopy. *Physical Review B*, **96**:195135, (2017).

[117] I. Teramoto and S. Takayanagi. Relations between the electronic properties and the chemical bonding of $Sb_xBi_{2-x}Te_{3-y}Se_y$ system. *Journal of Physics and Chemistry of Solids*, **19**:124, (1961).

[118] I. A. Nechaev and E. V. Chulkov. Quasiparticle band gap in the topological insulator Bi_2Te_3. *Physical Review B*, **88**:165135, (2013).

[119] Y. P. Varshni. Temperature dependence of the energy gap in semiconductors. *Physica*, **34**:149, (1967).

[120] I. G. Austin. The optical properties of bismuth telluride Bi_2Te_3. *Proceedings of the Physical Society*, **72**:545, (1958).

[121] J. Black, E. M. Conwell, L. Seigle, and C. W. Spencer. Electrical and optical properties of some $\mathrm{m}_2^{V-B}\mathrm{n}_3^{VI-B}$ semiconductors. *Journal of Physics and Chemistry of Solids*, **2**:240, (1957).

[122] D. L. Greenaway and G. Harbeke. Band structure of bismuth telluride, bismuth selenide and their respective alloys. *Journal of Physics and Chemistry of Solids*, **26**(10):1585–1604, (1965).

[123] P. Di Pietro, F. M. Vitucci, D. Nicoletti, L. Baldassarre, P. Calvani, R. Cava, Y. S. Hor, U. Schade, and S. Lupi. Optical conductivity of bismuth-based topological insulators. *Physical Review B*, **86**:045439, (2012).

[124] A. Akrap, M. Tran, A. Ubaldini, J. Teyssier, E. Giannini, D. v. d. Marel, P. Lerch, and C. C. Homes. Optical properties of Bi_2Te_2Se at ambient and high pressures. *Physical Review B*, **86**:235207, (2012).

[125] A. A. Reijnders, Y. Tian, L. J. Sandilands, G. Pohl, I. D. Kivlichan, S. Y. Frank Zhao, S. Jia, M. E. Charles, R. J. Cava, N. Alidoust, S. Xu, M. Neupane, M. Z. Hasan, X.Wang, S. W. Cheong, and K. S. Burch. Optical evidence of surface state suppression in Bi-based topological insulators. *Physical Review B*, **89**:024201, (2014).

[126] B. van Zeghbroeck. *Principles of Semiconductor Devices.* Online textbook, 1 edition, (2011). Chapter 2.7.

[127] J. Yong, Y. Jiang, X. Zhang, J. Shin, I. Takeuchi, and R. L. Greene. Magnetotransport in nanocrystalline Smb_6 thin films. *AIP Advances*, **5**:077144, (2015).

[128] Y. Xu, I. Miotkowski, C. Liu, J. Tian, H. Nam, N. Alidoust, J. Hu, C.-K. Shih, M. Z. Hasan, and Y. P. Chen. Observation of topological surface state quantum hall effect in an intrinsic three-dimensional topological insulator. *Nature Physics*, **10**:956, (2014).

[129] Tuck C. Choy. *Effective Medium Theory*, volume 45. Oxford: Clarendon Press, (1999).

[130] J. Martin, N. Akerman, G. Ulbricht, T. Lohmann, J. H. Smet, K. von Klitzing, and A. Yacoby. Observation of electron-hole puddles in graphene using a scanning single-electron transistor. *Nature Physics*, **4**:144, (2008).

[131] Y. I. Rodionov and S. V. Syzranov. Conductivity of a weyl semimetal with donor and acceptor impurities. *Physical Review B*, **91**:195107, (2015).

[132] D. A. Pesin, E. G. Mishchenko, and A. Levchenko. Density of states andmagneto-transport in weyl semimetalswith long-range disorder. *Physical Review B*, **92**:174202, (2015).

[133] B. Skinner. Coulomb disorder in three-dimensional dirac systems. *Physical Review B*, **90**:060202(R), (2014).

[134] D. I. Khomskii. *Transition metal compounds*, volume 1. Cambridge University Press, (2014).

[135] Satoru Sugano. *Multiplets of Transition Metal Ions in Crystals*, volume 1. Academic Press, (1970).

[136] G. L. Stamokostas and G. A. Fiete. Mixing of $t_{2g} - e_g$ orbitals in 4d and 5d transition metal oxides. *Physical Review B*, **97**:085150, (2018).

[137] Natalia B. Perkins, Yuriy Sizyuk, and Peter Wölfle. Interplay of many-body and single-particle interactions in iridates and rhodates. *Physical Review B*, **89**:035143, (2014).

[138] John H. Van Vleck. *The Theory of Electric and Magnetic Susceptibilities*, volume . Oxford University Press, (1932).

[139] C. H. Sohn, H.-S. Kim, T. F. Qi, D. W. Jeong, H. J. Park, H. K. Yoo, H. H. Kim, J.-Y. Kim, T. D. Kang, D.-Y. Cho, G. Cao, J. Yu, S. J. Moon, and T. W. Noh. Mixing between $j_{eff} = 1/2$ and 3/2 orbitals in Na_2IrO_3: A spectroscopic and density functional calculation study. *Physical Review B*, **88**:085125, (2013).

[140] Beom Hyun Kim, G. Khaliullin, and B. I. Min. Electronic excitations in the edge-shared relativistic Mott insulator: Na_2IrO_3. *Physical Review B*, **89**:081109, (2014).

[141] R. Comin, G. Levy, B. Ludbrook, Z.-H. Zhu, C. N. Veenstra, J. A. Rosen, Y. Singh, P. Gegenwart, D. Stricker, J. N. Hancock, D. v. d. Marel, I. S. Elfimov, and A. Damascelli. Na_2IrO_3 as a novel relativistic Mott insulator with a 340 mev gap. *Physical Review Letters*, **109**:266406, (2012).

[142] K. W. Plumb, J. P. Clancy, L. J. Sandilands, V. V. Shankar, Y. F. Hu, K. S. Burch, H.-Y. Kee, and Y.-J. Kim. α-$RuCl_3$: A spin-orbit assisted Mott insulator on a honeycomb lattice. *Physical Review B*, **90**:041112, (2014).

[143] L. J. Sandilands, Y. Tian, K. W. Plumb, and Y.-June Kim. Scattering continuum and possible fractionalized excitations in $RuCl_3$. *Physical Review Letters*, **114**(147201), (2015).

[144] A. Koitzsch, C. Habenicht, E. Müller, M. Knupfer, B. Büchner, H. Kandpal, J. v. d. Brink, D. Nowak, A. Isaeva, and T. Doert. j_{eff} description of the honeycomb Mott insulator α-$RuCl_3$. *Physical Review Letters*, **117**:126403, (2016).

[145] F. Hund. Deutung der Molekelspektren, i und ii. *Zeitschrift für Physik*, **40**:742, (1927).

[146] A. Abraham and B. I. Bleaney. *Electron Paramagnetic Resonance of Transition Ions*, volume 1. Oxford: Clarendon Press, (1970).

[147] E. M. Plotnikova, M. Daghofer, J. v. d. Brink, and K. Wohlfeld. Jahn-teller effect in systems with strong on-site spin-orbit coupling. *Physical Review Letters*, **116**(106401), (2016).

[148] G. Jackeli and G. Khaliullin. Mott insulators in the strong spin-orbit coupling limit:from Heisenberg to a quantum compass and Kitaev models. *Physical Review Letters*, **102**:017205, (2009).

[149] G. Khaliullin. Orbital order and fluctuations in Mott insulators. *Progress of Theoretical Physics Supplements*, **160**:155, (2005).

[150] Alexei Kitaev. Anyons in an exactly solved model and beyond. *Annals of Physics*, **321**:2, (2006).

[151] J. G. Rau, E. K.-H. Lee, and H.-Y. Kee. Generic spin model for the honeycomb iridates beyond the Kitaev limit. *Physical Review Letters*, **112**(077204), (2014).

[152] J. G. Rau, E. K.-H. Lee, and H.-Y. Kee. Spin-orbit physics giving rise to novel phases in correlated systems: iridates and related materials. *Annual Review of Condensed Matter Physics*, **7**:195, (2016).

[153] S. Trebst and P. Gegenwart. Spinorbit physics: Kitaev matter. *Nature Physics*, **11**:444, (2015).

[154] J. Chaloupka, G. Jackeli, and G. Khaliullin. Zigzag magnetic order in the iridium oxide Na_2IrO_3. *Physical Review Letters*, **110**:097204, (2013).

[155] R. D. Johnson, S. C. Williams, A. A. Haghighirad, J. Singleton, V. Zapf, P. Manuel, I. I. Mazin, Y. Li, H. O. Jeschke, R. Valentí, and R. Coldea. Monoclinic crystal structure of α-$RuCl_3$ and the zigzag antiferromagnetic ground state. *Physical Review B*, **92**:235119, (2015).

[156] L. Binotto, I. Pollini, and G. Spinolo. Optical and transport properties of the magnetic semiconductor α-$RuCl_3$. *Physica Status Solidi b*, **44**:245, (1971).

[157] I. Pollini. Electronic properties of the narrow-band material α-$RuCl_3$. *Physical Review B*, **53**:12769, (1996).

[158] H.B. Cao, A. Banerjee, J.-Q. Yan, C.A. Bridges, M.D. Lumsden, D.G. Mandrus, D.A. Tennant, B.C. Chakoumakos, and S.E. Nagler. Low-temperature crystal and magnetic structure of α-$RuCl_3$. *Physical Review B*, **93**:134423, (2016).

[159] S. Agrestini, C.-Y. Kuo, K.-T. Ko, Z. Hu, D. Kasinathan, H. B. Vasili, J. Herrero-Martin, S. M. Valvidares, E. Pellegrin, L.-Y. Jang, A. Henschel, M. Schmidt, A. Tanaka, and L. H. Tjeng. Electronically highly cubic conditions for Ru in α-$RuCl_3$. *Physical Review Letters*, **96**:161107, (2017).

[160] J. A. Sears, M. Songvilay, K. W. Plumb, J. P. Clancy, Y. Qiu, Y. Zhao, D. Parshall, and Young-June Kim. Magnetic order in α-$RuCl_3$: A honeycomb-lattice quantum magnet with strong spin-orbit coupling. *Physical Review B*, **91**:144420, (2015).

[161] A. Banerjee, C. A. Bridges, J.-Q. Yan, A. A. Aczel, L. Li, M. B. Stone, G. E. Granroth, M. D. Lumsden, Y. Yiu, J. Knolle, S. Bhattacharjee, D. L. Kovrizhin, R. Moessner, D. A. Tennant, D. G. Mandrus, and S. E. Nagler. Proximate Kitaev quantum spin liquid behaviour in a honeycomb magnet. *Nature Materials*, **15**:733, (2016).

[162] Y. Kubota, H. Tanaka, T. Ono, Y. Narumi, and K. Kindo. Successive magnetic phase transitions in α-$RuCl_3$: XY-like frustrated magnet on the honeycomb lattice. *Physical Review B*, **91**:094422, (2015).

[163] M. Majumder, M. Schmidt, H. Rosner, A. A. Tsirlin, H. Yasuoka, and M. Baenitz. Anisotropic Ru^3+ $4d^5$ magnetism in the α-$RuCl_3$ honeycomb system: Susceptibility, specific heat, and zero-field nmr. *Physical Review B*, **91**:180401, (2015).

[164] I. A. Leahy, C. A. Pocs, P. E. Siegfried, D. Graf, S.-H. Do, K.-Y. Choi, B. Normand, and M. Lee. Anomalous thermal conductivity and magnetic torque response in the honeycomb magnet α-RuCl$_3$. *Physical Review Letters*, **118**:187203, (2017).

[165] S. Reschke, F. Mayr, Z. Wang, S.-H. Do, K.-Y. Choi, and A. Loidl. Electronic and phonon excitations in α-RuCl$_3$. *Physical Review B*, **96**:165120, (2017).

[166] A. Glamazda, P. Lemmens, S.-H. Do, Y. S. Kwon, and K.-Y. Choi. Relation between Kitaev magnetism and structure in α-RuCl$_3$. *Physical Review B*, **95**:174429, (2017).

[167] I. I. Mazin, Harald O. Jeschke, Kateryna Foyevtsova, Roser Valentí, and D. I. Khomskii. Na$_2$IrO$_3$ as a molecular orbital crystal. *Physical Review Letters*, **109**:197201, (2012).

[168] B. H. Kim, T. Shirakawa, and S. Yunoki. From a quasimolecular band insulator to a relativistic Mott insulator in t_{2g}^5 systems with a honeycomb lattice structure. *Physical Review Letters*, **117**:187201, (2016).

[169] S. Sinn, C. H. Kim, B. H. Kim, K. D. Lee, C. J. Won, J. Seop, M. Han, Y. J. Chang, N. Hur, H. Sato, B.-G. Park, C. Kim, H.-D. Kim, and T. W. Noh. Electronic structure of the Kitaev material α-RuCl$_3$ probed by photoemission and inverse photoemission spectroscopies. *Scientific Reports*, **6**:39544, (2016).

[170] Y. Kobayashi, T. Okada, K. Asai, M. Katada, H. Sano, and F. Ambe. Moessbauer spectroscopy and magnetization studies of α- and β-RuCl$_3$. *Inorganic Chemistry*, **31**:4570, (1992).

[171] L. J. Sandilands, Y. Tian, A. A. Reijnders, H.-S. Kim, K. W. Plumb, and Y.-J. Kim. Spin-orbit excitations and electronic structure of the putative Kitaev magnet α-RuCl$_3$. *Physical Review B*, **93**:075144, (2016).

[172] Xiaoqing Zhou, Haoxiang Li, J. A. Waugh, S. Parham, Heung-Sik Kim, J. A. Sears, A. Gomes, Hae-Young Kee, Young-June Kim, and D. S. Dessau. Angle-resolved photoemission study of the Kitaev candidate α-RuCl$_3$. *Physical Review B*, **94**:161106, (2016).

[173] B. N. Figgis, J. Lewis, F. E. Mabbs, and G. A. Webb. *Magnetic properties of some iron(III) and ruthenium(III) low-spin complexes*, volume 1. Journal of the Chemical Society A, 422-426, (1966).

[174] B. N. Figgis and M. A. Hitchman. *Ligand Field Theory and its Applications*, volume 1. Wiley-VCH, (1999).

[175] R. Yadav, N. A. Bogdanov, V. M. Katukuri, S. Nishimoto, J. v. d. Brink, and L. Hozoi. Kitaev exchange and field-induced quantum spin-liquid states in honeycomb α-RuCl$_3$. *Scientific Reports*, **6**:37925, (2016).

[176] J. Eroles. Temperature dependence of the spin dynamics in CuO layers. *Physical Review B*, **65**:092404, (2002).

[177] E. Gagliano, F. Lema, S. Bacci, J. J. V. Alvarez, and J. Lorenzana. Optical absorption of CuO_3 antiferromagnetic chains at finite temperatures. *Physical Review B*, **62**:1218, (2000).

[178] J. Deisenhofer, I. Leonov, M. V. Eremin, C. Kant, P. Ghigna, F. Mayr, V. V. Iglamov, V. I. Anisimov, and D. van der Marel. Optical evidence for symmetry changes above the Neel temperature of $KCuF_3$. *Physical Review Letters*, **101**:157406, (2008).

[179] S. M. Winter, K. Riedl, P. A. Maksimov, A. L. Chernyshev, A. Honecker, and R. Valentí. Breakdown of magnons in a strongly spin-orbital coupled magnet. *Nature Communications*, **8**:1152, (2017).

[180] M. Grüninger, D. van der Marel, A. Damascelli, A. Erb, T. Nunner, and T. Kopp. Midinfrared absorption in $yba_2Cu_3O_6$: Evidence for a failure of spin-wave theory for spin 1/2 in two dimensions. *Physical Review B*, **62**:12422, (2000).

[181] M. Windt, M. Grüninger, T. Nunner, C. Knetter, K. P. Schmidt, G. S. Uhrig, T. Kopp, A. Freimuth, U. Ammerahl, B. Büchner, and A. Revcolevschi. Observation of two-magnon bound states in the two-leg ladders of $(ca,la)_{14}Cu_{24}O_{41}$. *Physical Review Letters*, **87**:127002, (2001).

[182] S. M. Winter, Y. Li, H. O. Jeschke, and R. Valentí. Challenges in design of Kitaev materials: Magnetic interactions from competing energy scales. *Physical Review B*, **93**:214431, (2016).

[183] C. G. Fatuzzo, M. Dantz, S. Fatale, P. Olalde-Velasco, N. E. Shaik, B. Dalla Piazza, S. Toth, J. Pelliciari, R. Fittipaldi, A. Vecchione, N. Kikugawa, J. S. Brooks, H. M. Rønnow, M. Grioni, Ch. Rüegg, T. Schmitt, and J. Chang. Spin-orbit-induced orbital excitations in Sr_2RuO_4 and Ca_2RuO_4: A resonant inelastic x-ray scattering study. *Physical Review B*, **91**:155104, (2015).

[184] C. N. Veenstra, Z.-H. Zhu, M. Raichle, B. M. Ludbrook, A. Nicolaou, B. Slomski, G. Landolt, S. Kittaka, Y. Maeno, J. H. Dil, I. S. Elfimov, M.W. Haverkort, and A. Damascelli. Spin-orbital entanglement and the breakdown of singlets and triplets in Sr_2RuO_4 revealed by spin- and angle-resolved photoemission spectroscopy. *Physical Review Letters*, **112**:127002, (2014).

[185] I. Prigogine. *Advances in Chemical Physics*, volume 5. Wiley-VCH, (1963).

[186] J. P. Clancy, N. Chen, C. Y. Kim, W. F. Chen, K. W. Plumb, B. C. Jeon, T. W. Noh, and Y.-J. Kim1. Spin-orbit coupling in iridium-based 5d compounds probed by x-ray absorption spectroscopy. *Physical Review B*, **86**:195131, (2012).

[187] V. M. Katukuri, S. Nishimoto, V. Yushankhai, A. Stoyanova, H. Kandpal, R. Coldea, I. Rousochatzakis, L. Hozoi, and J. v. d. Brink. Kitaev interactions between j = 1/2 moments in honeycomb Na_2IrO_3 are large and ferromagnetic: insights from ab initio quantum chemistry calculations. *New Journal of Physics*, **16**:013056, (2014).

[188] Y. Singh and P. Gegenwart. Antiferromagnetic Mott insulating state in single crystals of the honeycomb lattice material Na_2IrO_3. *Physical Review B*, **82**:064412, (2010).

[189] S. H. Chun, J. Kim, J. Kim, H. Zheng, C. C. Stoumpos, C. D. Malliakas, J. F. Mitchell, K. Mehlawat, Y. Singh, Y. Choi, T. Gog, A. Al-Zein, M. M. Sala, M. Krisch, J. Chaloupka, G. Jackeli, G. Khaliullin, , and B. J. Kim. Direct evidence for dominant bond-directional interactions in a honeycomb lattice iridate Na_2IrO_3. *Nature Physics*, **11**:462, (2015).

[190] Y. Singh, S. Manni, J. Reuther, T. Berlijn, R. Thomale, W. Ku, S. Trebst, and P. Gegenwart. Relevance of the Heisenberg-Kitaev model for the honeycomb lattice iridates A_2IrO_3. *Physical Review Letters*, **108**:127203, (2013).

[191] X. Liu, T. Berlijn, W.-G. Yin, W. Ku, A. Tsvelik, Y.-J. Kim, H. Gretarsson, Y. Singh, P. Gegenwart, and J. P. Hill. Long-range magnetic ordering in Na_2IrO_3. *Physical Review B*, **83**:220403, (2011).

[192] F. Ye, S. Chi, H. Cao, B. C. Chakoumakos, J. A. F.-Baca, R. Custelcean, T. F. Qi, O. B. Korneta, and G. Cao. Direct evidence of a zigzag spin-chain structure in the honeycomb lattice: A neutron and x-ray diffraction investigation of single-crystal Na_2IrO_3. *Physical Review B*, **85**:180403, (2012).

[193] H. Gretarsson, J. P. Clancy, Yogesh Singh, P. Gegenwart, J. P. Hill, J. Kim, M. H. Upton, A. H. Said, D. Casa, T. Gog, and Y.-J. Kim. Magnetic excitation spectrum of Na_2IrO_3 probed with resonant inelastic x-ray scattering. *Physical Review B*, **87**:220407, (2013).

[194] B. J. Kim, H. Jin, S. J. Moon, J.-Y. Kim, B.-G. Park, C. S. Leem, J. Yu, T. W. Noh, C. Kim, S.-J. Oh, J.-H. Park, V. Durairaj, G. Cao, and E. Rotenberg. Novel $j_{eff} = 1/2$ Mott state induced by relativistic spin-orbit coupling in Sr_2IrO_4. *Physical Review Letters*, **101**:076402, (2008).

[195] V. Hermann, J. Ebad-Allah, F. Freund, I. M. Pietsch, A. Jesche, A. A. Tsirlin, J. Deisenhofer, M. Hanfland, P. Gegenwart, and C. A. Kuntscher. High-pressure versus isoelectronic doping effect on the honeycomb iridate Na_2IrO_3. *Physical Review B*, **96**:195137, (2017).

[196] B. Andlauer, J. Schneider, and W. Tolksdorf. Optical absorption, fluorescence, and electron spin resonance of Ir^{4+} on octahedral sites in $Y_3Ga_5O_{12}$. *Physica status solidi b*, **73**:533, (1976).

[197] K. W. Blazey and F.Levy. Epr of rhodium, osmium and iridium-doped rutile. *Solid State Communications*, **59**:335, (1986).

[198] H. Gretarsson, J. P. Clancy, X. Liu, J. P. Hill, E. Bozin, Y. Singh, S. Manni, P. Gegenwart, J. Kim, A. H. Said, D. Casa, T. Gog, M. H. Upton, H.-S. Kim, J. Yu, V. M. Katukuri, L. Hozoi, J. v. d. Brink, and Y.-J. Kim. Crystal-field splitting and correlation effect on the electronic structure of A_2IrO_3. *Physical Review Letters*, **110**:076402, (2013).

[199] Y. Li, K. Foyevtsova, H. O. Jeschke, and R. Valentí. Analysis of the optical conductivity for A_2IrO_3 (a=na, li) from first principles. *Physical Review B*, **91**:161101, (2015).

[200] K. Foyevtsova, H. O. Jeschke, I. I. Mazin, D. I. Khomskii, and R. Valent. Ab initio analysis of the tight-binding parameters and magnetic interactions in Na_2IrO_3. *Physical Review B*, **88**:035107, (2013).

[201] M. Kim, B. H. Kim, and B. I. Min. Insulating nature of Na_2IrO_3: Mott-type or Slater-type. *Physical Review B*, **93**:195135, (2016).

[202] S. K. Choi, R. Coldea, A. N. Kolmogorov, T. Lancaster, I. I. Mazin, S. J. Blundell, P. G. Radaelli, Y. Singh, P. Gegenwart, K. R. Choi, S.-W. Cheong, P. J. Baker, C. Stock, and J. Taylor. Spin waves and revised crystal structure of honeycomb tridate Na_2IrO_3. *Physical Review B*, **108**:127204, (2012).

[203] X. Liu, Vamshi M. Katukuri, L. Hozoi, Wei-Guo Yin, M. P. M. Dean, M. H. Upton, J. Kim, D. Casa, A. Said, T. Gog, T. F. Qi, G. Cao, A. M. Tsvelik, J. v. d. Brink, , and J. P. Hill. Testing the validity of the strong spin-orbit-coupling limit for octahedrally coordinated iridate compounds in a model system Sr_3CuIrO_6. *Physical Review Letters*, **109**:157401, (2012).

[204] A. Gössling, R. Schmitz, H. Roth, M. W. Haverkort, T. Lorenz, J. A. Mydosh, E. M.-Hartmann, and M. Grüninger. Mott-Hubbard exciton in the optical conductivity of $YTiO_3$ and $SmTiO_3$. *Physical Review B*, **78**:075122, (2008).

[205] B. H. Kim, G. Khaliullin, and B. I. Min. Magnetic couplings, optical spectra, and spin-orbit exciton in 5*d* electron Mott insulator Sr_2IrO_4. *Physical Review Letters*, **109**:167205, (2012).

[206] Y. Sizyuk, C. Price, P. Wölfle, and N. B. Perkins. Importance of anisotropic exchange interactions in honeycomb iridates: Minimal model for zigzag antiferromagnetic order in Na_2IrO_3. *Physical Review B*, **90**:155126, (2014).

Acknowledgment

I do not know whether the mentoring I received is the nominal condition, but I know that I can count myself lucky for working in the group of Prof. Markus Grüninger. In the last years Markus taught me scientific working, starting from naming files by the important information about the measurement rather than the date and the number of the batch. Via storing all data not in one folder but in subfolders. Through to scientific writing, which was most probably the greatest challenge. Besides teaching these skills Markus had always time for discussions. Of which I took often advantage, since discussions with a smart person who knows more than oneself are the best way to learn, especially if one is treated as equal. Therefore I am grateful.

However, within the work group I had many discussions fruitful discussions as well, especially with Malte Langenbach and Alessandro Revelli, but as well with Ignatio Vergara, Philipp Warzanowski, and Chin Chyi Loo. I appreciated the extremely cooperative and friendly atmosphere in the group. This atmosphere can be obtained in the whole institute and physics department. I like to think of the work that was done in collaboration with Jonathan Lux, Achim Rosch and Paul van Loosdrecht and the project with Thomas Michely, Jolie Wouter and Timo Knispel.

An experimental physicist is usually depending on samples, especially their quality. Since I got many excellent samples, I want to thank everybody who synthesized samples for me, namely Zhiwei Wang and the group of Yoichi Ando and Petra Becker-Bohatý. Additionally, I must not forget Gregor Mussler in the group of Detlef Grützmacher.

I own this work to my friends and my girlfriend Hille, since they support me and are responsible for my work-life balance. Finally, I want to thank my parents for supporting me and especially for raising me to this happy person which I am, even though you cannot always tell this from my face.

Ich versichere, dass ich die von mir vorgelegte Dissertation selbständig angefertigt, die benutzten Quellen und Hilfsmittel vollständig angegeben und die Stellen der Arbeit -einschlielich Tabellen, Karten und Abbildungen-, die anderen Werken im Wortlaut oder dem Sinn nach entnommen sind, in jedem Einzelfall als Entlehnung kenntlich gemacht habe; dass diese Dissertation noch keiner anderen Fakultät oder Universität zur Prüfung vorgelegen hat; dass sie -abgesehen von unten angegebenen Teilpublikationen- noch nicht veröffentlicht worden ist sowie, dass ich eine solche Veröffentlichung vor Abschluss des Promotionsverfahrens nicht vornehmen werde. Die Bestimmungen der Promotionsordnung sind mir bekannt. Die von mir vorgelegte Dissertation ist von Prof. Dr. Markus Grüninger betreut worden.

Teilpublikation:

N. Borgwardt, J. Lux, I. Vergara, Z. Wang, A. A. Taskin, K. Segawa, P. H. M. v. Loosdrecht, Y. Ando, A. Rosch, and M. Grüninger, Self-organized charge puddles in a three-dimensional topological material, **93**, 245149 (2016).

T. Knispel, W. Jolie, N. Borgwardt, J. Lux, Zhiwei Wang, Yoichi Ando, A. Rosch, T. Michely, and M. Grüninger, Charge puddles in the bulk and on the surface of the topological insulator $BiSbTeSe_2$ studied by scanning tunneling microscopy and optical spectroscopy, Physical Review B, **96**, 195135 (2017).